



Journal of
*Marine Science
and Engineering*

Climate Change and Marine Geological Dynamics

Edited by
George Kontakiotis and Assimina Antonarakou

Printed Edition of the Special Issue Published in
Journal of Marine Science and Engineering

Climate Change and Marine Geological Dynamics

Climate Change and Marine Geological Dynamics

Editors

George Kontakiotis

Assimina Antonarakou

MDPI • Basel • Beijing • Wuhan • Barcelona • Belgrade • Manchester • Tokyo • Cluj • Tianjin



Editors

George Kontakiotis	Assimina Antonarakou
Department of Historical Geology-Paleontology National and Kapodistrian University of Athens, School of Earth Sciences, Faculty of Geology and Geoenvironment Athens Greece	Department of Historical Geology-Paleontology National and Kapodistrian University of Athens, School of Earth Sciences, Faculty of Geology and Geoenvironment Athens Greece

Editorial Office

MDPI
St. Alban-Anlage 66
4052 Basel, Switzerland

This is a reprint of articles from the Special Issue published online in the open access journal *Journal of Marine Science and Engineering* (ISSN 2077-1312) (available at: www.mdpi.com/journal/jmse/special_issues/cynthia.climate.change.marine.geological.dynamics).

For citation purposes, cite each article independently as indicated on the article page online and as indicated below:

LastName, A.A.; LastName, B.B.; LastName, C.C. Article Title. <i>Journal Name</i> Year , <i>Volume Number</i> , Page Range.
--

ISBN 978-3-0365-1698-1 (Hbk)

ISBN 978-3-0365-1697-4 (PDF)

© 2021 by the authors. Articles in this book are Open Access and distributed under the Creative Commons Attribution (CC BY) license, which allows users to download, copy and build upon published articles, as long as the author and publisher are properly credited, which ensures maximum dissemination and a wider impact of our publications.

The book as a whole is distributed by MDPI under the terms and conditions of the Creative Commons license CC BY-NC-ND.

Contents

About the Editors	vii
Preface to "Climate Change and Marine Geological Dynamics"	ix
George Kontakiotis, Leonidas Moforis, Vasileios Karakitsios and Assimina Antonarakou Sedimentary Facies Analysis, Reservoir Characteristics and Paleogeography Significance of the Early Jurassic to Eocene Carbonates in Epirus (Ionian Zone, Western Greece) Reprinted from: <i>Journal of Marine Science and Engineering</i> 2020, 8, 706, doi:10.3390/jmse8090706 .	1
Christina Giamali, George Kontakiotis, Efterpi Koskeridou, Chryssanthi Ioakim and Assimina Antonarakou Key Environmental Factors Controlling Planktonic Foraminiferal and Pteropod Community's Response to Late Quaternary Hydroclimate Changes in the South Aegean Sea (Eastern Mediterranean) Reprinted from: <i>Journal of Marine Science and Engineering</i> 2020, 8, 709, doi:10.3390/jmse8090709 .	27
Stergios D. Zarkogiannis, Assimina Antonarakou, Vincent Fernandez, P. Graham Mortyn, George Kontakiotis, Hara Drinia and Mervyn Greaves Evidence of Stable Foraminifera Biomineralization during the Last Two Climate Cycles in the Tropical Atlantic Ocean Reprinted from: <i>Journal of Marine Science and Engineering</i> 2020, 8, 737, doi:10.3390/jmse8100737 .	51
Stergios D. Zarkogiannis, George Kontakiotis, Georgia Gkaniatsa, Venkata S. C. Kuppili, Shashidhara Marathe, Kazimir Wanelik, Vasiliki Lianou, Evangelia Besiou, Panayiota Makri and Assimina Antonarakou An Improved Cleaning Protocol for Foraminiferal Calcite from Unconsolidated Core Sediments: HyPerCal—A New Practice for Micropaleontological and Paleoclimatic Proxies Reprinted from: <i>Journal of Marine Science and Engineering</i> 2020, 8, 998, doi:10.3390/jmse8120998 .	69
George Kontakiotis, Eirini Efstathiou, Stergios D. Zarkogiannis, Evangelia Besiou and Assimina Antonarakou Latitudinal Differentiation among Modern Planktonic Foraminiferal Populations of Central Mediterranean: Species-Specific Distribution Patterns and Size Variability Reprinted from: <i>Journal of Marine Science and Engineering</i> 2021, 9, 551, doi:10.3390/jmse9050551 .	81
Stergios D. Zarkogiannis Disruption of the Atlantic Meridional Circulation during Deglacial Climates Inferred from Planktonic Foraminiferal Shell Weights Reprinted from: <i>Journal of Marine Science and Engineering</i> 2021, 9, 519, doi:10.3390/jmse9050519 .	105
Panayota Makri, Eleni Stathopoulou, Demetrios Hermides, George Kontakiotis, Stergios D. Zarkogiannis, Hariklia D. Skilodimou, George D. Bathrellos, Assimina Antonarakou and Michael Scoullou The Environmental Impact of a Complex Hydrogeological System on Hydrocarbon-Pollutants' Natural Attenuation: The Case of the Coastal Aquifers in Eleusis, West Attica, Greece Reprinted from: <i>Journal of Marine Science and Engineering</i> 2020, 8, 1018, doi:10.3390/jmse8121018	123
Demetrios Hermides, Panayota Makri, George Kontakiotis and Assimina Antonarakou Advances in the Coastal and Submarine Groundwater Processes: Controls and Environmental Impact on the Thriassion Plain and Eleusis Gulf (Attica, Greece) Reprinted from: <i>Journal of Marine Science and Engineering</i> 2020, 8, 944, doi:10.3390/jmse8110944 .	137

Qiang Shu, Shunjie Zhang and Ye Chen

Physicochemical Property Indexes of Sediment Lixiviums in Sea-Land Interaction Zone of Subei Basin and Their Significance to Transgression

Reprinted from: *Journal of Marine Science and Engineering* **2021**, 9, 719, doi:10.3390/jmse9070719 . **157**

About the Editors

George Kontakiotis

George Kontakiotis achieved a Ph.D. degree in Paleoceanography in 2012 at the University of Athens, where he later worked as Laboratory and Teaching Staff in the fields of Marine Geology and Sedimentology. His major research contributions include developing novel approaches on the distribution and pathways of diagenesis in Mg/Ca paleothermometry. He has further worked on sedimentological and paleoceanographic reconstructions at different time scales by means of marine cores and land sections and related processes. His main research topics are summarized as follows: environmental sedimentology; marine petroleum systems and the exploitation of natural energy resources; integrated bio-cyclo-tephro-stratigraphy; coastal engineering; calibration-validation and the application of geochemical proxies for sea surface temperature (SST) and salinity (SSS); applied environmental micropaleontology as a bio-monitoring tool; Holocene sea-level variations; and ocean/climate changes during the Quaternary Period.

Assimina Antonarakou

Assimina Antonarakou is a Professor of Marine Geology–Micropaleontology–Didactics on Geosciences, and Vice President of the Faculty of Geology and Geoenvironment at the University of Athens. Her PhD Thesis dealt with Miocene cyclic sedimentary successions of the eastern Mediterranean in terms of orbital periodicities and paleoclimatic variations based on planktonic foraminiferal assemblages. Her main research topics are summarized as follows: planktonic foraminiferal eco-biostratigraphy, geobiology and paleoceanography; astronomical frequencies in paleoclimates; extreme geological events; marine environmental monitoring; ocean dynamics and sea-level changes; natural and human environmental stressors; and foraminiferal trace metals and stable isotopes. She has participated in several national and international projects focused on multiproxy ecosystem responses to past and present environmental events, and she is the co-author of more than 50 peer-reviewed publications in international journals.

Preface to "Climate Change and Marine Geological Dynamics"

This Special Issue contains nine scientific papers related to determination of the nature, timing and magnitude of natural hydroclimate variability during modern and past geological times. Such an approach will be essential for addressing the challenges posed by climate change in the sedimentary archive, the hydrological regime, and the subsequent response of the marine biota through time. The editors wish to thank the contributors and the support of the *JMSE* editorial staff, whose professionalism and dedication have made this Special Issue possible. Finally, we kindly thank all authors for their participation and contribution to the volume, as well as all reviewers who have diligently reviewed the submitted manuscripts, and substantially contributed to the high quality of these published papers. We also highly appreciate the editorial support provided by the *Journal of Marine Science and Engineering*.

George Kontakiotis, Assimina Antonarakou

Editors

Article

Sedimentary Facies Analysis, Reservoir Characteristics and Paleogeography Significance of the Early Jurassic to Eocene Carbonates in Epirus (Ionian Zone, Western Greece)

George Kontakiotis *, Leonidas Moforis *, Vasileios Karakitsios and Assimina Antonarakou

Department of Historical Geology and Paleontology, Faculty of Geology and Geoenvironment, National and Kapodistrian University of Athens, Panepistimiopolis, 15784 Athens, Greece; vkarak@geol.uoa.gr (V.K.); aantonar@geol.uoa.gr (A.A.)

* Correspondence: gkontak@geol.uoa.gr (G.K.); leomof@geol.uoa.gr (L.M.); Tel.: +30-2107274804 (G.K.)

Received: 27 August 2020; Accepted: 10 September 2020; Published: 11 September 2020



Abstract: Sedimentological, micropalaeontological, and marine geological results from the Early Jurassic to Eocene carbonate formations of the Ionian zone, from six localities of Epirus, provide new insights into the basin palaeogeographic evolution and better correlation with coeval analogous tectono-stratigraphic successions along the southern margin of the Neo-Tethys Ocean. Facies analysis allowed the recognition of several microfacies types and their depositional characteristics. During the Early Jurassic, autochthonous carbonates (Pantokrator Limestones) were deposited in shallow-water environment. The overlying (hemi)pelagic Siniais or their lateral equivalent Louros Limestones were deposited to the basin borders and mark the general deepening of the Ionian domain. During Toarcian to Tithonian, the Ionian Basin was characterized by an internal differentiation in small sub-basins with half-graben geometry presenting abrupt thickness and facies changes. The deeper parts were characterized by continuous sedimentation, while the elevated parts were marked by unconformities. The Early Cretaceous marks the homogenization of sedimentation by the deposition of the pelagic Vigla Limestones all over the Ionian zone. The transition from the Early to Late Cretaceous records a significant carbonate diversification in terms of biota assemblages, and related mineralogy due to intense tectonic activity in the region. From Late Cretaceous to Paleogene, allochthonous carbonates were transported to the outer shelf by turbidity currents (calciturbidites) and/or debris flows (limestones with breccia) formed by the gravitational collapse of the platform margin. Additional porosity and bulk density measurements showed that petrophysical behavior of these carbonates are controlled by the depositional environment and further influenced by diagenetic processes. The partly dolomitized neritic Jurassic carbonates, but mainly the Senonian calciturbidites and the microbrecciated Paleocene/Eocene limestones display the higher average porosity values, and therefore present enhanced carbonate reservoir quality.

Keywords: microfacies types; Pantokrator Limestones; Vigla Formation; Senonian calciturbidites; Eocene brecciated limestones; carbonate porosity; petroleum prospectivity; stratigraphic correlations; marine biogenic carbonates; depositional environment

1. Introduction

Marine biogenic carbonates are among the most important archives of Earth's history reflecting past changes in ocean chemistry, water mass circulation and the evolution of life [1–10]. Particularly during the Cretaceous, changes in climate, oceanographic circulation, sea level, tectonic and volcanic activity contributed to triggering widespread crisis events, which resulted in world-wide anoxic

episodes [11–17], drastic facies variations and biotic changes [18–23], and diffusion of bauxite deposits [24,25], among others. Such complex events were reflected on biotic and non-biotic constituents of the carbonate platforms and on the architecture of their depositional systems.

Within the Mediterranean Tethys (Neo-Tethys) Ocean, the Mesozoic-Paleogene Eras witnessed the development of vast carbonate platform belts that fringed its margins and passed into deep marine equivalents, completing thus the marginal succession in the deeper parts of the basin [26–29]. These successions, including the slope deposits in the platform margins, provide an excellent example of the evolution of depositional sequences ranging from the platform through rimmed carbonate-shelf to pelagic depositional settings, and further characterize long intervals in the rifting and subsidence history of past peri-Tethyan continents. Among them, the carbonate platform to basin transition can give rise to fragmentary distribution of marginal slope successions as fault-bounded units [30–32]. Such confined carbonate units are also considered to be aquifer systems, hydraulically independent of their siliciclastic cover, and therefore, can build prolific reservoirs and become potential exploration targets for oil and gas throughout the entire Mediterranean basin.

Within the Ionian Zone, both the Early Jurassic neritic limestones and dolomites, and the Late Cretaceous to Eocene re-sedimented carbonates (calcareous turbidites and coarser breccia) are considered the main reservoir successions and exploration targets for oil and gas in western Greece [33–35], central and southern Adriatic offshore Italy [36,37], and onshore Albania [35,38–40]. The Jurassic karstified platform carbonate facies represent an excellent analogue for the carbonate reservoirs, where the sea-level drawdown and subaerial exposure of the carbonate reef enhanced the facies reservoir quality. Moreover, the calciturbidites can be of great economic importance and they can serve as reservoir rocks [39,41,42], due to their high porosity and bulk density values, which can be additionally enhanced by the development of chert nodules [43]. However, the nature and distribution of these deposits along with their depositional mechanism processes and environmental conditions, especially in western Greece, are still poorly constrained. The high heterogeneity related to fabric, texture, fractures that usually characterize such kind of reservoirs has been highlighted by several authors [42,44–51]. Understanding heterogeneity of carbonate reservoir helps predicting reservoir petrophysical and geomechanical behaviors [52–54], which in turn play a crucial role in their exploration, production, and development [55–57]. In this regard, high-resolution sedimentological outcrop data are essential, because they help to fill the gap with respect to subsurface data, which assists in refining reservoir models. Petrographic constraints based on facies analysis provide sedimentological features and micro-textural characteristics, which are the key-link between the rock depositional/diagenetic history and its physical properties.

In the present study, we introduce a complete record of the marginal successions in the western (Ionian basin) segment of the southern Tethys, which consists of the Early Jurassic to Eocene carbonate platform and slope to basin successions from the Epirus region (Figure 1). This integrated study aims to define the Mesozoic-Paleogene depositional history, based on lithostratigraphic characteristics and reservoir petrophysical behaviors in the central Ionian domain, a major hydrocarbon prolific basin in western Greece. This was accomplished by detailed sedimentological and geomechanical/petrophysical analyses of the carbonate succession, in conjunction with a synthetic paleogeographic reconstruction. Beyond the hydrocarbon prospectivity, this work has further implications for regional geology, since it contributes to describing the evolution of these carbonates, and to a better understanding of the Ionian zone (pre-, syn- and post-rift stages; [34,58]) in western Greece, a region with crucial economic and strategic importance.

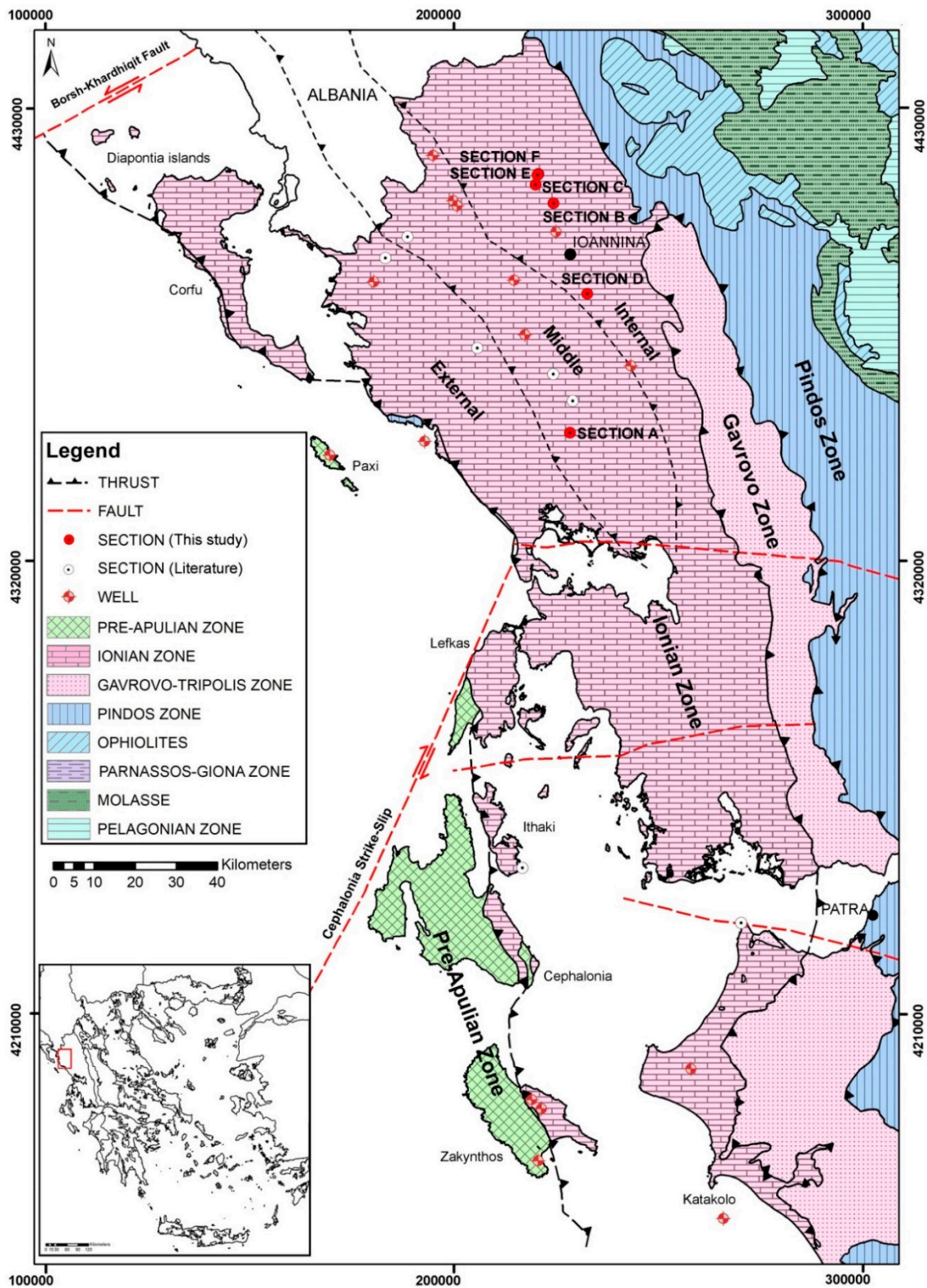


Figure 1. Geological map of the external Hellenides in NW Greece (modified from [34,35]) illustrating the principal tectonostratigraphic zones: Pre-Apulia, Ionian, Gavrovo, Pindos. The red box shows the study area, the northwestern part of the Epirus region, where the separation of Ionian zone to external, middle, and internal sub-basins along with the regional locations of the study sections to be also indicated. Legend interpretations are presented in the inset.

2. Geological Setting

2.1. Tectonostratigraphic Evolution of Ionian Basin

Western Greece is dominated by the external zones of the Hellenides fold-and-thrust belt, namely the pre-Apulian, Ionian and Gavrovo-Tripolis zones. At a regional scale (hundreds of kilometers), this Alpine belt records the initiation, development and final destruction of the southeastern margin of the Tethys Ocean and the consequent continent-continent collision between the Apulian and Pelagonia micro-continents to the east [34,58–63]. On a smaller scale (tens of kilometers), the various sub-basins of the Hellenic Tethyan margin have been inverted to produce the main Hellenic thrust sheets or folded zones [58,59,64]. The Ionian zone, which is bounded westwards by the Ionian thrust and eastwards by the Gavrovo thrust, extends from Albania to the north, forms most of the Epirus region and parts of the Ionian islands and continues southwards to central Greece, Crete and the Dodecanese. According to [65,66], the Ionian basin was subdivided into the internal, central and external Ionian sub-basins (Figure 1).

The tectonostratigraphic evolution of the Ionian zone is reflected on the deposition of three distinct sequences indicative of different tectonic regimes [34,58]: (1) a pre-rift sequence is represented by the Early Jurassic platform Pantokrator Limestones, which overly Early to Mid-Triassic evaporites through Foustapidima Limestones of Ladinian-Rhetian age, (2) a syn-rift sequence (Pliensbachian-Tithonian) deposited during extensional faulting and halokinesis of the Triassic evaporites, which caused the formation of the Ionian basin and its internal synrift differentiation into smaller sub-basins characterized by asymmetric half-graben geometry and different carbonate thickness accumulation [42,58]. Complete Toarcian-Tithonian syn-rift pelagic sequences (Siniais and lateral equivalent Louros Limestones, Ammonitico Rosso or lower Posidonia beds, Limestone with filaments, Upper Posidonia beds) are located in the deeper part of the half-grabens, while unconformities interrupt these sequences in the rift shoulders, (3) a post-rift sequence (Early Cretaceous-Eocene) deposited after the cessation of extensional faulting, is defined by a synchronous throughout the basin Early Berriassian break-up, which is marked by an unconformity at the base of the pelagic Vigla Limestones. The Mesozoic to Eocene carbonate succession passes upwards to the flysch synorogenic sedimentation (siliciclastic turbidites), which began at the Eocene–Oligocene boundary and revealed progressively diminishing thicknesses from the internal to the external areas. Until the Early Miocene, the basin was filled with submarine fan deposits, in response to movement of Pindos thrust, compressional structures, deformation of the external Hellenides which migrated westwards, uplift of the entire Hellenides orogenic belt, and development of a foreland basin at the edge of the Apulian microcontinent [67–71].

2.2. Lithostratigraphy of Jurassic-Eocene Formations in the Ionian Basin

All the study sections are situated within the middle-internal Ionian Zone, in Epirus region near Ioannina (Figure 2A–E). They represent to the Mesozoic-Paleogene pre- to post-rift sequences of Ionian zone, and particularly the upper part of Early Jurassic Pantokrator Limestones, the pelagic Early Cretaceous Vigla Limestones, the Late Cretaceous Senonian Limestones, and the microbreccious limestones of Paleocene/Eocene age. These formations are described in stratigraphic order as follows.

2.2.1. Pantokrator Limestones and Lateral Equivalents

Early Jurassic (Hettangian to Sinemurian) Pantokrator Limestones represent the upper part of the pre-rift sequence of the Ionian zone [64,72]. This formation can be described as a neritic formation, consisted of limestones and dolomites with calcareous algae and benthic foraminifera of more than 1000 m of total thickness. These shallow-water limestones overlie Early to Middle Triassic evaporites (>2000 m thick) and the Foustapidima Limestones of the Ladinian–Rhaetian. Due to their remarkable facies' homogeneity, such Jurassic marine deposits represent an extensive carbonate platform at that time covering the entire region from the Apulian to the Gavrovo zone [58]. The overlying syn-rift sequence in the deeper part of the half-graben sub-basins begins with the Pliensbachian pelagic Siniais

Limestones and its lateral equivalent Louros Limestones (both indicative of the first deepening event of the Ionian basin), overlain in some sub-basins by the succession “Ammonitico Rosso”, “Limestones with filaments”, and “Upper Posidonia Beds”, while in others, the “Ammonitico Rosso” is replaced by the coeval “Lower Posidonia Beds” in the previous sequence, or even the whole sequence is represented by the undifferentiated Posidonia Beds [34,58]. The boundary between the Pantokrator Limestones and Louros or Siniais Limestones is gradational.

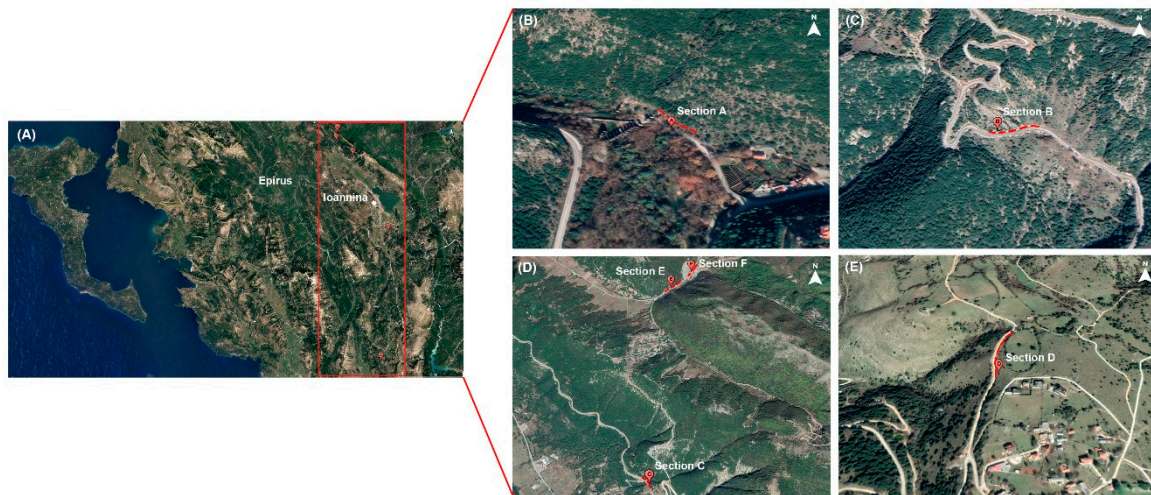


Figure 2. Google Earth maps of (A) Studied region in Epirus (NW Greece) into the red box; (B) Agios Georgios section (lat: 39°16′14.99″ N, lon: 20°50′59.43″ E); (C) Perivleptos section (lat: 39°46′21.90″ N, lon: 20°46′48.34″ E); (D) Vigla (lat: 39°48′33.45″ N, lon: 20°43′38.73″ E), Asprageli-1 (lat: 39°45′57.42″ N, lon: 20°43′58.25″ E) and Asprageli-2 (lat: 39°49′54.00″ N, lon: 20°43′58.25″ E) sections; (E) Koloniatia section (lat: 39°34′52.46″ N, lon: 20°53′11.41″ E). The orange symbols mark the locations of the six study sections, and red dashed lines correspond to the major studied outcrops respectively.

2.2.2. Vigla Formation

This pelagic formation can be described as sub-lithographic thin-bedded to platy deposits, rich in planktonic organisms (*Calpionelles*, *Radiolaires*, and *Globotruncanes*) of Cretaceous age. Their continuity is usually interrupted by thin intercalations, chert lenses, or even thin chert layers. Its dominant lithology consists of light grey to yellowish micrites and radiolarian biomicrites (wackestones to packstones). More explicitly, the calcareous beds (Vigla Limestones) of the lower part consist of mudstones-wackestones, biomicrites with foraminifera and radiolaria, and siliceous wackestones and packstones [42]. In the upper part, this formation consists of the Vigla Shale member (also known as “Upper siliceous zone”; [66]) composed by yellow marly or shaly limestones and shales with chert intercalations, and red to green or locally black clay layers. The latter contains the equivalent of the anoxic events of Selli (OAE1a) during the Aptian-Albian, Paquier Evet (OAE1b) of Early Albian age and Bonarelli (OAE2) at the Cenomanian-Turonian boundary in the Ionian zone [12,14,73,74], and extends to Italy and Albania. Vigla Limestones generally feature considerable lateral variations in thickness, mainly in the basin borders where its thickness may reach the double of its average, which is indicative of persistent differential subsidence [34,58,59]. In the internal sub-basin, the Vigla Limestones consist of compact, thick-bedded, often bituminous, dolomitic limestones, with lenses of slightly dolomitized microbreccia and thin cherty intercalated layers or nodules. It is also characterized by the presence of several aptychus in its lower part [59,64]. In Epirus, along the eastern border of the central Ionian zone, phosphatic horizons are intercalated with the uppermost horizons of the Vigla Limestone formation, stratigraphically above the Vigla Shale member. Overall, this formation corresponds to the first post-rift sediments of the Ionian zone [58,59,64].

2.2.3. Senonian Limestones

This formation corresponds to thick pelagic strata (1 to 3 m) intercalated with calciturbidites, comprising limestones with fragments of globotruncanids and rudists and fine-grained breccia intervals with limestones and rudist fragments within calcareous cement containing pelagic fauna. Calciturbidites are usually alternated with sub-lithographic pelagic limestones and cherts [34,35]. Overall, this formation corresponds to a period of basinal sedimentation, with significant variations of its lithological characteristics and sedimentary facies from the external (western) to the internal (eastern) parts of the Ionian basin. In the external sub-basin, they have been described as “clastic limestones” [75] containing floatstones, rudstones and rare grainstones and packstones with a micritic matrix, biomicritic intercalations, and rare cherty nodules. In the middle sub-basin, these carbonates are characterized as microclastic, bioclastic or polygenic microbreccias with a micritic matrix (wackestone, packstones), intercalated with (bio)micrites. In the internal sub-basin, the Senonian Limestones are massive, thick bedded microbreccias to breccias containing rudists and coral fragments, with only local appearance of thin-bedded or nodular chert [65,66,76].

2.2.4. Paleocene-Eocene Limestones

This formation also known as “Limestones with microbreccia” [75] is characterized by the same sedimentary facies with the underlying formation, with prominent microbreccia derived from the erosion of Cretaceous carbonates from both the Gavrovo (to the east) and Apulian (to the west) platforms. On Late Paleocene and progressively through the Early Eocene, the supply of calciclastic material diminished significantly, especially in the central Ionian Basin. The main depositional facies during the Eocene were platy wackestone and mudstone with Globigerinidae and chert nodules, analogous to those of the Vigla Limestones, but lack continuous siliceous intervals [34].

3. Materials and Methods

Six sections (A–F; Figure 2A–E) were sampled every 1 m and studied in terms of their reservoir parameters, paleodeposition environment, and paleogeographic significance.

Section A (Agios Georgios Section) is situated at the entrance of Agios Georgios village (lat: 39°16′14.99″ N, lon: 20°50′59.43″ E; Figure 2B). This section belongs to the Pantokrator Limestones (Figure 3), with a total length of 50 m, where 50 samples have been collected (Figure 4).

Section B (Perivleptos section) is situated at the north part of Perivleptos village (lat: 39°46′21.90″ N, lon: 20°46′48.34″ E; Figure 2C). This section covers parts of Pantokrator Limestones and Vigla Shales (Figure 3). The total length of the section is 20 m, where 20 samples have been collected (Figure 4).

Section C (Vigla Section) is situated at the south part of Asprageli village (lat: 39°48′33.45″ N, lon: 20°43′38.73″ E; Figure 2D). This section covers partially the Vigla Limestones (Figure 3) with a total length of 20 m, where 20 samples have been collected (Figure 4).

Section D (Koloniati section) is situated at the north part of Koloniati village (lat: 39°34′52.46″ N, lon: 20°53′11.41″ E; Figure 2E). This section covers the upper part of the Vigla Limestones and the lower part of the Senonian Limestones, which are separated by an unconformity (Figure 3). The total length of the section is 60 m, where 30 samples have been collected every 2 m (Figure 4).

Section E (Asprageli-2 Section) is situated at the north-east part of Asprageli village, near the section C (lat: 39°49′54.00″ N, lon: 20°43′58.25″ E; Figure 2D). This section covers the Senonian Limestones (Figure 3), with a total length of 10 m, where 10 samples have been collected (Figure 4).

Section F (Asprageli-1 Section) is situated at the north-east part of Asprageli village (lat: 39°45′57.42″ N, lon: 20°43′58.25″ E; Figure 2D). This section covers the part of Paleocene-Eocene limestones (Figure 3), with a total length of 25 m, where 25 samples have been collected (Figure 4).

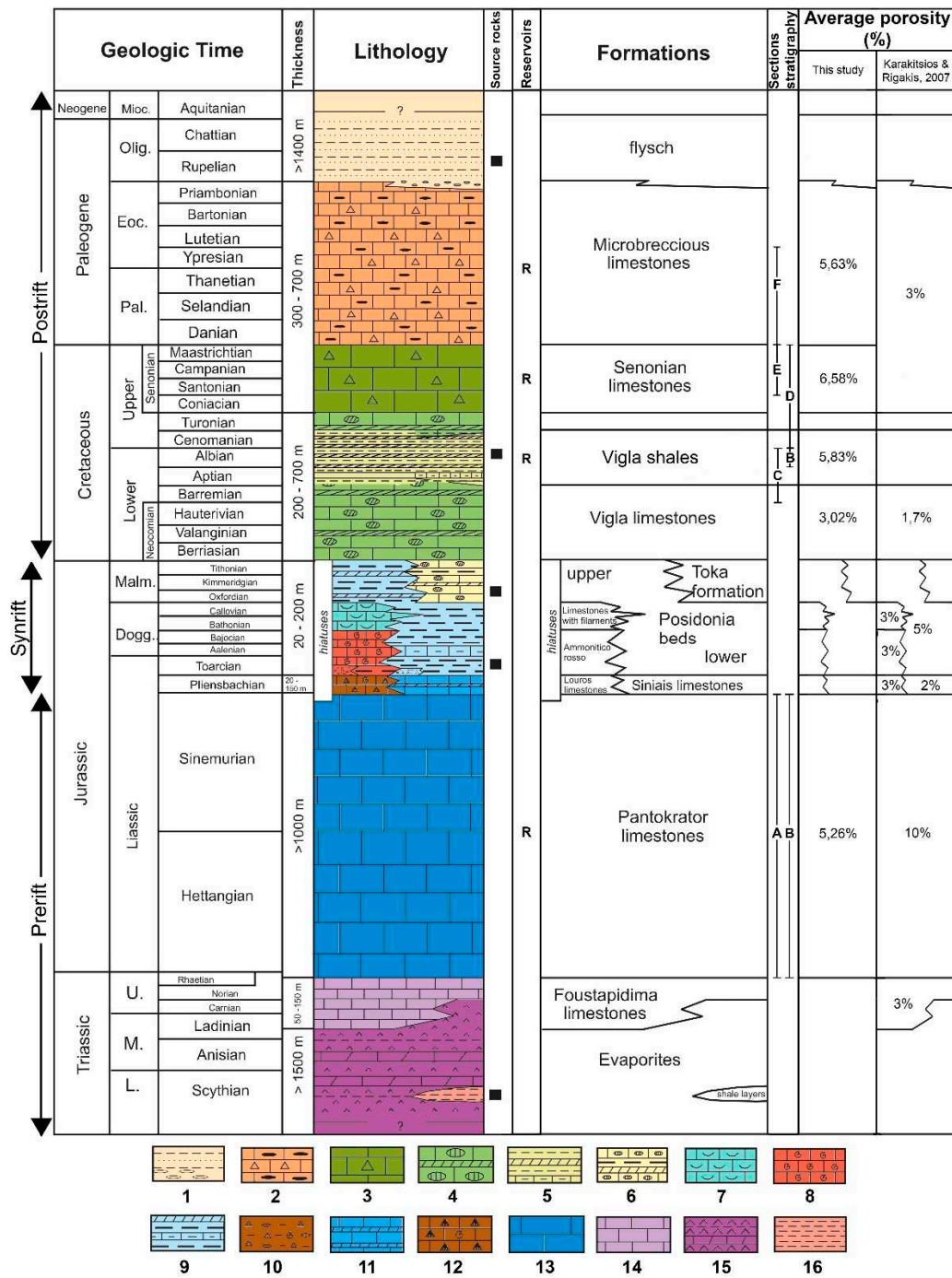


Figure 3. Synthetic lithostratigraphic column of the Ionian zone (modified from [34]), along with the correspondence of study sections stratigraphy with Ionian formations and their average porosity values as potential reservoir rocks. The colors in the lithostratigraphic column are consistent with the relevant colors of the International Chronostratigraphic Chart (v2020/01). (1) Shales and sandstones; (2) limestones with rare cherty intercalations, occasionally microbreccious; (3) pelagic limestones with clastic platform elements; (4) pelagic limestones with cherts; (5) cherty beds with shale and marl intercalations; (6) pelagic limestones with cherty nodules and marls; (7) pelagic limestones with bivalves; (8) pelagic, nodular red limestones with ammonites; (9) marly limestones and laminated marls; (10) conglomerates-breccias and marls with ammonites; (11) pelagic limestones with rare cherty intercalations; (12) external platform limestones with brachiopods and small ammonites in upper part; (13) platform limestones; (14) thin-bedded black limestones; (15) evaporites; (16) shales.

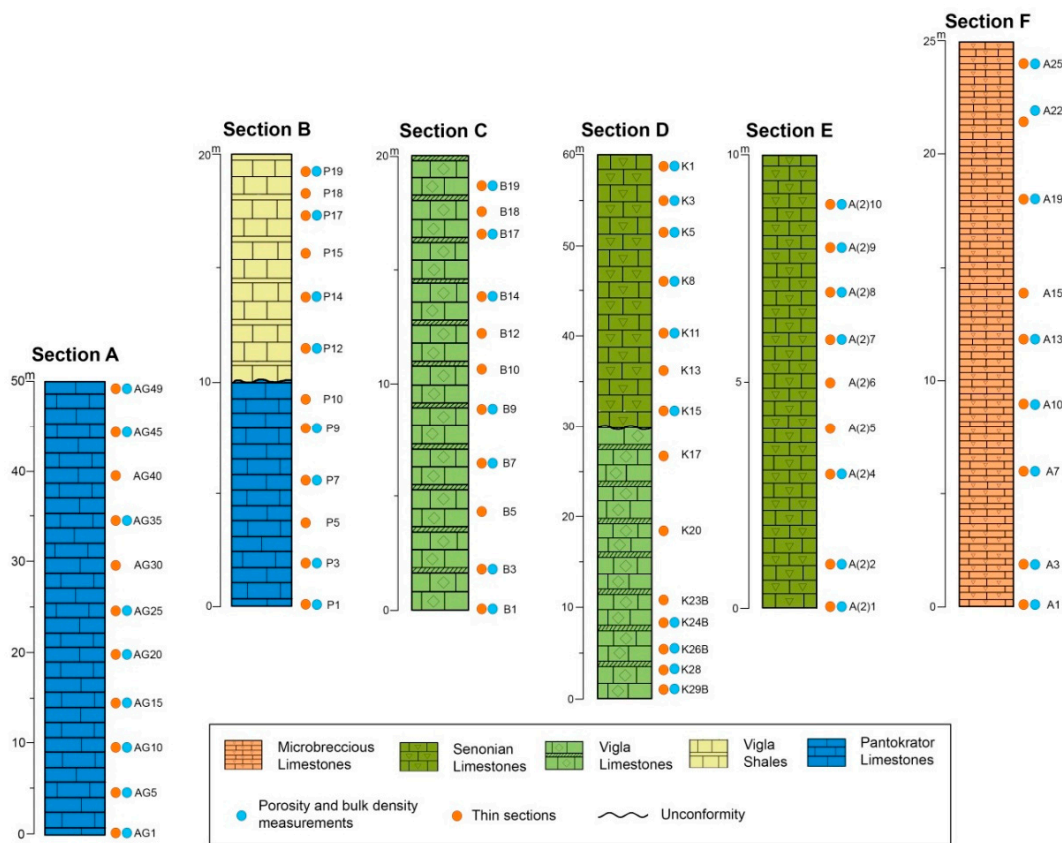


Figure 4. Lithology of the 6 study sections in Epirus region. The orange and blue circles at the right of each column represent the sampling intervals for thin sections as well as porosity and bulk density measurements.

The study of the Jurassic to Eocene sediments' distribution was based on tectonic, stratigraphic, paleontologic, and sedimentologic observations. Depending mostly on outcropping conditions, an average sampling interval of approximately 1 m has been used. An overall number of 150 samples were collected, among which 70 used for sedimentary facies analysis and 50 for measuring porosity and bulk density. Microfacies definition and textural characters analysis of the carbonate rocks, including both biogenic and inorganic dominant components, were done according to carbonate classification schemes of [77], which later modified by [78], based on the Standard Microfacies Types (SMF) in the facies zones (FZ) of the rimmed carbonate platform model. Depositional environments were reconstructed based on the derived sedimentological features and through comparison with additional standard facies reconstructions [79–85]. Therefore, assemblages consisting of several SMF types characterize all depositional environments. Thin sections were prepared in the Historical Geology and Paleontology Laboratory (National and Kapodistrian University of Athens; NKUA), biostratigraphically and sedimentologically studied under a polarized LEICA DM LP microscope, and photos have been performed with OLYMPUS UC30 Microscope Digital Camera. The reservoir potential of these carbonates was also obtained through the examination of porosity and bulk density parameters on representative of each stratigraphic formation samples, with the use of GeoPyc 1360 Envelope Density Analyzer and helium AccuPyc 1330 Pycnometer, respectively, also at NKUA. All measurements were made on dry samples that were previously dried in the oven at 40 °C for 24 h. The petroleum potential information was further compared with existing regional data covering the studied stratigraphic interval. Finally, ArcGIS software was used to visualize the results of the study area, along with additional data known from the literature, outcropped and well data [33,35,42,59,86] expanding the entire Ionian zone within paleogeographic/paleoenvironmental maps for the relevant time interval.

4. Results

4.1. Description of the Study Sections

Figure 5 illustrates a general view of the studied sections, regarding the Jurassic-Eocene carbonates of the Ionian zone in the study area. Agios Georgios section consists of 50 m of a uniform, largely condensed shallow-water limestone unit (Figure 5a,b) with calcareous algae, benthic foraminifera, and, rarely, brachiopods. The middle part of this succession (samples L15–L20) is recrystallized and slightly dolomitized, a phenomenon that usually occurred during the Jurassic in the Ionian zone. Such Early Jurassic sediments represent the lower part of the carbonate unit in western Greece. The basal 10 m of Perivleptos section contains neritic Pantokrator Limestones, overlain unconformably by reddish and green organic matter-rich shales with thin- to medium-bedded marly limestone interbeds and siliceous lenses, the Vigla Shales (Figure 5c–e).



Figure 5. Outcrop photographs of the study sections along with enlargements indicative of their characteristics: (a) General panoramic view of the Agios Georgios section; (b) Early Jurassic Pantokrator Limestones of Agios Georgios section; (c) general panoramic view of Perivleptos section. The red dashed line marks the unconformity between the lower (Pantokrator Limestones) and the upper (Vigla Shales) part of the section; (d) Pantokrator Limestones of the lower part of Perivleptos section; (e) Vigla Shales

of the upper part of Perivleptos section; (f) general panoramic view of Vigla section; (g) enlargement of the Vigla section, showing pelagic limestones and with chert intercalations; (h) general panoramic view of Koloniati section; (i) Vigla Limestones of the lower part of Koloniati section. The red dashed line marks the unconformity between the lower (Vigla Limestones) and the upper (Senonian Limestones) part of the section; (j) Senonian Limestones of the upper part of Koloniati section; (k) enlargement of the Vigla Limestones, showing pelagic limestones intercalated with flattened cherty nodules; (l) general panoramic view of Asprageli-2 section; (m) Senonian Limestones of Asprageli-2 section; (n) general panoramic view of Asprageli-1 section; (o) Paleocene-Eocene microbrecciated limestones of Asprageli-1 section.

The Vigla section, which has a thickness of 20 m, is characterized by typical Vigla formation deposits, such as pelagic limestones interbedded with centimeter- to decimeter-thick radiolarian chert beds (Figure 5f,g). Koloniati section (60 m thickness) consist of Cretaceous deposits of both Vigla and Senonian Limestones formations separated by an unconformity (Figure 5i). The lower half consists of pelagic massive limestones with rare intercalations of chert beds, and spherical, but also flattened, cherty nodules (Figure 5i,k). The siliceous nodules are beige, or light grey to dark grey color. The lithology of the upper half is described as solid, thick-bedded limestones that can be easily separated from the underlain thin-bedded ones (Figure 5j). In the uppermost part of the section brecciated horizons have been observed. Similar microbreccia bioclastic limestones with rudist fragments were observed in the 10 m thick Asprageli-2 section (Figure 5l,m). Finally, at the top of the studied carbonate succession, the 25 m thick Asprageli-1 section consists of grey-light micro- to mesoporous, turbiditic limestones with abundant radiolaria and planktonic foraminifera (Figure 5n,o).

4.2. Sedimentary Facies Analysis

Section A (Agios Georgios Section): The principal lithofacies of this section is boundstone, composed of red algal communities, and less frequent benthic foraminifera within a micritic clotted matrix (Figure 6a,b). Some lime horizons are dolomitized.

Section B (Perivleptos section): The lower part of this section is characterized by the lithofacies recrystallized grainstone of peloids with signals of dolomitization and fracturing (Figure 6c,d), while the upper part consists of mudstone-wackstone with radiolarians and/or planktonic foraminifera (Figure 6e).

Section C (Vigla Section): Section E consists of radiolarian biomicrite wackstone (Figure 6f,g).

Section D (Koloniati section): Within this section biomicrite mudstone-wackstone with planktonic foraminifera (Figure 6h), allochthonous bioclastic packstone with abundant benthic foraminifera (Figure 6i), and ooid lithofacies (Figure 6j,k) were observed.

Section E (Asprageli-2 Section): In Section D, the following two lithofacies have been observed: (i) bioclastic packstone, (Figure 6l), and (ii) biomicrite wackstone-packstone-floatstone with planktonic foraminifera, (Figure 6m).

Section F (Asprageli-1 Section): In Section C a packstone with planktonic foraminifera and some scattered mollusc and benthic foraminifera (Figure 6n,o) has been identified.

Generally, high energy environments such as platform, fore-shoal, and intertidal channel display grain supported textures. On the contrary, in low energy environments such as deep shelf and open marine, mud supported textures developed. In between, medium energy settings include platform slope environments, deposits of which are characterized by significant debris of rudists, algae, porcelaneous benthic foraminifera, and rarely variable shell fragments (bivalves, bryozoans). Grainy or micritic texture also strongly affected porosity, fluid flow, and diagenetic processes.

4.3. Biostratigraphic Analysis

Section A (Agios Georgios Section): Calcareous green algae of *Paleodasycladus* sp. and *Paleodasycladus mediterraneus* and *Thaumatoporella parvovesiculifera*, *Thaumatoporella* sp. build boundstones. Benthic foraminifers are represented by *Textularia* sp., Miliolidae and Ataxophragmiidae.

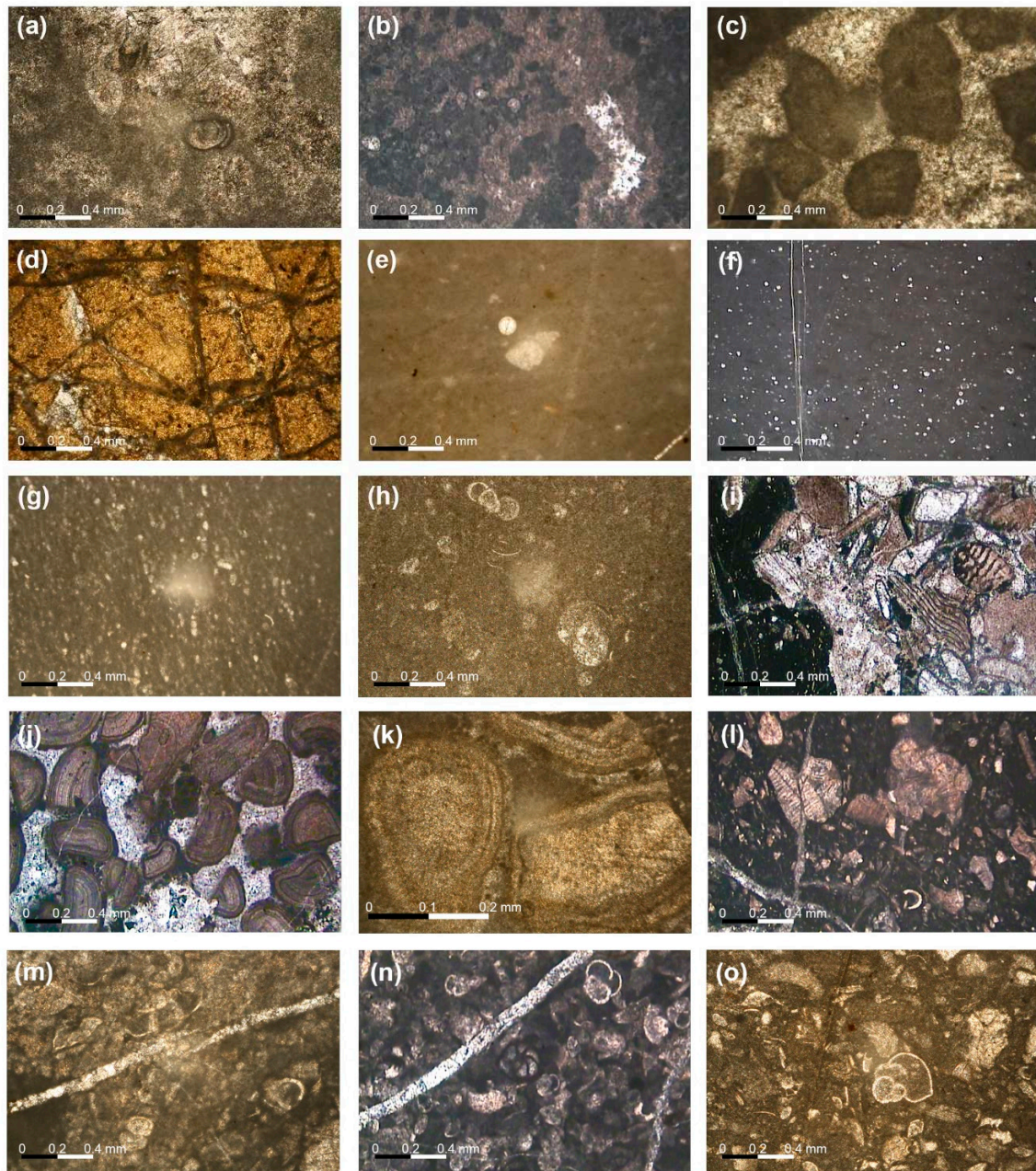


Figure 6. Characteristic Early Jurassic to Paleogene microfacies types of Ionian zone (Epirus region, NW Greece). (a,b) Dolomized boundstone with calcareous algae and benthic foraminifera within a micritic clotted matrix (samples AG1, AG15); (c,d) recrystallized grainstone of peloids with signals of dolomitization and fracturing (samples P3, P9); (e) mudstone-wackestone with radiolarian and planktonic foraminifera (sample P19); (f,g) wackestone with radiolarians (samples B1, B10); (h) Pelagic wackestone with radiolarians and planktonic foraminifera (sample K2); (i) Allochthonous bioclastic packstone with medium- and large-sized bioclasts benthics and rudist fragments (sample K5); (j,k) grainstone of ooids with sparitic cement (samples K4, K9); (l) bioclastic packstone of orientated and transported larger benthic foraminifera and rudists (sample A(2)7); (m) Pelagic wackestone-packstone of radiolarian and planktonic foraminifera, among which carenate forms are presented (sample A(2)9); (n,o) packstone with in situ planktonic foraminifera and scattered, transported benthics and mollusks (samples A7, A13).

Section B (Perivleptos section): Benthic foraminifera (e.g., *Glomospira* sp., *Glomospirella* sp., *Globochaete* sp., *Textularia* sp., *Valvulina* sp., Miliolidae, *Clypeina jurassica*, *Protopenneroplis striata*) and

fragments of hermatypic corals, calcareous green algae, gastropods, were identified in the lower part of the section and suggest a Hettangian-Sinemurian age. Radiolarians and planktonic foraminifera *Ticinella roberti*, *Biticinella breggiensis*, *Hedbergella delrioensis*, *Hedbergella planispira*, place the upper part of this section to the Middle-Late Albian.

Section C (Vigla Section): Assemblages of small-to-medium-sized morphotypes of *Calpionella alpina* followed by the acme of *Calpionella elliptica* at the basal part of the section suggest an Early Berriasian age, while progressively through the top of the section radiolarians and other planktonics (*Favusella hauterivica*, *Hedbergella sigali*, *Hedbergella dendroensis*) have been further identified. In the upper half of the section the Globigerinelloides “acme” and “eclipse” intervals, characterized by the abundant presence and the lack of representatives of this genus, respectively, show the evolution through the Barremian up to the Albian in the topmost meters of the Vigla Limestones.

Section D (Koloniati section): The lower part of the section assigned to Vigla Formation was characterized by the presence of the planktonic foraminiferal assemblage *Rotalipora appenninica*, *Rotalipora cushmani*, and *Praeglobotruncana gibba* suggesting the early Late Cretaceous and particularly the Cenomanian-Turonian boundary interval. The upper part has a Coniacian-Maastrichtian age and contains the foraminifera *Globotruncana cf. arca*, *Globotruncana cf. linnei*, *Orbitoides sp.*, *Quinqueloculina sp.*, *Spiroloculina sp.*, *Pseudolituonella sp.*, *Cuneolina sp.*, Textulariidae, and Miliolidae.

Section E (Asprageli-2 Section): This section covers the Santonian-Maastrichtian time span based on the variable fauna containing mainly Globotruncanids (e.g., *Globotruncanita stuarti stuartiformis*, *Rugoglobigerina rugosa*, *Globotruncana cf. bulloides*, *Globotruncana arca*, *Abathomphalus mayaroensis*, *Contusotruncana sp.*), but also benthic foraminifera (e.g., Miliolidae, *Siderolites sp.*, *Cuneolina sp.*, *Orbitoides cf. media*, *Orbitoides apiculata*), as well as rudist and mollusc fragments.

Section F (Asprageli-1 Section): The genera *Subbotina*, *Acarinina*, and *Morozovella* are the dominant groups of Paleocene-Early Eocene assemblages. More explicitly, the lower part of the section contains carbonates enriched on radiolarians and planktonic foraminifera (*Parasubbotina pseudobulloides*, *Acarinina sp.*, *Subbotina sp.*, *Igorina pussila*, *Chiloguembelina sp.*), which deposited during the Early Paleocene (Selandian). Progressively through the top of the section, the increase of highly and full body ornamented Morozovellid species (e.g., *Morozovella aequa* and *Morozovella subbotinae*, *Morozovella velascoensis*) and quadrate Acarininids (e.g., *Acarinina wilcoxensis* and *Acarinina pseudotopilensis*) are indicative to the end of the Paleocene and the start of the Eocene (Ypresian).

Overall, the age determination supports the pre-existing results mentioned in the geological maps (Ioannina, Doliana, Pappadai, and Tsepelovo sheets; [87–90]) regarding the Ionian zone rock exposures. Particularly, they confirm the Early Jurassic (Hettangian-Sinemurian) for the Pantokrator Limestones, the Early Cretaceous-early Late Cretaceous (Berriasian-Turonian) for the Vigla Limestones, the early Late Cretaceous (Albian) for the Vigla Shales, the Late Cretaceous (Coniacian-Maastrichtian) for the Senonian Limestones, and the Paleocene/Early Eocene age for the microbreccious limestones respectively.

4.4. Porosity and Bulk Density Measurements

The results of porosity and bulk density measurements of the studied carbonates are listed in Table 1, while the average values per formation in Table 2. With the exception of Vigla Shales, which present the lowest measured bulk density values (2.60–2.63; average 2.62 gr/cm³), the bulk density is quite homogeneous for all carbonate samples, ranging from 2.64 to 2.74 gr/cm³, with an average of 2.68–2.70 gr/cm³, respectively, per study formation (Table 2). On the contrary the total porosity values evaluated with the pycnometer present significant variability between the different sections and stratigraphic formations. In Agios Georgios section porosity values range between 2.31% and 9.71%, with an average value of 4.97% (Table 1). Significant porosity values above the average value for the Jurassic deposits were recorded in some horizons of this unit (samples AG10-20), where the limestones seem to be dolomitized. These values approximate the maximum porosities (~10%) that have been reported for this formation for the entire Ionian zone [33]. The total average porosity for the

Pantokrator Limestones, including both Agios Georgios and the lower part of Perivleptos sections, is 5.26% (Table 2).

Table 1. Porosity and bulk density measurements displayed from all the study sections.

Section	Formation	Sample ID	Height (m)	Porosity (%)	Bulk Density (g/cm ³)
Section F (Asprageli-1)	Limestones with breccia	A1	0	9.35	2.64
		A3	2	3.90	2.61
		A7	6	7.38	2.65
		A10	9	8.55	2.68
		A13	12	2.50	2.71
		A19	18	3.46	2.67
		A23	22	4.32	2.72
		A25	24	5.60	2.74
Section E (Asprageli-2)	Senonian Limestones	A(2)1	0	3.31	2.72
		A(2)2	1	4.52	2.72
		A(2)4	3	2.60	2.74
		A(2)7	6	8.64	2.69
		A(2)8	7	9.63	2.73
		A(2)9	8	7.36	2.62
		A(2)10	9	8.99	2.70
Section D (Koloniati)	Senonian Limestones	K1	0	8.88	2.69
		K3	4	9.26	2.68
		K5	8	5.47	2.69
		K8	14	3.86	2.72
		K11	20	6.56	2.72
		K15	26	5.46	2.72
	Vigla Limestones	K28	52	1.28	2.67
		K24B	44	2.33	2.69
		K26B	48	3.87	2.69
		K29B	54	5.65	2.69
Section C (Vigla)	Vigla Limestones	B1	0	3.36	2.73
		B3	2	3.86	2.70
		B7	6	1.81	2.71
		B10	9	3.52	2.68
		B14	13	2.45	2.71
		B18	17	2.07	2.73
		B20	19	2.98	2.69
Section B (Perivleptos)	Vigla Shales	Π20	19	6.00	2.63
		Π18	17	8.10	2.60
		Π15	14	5.82	2.62
		Π12	11	3.38	2.61
	Pantokrator Limestones	Π9	8	8.18	2.72
		Π7	6	7.67	2.72
		Π3	2	3.75	2.72
		Π1	0	4.02	2.66
Section A (Agios Georgios)	Pantokrator Limestones	AG1	0	2.49	2.70
		AG5	4	3.55	2.73
		AG10	9	9.71	2.72
		AG15	14	9.62	2.68
		AG20	19	7.56	2.69
		AG25	24	3.28	2.73
		AG35	34	2.31	2.70
		AG45	44	3.76	2.65
AG50	49	2.45	2.66		

Porosity measurements of the Perivleptos section document steadily high values for both lithostratigraphic members, with quite similar values (3.75–8.18%, average 5.91%; Table 1) for the basal Jurassic interval and the overlying Vigla Shales (3.38–8.10%, average 5.83%; Table 1). On the

contrary, the typical Vigla Limestones in both Vigla section and the lower part of Koloniati outcrop display the lowest values ranging between 1.81% and 3.86% (average 2.86%) in the former and 1.28% and 5.65% (average 3.28%) in the latter (Table 1). Overall, the average porosity for Vigla Limestones, taking into account the data from both aforementioned areas, equals to 3.02% (Table 2). The analyzed samples from the upper part of Koloniati section characterized as Senonian Limestones showed steadily high porosity in the range of 3.86% to 9.26% (average 6.58%), especially at the top of this unit, where brecciated limestones with the maximum porosities of about 10% were identified (Table 1). The same range showing the tendency for increased porosity values (2.60–9.63%, average 6.44%; Table 1) was observed in Asprageli-2 section, with the hemipelagic calciturbidites and fractured resedimented microbreccia. The total average porosity measured for this Late Cretaceous carbonate unit is 6.50% (Table 2). The porosity of Asprageli-1 brecciated Paleogene limestones is in the range of 2.50–9.35% (Table 1), with the average of 5.63% (Table 2).

Table 2. Average porosity and bulk density values per studied formation of the Ionian zone.

Formation	Stratigraphy	Average Porosity (%)	Average Bulk Density (gr/cm ³)
Limestones with microbreccia	Paleocene/Eocene	5.63	2.68
Senonian calciturbidites	Late Cretaceous	6.50	2.70
Vigla Shales	late Early Cretaceous	5.83	2.62
Vigla Limestones	Early Cretaceous	3.02	2.70
Pantokrator Limestones	Early Jurassic	5.26	2.70

5. Discussion

5.1. Microfacies Types and Depositional Environments

The main textural and compositional characteristics, as well as the sedimentary features of the distinguished microfacies, are summarized in Table 3, corresponding to different depositional environments or facies zones (FZ) defined by [84,85] (Figure 7). More specifically, the Pantokrator Limestones were classified as boundstone of algae (SMF 7) and bioclastic grainstone (SMF 11) in the Agios Georgios and Perivleptos sections respectively, giving evidence of a depositional environment characterized by a platform, with both intertidal and subtidal environments (FZ5-6). Recrystallization-dolomitization and fracturing of some redeposited carbonate clasts points a subaerial exposure of parts of the platform. Vigla Limestones consist of mudstone-wackestone with radiolarians and planktonic foraminifera (SMF 2-3), characterizing a low energy, relatively deep environment, such as the toe of slope (FZ3) and/or deep shelf (FZ2). Senonian Limestones present a variety of lithofacies, which correspond to environments ranging from the slope to deep shelf. They mostly include in-situ wackestone-packstone with planktonic foraminifera along with microbreccia bioclastic packstone with fragments of shallow water fauna (rudists and benthic foraminifera) (SMF 4), and micrite with transported ooids (SMF 13), which in total represent a medium-to-high-energy environment (e.g., slope), possibly due to the transportation of the sediments within the basin from the platform.

The above facies distribution reflects the separation of the deep Ionian Basin into a central topographically-higher area characterized by reduced sedimentation, and two surrounding talus slopes with increased sedimentation [66]. Locally, micritic peloids and dark-gray intraclasts, floating in an overall micritic matrix were also observed within these carbonates. The range of depositional interpretations of these formations includes supratidal settings, vadose-marine inorganic precipitation in inter- and subtidal environments of formation in marine seepage or groundwater springs [85]. Overall, Late Cretaceous calciturbidites suggest relatively deep-slope depositional conditions (FZ3-4). Relatively similar and possibly deeper depositional conditions apply for the Paleogene biomicritic packstones with radiolaria (mostly at the Early Paleocene) and planktonic foraminifera (through the Eocene) (SMF3), suggesting a basinal environment (FZ2).

Table 3. Detailed description of representative thin sections, where sedimentary facies, lithology, formation, age, and the depositional environments of the studied deposits are presented.

Section	Samples	Formation	Lithology	Facies Description	Figures	Depositional Environment	Stratigraphy (Stages)
F: Asprageli-1	A7, A13	Limestones with microbreccia	Hemipelagic calciturbidites with microbreccia	Packstone with in-situ planktonic foraminifera and scattered, benthic foraminifera and mollusks (SMF 3)	Figure 6n,o	Shelf slope (FZ3) to deep shelf (FZ2) (medium energy)	Paleocene to Eocene
E: Asprageli-2	A7, A9	Senonian Limestones	Microbrecciated bioclastic to pelagic turbiditic limestones	(a) Allochthonous bioclastic packstone with rudists and benthic foraminifera (SMF 5), (b) Pelagic wackestone-packstone with radiolarian and planktonic foraminifera (SMF 4-5)	Figure 6l,m	Slope (FZ4) - toe of slope (FZ 3) to deep shelf (FZ 2) (medium energy)	Late Cretaceous (Santonian-Maastrichtian)
D: Koloniati (upper part)	K2, K9, K4, K5	Senonian Limestones	Bioclastic Limestones (often brecciated)	(a) Allochthonous bioclastic packstone to grainstone with rudist fragments and benthic foraminifera (SMF 5), (b) Mudstone-wackestone with planktonic foraminifera (SMF 4-5), (c) Grainstone of ooids with sparite cement (SMF 5)	Figure 6h,i,j,k	Slope (FZ 4) (medium to high energy)	Late Cretaceous (Santonian-Maastrichtian)
C: Vigla, D: Koloniati (lower part)	B1, B10	Vigla Formation	Limestones intercalated with cherts	Wackestone with radiolarians and planktonic foraminifera (SMF 3)	Figure 6f,g	Toe of slope (FZ 3) (low energy)	Early Cretaceous-early Late Cretaceous (Berriasian-Turonian)
B: Perivleptos (upper part)	P19	Vigla Formation	Shales with marly limestone interbeds and siliceous nodules	Mudstone-wackestone with radiolarians and planktonic foraminifera (SMF 3)	Figure 6e	Deep shelf (FZ 2) (low energy)	late Early Cretaceous-early Late Cretaceous (Aptian-Turonian)
B: Perivleptos (lower part)	P3, P9	Pantokrator Limestones	Neritic limestones	Recrystallized grainstone of peloids with lithoclasts (SMF 5). Signals of dolomitization and fracturing	Figure 6c,d	Inner platform with intertidal and subtidal environments (FZ 4) (moderate energy)	Early Jurassic (Hettangian-Sinemurian)
A: Agios Georgios	AG1, AG15	Pantokrator Limestones	Limestones locally dolomitized	Dolomitized boundstone with calcareous algae and benthic foraminifera within a micritic clotted matrix (SMF 7)	Figure 6a,b	Platform (FZ 5) (high energy)	Early Jurassic (Hettangian-Sinemurian)

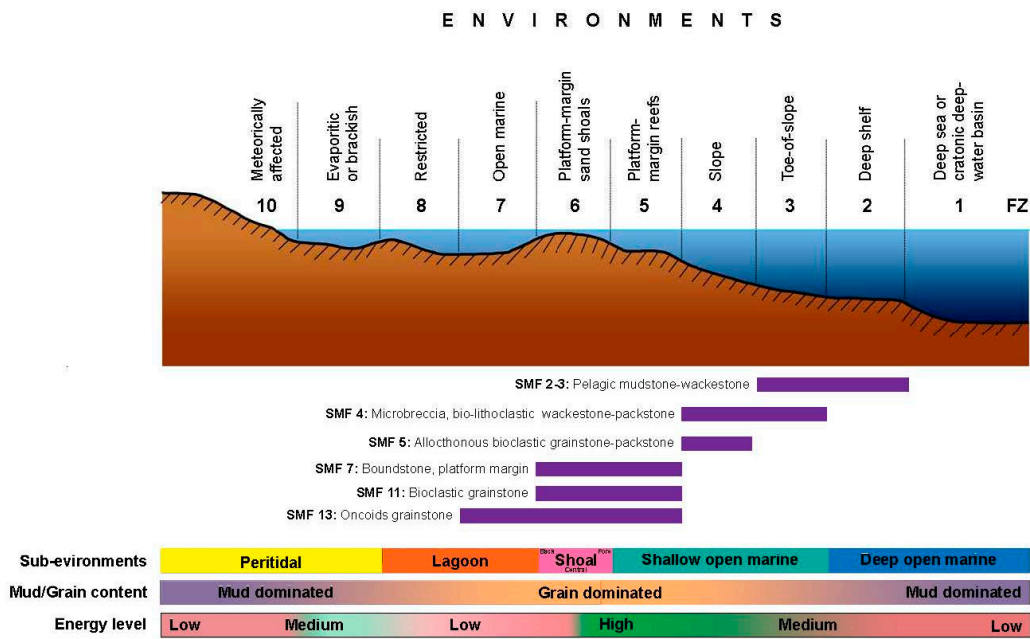


Figure 7. Depositional distribution model in the Ionian zone. The sedimentary changes display good correlation with the energy level of environments and facies changes.

5.2. Reservoir Potential of the Early Jurassic to Eocene Carbonate Rocks of the Ionian Zone

Reservoir characterization deals with physical characteristics of the reservoir, including petrophysics (porosity–bulk density and grain density measurements, capillary pressure measurements), fluid properties (e.g., reservoir fluid saturations) and reservoir drive mechanisms [51,91]. Moreover, reservoir quality is defined as the amount of porosity and bulk density in a reservoir and can be a function of many control factors for both carbonates and sandstones [92–94]. In the present study, the reservoir properties, porosity and bulk density, are comparatively examined in the studied sections on a large intra-basin scale in order to assess the quality of carbonate reservoirs of the Ionian zone. Measuring porosity and bulk density of a given reservoir is a direct measure for the storage and flow capacity. Though porosity seems to be a main contributor to the flow capacity, bulk density is mostly controlled by the pore throat distribution [95]. However, they are difficult to predict, since they depend on both initial depositional processes and diagenetic overprinting. Particularly, their complexity in carbonate reservoirs should be attributed to the different interplays, among other factors, of hydrodynamic conditions, carbonate cementation or dissolution, and tectonic setting that form the architecture of the marine setting [96].

The surveyed carbonates showed remarkable average porosities (3.02–6.50%; Table 2) accompanied by even lower bulk densities (2.62–2.70%), and therefore, the quality of the reservoir has been described as poor to fair. Low and homogeneous bulk density values are in good agreement with the literature data for pure calcite rocks [97–99]. Average porosity values are quite variable in the study sections, with a tendency to slightly higher values in section E and upper part of section D both of Senonian age, as well as in the upper part of section B corresponding to the Vigla Shales. On the contrary, the lowest porosity (and bulk density) values were reported for the biomicritic mudstone-wackestone depositional facies with pelagic fauna of Vigla formation. The Pantokrator Limestones present significant porosity and bulk density values only on dolomitized horizons, explaining the significant variability observed into this formation. Generally, this intra-zone original porosity evolution characterized by an increased tendency from the Early Cretaceous pelagic limestones to the Late Cretaceous calciturbidites, which are also slightly more permeable, is consistent with previous findings in the Ionian zone of NW Greece [33,100,101]. Particularly, the overall evolution in the study area display a quite variable average porosity pattern, characterized mostly by low to moderate

values (~3–7%), while some high individual values around 10% also recorded. The levels with such a sudden porosity increase may be related to burial diagenesis and dolomitization, which increase the reservoir quality to good.

Factors related to sequence architecture, including the occurrence of intervals with clay laminations (e.g., Vigla Shales; promoting chemical compaction and associated cementation) and the distribution of early dolomitization (promoting porosity preservation during burial), generally increases secondary fracture porosity. A higher increase of porous within the marly limestones of Vigla Shales formation than in Senonian calciturbidites, could be caused due to fracturing due to the nodule's development, in the manner described by [43]. Intracrystalline porosity could be also developed within dolomitized intervals and therefore some breccia limestones may form potential reservoirs. Especially for the Ionian zone, it is documented that the dolomitization front has changed through time [33]. In the internal and external parts of the Ionian zone, dolomitization continued well into the Cretaceous, whilst in the central part, it did not continue after the Middle Jurassic. However, it is worth noting that the low porosity and bulk density identified within the study formations could either imply high fluid pressures or fluid migration through permeable "fracture conduits" in the vicinity of fault zones. The observed porosity values correspond to microporosity that does not take into consideration the fracture porosity related to thrusts which considerably increases the carbonate reservoir quality. Some of the porosity variations observed in this study may due to the vicinity/distance of the samples with the tectonic zones. In any case, distribution of Ionian tectonic zones is related to the prevailing tectonic style of the Ionian zone, which is a combination of thick- and thin-skinned deformation [33]. The elucidation of the predominance of tectonic style has not been achieved to date, due to the fact that deep seismic surveillance is hindered by the subsurface Ionian evaporites [34,58,70,71].

The incorporation of the depositional with the carbonate reservoir quality data indicate that there is not a clear view for the reservoir quality that can be associated with a specific depositional environment. Generally, in western Greece, most of the fair to good potential reservoirs are deposited in shallow to restricted platforms (e.g., Gavrovo platform carbonates close to its transition to the Ionian zone, in the thrust sheets of Ionian and pre-Apulian zones) [33,34,40]. In the Ionian zone, similar medium to high energy environments, such as tidal domains, reef barriers, and slopes were recorded during Jurassic (e.g., Pantokrator Limestones, Posidonia beds) and Late Cretaceous to Paleocene/Eocene (e.g., Limestones with microbreccia), respectively [35,40]. However, Jurassic studied sediments do not contain any proven reservoirs with the most significant porosities to be associated with the development of fracture and/or diagenetic zones. This study shows that deeper depositional (deep marine basinal and/or slope) environments can also be associated with the deposition of good potential reservoirs. On this regard, potential reservoir rocks within the Ionian zone further include the upper part of pelagic Vigla Limestones, Senonian Limestones, and the microbrecciated intervals of the Paleocene/Eocene limestones, all presented very good porosity values up to 10%.

5.3. Paleogeographic Analysis of the Ionian Zone

In Epirus area only the Jurassic to Eocene carbonate succession occurs. The carbonate platform sediments begin at the base with thick-bedded neritic Jurassic Pantokrator Limestones, which feature remarkable facies homogeneity, indicating that an extensive shallow sea was spread all over the study area during that time. In Perivleptos and Agios Georgios sections, this facies association is mostly represented by biolithitic boundstones and biosparite grainstones with calcareous algae and benthonic foraminifera, implying a carbonate margin platform with both intertidal and subtidal environments (Figure 8A). These extensive platforms are developed until the Hettangian–Pliensbachian age, when the overlying synrift sequence begins. Pliensbachian Siniais Limestones correspond to the general deepening of the Ionian Basin. The structural differentiation that followed caused the fragmentation of the initial basin into smaller paleogeographic units with half-graben geometry. This is recorded in the abruptly changing thickness of the synrift formations that take the form of syn-sedimentary wedges [34]. In the deeper parts of the half grabens, these wedges include complete

Toarcian-Tithonian successions, whereas in the shallower parts of the half grabens, the successions are interrupted by unconformities. However, this topmost part of the Jurassic is not recorded in the studied sections. In Koloniati section, there is an unconformity between the base of the Vigla Shales and the topmost horizons of the underlying Pantokrator formation, which marks a period of uplift and erosion at the beginning of the Toarcian. This led to occasional karstification of Pantokrator Limestones.

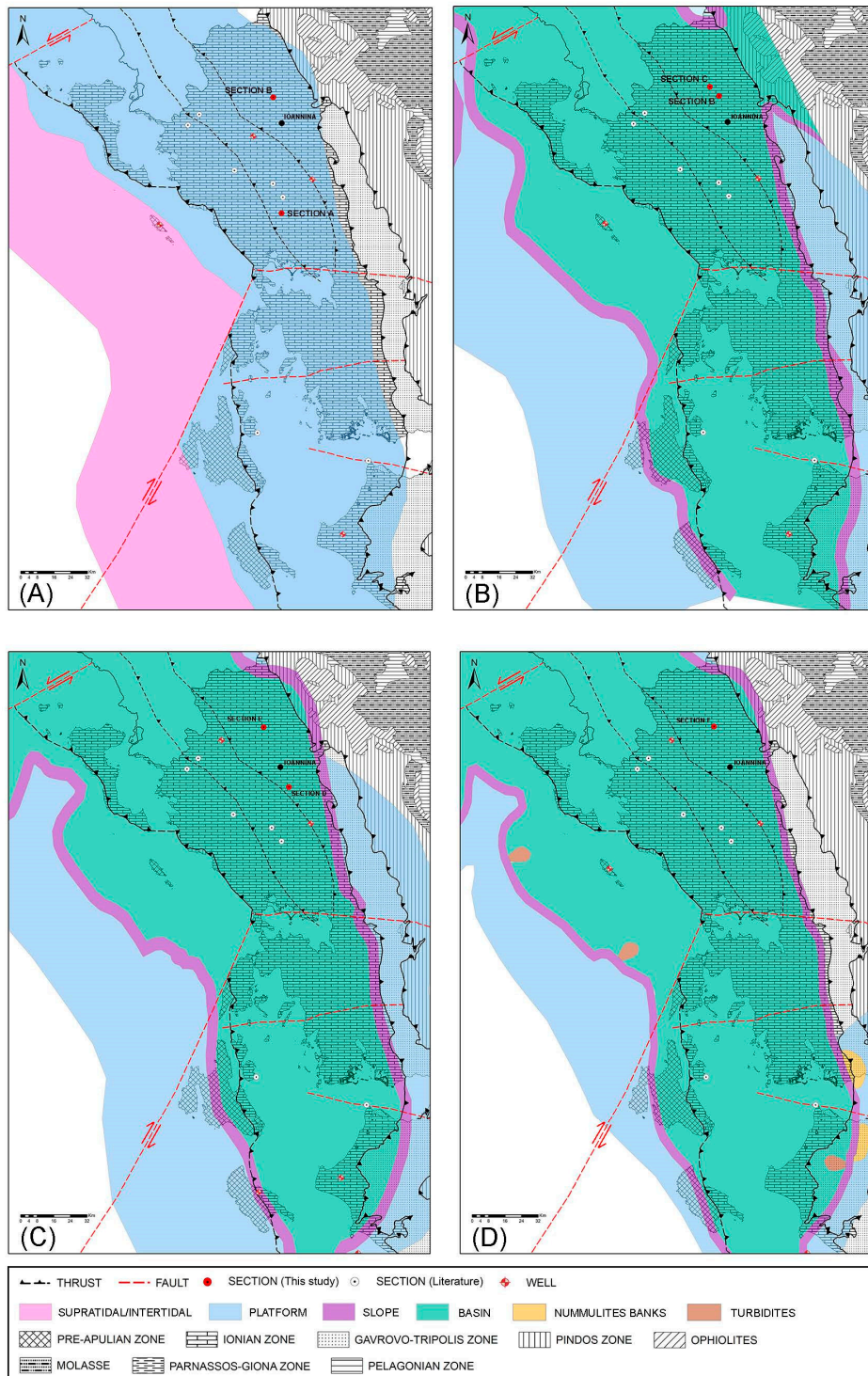


Figure 8. Paleoenvironmental map of the study area during the (A) Early Jurassic, (B) Early Cretaceous, (C) Late Cretaceous, and (D) Paleocene-Eocene based on outcropped- (red circles from this study and white ones from the literature) and well-data (white-red symbols) [33,35,42,59,86].

The post-rift sequence begins with the pelagic Vigla Limestones, whose deposition was synchronous throughout the Ionian Basin, beginning in the Early Berriasian [73,102]. The basal sequence of the Vigla limestones, consisted of thin layered, sub-lithographic, pelagic limestones, with abundant radiolarian and frequent cherty beds enriched with radiolarian, is related to the Early Cretaceous subsidence caused deepening in the entire basin (Figure 8B). Towards the upper part of this formation, chert layers become more abundant, containing intercalations of green, red, and locally black shales, named as the “Vigla Shales” member, indicative of basinal sedimentation. The microfacies analysis of the Koloniati (lower part) and Vigla sections suggest that these carbonate sediments represent a low energy, relatively deep environment, like the toe of slope and the deep shelf of the basin. Apart from the halokinetic movements, which probably caused the variation in thickness of Vigla Limestones [34] from the western (external) to the eastern (internal) parts of the basin, the pelagic depositional conditions persisted until the Late Eocene, when flysch sedimentation began.

During the Late Cretaceous, the Senonian Limestones formation consisted of hemipelagic calciturbidites and resedimented microbreccia, reflect similar deep marine slope environments. In particular, sedimentary facies analysis of the Koloniati (upper part) and Asprageli-2 samples suggests that they were deposited in a deep-water toe of slope and platform margin environment, respectively, where microbrecciated carbonates were transported and accumulated (Figure 8C). The allochthonous bioclastic material identified in the analysed samples consists mainly of rudist (typical reef builder) fragments and benthic foraminifera (e.g., forereef dweller *Orbitoides*; [103] and/or inner platform taxa *Cuneolina*, Textulariids and Miliolids; [85,103,104]), originated and transported from a nearby shallow shelf environment (e.g., platform or reef). Such shelf margins of the nearby pre-Apulian and Gavrovo platforms [75] and/or internally to the Ionian basin [101] were characterized by high productivity of such skeletal material, transported and redeposited in the deeper parts of the Ionian basin [34]. These bioclasts are also accompanied by pelagic Globotruncanids and radiolarian specimens observed in the in situ micritic matrix. Moreover, ooid lithofacies and some reworked lithoclasts observed in the upper part of the Koloniati Senonian Limestones indicate shallow-water conditions that were exposed during the uppermost interval of the Cretaceous (Maastrichtian). This is further reinforced by extensional tectonics, while possible sea level effects cannot be ruled-out and could also be related to the eustatic sea level low-stand (~150 m sea-level drop) that took place between the Late Cretaceous and the Paleocene [105,106]. Our paleoenvironmental observations from the Late Cretaceous interval in Epirus fully agree with recent sedimentary findings of [42] for the Araxos area (internal Ionian zone), as well as with the previous literature [34,35,75] for the entire Ionian zone. Overall, the facies distribution of the Senonian reflects the separation of the Ionian Basin into a central area (middle and outer part of the Ionian Zone) characterized by deeper water sedimentation and two surrounding talus slopes, issued from western Gavrovo platform and western Apulian platforms. Both platforms provided the clastic carbonate material that was transported by turbidity currents into the Ionian Basin.

The study of the Asprageli-1 samples provides evidence that the supply of clastic material due to tectonics diminished significantly during the Paleocene/Eocene. However, despite the reduced tectonic activity during that time, the slumping of platform edge sediments produced turbidity currents resulting to the deposition of Limestones with microbreccia and calciturbidites. The main depositional facies of platy mudstone-wackestone with Globigerinidae, Globorotaliidae and rare siliceous nodules, analogous to those of the Vigla Limestones, imply that the depositional environments during that period did not change significantly from the Late Cretaceous (Figure 8D). The greatest thicknesses of the Eocene units can be found in the marginal parts of the Ionian Zone, where the microbreccias are more frequent.

6. Conclusions

The Ionian zone consists of a heterogeneous multi-layered calciclastic reservoir in Epirus region (western Greece). The identified carbonate formations display various facies ranging in a full spectrum

of depositional conditions, from shallow platforms (reefs) to slope (platform margin) environments, even to the open marine settings, with different lithologies, sedimentary features, energy conditions, and diagenetic overprints. This heterogeneity also explains the rock petrophysical/geomechanical variation of these carbonate rocks. The Early Jurassic limestones (biolithites boundstone) do not contain any proven reservoirs due to relatively low porosities, with the exception of the microcrystallized or dolomited horizons, which increase the reservoir quality in a local scale. The Early Cretaceous limestones and cherts (biomicrites mudstone-wackestone) of Vigla formation has been described as the poorest of the studied carbonates, in terms of their reservoir potential. On the contrary, the Late Cretaceous (Senonian Limestones) and the Paleocene/Eocene carbonate units can be considered the primary target for oil/gas exploration in the study area, since they contain calciturbidites deposited mainly in the slope (bioclastic packstone-rudstone with rudist fragments and benthic foraminifera) and the deep shelf (planktonic foraminiferal biomicrites mudstone-wackestone). The highest porosity values recorded in those carbonates may be further associated with the development of fracture networks and/or diagenetic zones. Overall, the results of this study may have implication for reservoir- and/or source-rock-geologists and diagenetic modelling approaches in the presented area and elsewhere within the eastern Mediterranean Sea [42,86,100,101,107,108], implying that sample specific analyses or a very well understood regional diagenetic framework are required for accurate prediction of reservoir quality.

Author Contributions: Conceptualization, G.K., L.M.; methodology, G.K., L.M.; software, L.M., G.K.; validation, G.K., L.M.; formal analysis, G.K., L.M.; investigation, G.K., L.M., V.K., A.A.; resources, L.M., V.K.; data curation, G.K., L.M., V.K., A.A.; writing—original draft preparation, G.K.; writing—review and editing, G.K., L.M., V.K., A.A.; visualization, G.K., L.M.; supervision, V.K., A.A.; project administration V.K., A.A.; funding acquisition, L.M., V.K. All authors have read and agreed to the published version of the manuscript.

Funding: This research received no external funding.

Acknowledgments: The authors are grateful to Andreas Kostis for his significant contribution to the fieldwork. Jean-Jacques Cornée and Fotini Pomoni-Papaioannou are warmly thanked for her kind assistance during the sedimentary facies analysis and her constructive suggestions regarding the interpreted depositional paleoenvironments. Four anonymous reviewers are deeply acknowledged for useful and constructive comments on the manuscript, and Victoria Li (Assistant Editor) is also thanked for her editorial handling.

Conflicts of Interest: The authors declare no conflict of interest.

References

1. Morse, J.W.; Mackenzie, F.T. *Geochemistry of Sedimentary Carbonates*; Elsevier Science: Oxford, UK, 1990; Volume 48.
2. Schlager, W.; Philip, J. Cretaceous Carbonate Platforms. In *Cretaceous Resources, Events and Rhythms*; Ginsburg, R.N., Beaudoin, B., Eds.; NATO ASI Series (Series C: Mathematical and Physical Sciences); Springer: Dordrecht, The Netherlands, 1990; Volume 304.
3. Bruckschen, P.; Oesmann, S.; Veizer, J. Isotope stratigraphy of the European Carboniferous: Proxy signals for ocean chemistry, climate and tectonics. *Chem. Geol.* **1999**, *161*, 127–163. [[CrossRef](#)]
4. Erba, E.; Bartolini, A.; Larson, R.L. Valanginian Weissert oceanic anoxic event. *Geology* **2004**, *32*, 149–152. [[CrossRef](#)]
5. Volery, C.; Davaud, E.; Foubert, A.; Caline, B. Shallow-marine microporous carbonate reservoir rocks in the Middle East: Relationship with seawater Mg/Ca ratio and eustatic sea level. *J. Pet. Geol.* **2009**, *32*, 313–325. [[CrossRef](#)]
6. Caruso, A.; Pierre, C.; Blanc-Valleron, M.-M.; Rouchy, J.M. Carbonate deposition and diagenesis in evaporitic environments: The evaporative and sulphurbearing limestones during the settlement of the Messinian salinity crisis in Sicily and Calabria. *Palaeogeogr. Palaeoclimatol. Palaeoecol.* **2015**, *429*, 136–162. [[CrossRef](#)]
7. Kontakiotis, G.; Karakitsios, V.; Mortyn, P.G.; Antonarakou, A.; Drinia, H.; Anastasakis, G.; Agiadi, K.; Kafousia, N.; De Rafelis, M. New insights into the early Pliocene hydrographic dynamics and their relationship to the climatic evolution of the Mediterranean Sea. *Palaeogeogr. Palaeoclimatol. Palaeoecol.* **2016**, *459*, 348–364. [[CrossRef](#)]

8. Kontakiotis, G.; Besiou, E.; Antonarakou, A.; Zarkogiannis, S.D.; Kostis, A.; Mortyn, P.G.; Moissette, P.; Cornée, J.-J.; Schulbert, C.; Drinia, H.; et al. Decoding sea surface and paleoclimate conditions in the eastern Mediterranean over the Tortonian-Messinian Transition. *Palaeogeogr. Palaeoclimatol. Palaeoecol.* **2019**, *534*, 109312. [[CrossRef](#)]
9. Coccioni, R.; Sideri, M.; Frontalini, F.; Montanari, A. The *Rotalipora cushmani* extinction at Gubbio (Italy): Planktonic foraminiferal testimonial of the onset of the Caribbean large igneous province emplacement? *Geol. Soc. Am. Spec. Pap.* **2016**, *524*, 79–96.
10. Ferraro, S.; Coccioni, R.; Sabatino, N.; Del Core, M.; Sprovieri, M. Morphometric response of late Aptian planktonic foraminiferal communities to environmental changes: A case study of *Paraticinella rohri* at Poggio le Guaine (central Italy). *Palaeogeogr. Palaeoclimatol. Palaeoecol.* **2020**, *538*, 109384. [[CrossRef](#)]
11. Jenkyns, H. Cretaceous anoxic events: From continent to oceans. *J. Geol. Soc. London* **1980**, *137*, 171–188. [[CrossRef](#)]
12. Tsikos, H.; Karakitsios, V.; Van Breugel, Y.; Walsworth-Bell, B.; Bombardiere, L.; Petrizzo, M.; Sinninghe Damste, J.S.; Schouten, S.; Erba, E.; Premoli-Silva, I.; et al. Organic-carbon deposition in the Cretaceous of the Ionian Basin, NW Greece: The Paquier Event (OAE 1b) revisited. *Geol. Mag.* **2004**, *141*, 401–416. [[CrossRef](#)]
13. Coccioni, R.; Luciani, V.; Marsili, A. Cretaceous oceanic anoxic events and radially elongated chambered planktonic foraminifera: Paleoeological and paleoceanographic implications. *Palaeogeogr. Palaeoclimatol. Palaeoecol.* **2006**, *235*, 66–92. [[CrossRef](#)]
14. Karakitsios, V.; Tsikos, H.; Van Breugel, Y.; Koletti, L.; Sinninghe Damste, J.S.; Jenkyns, H.C. First evidence for the Cenomanian-Turonian oceanic anoxic event (OAE2 or “Bonarelli” event) from the Ionian zone, western continental Greece. *Int. J. Earth Sci.* **2007**, *96*, 343–352. [[CrossRef](#)]
15. Karakitsios, V.; Tzortzaki, E.; Giraud, F.; Pasadakis, N. First evidence for the early Aptian Oceanic Anoxic Event (OAE1a) from the Western margin of the Pindos Ocean (NW Greece). *Geobios* **2018**, *51*, 187–210. [[CrossRef](#)]
16. Graziano, R. Sedimentology, biostratigraphy and event stratigraphy of the Early Aptian Oceanic Anoxic Event (OAE1A) in the Apulia Carbonate Platform Margin-Ionian Basin System (Gargano Promontory, southern Italy). *Cretac. Res.* **2013**, *39*, 78–111. [[CrossRef](#)]
17. Kuhnt, W.; Holbourn, A.; Moullade, M. Transient global cooling at the onset of early Aptian oceanic anoxic event (OAE) 1a. *Geology* **2011**, *39*, 323–326. [[CrossRef](#)]
18. Premoli-Silva, I.; Sliter, W.V. Cretaceous planktonic foraminiferal biostratigraphy and evolutionary trends from the Bottaccione section, Gubbio, Italy. *Palaeontogr. Ital.* **1995**, *82*, 1–89.
19. Premoli-Silva, I.; Erba, E.; Salvini, G.; Verga, D.; Locatelli, C. Biotic changes in Cretaceous anoxic events. *J. Foramin. Res.* **1999**, *29*, 352–370.
20. Leckie, R.M.; Bralower, T.J.; Cashman, R. Oceanic anoxic events and plankton evolution: Biotic response to tectonic forcing during the mid-Cretaceous. *Paleoceanography* **2002**, *17*, 13–29. [[CrossRef](#)]
21. Coccioni, R.; Luciani, V. Planktonic foraminifera across the Bonarelli Event (OAE2, latest Cenomanian): The Italian record. *Palaeogeogr. Palaeoclimatol. Palaeoecol.* **2005**, *224*, 167–185. [[CrossRef](#)]
22. Coccioni, R.; Luciani, V. *Guembelitra irregularis* bloom at the K-T boundary: Morphological abnormalities induced by impact related extreme environmental stress. In *Biological Processes Associated with Impact Events: Impact Studies*; Cockell, C., Koeberl, C., Gilmour, I., Eds.; Springer: Heidelberg, Germany, 2006; Volume 8, pp. 179–196. [[CrossRef](#)]
23. Pomoni-Papaioannou, F.; Photiades, A. Chlorozoan vs. foramol carbonate sedimentary systems in an Upper Jurassic-Cretaceous Pelagonian margin Rhodiani area (West Macedonia, Greece). *Boll. Soc. Geol. It. Ital. J. Geosci.* **2007**, *126*, 172, 32/05–130.
24. Simone, L.; Carannante, G. Peri-Tethyan Cretaceous shallow-water carbonate systems: Sedimentary patterns and lithofacies. *Geoacta* **2008**, *1*, 193–216.
25. Simone, L.; Bravi, S.; Carannante, G.; Masucci, I.; Pomoni-Papaioannou, F. Arid versus wet climatic evidence in the “middle Cretaceous” calcareous successions of the Southern Apennines (Italy). *Cretac. Res.* **2012**, *36*, 6–23. [[CrossRef](#)]
26. Bernoulli, D.; Jenkyns, H.C. Alpine, Mediterranean, and Central Atlantic Mesozoic facies in relation to the early evolution of the Tethys. In *Modern and Ancient Geosynclinal Sedimentation*; Dott, R.H., Shaver, R.H., Eds.; SEPM Special Publications; SEPM: Tulsa, OK, USA, 1974; Volume 19, pp. 129–160.

27. Philip, J.; Masse, J.P.; Camoin, G. Tethyan carbonate platforms. In *The Ocean Basins and Margins*; Nairn, A.E.M., Ricou, L.E., Vrielynck, B., Dercourt, J., Eds.; The Tethys Ocean Plenum Press: New York, NY, USA, 1995; Volume 8, pp. 239–265.
28. Dercourt, J.; Gaetani, M.; Vrielynck, B.; Barrier, E.; Biju-Duval, B.; Brunet, M.F.; Cadet, J.P.; Crasquin, S.; Sandulescu, M. *Atlas PeriTethys, Palaeogeographical Maps*; CCGM/CGMW: Paris, France, 2000; p. 269.
29. Kiessling, W.; Flügel, E.; Golonka, J. Patterns of Phanerozoic carbonate platform sedimentation. *Lethaia* **2003**, *36*, 195–225. [[CrossRef](#)]
30. Bernoulli, D. Mesozoic-Tertiary carbonate platforms, slopes and basins of the external Apennines and Sicily. In *Anatomy of an Orogen: The Apennines and Adjacent Mediterranean Basins*; Vai, G.B., Martini, I.P., Eds.; Kluwer Academic Publishers: London, UK, 2001; pp. 307–326.
31. Vlahović, I.; Tisljar, J.; Velić, I.; Matićec, D. Evolution of the Adriatic Carbonate Platform: Palaeogeography, main events and depositional dynamics. *Palaeogeogr. Palaeoclimatol. Palaeoecol.* **2005**, *220*, 333–360. [[CrossRef](#)]
32. Korbar, T. Orogenic evolution of the external Dinarides in the NE Adriatic region: A model constrained by tectonostratigraphy of Upper Cretaceous to Paleogene carbonates. *Earth Sci. Rev.* **2009**, *96*, 296–312. [[CrossRef](#)]
33. Karakitsios, V.; Rigakis, N. Evolution and petroleum potential of western Greece. *J. Petr. Geol.* **2007**, *30*, 197–218. [[CrossRef](#)]
34. Karakitsios, V. Western Greece and Ionian Petroleum systems. *AAPG Bull.* **2013**, *97*, 1567–1595. [[CrossRef](#)]
35. Zelilidis, A.; Maravelis, A.G.; Tserolas, P.; Konstantopoulos, P.A. An overview of the petroleum systems in the Ionian Zone, onshore NW Greece and Albania. *J. Petr. Geol.* **2015**, *38*, 331–348. [[CrossRef](#)]
36. Cazzola, C.; Soudet, H.J. Facies and Reservoir Characterization of Cretaceous-Eocene Turbidites in the Northern Adriatic. In *Accumulation and Production of Europe's Hydrocarbons III Generation*; Spencer, A.M., Ed.; Special Publication of the European Association of Petroleum Geoscientists; Springer: Berlin/Heidelberg, Germany, 1993; Volume 3.
37. Cazzini, F.; Dal Zotto, O.; Fantoni, R.; Ghielmi, M.; Ronchi, P.; Scotti, P. Oil and gas in the Adriatic foreland, Italy. *J. Petr. Geol.* **2015**, *38*, 255–279. [[CrossRef](#)]
38. Velaj, T.; Davison, I.; Serjani, A.; Alsop, I. Thrust tectonics and the role of evaporites in the Ionian Zone of the Albanides. *AAPG Bull.* **1999**, *83*, 1408–1425.
39. Van Geet, M.; Swennen, R.; Durmishi, C.; Roure, F.; Muchez, P. Paragenesis of Cretaceous to Eocene carbonate reservoirs in the Ionian fold and thrust belt (Albania): Relation between tectonism and fluid flow. *Sedimentology* **2002**, *49*, 696–718. [[CrossRef](#)]
40. Zelilidis, A.; Piper, D.J.W.; Vakalas, J.; Avramidis, P.; Getsos, K. Oil and gas plays in Albania: Do equivalent plays exist in Greece? *J. Petr. Geol.* **2003**, *26*, 29–48. [[CrossRef](#)]
41. Casabianca, D.; Bosence, D.; Beckett, D. Reservoir potential of Cretaceous platform-margin breccias, central Italian Apennines. *J. Petr. Geol.* **2002**, *25*, 179–202. [[CrossRef](#)]
42. Bourli, N.; Pantopoulos, G.; Maravelis, A.G.; Zoumpoulis, E.; Iliopoulos, G.; Pomoni-Papaioannou, F.; Kostopoulou, S.; Zelilidis, A. Late Cretaceous to early Eocene geological history of the eastern Ionian Basin, southwestern Greece: A sedimentological approach. *Cretac. Res.* **2019**, *98*, 47–71. [[CrossRef](#)]
43. Spence, G.H.; Finch, E. Influences of nodular chert rhythmites on natural fracture networks in carbonates: An outcrop and two-dimensional discrete element modelling study. In *Advances in the Study of Fractured Reservoirs*; Spence, G.H., Redfern, J., Aguilera, R., Bevan, T.G., Cosgrove, J.W., Couples, G.D., Daniel, J.M., Eds.; Geological Society of London Special Publications; Geological Society of London: London, UK, 2015; Volume 374, pp. 211–249.
44. Coniglio, M.; Dix, G.R. Carbonate slopes. In *Facies Models*; Walker, R.G., James, N.P., Eds.; Geological Association of Canada: St. Johns, NL, Canada, 1992; p. 409.
45. Anselmetti, F.S.; Eberli, G.P.; Bernoulli, D. Seismic modeling of a carbonate platform margin (Montagna della Maiella, Italy): Variations in seismic facies and implications for sequence stratigraphy. *Carbonate Seismol.* **1997**, *6*, 373–406.
46. Cilona, A.; Baud, P.; Tondi, E.; Agosta, F.; Vinciguerra, S.; Rustichelli, A.; Spiers, C.J. Deformation bands in porous carbonate grainstones: Field and laboratory observations. *J. Struct. Geol.* **2012**, *45*, 137–157. [[CrossRef](#)]
47. Cilona, A.; Faulkner, D.R.; Tondi, E.; Agosta, F.; Mancini, L.; Rustichelli, A.; Baud, P.; Vinciguerra, S. The effects of rock heterogeneity on compaction localization in porous carbonates. *J. Struct. Geol.* **2014**, *67*, 75–93. [[CrossRef](#)]

48. Eberli, G.P.; Baechle, G.T.; Anselmetti, F.S.; Incze, M.L. Factors controlling elastic properties in carbonate sediments and rocks. *Lead. Edge* **2003**, *22*, 654–660. [[CrossRef](#)]
49. Rustichelli, A.; Torrieri, S.; Tondi, E.; Laurita, S.; Strauss, C.; Agosta, F.; Balsamo, F. Fracture characteristics in Cretaceous platform and overlying ramp carbonates: An outcrop study from Maiella Mountain (central Italy). *Mar. Pet. Geol.* **2016**, *76*, 68–87. [[CrossRef](#)]
50. Trippetta, F.; Carpenter, B.M.; Mollo, S.; Scuderi, M.M.; Scarlato, P.; Collettini, C. Physical and transport property variations within carbonate-bearing fault zones: Insights from the Monte Maggio fault (Central Italy). *Geochem. Geophys. Geosyst.* **2017**, *18*, 4027–4042. [[CrossRef](#)]
51. Trippetta, F.; Ruggieri, R.; Brandano, M.; Giorgetti, C. Petrophysical properties of heavy oil-bearing carbonate rocks and their implications on petroleum system evolution: Insights from the Majella Massif. *Mar. Pet. Geol.* **2020**, *111*, 350–362. [[CrossRef](#)]
52. Fabricius, I.L.; Røgen, B.; Gommessen, L. How depositional texture and diagenesis control petrophysical and elastic properties of samples from five North Sea chalk fields. *Petrol. Geosci.* **2007**, *13*, 81–95. [[CrossRef](#)]
53. Fabricius, I.; Bächle, G.; Eberli, G. Elastic moduli of dry and water-saturated carbonates-effect of depositional texture, porosity, and permeability. *Geophysics* **2010**, *75*, N65–N78. [[CrossRef](#)]
54. Fitch, P.J.R.; Lovell, M.A.; Davies, S.J.; Pritchard, T.; Harvey, P.K. An integrated and quantitative approach to petrophysical heterogeneity. *Mar. Petrol. Geol.* **2015**, *63*, 82–96. [[CrossRef](#)]
55. Fjaer, E.H.; Raaen, A.M.; Risnes, R. *Petroleum Related Rock Mechanics*; Elsevier Science: Amsterdam, The Netherlands, 1992; p. 514.
56. Mateus, J.; Saavedra, N.; Carrillo, Z.C.; Mateus, D. Correlation development between indentation parameters and uniaxial compressive strength for Colombian sandstones. *CT&F Ciencia Tecnol. Y Futur.* **2007**, *3*, 125–136.
57. Garcia, R.A.; Saavedra, N.F.; Calderon-Carrillo, Z.; Mateus, D. Development of experimental correlations between indentation parameters and unconfined compressive strength (UCS) values in shale samples. *CT&F Ciencia Tecnol. Futur.* **2008**, *3*, 61–81.
58. Karakitsios, V. The influence of pre-existing structure and halokinesis on organic matter preservation and thrust system evolution in the Ionian basin, northwestern Greece. *AAPG Bull.* **1995**, *79*, 960–980.
59. Karakitsios, V. Ouverture et inversion tectonique du bassin Ionien (Epire, Grèce). *Ann. Géol. Pays Hellén.* **1992**, *35*, 185–318.
60. Doutsos, T.; Koukouvelas, I.; Xypolias, P. A new orogenic model for the External Hellenides. In *Tectonic Evolution of the Eastern Mediterranean Regions*; Robertson, A.H.F., Mountrakis, D., Brun, J.-P., Eds.; Geological Society of London Special Publications; Geological Society of London: London, UK, 2006; pp. 507–520.
61. Maravelis, A.; Makrodimitras, G.; Zelilidis, A. Hydrocarbon prospectivity in the Apulian platform and Ionian zone, in relation to strike-slip fault zones, foreland and back-thrust basins of Ionian thrust, in Greece. *Oil Gas Europ. Mag.* **2012**, *38*, 64–89.
62. Konstantopoulos, P.A.; Zelilidis, A. Provenance analysis of Eocene-Oligocene turbidite deposits in Pindos Foreland Basin, fold and thrust belt of SW Greece: Constraints from framework petrography and bulk-rock geochemistry. *Arab. J. Geosci.* **2013**, *6*, 4671–4700. [[CrossRef](#)]
63. Konstantopoulos, P.A.; Maravelis, A.; Zelilidis, A. The implication of transfer faults in foreland basin evolution. Application on Pindos Foreland Basin, West Peloponnesus, Greece. *Terra Nova* **2013**, *25*, 323–336. [[CrossRef](#)]
64. Karakitsios, V. Chronologie et Géométrie de L’ouverture d’un Bassin et de Son Inversion Tectonique: Le Bassin Ionien (Epire, Grèce). Ph.D. Thesis, University of Pierre and Marie Curie, Paris, France, 1990; p. 310.
65. Aubouin, J. Contribution à l’étude géologique de la Grèce septentrionale: Le confins de l’Epire et de la Thessalie. *Ann. Geol. Des. Pays Hell.* **1959**, *10*, 1–483.
66. IGRS-IFP (Institut de Géologie et Recherches du Sous-sol Institut Français du Pétrole). *Etude Géologique de L’EPIRE (Grèce Nord-Occidentale)*; Technip, Ed.; IGRS-IFP: Paris, France, 1966; p. 306.
67. Avramidis, P.; Zelilidis, A. The nature of deep-marine sedimentation and palaeocurrent trends as an evidence of Pindos foreland basin fill conditions. *Episodes* **2001**, *24*, 252–256. [[CrossRef](#)]
68. Avramidis, P.; Zelilidis, A.; Vakalas, I.P.; Kontopoulos, N. Interactions between tectonic activity and eustatic sea-level changes in the Pindos and Mesohellenic Basins, NW Greece: Basin evolution and hydrocarbon potential. *J. Pet. Geol.* **2002**, *25*, 53–82. [[CrossRef](#)]
69. Pantopoulos, G.; Vakalas, I.; Maravelis, A.; Zelilidis, A. Statistical analysis of turbidite bed thickness patterns from the Alpine fold and thrust belt of western and southeastern Greece. *Sed. Geol.* **2013**, *294*, 37–57. [[CrossRef](#)]

70. Karakitsios, V.; Roveri, M.; Lugli, S.; Manzi, V.; Gennari, R.; Antonarakou, A.; Triantaphyllou, M.; Agiadi, K.; Kontakiotis, G. Remarks on the Messinian evaporites of Zakynthos Island (Ionian Sea, Eastern Mediterranean). *Bull. Geol. Soc. Gr.* **2013**, *47*, 146–156.
71. Karakitsios, V.; Roveri, M.; Lugli, S.; Vinicio, M.; Rocco, G.; Antonarakou, A.; Triantaphyllou, M.; Agiadi, K.; Kontakiotis, G.; Kafousia, N.; et al. A record of the Messinian Salinity Crisis in the eastern Ionian tectonically-active domain (Greece, eastern Mediterranean). *Bas. Res.* **2017**, *29*, 203–233. [[CrossRef](#)]
72. Karakitsios, V.; Tsaila-Monopolis, S. Données nouvelles sur les niveaux supérieurs (Lias inférieur-moyen) des Calcaires de Pantokrator (zone ionienne moyenne, Epire, Grèce continentale). Description des Calcaires de Louros. *Rev. Micropaleont.* **1988**, *31*, 49–55.
73. Danelian, T.; De Wever, P.; Azéma, J. Palaeoceanographic significance of new and revised palaeontological datings for the onset of Vigla Limestone sedimentation in the Ionian zone of Greece. *Geol. Mag.* **1997**, *134*, 869–872. [[CrossRef](#)]
74. Karakitsios, V.; Tsikos, H.; van Breugel, Y.; Bakopoulos, I.; Koletti, L. Cretaceous oceanic anoxic events in western continental Greece. *Bull. Geol. Soc. Gr.* **2004**, *34*, 846–855. [[CrossRef](#)]
75. Skourtsis-Coroneou, V.; Solacios, N.; Constantinidis, I. Cretaceous stratigraphy of the Ionian Zone, Hellenides, western Greece. *Cretac. Res.* **1995**, *16*, 539–558. [[CrossRef](#)]
76. BP (British Petroleum) Co. Ltd. The geological results of petroleum exploration in western Greece: Institute for Geology and Subsurface Research (now Institute of Geology and Mineral Exploration). *Spec. Rep.* **1971**, *10*, 1–73.
77. Dunham, R.J. Classification of Carbonate Rocks According to Depositional Texture. In *Classification of Carbonate Rocks*; Hamm, W.E., Ed.; A Symposium; American Association of Petroleum Geologists: Tulsa, OK, USA, 1962.
78. Embry, A.F.; Klovan, J.E. A late devonian reef tract on northeastern banks island. *N.W.T. Bull. Can. Pet. Geol.* **1971**, *19*, 730–781. [[CrossRef](#)]
79. Wilson, J.L. *Carbonate Facies in Geological History*; Springer: Berlin/Heidelberg, Germany, 1975; p. 471.
80. Buxton, M.W.N.; Pedley, H.M. A standardized model for Tethyan Tertiary carbonates ramps. *J. Geol. Soc.* **1989**, *146*, 746–748. [[CrossRef](#)]
81. Burchette, T.P.; Wright, V.P. Carbonate ramp depositional systems. *Sediment. Geol.* **1992**, *79*, 3–57. [[CrossRef](#)]
82. Pedley, M. A review of sediment distributions and processes in Oligo-Miocene ramps of southern Italy and Malta (Mediterranean divide). *Geol. Soc. London Spec. Publ.* **1998**, *149*, 163–179. [[CrossRef](#)]
83. Pomar, L. Types of carbonate platforms: A genetic approach. *Basin Res.* **2001**, *13*, 313–334. [[CrossRef](#)]
84. Flügel, E. *Microfacies Analysis of Limestones: Analysis, Interpretation and Application*; Springer Verlag: Berlin, Germany, 2004; p. 976.
85. Flügel, E. *Microfacies Analysis of Carbonate Rocks*; Springer Verlag: Berlin, Germany, 2010; p. 745.
86. Moforis, L. Stratigraphy, Reservoir Characteristics and Paleogeographic Distribution of the Triassic to Eocene Carbonates in Western Greece and Albania, Based on Field, Laboratory and Well Data. Master's Thesis, National and Kapodistrian University of Athens, Athens, Greece, 2016; pp. 1–122.
87. I.G.S.R. *Geological Map of Greece Series, Pappadaitai Sheet, Scale 1:50.000*; Institute for Geology and Subsurface Research: Athens, Greece, 1966.
88. I.G.S.R. *Geological Map of Greece Series, Ioannina Sheet, Scale 1:50.000*; Institute for Geology and Subsurface Research: Athens, Greece, 1967.
89. I.G.S.R. *Geological Map of Greece Series, Doliana Sheet, Scale 1:50.000*; Institute for Geology and Subsurface Research: Athens, Greece, 1968.
90. I.G.S.R. *Geological Map of Greece Series, Tsepelovo Sheet, Scale 1:50.000*; Institute for Geology and Subsurface Research: Athens, Greece, 1970.
91. Ahr, W.M. *Geology of Carbonate Reservoirs: The Identification, Description, and Characterization of Hydrocarbon Reservoirs in Carbonate Rocks*; John Wiley & Sons Inc.: Hoboken, NJ, USA, 2008.
92. Brown, A. Porosity variation in carbonates as a function of depth: Mississippian Madison Group, Williston basin. In *Reservoir Quality Prediction in Sandstones and Carbonates*; Kupecz, J.A., Gluyas, J., Bloch, S., Eds.; AAPG Memoir: Tulsa, OK, USA, 1997; Volume 69, pp. 29–46.
93. Ehrenberg, S.N.; Nadeau, P.H. Sandstone versus carbonate petroleum reservoirs: A global perspective on porosity-depth and porosity-permeability relationships. *AAPG Bull.* **2005**, *89*, 435–445. [[CrossRef](#)]



94. Ehrenberg, S.N.; Eberli, G.P.; Keramati, M.; Moallemi, S.A. Porosity-permeability relationships in interlayered limestone-dolostone reservoirs. *Am. Assoc. Pet. Geol. Bull.* **2006**, *90*, 91–114. [[CrossRef](#)]
95. Budd, D.A. Permeability loss with depth in the Cenozoic carbonate platform of west-central Florida. *AAPG Bull.* **2001**, *85*, 1253–1272.
96. Hosa, A.; Wood, R.A.; Corbett, P.W.M.; Souza, R.S.; Roemers, E. Modelling the impact of depositional and diagenetic processes on reservoir properties of the crystal-shrub limestones in the ‘Pre-Salt’ Barra Velha Formation, Santos Basin, Brazil. *Mar. Petr. Geol.* **2020**, *112*, 104100. [[CrossRef](#)]
97. Gudmundsson, A. *Rock Fractures in Geological Processes*; Cambridge University Press: Cambridge, UK, 2011.
98. Jaeger, J.C.; Cook, N.G.W.; Zimmerman, R.W. *Fundamentals of Rock Mechanics*; Blackwell Publishing: Oxford, UK, 2007.
99. Mavko, G.; Mukerji, T.; Dvorkin, J. *The Rock Physics Handbook: Tools for Seismic Analysis of Porous Media*; Cambridge University Press: Cambridge, UK, 2009.
100. Karakitsios, V.; Rigakis, N.; Bakopoulos, I. Migration and trapping of the Ionian series hydrocarbons (Epirus, NWGreece). *Bull. Geol. Soc. Gr.* **2001**, *34*, 1237–1245.
101. Bourli, N.; Kokkaliari, M.; Iliopoulos, I.; Pe-Piper, G.; Piper, D.J.W.; Maravelis, A.G.; Zelilidis, A. Mineralogy of siliceous concretions, cretaceous of Ionian zone, western Greece: Implication for diagenesis and porosity. *Mar. Pet. Geol.* **2019**, *105*, 45–63. [[CrossRef](#)]
102. Karakitsios, V.; Koletti, L. Critical Revision of the Age of the Basal Vigla Limestones (Ionian Zone, Western Greece), Based on Nannoplankton and Calpionellids, with Paleogeographical Consequences. In *Knihovnicka Zemniho Plynu a Nafty, Proceedings of the 4th International Nannoplankton Association Conference, Prague, Czech Republic, 1 September 1992*; Hamrsmid, B., Young, J., Eds.; Knihovnicka ZPN: Prague, Czech; Volume 14a, pp. 165–177.
103. BouDagher-Fadel, M.K. Evolution and Geological Significance of Larger Benthic Foraminifera. *Dev. Palaeontol. Stratigr.* **2008**, *21*, 1–548.
104. Höntzsch, S.; Scheibner, C.; Kuss, J.; Marzouk, A.M.; Michael, W.; Rasser, M.W. Tectonically driven carbonate ramp evolution at the southern Tethyan shelf: The Lower Eocene succession of the Galala Mountains, Egypt. *Facies* **2011**, *57*, 51–72. [[CrossRef](#)]
105. Haq, B.U.; Hardenbol, J.; Vail, P.R. Chronology of fluctuating sea levels since the Triassic. *Science* **1987**, *235*, 1156–1166. [[CrossRef](#)] [[PubMed](#)]
106. Miller, K.G.; Mountain, G.S.; Wright, J.D.; Browning, J.V. A 180-million-year record of sea level and ice volume variations from continental margin and deep-sea isotopic records. *Oceanography* **2011**, *24*, 40–53. [[CrossRef](#)]
107. Kontakiotis, G.; Karakitsios, V.; Cornée, J.; Moissette, P.; Zarkogiannis, S.D.; Pasadakis, N.; Koskeridou, E.; Manoutsoglou, E.; Drinia, H.; Antonarakou, A. Preliminary results based on geochemical sedimentary constraints on the hydrocarbon potential and depositional environment of a Messinian sub-salt mixed siliciclastic-carbonate succession onshore Crete (Plouti section, eastern Mediterranean). *Med. Geosc. Rev.* **2020**, *2*, 247–265. [[CrossRef](#)]
108. Grohmann, S.; Fietz, W.; Nader, F.; Romero-Sarmiento, M.; Baudin, F.; Littke, R. Characterization of Late Cretaceous to Miocene source rocks in the Eastern Mediterranean Sea: An integrated numerical approach of stratigraphic forward modeling and petroleum system modeling. *Basin Res.* **2020**. [[CrossRef](#)]



© 2020 by the authors. Licensee MDPI, Basel, Switzerland. This article is an open access article distributed under the terms and conditions of the Creative Commons Attribution (CC BY) license (<http://creativecommons.org/licenses/by/4.0/>).

Article

Key Environmental Factors Controlling Planktonic Foraminiferal and Pteropod Community's Response to Late Quaternary Hydroclimate Changes in the South Aegean Sea (Eastern Mediterranean)

Christina Giamali ^{1,2,*}, George Kontakiotis ^{1,*} , Efterpi Koskeridou ¹ , Chryssanthi Ioakim ³ and Assimina Antonarakou ¹

¹ Department of Historical Geology and Paleontology, Faculty of Geology and Geoenvironment, National and Kapodistrian University of Athens, Panepistimiopolis, 15784 Athens, Greece; ekosker@geol.uoa.gr (E.K.); aantonar@geol.uoa.gr (A.A.)

² The Goulandris Natural History Museum, Levidou 13, 14562 Kifissia, Greece

³ Institute of Geology and Mineral Exploration (I.G.M.E.), Olympic Village, 13677 Acharnae, Greece; cioakim@otenet.gr

* Correspondence: gchristi@geol.uoa.gr (C.G.); gkontak@geol.uoa.gr (G.K.); Tel.: +30-210-8015-870 (ext. 510) (C.G.); +30-210-7274-804 (G.K.)

Received: 27 August 2020; Accepted: 10 September 2020; Published: 14 September 2020



Abstract: A multidisciplinary study was conducted in order to investigate the environmental factors affecting the planktonic foraminiferal and pteropod communities of the south Aegean Sea. Aspects of the Late Quaternary paleoceanographic evolution were revealed by means of quantitative analyses of planktonic foraminiferal and pteropod assemblages (including multivariate statistical approach; principal component analysis (PCA)), the oxygen ($\delta^{18}\text{O}$) and carbon ($\delta^{13}\text{C}$) isotopic composition of planktonic foraminifera and related paleoceanographic (planktonic paleoclimatic curve (PPC), productivity (E-index), stratification (S-index), seasonality) indices, extracted by the gravity core KIM-2A derived from the submarine area between Kimolos and Sifnos islands. Focusing on the last ~21 calibrated thousands of years before present (ka BP), cold and eutrophicated conditions were identified during the Late Glacial period (21.1–15.7 ka BP) and were followed by warmer and wetter conditions during the deglaciation phase. The beginning of the Holocene was marked by a climatic amelioration and increased seasonality. The more pronounced environmental changes were identified during the deposition of the sapropel sublayers S1a (9.4–7.7 ka BP) and S1b (6.9–6.4 ka BP), with extremely warm and stratified conditions. Pteropod fauna during the sapropel deposition were recorded for the first time in the south Aegean Sea, suggesting arid conditions towards the end of S1a. Besides sea surface temperature (SST), which shows the highest explanatory power for the distribution of the analyzed fauna, water column stratification, primary productivity, and seasonality also control their communities during the Late Quaternary.

Keywords: paleoceanographic evolution; planktonic foraminifera; pteropods; stable isotopes; sea surface temperature (SST); stratification; productivity; sapropel S1; Aegean Sea; Late Quaternary

1. Introduction

The Aegean Sea is an ideal archive to investigate climatic evolution at both global and local scale because of its intermediate position between the higher- and lower-latitude climate systems [1–3], high sedimentation rate marine records compared to the open Mediterranean Sea [4–7], and its paleo-latitudinal and land-locked configuration [8,9]. Such marginal seas are often more responsive to

paleoceanographic and paleoclimatic changes than global oceans, with climatic signals to be recorded in an amplified fashion in Mediterranean properties such as temperature, salinity and specific elemental concentrations, because of their smaller size and partial isolation [10], and therefore can be considered miniature oceans. In addition to interactions with the Black Sea, northern Aegean, and Levantine basins with remote and local atmospheric forcing [1,11], the south Aegean Sea is characterized by intense biogeochemical contrasts in its hydrology in response to a climatic gradient from mid-latitude to subtropical regimes that appears to be very sensitive to climate changes. However, most of the current paleoclimatic and paleoceanographic studies are still limited to deep marine records [6,12–15], and consequently little is known about the continental shelf and/or coastal areas within this marginal Sea [16–21].

Environmental changes related to the different water column and/or sediment characteristics can be recorded virtually instantaneously in paleoceanographic proxy data, such as stable isotope and other geochemical ratios [22–31], and micro-fossil abundances, such as planktonic foraminifera and pteropods [15,17,28,32–36]. This makes them extremely valuable for both stratigraphic correlations and paleoenvironmental/paleoclimate reconstructions [15,23,28,29,32,35,37–45]. Their significance in the study of modern and past marine ecosystems in the eastern Mediterranean Sea is well underlined [20,31,46–51]. Particularly, they are used as indicators of temperature, salinity, density, and nutrient content of the water column, making it possible to identify past circulation through the sedimentary record [7,15,29,47,52,53] and detect long- and short-term paleoclimatic and paleoceanographic changes in the study area [6,10,12,15,16,53–55] during the last glacial cycle.

Pteropods are widespread and abundant in the global ocean and entirely adapted to a pelagic life cycle [56,57]. Owing to the aragonite nature of their shells which increases their weight as settling particles and hence their sinking speed [58], their deposition is expected to be close to their habitat [59]. Particularly in the Mediterranean Sea, preservation of pteropods shells is excellent as a result of the relatively shallow water, high bottom water temperatures, and probably the limited number of mud feeders [60]. A considerable number of studies (e.g., [33,34,61–66]) have shown that Late Quaternary pteropod assemblages and their distribution pattern in the world oceans have changed with temperature and the overall climatic conditions that also affect the aragonite compensation depth (ACD). Recent studies [67] have shown that modern eastern Mediterranean pteropod communities are found to be more abundant than in those at western Mediterranean Sea. Their abundances are positively correlated with the aragonite saturation state (Ω_{ar}), O_2 concentration, pH, salinity and temperature, and negatively correlated with nutrient concentrations [67,68]. However, pteropod assemblages and their distribution in the Aegean Sea during the Late Quaternary are poorly documented.

The present study focuses on identifying and describing key environmental factors that control Late Quaternary planktonic foraminiferal and pteropod distribution in the south Aegean Sea, based on marine sediments retrieved by a 2-m long gravity (KIM-2A) core. In addition, paleoclimatic data were revealed from their distribution patterns coupled with variations of oxygen and carbon isotopic signals. The combination of the above data enables speculation on the factors' response to the climatic changes.

2. Regional and Climatic Setting

The Aegean Sea is in the northern sector of the eastern Mediterranean (Figure 1a), between the Turkish coastline to the east, the Greek mainland to the north and west, and bounded on the south by the island of Crete and Cretan Arc. It is connected to the Black Sea through the Straits of Bosphorus and Dardanelles, and to the Levantine Sea through several larger and deeper straits between Peloponnesus, the islands of Crete and Rhodes, and south-western Turkey (Figure 1b). It is characterized, in general, by a cyclonic water circulation, although the most active dynamic features are the mesoscale cyclonic and anticyclonic eddies, either permanent and/or recurrent [8]. It is separated into two major sub-basins with different climatic conditions: the “north” and the “south” Aegean Sea. The north is more humid than the semiarid south [8].

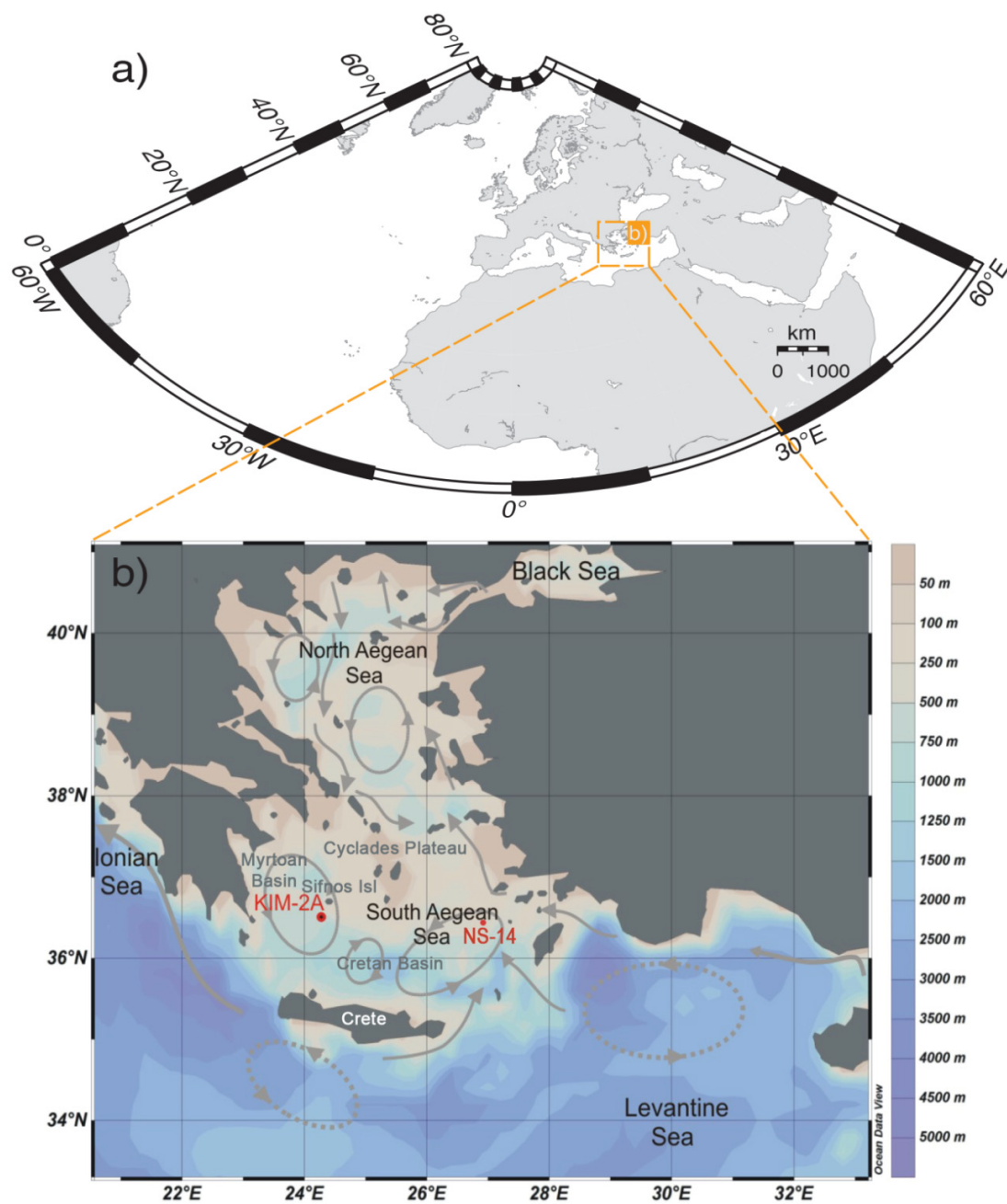


Figure 1. (a) Map of the Mediterranean Sea (including the Aegean Sea); (b) inset shows location of the south Aegean sediment core KIM-2A ($36^{\circ}95.464'N$, $24^{\circ}06.354'E$, 640 m depth; in red), and the main patterns of sea surface-water circulation (grey arrows), cyclonic (solid grey circles) and anticyclonic gyres (dashed grey circles) in the Levantine and Aegean Seas. Location of the core NS-14 [7,16], that was used for the age model construction. Map contours show paleobathymetry (water depth in meters) of the study area.

The south Aegean (extend in between $35^{\circ}N$ and $37^{\circ}N$) is one of the most oligotrophic areas in the Mediterranean Sea [8], with its surface water circulation mostly affected by arid climatic conditions, while it is also modulated by the effect of the Cretan gyre [69]. It mainly consists of the Cretan basin and the shallow shelf of the Cyclades Plateau, along with the Myrtoan Sea at the NW part of the region (Figure 1b). Milos and Kimolos islands lie in the westernmost sector of the Cyclades plateau. Both islands are part of the south Aegean Volcanic Arc; the most important geological structure of the Aegean Sea. The submarine area between Kimolos and Sifnos Islands is characterized by a rather

complex relief [70] as it is related to the volcanic arc. The sedimentary and Quaternary tectonic evolution of the aforementioned submarine area have been studied previously [71], and it is separated into three parts (the southern, the eastern, and the northern; [70]). The core studied derives from a submarine depression located at the northern part.

3. Materials and Methods

3.1. Location and Sampling Strategy of Core KIM-2A

A gravity core (KIM-2A; 200 cm length) was recovered with R/V Aegaeo in May 2015 from the south Aegean Sea and covers the Late Quaternary (the last ~21 ka BP). Core KIM-2A was collected from the Cyclades plateau, from a submarine depression (640 m water depth) located north of Kimolos Island (36°95.464'N, 24°06.354'E), as shown in Figure 1b. After splitting, the half core was stored as archival material, whereas the working half has been sampled for multiple analyses (micropaleontology, sedimentology, and geochemistry).

Fifty-eight samples were taken and used for paleontological (planktonic foraminifera and pteropods) and geochemical (Total Organic Carbon; TOC, stable oxygen and carbon isotopes; $\delta^{18}\text{O}$, $\delta^{13}\text{C}$) analyses between 196 cm and 4 cm. Samples were taken throughout the core but with different sampling resolutions. For the first gray interval corresponding to S1a, the sampling resolution was 1 cm; beyond these intervals the sampling was 2 cm, whereas the top 40 cm were sampled at a mean 8 cm resolution.

3.2. Micropaleontological Analyses

All samples were prepared following standard micropaleontological procedures. For the faunal analyses, approximately 3 cm³ of dried sediment was washed and sieved through a 63 μm screen, and residues were dried in an oven at 50 °C. Qualitative and quantitative analyses have been performed on both planktonic foraminiferal and pteropod assemblages for the >125 μm size fraction, split into aliquots, each one containing at least 300 specimens. It should be noted that the 125 μm fraction was selected since is the most common studied fraction in relevant investigations within the Aegean Sea, which analyze the Late Quaternary foraminiferal record [10,18,21,32,36], and implement a paleoclimatic analysis [6,15,20,72]. All shells were handpicked, identified following [73], counted in each sample, and then converted into percentages, based on the extrapolation of a counted split. Planktonic species with phylogenetic affinities and similar ecological characteristics [35,74] were counted together and grouped to better interpret distribution patterns. On this regard, all *Globigerinoides ruber* morphotypes (“Normal,” “Platys,” “Elongate,” and “Twin” types; [32]) were plotted together, distinguishing only the “alba” and “rosea” varieties due to their different ecological characteristics [75]. Furthermore, *Globigerina bulloides* group includes the species *G. bulloides* and *Globigerina falconensis*, the *Globigerinoides sacculifer* group includes *Globigerinoides trilobus* and *G. sacculifer*, and the *Globigerinella siphonifera* group includes the species *Globigerinella aequilateralis*, *Globigerina calida*, and *Globigerina digitata*. The species *Globigerinita glutinata* includes the morphotypes with and without bulla. Within the group of Neogloboquadriniids, two types were discerned: *Neogloboquadrina pachyderma* and *Neogloboquadrina dutertrei*.

3.3. Total Organic Carbon and Stable Isotopes

Total organic carbon (TOC) was determined based on the [76] methodology with the [77] adaptation at the Laboratory of the Hellenic Survey of Geology and Mineral Exploration (H.S.G.M.E.). For stable oxygen and carbon ($\delta^{18}\text{O}$, $\delta^{13}\text{C}$) isotope measurements, 30 specimens of the planktonic species *G. ruber* f. *alba* were picked from the 250–300 μm size fraction. In particular, we exclusively used the morphotype “Normal” of [32] (equivalent to *G. ruber sensu stricto* [75]) in order to minimize potential morphotype-specific differential responses in stable isotope compositions [24,78,79]. This narrow size fraction was used to minimize ontogenetic and growth rate effects on shell geochemistry [80]. The analyses were carried out at the Laboratory of Geology and Geophysics at Edinburgh University.

Foraminiferal $\delta^{18}\text{O}$ and $\delta^{13}\text{C}$ data were calibrated to National Bureau of Standards 19 (NBS19), and the isotope values are reported in ‰ relative to Vienna Pee Dee belemnite scale. The external standard errors of the stable carbon and oxygen isotope analyses are <0.06‰ and 0.08‰, respectively.

3.4. Chronology

The chronology of the core KIM-2A is based on five accelerator mass spectroscopy radiocarbon (AMS ^{14}C) dates (on *G. ruber* tests at Beta Analytics laboratories), supplemented by tie-points which correspond to well-dated bio-litho-stratigraphic horizons (e.g., sapropel and planktonic foraminiferal biozone boundaries) from nearby Aegean cores (Table 1). Conventional ^{14}C ages were calibrated by means of the Calib version 7.0.2 software [81] and the Marine13 data set with a regional reservoir age correction (ΔR) of 139 ± 40 years for the S1 interval [82] and of 58 ± 85 years outside the sapropel S1 interval [83]. The chronology adopted in this study for core KIM-2A was derived from a polynomial fit through the calibrated dates and the chronostratigraphic control points' dating as shown in Table 1. Hereafter, ages in this study are reported in calibrated thousands of years before present, notated ka BP.

Table 1. Calibrated radiocarbon dates (AMS ^{14}C) and chronostratigraphic control points' dates.

AMS & Chronostratigraphic Control Points	Depth (cm)	Conventional Radiocarbon Age (BP)	Two Sigma Calibrated Age Range (BP)	Mean Calibrated Age (ka BP)	References
Beta—425634	14.5	4890+/-30	4845–5325	5.08	
Ia/Ib boundary	20			5.2	[84]
Beta—425635	28	5320+/-30	5444–5855	5.65	
S1b top	40			6.4	[7,16]
Beta—425636	50.25	6790+/-30	7036–7292	7.16	
S1b base	52.5			7.3	[7,16]
S1a top	65.5			7.9	[7,16]
Beta—425637	79.5	8320+/-30	8532–8883	8.71	
S1a base	89			10	[7,16]
Ic/II boundary	109			11.3	[84]
II/III boundary	153			15.5	[84]
$\delta^{18}\text{O}_{G. ruber}$ depletion	159			15.9	[52]
Beta—425638	195	18890+/-70	21962–22508	22.24	

3.5. Multivariate Statistical Analyses

Principal component analyses (PCA) is used to reduce the dimensionality of a multivariate data set to a few principal factors that determine the distributions of species. For this analysis all raw data for the totality of the samples and specimens were used. Raw data were processed using PAST (2.17) multivariate statistical software package of [85]. The resulting factor scores show the contribution of each factor in every sample, and therefore the down-core contribution of each factor. The total number of factors was defined by minimizing the remaining “random” variability, and by the possibility to relate the factors to modern hydrographic conditions and planktonic foraminiferal and pteropod ecology.

3.6. Paleoceanographic Indices

The planktonic foraminiferal relative distributions were used as a first-order estimate of sea-surface temperature (SST) variations. An index of the SST variations was constructed based on the down-core variation of planktonic foraminiferal abundances, referred to as planktonic paleoclimatic curve (PPC). The PPC was obtained by the formula $100 \times (w - c)/(w + c)$, where *w* represents the warm-water indicators (*G. ruber* f. *alba*, *G. ruber* f. *rosea*, *Orbulina universa*, *G. sacculifer* gr., *Globoturbotalita rubescens*, and *G. siphonifera* gr.), and *c* the cold-water indicators (*Globorotalia inflata*, *Globorotalia truncatulinoides*, *Turbotalita quinqueloba*, *G. glutinata*, and *Globorotalia scitula*). The eutrophication index (E-index; [7]) was estimated using the sum of the eutrophic species (*N. pachyderma*, *N. dutertrei*, *G. bulloides*, *T. quinqueloba*,

and *G. inflata*) versus the sum of the eutrophic plus oligotrophic species (*G. ruber alba*, *G. ruber rosea*, *G. rubescens*, *G. sacculifer*, *O. universa*, and *G. siphonifera*). The down-core ratio between *G. bulloides* and *G. ruber* was also estimated showing the degree of the stratification of the upper water column [86]. Following [7], this ratio is referred to as S-index, and its values reflect periods of strong summer stratification of the water column where oligotrophic taxa dominate (low values) and/or periods of strong winter mixing of the water column where eutrophic taxa dominate (high values).

4. Results

4.1. Lithological Description, Time Stratigraphic Framework, and Sedimentation Rates

Lithologically, the study core contains a distinct organic-rich dark interval, divided into two separate sub-units (S1a and S1b respectively), representing the regional expression of the most recent sapropel S1 [87,88] (Figure 2a). From the bottom up to 87.5 cm, light gray clay can be observed (Munsell soil color 5Y 7/1). The following 24 cm are of gray color (5Y 5/1) and correspond to the lower sub-unit (S1a) of the sapropel. Between 63.5 cm and 52 cm light gray clay (5Y 7/1) can be observed, indicative of the sapropel interruption (S1i). From 52 cm to 40 cm mud of gray color (5Y 5/2) characterizes the upper sapropel sub-unit (S1b). The clay continues up to 13.5 cm with a light gray clay (5Y 7/1) color. From this point to the top of the core watery clay of light-yellow color (5Y 7/4) can be observed (Figure 2a).

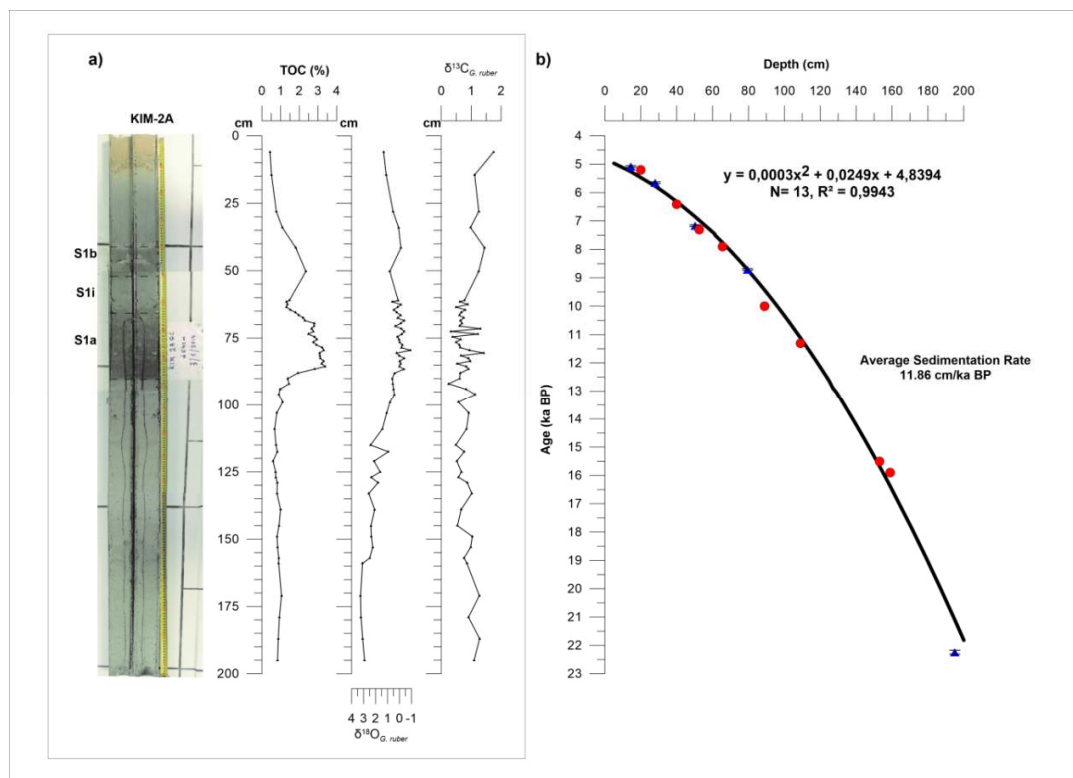


Figure 2. (a) Lithologic log of core KIM-2A along with the total organic carbon (TOC) concentration and $\delta^{18}O_{G.ruber}$ and $\delta^{13}C_{G.ruber}$ isotope values; (b) time stratigraphic framework of the study core; blue triangles represent AMS ^{14}C datings, whereas red dots represent control points and bio-litho-stratigraphic horizons used as stratigraphic markers. The errors of AMS ^{14}C datings are also shown.

Chronology adopted in this study for core KIM-2A derived from a polynomial fit through the five AMS ^{14}C datings mentioned above, and the time markers correlative to the start and end of sapropel deposition, as well as the planktonic foraminiferal biozone Ia/Ib, Ib/Ic, Ic/II and II/III boundaries of [84]

in the Mediterranean Sea (Table 1). The resulting age model is illustrated in Figure 2b and is consistent with the multi-proxy chronological framework of [37] for the Aegean sediment cores, thus supporting the robustness of our chronology. For the ages of the onset and termination of sapropel deposition, we have used the relevant ages from the nearby core NS-14 [7,16,17]. Additional control points related to the planktonic foraminiferal biozone boundaries were used for the age model construction, since they are useful chronologic standards for dating late Quaternary sequences in the central and eastern Mediterranean (including the Aegean Sea; [6,7,52,89] due to their Mediterranean-wide applicability and synchronicity [90–92].

Based on the relative abundances of the planktonic foraminifera species (Figure 3) the interval between 196 cm and 153 cm is characterized by the dominance of *N. pachyderma*, *T. quinqueloba*, *G. scitula* and *G. glutinata* with additional components the species *G. ruber* f. *alba* and *G. bulloides*. This glacial fauna corresponds to assemblage III and it has been recognized throughout the Mediterranean Sea (e.g., [6,52]). The interval between 153 cm and 109 cm corresponds to assemblage II and is characterized by high relative abundances of Neogloboquadrinids and *G. glutinata* and the presence of and *G. inflata*. In the lower part of this interval *G. ruber* f. *rosea* appears for the first time. Subzone Ic (109–40 cm) was identified by the warm subtropical species (*G. ruber* f. *rosea*, *G. siphonifera* gr. and *O. universa*). In addition it includes abundant *G. bulloides* and *G. rubescens* specimens. The sharp increase in the abundance of *G. inflata* at 41.5 cm is inferred to mark the onset of the Ib subzone. The Ia/Ib boundary (at 20 cm) is marked by the decrease of the latter species along with the decrease in the *N. pachyderma* abundance. In this core the Bioevent “Start of $\delta^{18}\text{O}_{\text{ruber}}$ depletion T1a” of [52], was also detected at 159 cm.

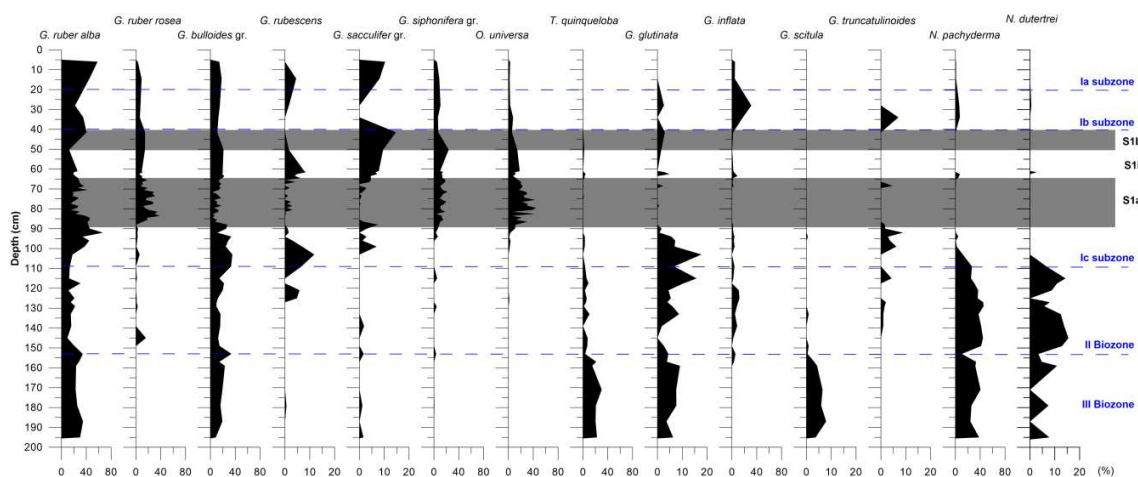


Figure 3. Frequency curves of the most indicative planktonic foraminiferal species in core KIM-2A. The dashed blue lines represent the Ia/Ib, Ib/Ic, Ic/II and II/III boundaries, whereas the gray bands the sapropel S1 sublayers respectively. X axes scales are of 80% and 20% corresponding to the high and low frequency abundances respectively.

According to our proposed age model (Figure 2b), the sedimentary horizons sampled in this study span the interval from the late glacial period, and the subsequent transition (Termination 1; T1) to the middle Holocene (Northgrippian stage) (i.e., ~5–22 ka BP). The average sedimentation rate is 11.86 cm/ka, and is in good agreement to those reported in the marginal Aegean basin [4,7,13,52]. These sedimentation rates were derived from the age model, assuming that the sediment accumulation has been moderately consistent throughout each interval. In particular, the average sedimentation rates are 8.10 cm/ka for the late glacial, 10.30 cm/ka for the Termination T1, and 16.46 cm/ka for the Holocene.

4.2. Planktonic Foraminifera Distribution Pattern

The qualitative analysis revealed 19 planktonic foraminiferal species lumped into 14 groups: *G. ruber* f. *alba*, *G. ruber* f. *rosea*, *G. sacculifer* group, *G. bulloides* group, *G. siphonifera* group, *G. scitula*, *G. truncatulinoidea*, *G. inflata*, *O. universa*, *T. quinqueloba*, *G. glutinata*, *G. rubescens*, *N. pachyderma*, *N. dutertrei*. The down-core stratigraphic distributions of their relative abundance are shown in Figure 3.

From the bottom of the core up to 153 cm, the fauna is characterized by high relative abundances of the species *G. ruber* f. *alba* (22–34%), *N. pachyderma* (10–40%), *T. quinqueloba* (3–30%), and *G. bulloides* gr. (8–33%). Additional components of the fauna are *N. dutertrei*, *G. glutinata*, and *G. scitula*. After the 153 cm, an abrupt decline in Neogloboquadrinids and *T. quinqueloba* can be observed, while *G. bulloides* follows an opposite trend with relative abundance of 33%. From that point up to 127 cm *N. pachyderma* and *N. dutertrei* reach their maximum abundances (45% and 15% respectively), whereas *T. quinqueloba* is still present but with low percentages (up to 10%). The relative abundance of *G. bulloides* does not exceed 16% and *G. ruber* f. *alba* is also present but with equally low frequency (lower than 20%). Between 127 cm and 100 cm the fauna is characterized by the dominance of *G. bulloides*, *N. pachyderma*, *N. dutertrei*, *G. ruber* f. *alba*, *G. glutinata*, and *G. rubescens*. Additional components, with lower percentages, are the species *T. quinqueloba* and *G. inflata*. The interval between 100 cm and 41.5 cm is characterized by a shift in fauna. Most of the species dominating the previous interval are decreasing or becoming absent (*T. quinqueloba*, Neogloboquadrinids, *G. glutinata* and *G. inflata*). Prevailing species of this interval are *O. universa* (44%), *G. ruber* f. *rosea* (38%), *G. bulloides* gr. (27%), *G. siphonifera* gr. (20%), and *G. sacculifer* gr. (14%). In the final segment of the core, from 41.5 cm to the top, the sampling presents poor resolution, but certain significant changes can be observed. The *G. ruber* f. *alba*, *G. inflata* and *G. truncatulinoidea* present a peak (57%, 31%, and 7% respectively) and the relative abundances of *G. ruber* f. *rosea*, *O. universa*, and *G. siphonifera* gr. are decreasing. *N. pachyderma*, *G. inflata*, and *G. glutinata* are re-appearing, but with low percentages.

4.3. Pteropod Distribution Pattern

All samples examined for foraminifera include significant amounts of aragonitic pteropods indicating excellent preservation (without any signals of dissolution) along with the strong carbonate preservation potential of the eastern Mediterranean basin [72,93]. A total of 12 species of Euthecosomata (*Heliconoides inflatus*, *Limacina trochiformis*, *Limacina bulimoides*, *Limacina retroversa*, *Creseis acicula*, *Creseis* sp., *Boasia chierchiaie*, *Hyalocyclis striata*, *Styliola subula*, *Clio pyramidata* s.l., *Diacria trispinosa*, *Cavolinia* spp.) were identified. Adult specimens, when present, were fragmented (*Cavolinia* spp., *C. pyramidata*). The protoconchs (*Clio*, *Diacria* and *Cavolina*) made the identification of certain species and genera possible, as they were the only residue left. The down-core variation of their abundance is presented in Figure 4.

Within the basal part of the core sequence, the fauna is composed almost exclusively of the pteropod *L. retroversa*. An additional component is the species *C. pyramidata*, but with very low percentages (<3.5%). Between 153 cm to 127 cm the pteropodal fauna becomes more diverse with the species *H. inflatus*, *D. trispinosa*, *C. acicula*, and *B. chierchiaie* appearing in the fauna. The relative abundance of *C. pyramidata* gradually increases (up to 45%), in contrast to the decline of *L. retroversa* (drops to ~40%). The latter disappears completely from the fauna at 105 cm. Between 109 cm and 85 cm the pteropod fauna consists mainly of *H. inflatus*, *C. acicula*, *C. pyramidata*, and *D. trispinosa*, with *L. bulimoides* appearing for the first time at 109 cm. The species *C. pyramidata* and *D. trispinosa* are exponentially decreasing until, and including, the top of the core sample. In the last 85 cm of the core, *Cavolinia* spp. appears in the fauna, reaching its maximum abundance (58%) at 41.25 cm and 85.5 cm, with the species *H. inflatus* and *B. chierchiaie* (15–58% and 3–40% respectively) as additional components. At 65.5 cm, *L. trochiformis* presents a short occurrence and between 65 cm and 60 cm *Creseis* sp. presents its maximum relative abundance (36%). Towards the top of the core *L. trochiformis* and *S. subula* present their highest percentages (~6% and 15% respectively).

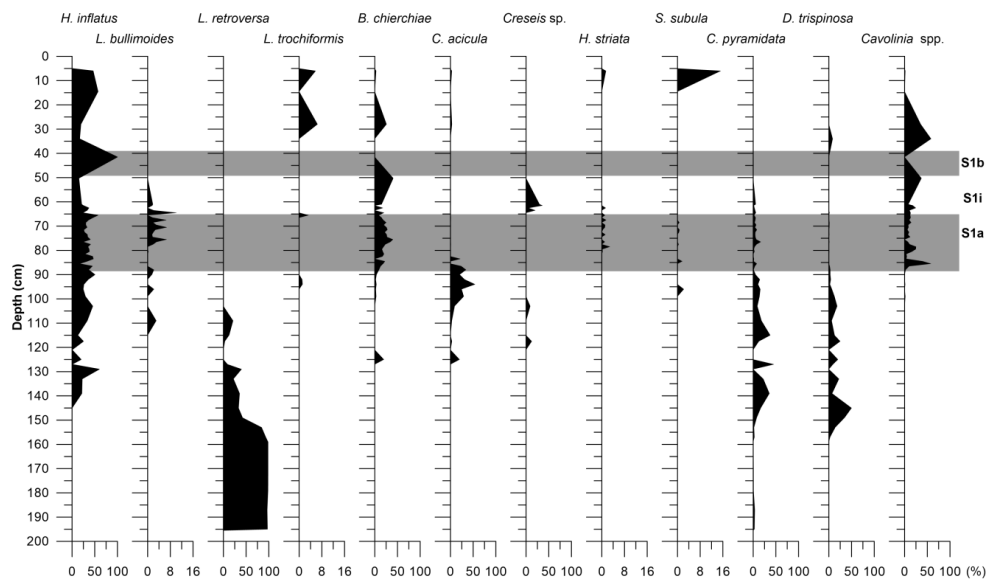


Figure 4. Frequency curves of the most indicative pteropods in core KIM-2A. Gray bands represent the sapropel S1 sublayers. X axes scales are of 100% and 16% corresponding to the high and low frequency abundances respectively.

4.4. Total Organic Carbon and Stable Isotopes

Total organic carbon (TOC) in KIM-2A generally exhibits values around 1%. This pattern is interrupted in two intervals related to the sapropel sub-units deposition. The first interval (S1a; 89–64 cm) is characterized by high TOC concentration, ranging from 1.5% to 3.4%, and in the second interval (S1b; 52.5–40 cm), TOC concentration ranges from 1.8% to 2.4% (Figure 2a). Thus, the deposition of S1 sapropel layer started at 89 cm and terminated at 40 cm. The interruption of sapropel S1 layer (S1i) is detected between 64 cm and 52.5 cm, as suggested by the TOC content (~1.3%).

As shown in Figure 2a, between 196 cm and 159 cm, $\delta^{18}\text{O}_{G. ruber}$ values range from +2.9 to +3.2‰. From 157 cm to 115 cm, a depletion in $\delta^{18}\text{O}_{G. ruber}$ values is observed (up to +0.9‰) and persists until the 34 cm with even lower values. More precisely, the depleted values were recorded from two intervals (88.5–65.5 cm and 50.25–34 cm) with an average value of -0.08‰ and $+0.25\text{‰}$ respectively. In the interval corresponding to 66.5–61 cm, slightly heavier $\delta^{18}\text{O}_{G. ruber}$ values were observed (+0.6 to -0.1‰). In the final unit of the core, from 28 cm until the top, a core enrichment in $\delta^{18}\text{O}_{G. ruber}$ is recorded. The $\delta^{13}\text{C}_{G. ruber}$ values of KIM-2A core exhibit more scatter than the $\delta^{18}\text{O}$ records. In the basal part of the core (200–88 cm) values range between +1.3 to +0.2‰. In the interval between 88 cm and 61 cm the $\delta^{13}\text{C}_{G. ruber}$ ranges between 0.3 and 0.9‰ with the exception of three high-positive peaks at 80.5 cm, 73.5 cm, and 71.5 cm with values of 1.4‰, 1.2‰, and 1.3‰ respectively. From 50.25 cm to the top of the core, $\delta^{13}\text{C}_{G. ruber}$ exhibits heavier values with an average of +1.29‰ (Figure 2a).

4.5. Principal Component Analysis

A standardized principal component analysis (PCA) was carried out on the total data set using the varimax method, in order to determine the impact of various environmental parameters on the planktonic distribution. The application of this statistical analysis yielded a three-factor model for both planktonic foraminiferal and pteropod communities (Supplementary Materials; including PCA scores and biplots). The interpretation of the three components in each case was based on the screen plots of eigen values, and the factor loadings of the planktonic foraminiferal and pteropod species respectively. The 3 distinguished factors were considered to account for 81.57% and 82.81% of the total variance in each category respectively (Tables 2 and 3), with their factor loadings showing the contribution of each factor in every sample and therefore the downcore contribution of each factor (Tables 4 and 5; Figure 5).

In the case of a bipolar factor, which has extremes of positive and negative loadings, high positive factor scores are related to the positive pole and high negative scores to the negative pole, respectively.

Table 2. Principle component analysis (PCA) factors based on planktonic foraminifera and their percentages of the total variability for core KIM-2A.

PCA Factors	Eigenvalue	% Variance	Cumulative % of the Total Variance
1	432.137	50.26	50.26
2	193.038	22.45	72.70
3	76.2131	8.86	81.57
4	53.3399	6.20	87.77
5	38.4841	4.47	92.25
6	24.4952	2.85	95.09
7	15.5611	1.81	96.90
8	7.97016	0.93	97.83
9	7.63218	0.89	98.72
10	5.03693	0.58	99.30
11	2.88765	0.33	99.64
12	2.25794	0.26	99.90
13	0.666282	0.08	99.98
14	0.159802	0.02	100.00

Table 3. PCA factors based on pteropods and their percentages of the total variability for core KIM-2A.

PCA	Eigenvalue	% Variance	Cumulative % of the Total Variance
1	1209.14	58.66	58.66
2	273.91	13.29	71.95
3	223.817	10.86	82.81
4	104.846	5.09	87.89
5	100.727	4.89	92.78
6	63.5077	3.08	95.87
7	53.2518	2.58	98.45
8	23.7844	1.15	99.60
9	4.32791	0.21	99.81
10	2.86233	0.14	99.95
11	0.755953	0.04	99.99
12	0.236728	0.01	100.00

Table 4. Ranking of the planktonic foraminiferal species and their factor loadings along the PCA factors in core KIM-2A. Bold data indicate the most important factor loadings in each factor.

Variables	Factor 1	Factor 2	Factor 3
<i>O. universa</i>	-0.511	0.363	0.194
<i>G. ruber</i> f. alba	-0.158	-0.776	0.443
<i>G. ruber</i> f. rosea	-0.375	0.302	0.101
<i>G. sacculifer</i> gr.	-0.028	-0.091	-0.122
<i>G. siphonifera</i> gr.	-0.251	0.099	-0.152
<i>G. inflata</i>	0.079	-0.020	-0.136
<i>G. bulloides</i> gr.	0.094	-0.199	-0.691
<i>G. rubescens</i>	0.008	-0.012	-0.209
<i>N. pachyderma</i>	0.643	0.320	0.305
<i>N. dutertrei</i>	0.155	0.100	0.051
<i>T. quinqueloba</i>	0.197	0.001	0.258
<i>G. truncatulinoides</i>	0.007	-0.060	0.004
<i>G. glutinata</i>	0.129	-0.014	-0.110
<i>G. scitula</i>	0.032	-0.009	0.064

Table 5. Ranking of the pteropod species and their factor loadings along the PCA factors in core KIM-2A. Bold data indicate the most important factor loadings in each factor.

Species	Factor 1	Factor 2	Factor 3
<i>H. inflatus</i>	-0.387	0.693	0.453
<i>L. bulimoides</i>	-0.015	-0.012	0.010
<i>L. retroversa</i>	0.895	0.175	0.304
<i>L. trochiformis</i>	-0.005	0.000	0.008
<i>B. chierchiaie</i>	-0.154	-0.334	0.286
<i>C. acicula</i>	-0.064	0.227	-0.328
<i>Creseis</i> sp.	-0.027	-0.031	-0.038
<i>H. striata</i>	-0.004	-0.002	0.008
<i>S. subula</i>	-0.006	0.015	0.004
<i>C. pyramidata</i>	0.009	-0.024	-0.437
<i>D. trispinosa</i>	0.051	-0.020	-0.420
<i>Cavolinia</i> sp.	-0.131	-0.570	0.380

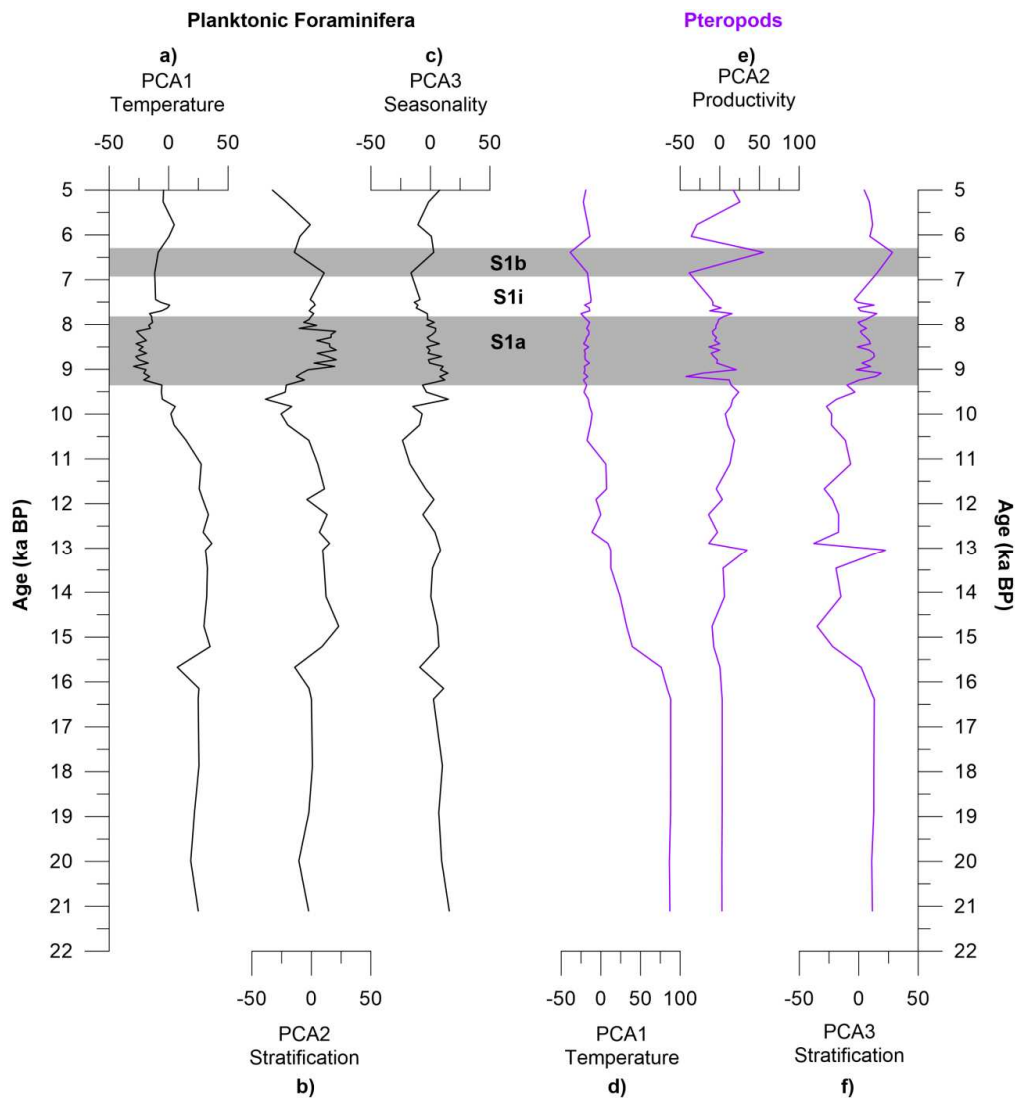


Figure 5. Environmental factors controlling planktonic foraminifera and pteropod distribution resulting from the PCA. (a) PCA1 of planktonic foraminifera as a temperature factor; (b) PCA2 of planktonic foraminifera as a stratification factor; (c) PCA3 of planktonic foraminifera as a seasonality factor; (d) PCA1 of pteropods as a temperature factor; (e) PCA2 of pteropods as a productivity factor; and (f) PCA3 of pteropods as a stratification factor.

4.5.1. Planktonic Foraminifera

The first varimax factor (PCA1; Figure 5a) accounts for 50.26% of the total variance (Table 2) and is interpreted as temperature indicator. Species with positive loadings (*N. pachyderma*, *T. quinqueloba*, *N. dutertrei*, *G. glutinata*, *G. inflata*, *G. bulloides*, and *G. scitula*; Table 4) thrive in cold-water masses, while the species with negative loadings (*O. universa*, *G. ruber* f. *rosea*, *G. siphonifera* gr., and *G. ruber* f. *alba*; Table 4) thrive in warm-water conditions. Factor PCA2 (Figure 5b) accounts for 22.5% of the total variance (Table 1), with the positive pole being expressed by species living in a highly stratified water column (*O. universa*, *G. ruber* f. *rosea* and Neogloboquadrinids) and negative pole by species typical of the weak development of these conditions (*G. ruber* f. *alba* and *G. bulloides* gr.). The third varimax factor (PCA3) describes 8.9% of the total variance (Table 2), and also display a bipolar character, with its positive pole to be represented mainly by *G. ruber* f. *alba* and *N. pachyderma* and the negative pole by *G. bulloides*. The above species that characterize the PCA3 factor are the main exponents of the seasonal contrasts governing planktonic foraminiferal assemblages in the Mediterranean Sea during the last glacial cycle [94–96]. Thus, the third varimax factor (PCA3; Figure 5c) is referred to as a seasonality factor.

4.5.2. Pteropods

The first varimax factor (PCA1; Figure 5e) accounts for 58.66% of the total variance (Table 3) and was interpreted as a temperature indicator. Negative loadings consist mainly of the warm-water species *H. inflatus*, whereas positive loadings consist mainly of the subarctic species *L. retroversa* (Table 5). The second factor (PCA2; Figure 5e) describes 13.29% of the total variance (Table 3) and was interpreted as a productivity factor, as its positive pole is represented mainly by the mesopelagic oligotrophic *H. inflatus*. The third varimax factor (PCA3; Figure 5f) explains 10.27% of the total variance (Table 3). The positively loading taxa expressed by the epipelagic *Cavolinia* sp., *L. retroversa* and *B. chierchiaie*, as well as the mesopelagic and tolerant to low oxygen concentration *H. inflatus*, whereas the negatively loading taxa (mesopelagic *C. pyramidata* and *D. trispinosa*) prefer a well-ventilated water column (Table 5). Thus, the third factor (PCA3) can be regarded as a stratification factor.

5. Discussion

5.1. Factors Controlling Planktonic Fauna Distribution in the Aegean Sea

Of the oceanographic factors typically considered, SST shows the highest explanatory power for the distribution of the planktonic fauna during the Late Quaternary. This is in accordance with previously published studies showing temperature as the dominant factor controlling the biogeography of planktonic foraminifera and pteropods at both global and local scales [61,67,97]. However, the 2 remaining factors (PCA-2, PCA-3) exhibit a bipolar character and could be considered as indicators of the annual stability of the water column. For the planktonic foraminifera fauna, they show that the faunal composition in the south Aegean Sea was not only controlled by SST, but also seems to be affected by the degree of development and location of a permanent or seasonal thermocline/pycnocline. Its vertical placement in the water column is a direct consequence of changes in sea surface salinity (SSS) and productivity (SSP), which ultimately reflected the seasonal fluctuations of the periods of vertical mixing of water in the periods of intense stratification. The interpretation of the second axis focused on the appearance depths of pycnocline and deep chlorophyll maximum (DCM) and the thickness of mixed layer. The interpretation of the third axis focused on upwelling currents and/or river inputs (e.g., *G. bulloides*), parameters which primarily control the food availability and reproductive cycles of foraminifera [73] and are directly correlated to the seasonal fluctuations they present [94,98–100]. Therefore, a useful additional dimension of planktonic foraminifera ecology that is underlined by the PCA conducted in this study is the degree of vertical stratification of the water column and the way it is recorded (seasonal presence/absence pycnocline and DCM and upwellings and runoff), which are inextricably linked with the factors of primary productivity and seasonality.

Similarly, the second and third factor (PCA2, PCA3) of pteropods are focused on the hydrological conditions and the overall oxygenation of the water column. Particularly, the down-core scores of the second factor coincide with the $\delta^{13}\text{C}$ and E-index values, indicating that variations in primary productivity have an impact on pteropod abundances. Even though nutrient concentrations are not a limited factor for their distribution [67], our data suggest that fluctuations in nutrients and salinity due to the increased freshwater inputs during the sapropel deposition favor the flourishing of some species (*Cavolinia* spp., *B. chierchiae*; Figure 4). Additionally, the third factor suggests that oxygen concentration, and thus the intensity of the oxygen minimum zone (OMZ), are parameters that affect pteropod distribution and particularly the mesopelagic species [66].

5.2. Paleoceanographic Reconstruction

The results of the multivariate statistical analyses, in combination with paleoceanographic indices and isotopic data (Figure 6), reveal a succession of Late glacial to Holocene paleoclimatic and paleoceanographic changes. The evidence of these changes is interpreted and discussed in terms of the events that mainly accompanied the transition out of the late glacial period and the deposition of sapropel S1 during the Holocene Climatic Optimum (HCO).

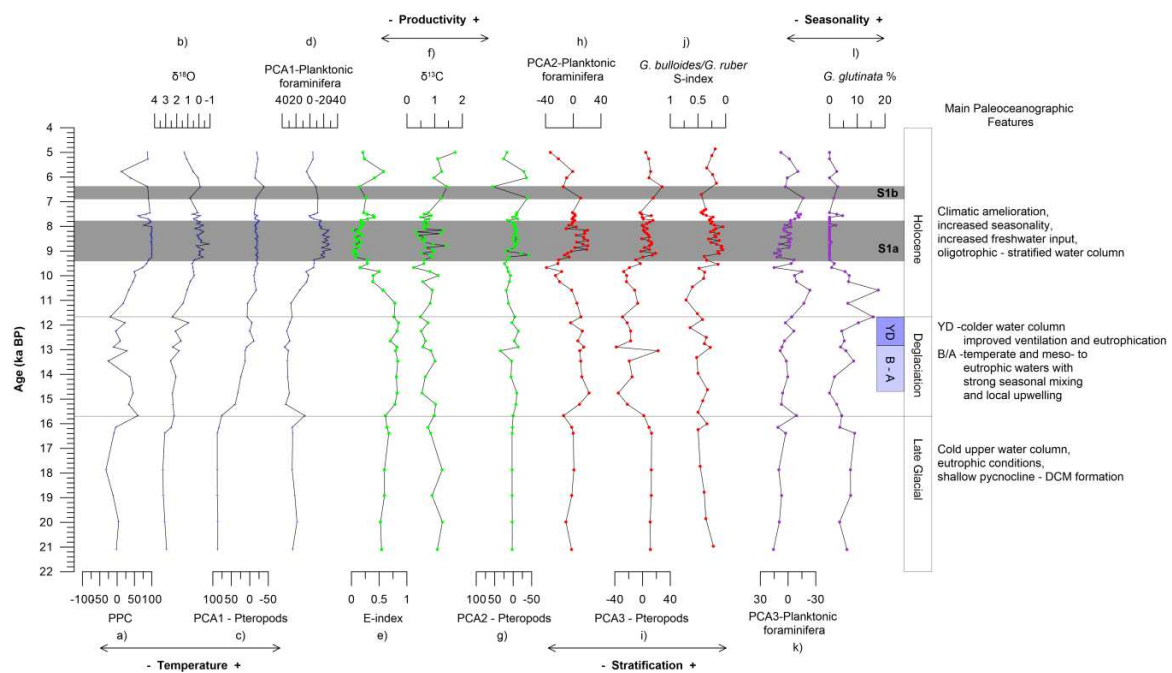


Figure 6. Comparison between down-core score plots of the factors revealed by PCA analysis, micropaleontological and geochemical results of core KIM-2A: (a) planktonic paleoclimatic curve (PPC); (b) oxygen isotope record ($\delta^{18}\text{O}_{G. ruber}$); (c) factor 1 of planktonic foraminifera (PCA1; temperature factor); (d) factor 1 of pteropods (PCA1; temperature indicator); (e) eutrophication index (E-index); (f) carbon isotope record ($\delta^{13}\text{C}_{G. ruber}$); (g) factor 2 of pteropods (PCA2; productivity factor); (h) factor 2 of planktonic foraminifera (PCA2; stratification factor); (i) factor 3 of pteropods (PCA3; stratification factor); (j) *G. bulloides/G. ruber* ratio (S-index); (k) factor 3 of planktonic foraminifera (PCA3; seasonality factor); and (l) *G. glutinata* %.

5.2.1. Late Glacial

During the late glacial period (21.1–15.7 ka BP), the heaviest $\delta^{18}\text{O}$ values (2.49–3.26‰), accompanied by relatively low PPC values (−32% to +4%), suggest a cold upper water column (Figure 6a,b). Particularly, this interval was characterized by high percentages of the cold water foraminifera species *T. quinqueloba* (~30%), accompanied by *G. glutinata* (9%), and *G. scitula* (8%), and significant percentages of the warm-water *G. ruber* f. *alba* (~34%), that are suggestive of milder

climate after the Last Glacial Maximum (LGM), which is in accordance with other records in the Mediterranean [101,102]. Pteropod fauna is composed mainly by the cold water species *L. retroversa* (98%) and the cold-tolerant mesopelagic *C. pyramidata* in very low percentages (3%) which is consistent with relevant late glacial Mediterranean records [33,61,103]. Eutrophic species are also abundant in this interval (*N. pachyderma*, *N. dutertrei*, *T. quinqueloba* and *G. bulloides*) and are associated with the high values of E-index (Figure 6e). Notably, the high abundance of *N. pachyderma* (26%) indicates shallowing of the pycnocline and the formation of a DCM layer. In addition, $\delta^{13}\text{C}$ values, around +1‰, and the trend to higher S-index values (Figure 6f,j), also support the development of eutrophicated waters. The moderate abundance of *G. bulloides* (5–17%; Figure 3) suggests little to no upwelling and/or runoff contribution in primary productivity. Therefore, the injection of nutrients into the euphotic zone can be attributed to the intensification and southward shift of westerly winds, as indicated by atmospheric circulation models for this time interval [104].

5.2.2. Deglaciation

At 15.7 ka BP an abrupt shift of PPC to positive values, accompanied by lighter $\delta^{18}\text{O}$ values (+2.2‰) (Figure 6a,b), are indicative of the climatic amelioration that occurred during the last deglaciation. These warmer conditions are also supported by the occurrence of the warm water species *H. inflatus* and *D. trispinosa* (up to 60% and 50% respectively), and the decrease in *L. retroversa* percentages (between 33% and 85%). This warming trend is in agreement with relevant paleoclimatic records from the eastern Mediterranean, and is attributed to the Bølling–Allerød (B-A) interstadial [7,13,14,105,106]. The increased SST and humidity are also recorded by the higher abundance of the terrestrial biomarkers in the south Aegean [17], and by a change in the benthic faunas from oxic to dysoxic indicator species [13]. In the beginning of this interval, Neogloboquadrinids were temporarily replaced by *G. bulloides* (26%), suggesting local upwelling. Though, later on the eutrophic *N. pachyderma* and *N. dutertrei* present their highest abundance (42% and 14% respectively). Additional components of this interval are *G. ruber* (both variants), *G. bulloides*, *T. quinqueloba*, and *G. inflata*, suggesting temperate and meso- to eutrophic waters, with strong seasonal mixing and local upwelling.

This state persisted until the onset of the Younger Dryas (YD) at about 12.9 ka BP, which is depicted in the abrupt decrease in PPC (from +28% to –10%) and in heavier values of $\delta^{18}\text{O}$ (1.0–2.5‰) (Figure 6a,b). The planktonic foraminiferal fauna shows an increase in cold water species (*N. pachyderma*, *T. quinqueloba*, *G. inflata* and *G. glutinata*). Pteropod fauna is composed mainly of the cold-water species epipelagic *L. retroversa* and the mesopelagic temperate to warm-water species *C. pyramidata* and *D. trispinosa*, while the warm-water *H. inflatus* presents a decreasing trend (Figure 3). This climate response of south Aegean depression to the YD event (12.9–11.7 ka BP) seems to be in accordance with relevant signals from other Aegean sub-basins [6,7]. Towards the end of YD (12.6–12.2 ka BP) the species *G. rubescens*, *C. acicula*, and *B. chierchiae* are added to the fauna suggesting that mild climatic conditions prevailed for a brief time interval of about 400 years within the YD event. This brief climatic amelioration in the mid YD, which has been attributed to the displacement of the polar front by a few degrees north [26], has been also observed in north-central Aegean marine records [7,106] and coincides with the pattern of GRIP and NGRIP ice-core records [107,108], pollen-based reconstructions from the Jura [109] and the Balkans [110], as well as chironomid-based reconstructions from North Italy [111]. The increases in the S-index and E-index at around 12.2 ka BP (Figure 6e,j) coincide with this amelioration, reflected by the improved ventilation and eutrophication of the water column.

5.2.3. Holocene

With the ending of the YD, a general climatic amelioration is seen in the records (increase in PPC, lighter values in $\delta^{18}\text{O}$, decline of temperature factors PCA1; Figure 6a–d) marking the beginning of the Holocene. Planktonic foraminifera fauna consists mainly by *G. ruber* f. *alba* that increases in abundance towards the onset of sapropel deposition, along with *G. bulloides* and *N. pachyderma*. The two latter species present an opposite trend, decreasing towards the onset of sapropel deposition. This trend

suggests the gradual development of stratified and oligotrophic surface waters. Pteropod fauna follows a similar pattern with the decreasing abundances of the species *D. trispinosa* and *C. pyramidata*, which are indicative of a well ventilated water column [112], and the increase in the epipelagic *B. chierchiae* and *C. acicula* (Figure 4). The reduction of E-index along with the values of $\delta^{13}\text{C}$ and the S-index (Figure 6e–j) are further evidence for the development of these conditions. The replacement of *G. inflata* by *G. glutinata* (Figure 3) may be tentatively explained in terms of increased seasonality, and of increased freshwater input, which reduced surface buoyancy loss and hence suppressed mixing during the beginning of the Holocene [7]. This was also enhanced by the presence of the epipelagic pteropods (*Creseis* spp.) that proliferate in low-salinity waters [113], and the seasonality factor (PCA3 of planktonic foraminifera; Figure 6k).

At around 9.4 ka BP, the deposition of sapropel S1 as witnessed by their high organic carbon content (C_{org} : 1.8–3.3%, Figure 2a), coincided with the start of the overall $\delta^{18}\text{O}$ depletion (+0.6‰ to –0.9‰; Figure 6b). The changes of the planktonic foraminifera fauna are characterized by an increase in *G. ruber* f. *rosea*, *G. ruber* f. *alba*, *G. siphonifera* and *O. universa* that are suggestive of extremely warm and stratified conditions (PPC ~100%; PCA1 low values; Figure 6b–d). The lower values of *G. bulloides*/*G. ruber* ratio in this interval are also indicative of strongly stratified water column and are in agreement with the stratification factor for both faunas (PCA2 of planktonic foraminifera and PCA3 of pteropod; Figure 6h–j). An increase in temperature and humidity around this time has been documented in all marine and terrestrial pollen records in the eastern Mediterranean region [6,7,14–16,114]. This paleoclimate change coincides with the Holocene summer precession-related insolation maximum in the Northern Hemisphere [115], and the monsoon intensification that resulted in a widespread increase in humidity over the Mediterranean region and concomitant increase of freshwater input to the Mediterranean Sea [116,117]. Pteropod fauna is characterized by the dominance of the warm oligotrophic *H. inflatus*, and the warm epipelagic *B. chierchiae*, *C. acicula*, and *Cavolinia* spp. (Figure 4). Mesopelagic species (*C. pyramidata* and *D. trispinosa*) are decreasing dramatically due to the enhanced stratification of the entire water column. Mesopelagic pteropods are affected by the OMZ alterations, which are climatically controlled [63,112]. In the humid and warmer conditions that persisted during the formation of S1, the subsequent stratification of the water column favored a strong and well developed OMZ that probably led to the reduction of mesopelagic species. The presence of the mesopelagic *H. inflatus* into the sapropel sublayers can be explained by its habitat. More explicitly, this species adopts a variable depth habitat during its growth stages, and it is more susceptible to the low oxygen concentration in the OMZ [63,118,119]. The presence of *L. bulimoides* in the upper part of S1a, with peaks at 8.4 ka BP, 8.1 ka BP, and 7.9 ka BP (~6%) and its absence in the S1b, suggest that during the end of S1a (8.6–7.7 ka BP) the conditions were more arid than during the onset of S1a (9.4–8.6 ka BP) and the interval of S1b (6.9–6.4 ka BP). In these two phases of S1a, $\delta^{13}\text{C}$ present a decreasing trend with an average value of +0.8‰ in the first phase and +0.6‰ in the second (Figure 6f).

The warm and stratified conditions favorable for the sapropel deposition were interrupted between 7.7 ka BP and 6.8 ka BP. This interval (S1i) is marked by the decrease in PPC (from 90% to 60%) and the heavier values of $\delta^{18}\text{O}$ (+0.5‰) and $\delta^{13}\text{C}$ (+0.8‰) as shown in Figure 6a,b,f. The subsequent cooling is also reflected in significant faunal changes, such as the increase in abundance of *G. inflata*, *T. quinqueloba*, *G. bulloides*, and *N. pachyderma* (Figure 3). These species are associated with relatively cold temperatures and increased food supply, suggesting high primary production and stronger mixing of the water column [46,52]. In addition, the pteropod *L. trochiformis*, which is related to the mixed layer of the water column and thrives in upwelling conditions [120–123], presents a peak at the beginning of S1i (Figure 4).

From 6.4 ka BP to the top of the core (~5.0 ka BP), a trend to heavier $\delta^{18}\text{O}$ values (from 0‰ to +1.3‰) and the drop of PPC (~60%) are recorded (Figure 6a,b). In planktonic foraminifera fauna an increase in *G. inflata*, *G. truncatulinoides* and *N. pachyderma* along with the reduction of *G. ruber* f. *rosea*, *G. siphonifera* gr. *O. universa* indicate lower SST, and stronger seafloor oxygenation due to vertical mixing. This latter is also suggested by the increase in the mesopelagic pteropod *D. trispinosa*. The peak

of *L. trochiformis* at 5.7 ka BP (Figure 4) is suggestive of upwelling conditions. At this point, and up to 5.0 ka BP, increased percentages of *G. bulloides* and *G. sacculifer* are indicative of increased productivity. This is also indicated by the high values of E-index, the heavy $\delta^{13}\text{C}$ (up to +1.7‰) and the PCA2 factor of pteropods (Figure 6e–g).

6. Conclusions

The results of the analysis of planktonic foraminifera and pteropods, combined with the results of principal component analysis and oxygen and carbon isotopic signals, describe the key factors controlling the formation of the micropaleontological assemblages, and therefore the paleoenvironmental and paleoclimatic changes during the last ~21 ka BP. Our data suggests that the sea surface temperature, stratification of the water column, seasonality, and productivity are the main controlling factors of the faunal distribution. During the Late Glacial, all the records indicate the occurrence of cold and eutrophicated waters. The time interval of 15.9–11.7 ka BP, corresponding to the deglaciation phase, was characterized by gradual climatic amelioration. During this interval, the warm interstadial Bølling–Allerød was identified, while low SST records at 12.9 ka BP revealed the onset of the YD. During this event, mild climate conditions were observed for around 400 years, and are attributed to the displacement of the polar front by a few degrees north. With the onset of the Holocene, a general climatic amelioration can be observed, with the gradual development of stratified oligotrophic surface waters. These conditions were intensified during the sapropel S1 deposition, which appears in two layers (S1a and S1b). The faunal and isotopic data suggest that conditions were more arid towards the end of S1a than at the onset of the S1a and the S1b. The interruption of sapropel deposition (S1i) and the post-sapropel interval are characterized by lower SST and stronger seafloor oxygenation due to vertical mixing.

Supplementary Materials: The following are available online at <http://www.mdpi.com/2077-1312/8/9/709/s1>, Figure S1: Planktonic foraminiferal PCA biplot of environmental factors of Temperature (Component 1) and Stratification (Component 2), Figure S2: Planktonic foraminiferal PCA biplot of environmental factors of Temperature (Component 1) and Seasonality (Component 3), Figure S3: Pteropods PCA biplot of environmental factors of Temperature (Component 1) and Productivity (Component 2), Figure S4: Pteropods PCA biplot of environmental factors of Temperature (Component 1) and Stratification (Component 3), Table S1: PCA scores based on planktonic foraminifera raw data, Table S2: PCA scores based on pteropods raw data.

Author Contributions: Conceptualization, C.G., G.K.; methodology, C.G., G.K., A.A.; software, C.G., G.K.; validation, C.G., G.K., A.A.; formal analysis, C.G., G.K., A.A.; investigation, C.G., G.K., C.I., A.A.; resources, C.G., C.I.; data curation, C.G., G.K.; writing—original draft preparation, C.G., G.K.; writing—review and editing, C.G., G.K., E.K., A.A.; visualization, C.G., G.K.; supervision, E.K., A.A.; project administration C.G., A.A.; funding acquisition, E.K., C.I. All authors have read and agreed to the published version of the manuscript.

Funding: This research was funded by EU/ESPA (NSRF; 2007–2013), YPOTHER project (351008) realized at the Institute of Geology and Mineral Exploration recent H.S.G.M.E. E.K. was funded by EU/ESPA (EPAnEK; 2014–2020), INNOVEXPO project (T1EDK-02363). The APC was funded by the Special Account for Research Grants, National and Kapodistrian University of Athens (Grant No. 16599).

Acknowledgments: We wish to thank the captain and crew of R/V Aegaeo (HCMR) for their technical assistance during the YPOTHER cruises, and N. Xirocostas and K. Vallianatou (H.S.G.M.E.) for the organic carbon analysis. We also thank M. Dagla for the English proofreading of the manuscript. Constructive comments by three anonymous reviewers have been essential in improving this manuscript and Victoria Li (Assistant Editor) is thanked for her editorial handling.

Conflicts of Interest: The authors declare no conflict of interest.

References

1. Zervakis, G.I.; Moncalvo, J.-M.; Vilgalys, R. Molecular phylogeny, biogeography and speciation of the mushroom species *Pleurotus cystidiosus* and allied taxa. *Microbiology* **2004**, *150*, 715–726. [CrossRef]
2. Giorgi, F.; Lionello, P. Climate change projections for the Mediterranean region. *Glob. Planet. Chang.* **2008**, *63*, 90–104. [CrossRef]
3. Rohling, E.J.; Grant, K.; Bolshaw, M.; Roberts, A.; Siddall, M.; Hemleben, C.; Kucera, M. Antarctic temperature and global sea level closely coupled over the past five glacial cycles. *Nat. Geosci.* **2009**. [CrossRef]

4. Aksu, A.E.; Yaşar, D.; Mudie, P.J. Paleoclimatic and paleoceanographic conditions leading to development of sapropel layer S1 in the Aegean Sea. *Palaeogeogr. Palaeoclim. Palaeoecol.* **1995**, *116*, 71–101. [[CrossRef](#)]
5. Roussakis, G.; Karageorgis, A.P.; Conispoliatis, N.; Lykousis, V. Last glacial–Holocene sediment sequences in N. Aegean basins: Structure, accumulation rates and clay mineral distribution. *Geo-Mar. Lett.* **2004**, *24*, 97–111. [[CrossRef](#)]
6. Geraga, M.; Ioakim, C.; Lykousis, V.; Tsaila-Monopolis, S.; Mylona, G. The high-resolution palaeoclimatic and palaeoceanographic history of the last 24,000 years in the central Aegean Sea, Greece. *Palaeogeogr. Palaeoclim. Palaeoecol.* **2010**, *287*, 101–115. [[CrossRef](#)]
7. Kontakiotis, G. Late Quaternary paleoenvironmental reconstruction and paleoclimatic implications of the Aegean Sea (eastern Mediterranean) based on paleoceanographic indexes and stable isotopes. *Quat. Int.* **2016**, *401*, 28–42. [[CrossRef](#)]
8. Lykousis, V.; Chronis, G.; Tselepidis, A.; Price, N.B.; Theocharis, A.; Siokou-Frangou, I.; Van Wambeke, F.; Danovaro, R.; Stavrakakis, S.; Duineveld, G.; et al. Major outputs of the recent multidisciplinary biogeochemical researches undertaken in the Aegean Sea. *J. Mar. Syst.* **2002**, *33–34*, 313–334. [[CrossRef](#)]
9. Poulos, S.E. The Mediterranean and Black Sea Marine System: An overview of its physico-geographic and oceanographic characteristics. *Earth Sci. Rev.* **2020**, *200*, 103004. [[CrossRef](#)]
10. Kontakiotis, G. Palaeoceanographic and Palaeoclimatic Study of Eastern Mediterranean During Late Quaternary, Based on Planktonic Foraminiferal Assemblages (in Greek, with English extended abstract). Ph.D. Thesis, National and Kapodistrian University of Athens, Athens, Greece, 2012.
11. Poulos, S.E.; Drakopoulos, P.G.; Collins, M.B. Seasonal variability in sea surface oceanographic conditions in the Aegean Sea (Eastern Mediterranean): An overview. *J. Mar. Syst.* **1997**, *13*, 225–244. [[CrossRef](#)]
12. Geraga, M.; Tsaila-Monopolis, S.; Ioakim, C.; Papatheodorou, G.; Ferentinos, G. Short-term climate changes in the southern Aegean Sea over the last 48,000 years. *Palaeogeogr. Palaeoclim. Palaeoecol.* **2005**, *220*, 311–332. [[CrossRef](#)]
13. Kuhnt, T.; Schmiedl, G.; Ehrmann, W.; Hamann, Y.; Hemleben, C. Deep-sea ecosystem variability of the Aegean Sea during the past 22 kyr as revealed by Benthic Foraminifera. *Mar. Micropaleontol.* **2007**, *64*, 141–162. [[CrossRef](#)]
14. Kotthoff, U.; Müller, U.C.; Pross, J.; Schmiedl, G.; Lawson, I.T.; van de Schootbrugge, B.; Schulz, H. Lateglacial and Holocene vegetation dynamics in the Aegean region: An integrated view based on pollen data from marine and terrestrial archives. *Holocene* **2008**, *18*, 1019–1032. [[CrossRef](#)]
15. Giamali, C.; Koskeridou, E.; Antonarakou, A.; Ioakim, C.; Kontakiotis, G.; Karageorgis, A.P.; Roussakis, G.; Karakitsios, V. Multiproxy ecosystem response of abrupt Holocene climatic changes in the northeastern Mediterranean sedimentary archive and hydrologic regime. *Quat. Res.* **2019**, *92*, 665–685. [[CrossRef](#)]
16. Triantaphyllou, M.V.; Ziveri, P.; Gogou, A.; Marino, G.; Lykousis, V.; Bouloubassi, I.; Emeis, K.-C.; Kouli, K.; Dimiza, M.; Rosell-Melé, A.; et al. Late Glacial–Holocene climate variability at the south-eastern margin of the Aegean Sea. *Mar. Geol.* **2009**, *266*, 182–197. [[CrossRef](#)]
17. Triantaphyllou, M.V.; Antonarakou, A.; Kouli, K.; Dimiza, M.; Kontakiotis, G.; Papanikolaou, M.D.; Ziveri, P.; Mortyn, P.G.; Lianou, V.; Lykousis, V.; et al. Late Glacial–Holocene ecostratigraphy of the south-eastern Aegean Sea, based on plankton and pollen assemblages. *Geo Mar. Lett.* **2009**, *29*, 249–267. [[CrossRef](#)]
18. Drinia, H.; Antonarakou, A.; Tsourou, T.; Kontakiotis, G.; Psychogiou, M.; Anastasakis, G. Foraminifera eco-biostratigraphy of the southern Evoikos outer shelf, central Aegean Sea, during MIS 5 to present. *Cont. Shelf Res.* **2016**, *126*. [[CrossRef](#)]
19. Koutrouli, A.; Anastasakis, G.; Kontakiotis, G.; Ballengee, S.; Kuehn, S.; Pe-Piper, G.; Piper, D.J.W. The early to mid-Holocene marine tephrostratigraphic record in the Nisyros-Yali-Kos volcanic center, SE Aegean Sea. *J. Volcanol. Geotherm. Res.* **2018**, *366*, 96–111. [[CrossRef](#)]
20. Antonarakou, A.; Kontakiotis, G.; Zarkogiannis, S.; Mortyn, P.G.; Drinia, H.; Koskeridou, E.; Anastasakis, G. Planktonic foraminiferal abnormalities in coastal and open marine eastern Mediterranean environments: A natural stress monitoring approach in recent and early Holocene marine systems. *J. Mar. Syst.* **2018**, *181*, 63–78. [[CrossRef](#)]
21. Louvari, M.A.; Drinia, H.; Kontakiotis, G.; Di Bella, L.; Antonarakou, A.; Anastasakis, G. Impact of latest-glacial to Holocene sea-level oscillations on central Aegean shelf ecosystems: A benthic foraminiferal palaeoenvironmental assessment of South Evoikos Gulf, Greece. *J. Mar. Syst.* **2019**, *199*, 103181. [[CrossRef](#)]

22. Kontakiotis, G.; Mortyn, P.G.; Antonarakou, A.; Martínez-Botí, M.A.; Triantaphyllou, M.V. Field-based validation of a diagenetic effect on *G. ruber* Mg/Ca paleothermometry: Core top results from the Aegean Sea (eastern Mediterranean). *Geochem. Geophys. Geosyst.* **2011**, *12*. [[CrossRef](#)]
23. Kontakiotis, G.; Karakitsios, V.; Mortyn, P.G.; Antonarakou, A.; Drinia, H.; Anastasakis, G.; Agiadi, K.; Kafousia, N.; De Rafelis, M. New insights into the early Pliocene hydrographic dynamics and their relationship to the climatic evolution of the Mediterranean Sea. *Palaeogeogr. Palaeoclim. Palaeoecol.* **2016**, *459*, 348–364. [[CrossRef](#)]
24. Antonarakou, A.; Kontakiotis, G.; Mortyn, P.G.; Drinia, H.; Sprovieri, M.; Besiou, E.; Tripsanas, E. Biotic and geochemical ($\delta^{18}\text{O}$, $\delta^{13}\text{C}$, Mg/Ca, Ba/Ca) responses of *Globigerinoides ruber* morphotypes to upper water column variations during the last deglaciation, Gulf of Mexico. *Geochim. Cosmochim. Acta* **2015**, *170*, 69–93. [[CrossRef](#)]
25. Le Houedec, S.; Mojtahid, M.; Bicchi, E.; de Lange, G.J.; Hennekam, R. Suborbital Hydrological Variability Inferred From Coupled Benthic and Planktic Foraminiferal-Based Proxies in the Southeastern Mediterranean During the Last 19 ka. *Paleoceanogr. Paleoclimatol.* **2020**, *35*, e2019PA003827. [[CrossRef](#)]
26. Cacho, I.; Grimalt, J.O.; Canals, M.; Saffi, L.; Shackleton, N.J.; Schönfeld, J.; Zahn, R. Variability of the western Mediterranean Sea surface temperature during the last 25,000 years and its connection with the Northern Hemisphere climatic changes. *Paleoceanography* **2001**, *16*, 40–52. [[CrossRef](#)]
27. Filippidi, A.; Triantaphyllou, M.; de Lange, G. Eastern-Mediterranean ventilation variability during sapropel S1 formation, evaluated at two sites influenced by deep-water formation from Adriatic and Aegean Seas. *Quat. Sci. Rev.* **2016**, *144*, 95–106. [[CrossRef](#)]
28. Kontakiotis, G.; Besiou, E.; Antonarakou, A.; Zarkogiannis, S.D.; Kostis, A.; Mortyn, P.G.; Moissette, P.; Cornée, J.J.; Schulbert, C.; Drinia, H.; et al. Decoding sea surface and paleoclimate conditions in the eastern Mediterranean over the Tortonian-Messinian Transition. *Palaeogeogr. Palaeoclim. Palaeoecol.* **2019**, *534*, 109312. [[CrossRef](#)]
29. Vasiliev, I.; Karakitsios, V.; Bouloubassi, I.; Agiadi, K.; Kontakiotis, G.; Antonarakou, A.; Triantaphyllou, M.; Gogou, A.; Kafousia, N.; de Rafélis, M.; et al. Large Sea Surface Temperature, Salinity, and Productivity-Preservation Changes Preceding the Onset of the Messinian Salinity Crisis in the Eastern Mediterranean Sea. *Paleoceanogr. Paleoclimatol.* **2019**, *34*, 182–202. [[CrossRef](#)]
30. Kontakiotis, G.; Mortyn, G.P.; Antonarakou, A.; Drinia, H. Assessing the reliability of foraminiferal Mg/Ca thermometry by comparing field-samples and culture experiments: A review. *Geol. Q.* **2016**, *60*, 547–560. [[CrossRef](#)]
31. Kontakiotis, G.; Karakitsios, V.; Cornée, J.-J.; Moissette, P.; Zarkogiannis, S.D.; Pasadakis, N.; Koskeridou, E.; Manoutsoglou, E.; Drinia, H.; Antonarakou, A. Preliminary results based on geochemical sedimentary constraints on the hydrocarbon potential and depositional environment of a Messinian sub-salt mixed siliciclastic-carbonate succession onshore Crete (Plouti section, eastern Mediterranean). *Mediterr. Geosci. Rev.* **2020**. [[CrossRef](#)]
32. Kontakiotis, G.; Antonarakou, A.; Mortyn, P.G.; Drinia, H.; Anastasakis, G.; Zarkogiannis, S.; Möbius, J. Morphological recognition of *Globigerinoides ruber* morphotypes and their susceptibility to diagenetic alteration in the eastern Mediterranean Sea. *J. Mar. Syst.* **2017**, *174*, 12–24. [[CrossRef](#)]
33. Wall-Palmer, D.; Smart, C.W.; Hart, M.B.; Leng, M.J.; Borghini, M.; Manini, E.; Aliani, S.; Conversi, A. Late Pleistocene pteropods, heteropods and planktonic foraminifera from the Caribbean Sea, Mediterranean Sea and Indian Ocean. *Micropaleontology* **2014**, *60*, 557–578.
34. Buccheri, G.; Capretto, G.; Di Donato, V.; Esposito, P.; Ferruzza, G.; Pescatore, T.; Russo Ermolli, E.; Senatore, M.R.; Sprovieri, M.; Bertoldo, M.; et al. A high resolution record of the last deglaciation in the southern Tyrrhenian Sea: Environmental and climatic evolution. *Mar. Geol.* **2002**, *186*, 447–470. [[CrossRef](#)]
35. Kontakiotis, G.; Antonarakou, A.; Zachariasse, W.J. Late Quaternary palaeoenvironmental changes in the Aegean Sea: Interrelations and interactions between north and south Aegean Sea. *Bull. Geol. Soc. Greece* **2013**, *47*, 167–177. [[CrossRef](#)]
36. Zarkogiannis, S.; Kontakiotis, G.; Antonarakou, A. Recent planktonic foraminifera population and size response to Eastern Mediterranean hydrography. *Rev. Micropaleontol.* **2020**, *69*, 100450. [[CrossRef](#)]
37. Casford, J.S.L.; Abu-Zied, R.; Rohling, E.J.; Cooke, S.; Fontanier, C.; Leng, M.; Millard, A.; Thomson, J. A stratigraphically controlled multiproxy chronostratigraphy for the eastern Mediterranean. *Paleoceanography* **2007**, *22*. [[CrossRef](#)]

38. Comeau, S.; Jeffree, R.; Teyssié, J.-L.; Gattuso, J.-P. Response of the Arctic Pteropod *Limacina helicina* to Projected Future Environmental Conditions. *PLoS ONE* **2010**, *5*, e11362. [[CrossRef](#)]
39. Lirer, F.; Sprovieri, M.; Vallefucio, M.; Ferraro, L.; Pelosi, N.; Giordano, L.; Capotondi, L. Planktonic foraminifera as bio-indicators for monitoring the climatic changes that have occurred over the past 2000 years in the southeastern Tyrrhenian Sea. *Integr. Zool.* **2014**, *9*, 542–554. [[CrossRef](#)]
40. Margaritelli, G.; Cisneros, M.; Cacho, I.; Capotondi, L.; Vallefucio, M.; Rettori, R.; Lirer, F. Climatic variability over the last 3000 years in the Central—Western Mediterranean Sea (Menorca Basin) detected by planktonic foraminifera and stable isotope records. *Glob. Planet. Chang.* **2018**, *169*, 179–187. [[CrossRef](#)]
41. Margaritelli, G.; Cacho, I.; Català, A.; Barra, M.; Bellucci, L.G.; Lubritto, C.; Rettori, R.; Lirer, F. Persistent warm Mediterranean surface waters during the Roman period. *Sci. Rep.* **2020**, *10*, 10431. [[CrossRef](#)]
42. Tsiolkakis, E.; Tsaila-Monopoli, S.; Kontakiotis, G.; Antonarakou, A.; Sprovieri, M.; Geraga, M.; Ferentinos, G.; Zissimos, A. Integrated paleohydrology reconstruction and Pliocene climate variability in Cyprus Island (eastern Mediterranean). *IOP Conf. Ser. Earth Environ. Sci.* **2019**, *362*, 012103. [[CrossRef](#)]
43. Zarkogiannis, S.; Kontakiotis, G.; Antonarakou, A.; Mortyn, P.; Drinia, H. Latitudinal Variation of Planktonic Foraminifera Shell Masses During Termination I. *IOP Conf. Ser. Earth Environ. Sci.* **2019**, *221*, 012052. [[CrossRef](#)]
44. Checa, H.; Margaritelli, G.; Pena, L.D.; Frigola, J.; Cacho, I.; Rettori, R.; Lirer, F. High resolution paleo-environmental changes during the Sapropel 1 in the North Ionian Sea, central Mediterranean. *Holocene* **2020**. [[CrossRef](#)]
45. Antonarakou, A.; Kontakiotis, G.; Karageorgis, A.P.; Besiou, E.; Zarkogiannis, S.; Drinia, H.; Mortyn, G.P.; Tripsanas, E. Eco-biostratigraphic advances on late Quaternary geochronology and palaeoclimate: The marginal Gulf of Mexico analogue. *Geol. Q.* **2019**, *63*. [[CrossRef](#)]
46. Pujol, C.; Grazzini, C. Distribution patterns of live planktic foraminifers as related to regional hydrology and productive systems of the Mediterranean Sea. *Mar. Micropaleontol.* **1995**, *25*, 187–217. [[CrossRef](#)]
47. Zarkogiannis, S.D.; Antonarakou, A.; Tripathi, A.; Kontakiotis, G.; Mortyn, P.G.; Drinia, H.; Greaves, M. Influence of surface ocean density on planktonic foraminifera calcification. *Sci. Rep.* **2019**, *9*, 533. [[CrossRef](#)]
48. Bazzicalupo, P.; Maiorano, P.; Girone, A.; Marino, M.; Combourieu-Nebout, N.; Pelosi, N.; Salueiro, E.; Incarbona, A. Holocene climate variability of the Western Mediterranean: Surface water dynamics inferred from calcareous plankton assemblages. *Holocene* **2020**, *30*, 691–708. [[CrossRef](#)]
49. Koskeridou, E.; Giamali, C.; Antonarakou, A.; Kontakiotis, G.; Karakitsios, V. Early Pliocene gastropod assemblages from the eastern Mediterranean (SW Peloponnese, Greece) and their palaeobiogeographic implications. *Geobios* **2017**, *50*, 267–277. [[CrossRef](#)]
50. Moissette, P.; Cornée, J.-J.; Antonarakou, A.; Kontakiotis, G.; Drinia, H.; Koskeridou, E.; Tsourou, T.; Agiadi, K.; Karakitsios, V. Palaeoenvironmental changes at the Tortonian/Messinian boundary: A deep-sea sedimentary record of the eastern Mediterranean Sea. *Palaeogeogr. Palaeoclim. Palaeoecol.* **2018**, *505*, 217–233. [[CrossRef](#)]
51. Karakitsios, V.; Roveri, M.; Lugli, S.; Manzi, V.; Gennari, R.; Antonarakou, A.; Triantaphyllou, M.; Agiadi, K.; Kontakiotis, G.; Kafousia, N.; et al. A record of the Messinian salinity crisis in the eastern Ionian tectonically active domain (Greece, eastern Mediterranean). *Basin Res.* **2017**, *29*, 203–233. [[CrossRef](#)]
52. Casford, J.S.L.; Rohling, E.J.; Abu-Zied, R.; Cooke, S.; Fontanier, C.; Leng, M.; Lykousis, V. Circulation changes and nutrient concentrations in the late Quaternary Aegean Sea: A nonsteady state concept for sapropel formation. *Paleoceanography* **2002**, *17*, 14–1–14–11. [[CrossRef](#)]
53. Casford, J.S.L.; Rohling, E.J.; Abu-Zied, R.H.; Fontanier, C.; Jorissen, F.J.; Leng, M.J.; Schmiedl, G.; Thomson, J. A dynamic concept for eastern Mediterranean circulation and oxygenation during sapropel formation. *Palaeogeogr. Palaeoclim. Palaeoecol.* **2003**, *190*, 103–119. [[CrossRef](#)]
54. Aksu, A.E.; Hiscott, R.; Isler, E. Late Quaternary chronostratigraphy of the Aegean Sea sediments: Special reference to the ages of sapropels S1–S5. *Turk. J. Earth Sci.* **2016**, *25*, 1–18. [[CrossRef](#)]
55. Howes, E.L.; Eagle, R.A.; Gattuso, J.-P.; Bijma, J. Comparison of Mediterranean Pteropod Shell Biometrics and Ultrastructure from Historical (1910 and 1921) and Present Day (2012) Samples Provides Baseline for Monitoring Effects of Global Change. *PLoS ONE* **2017**, *12*, e0167891. [[CrossRef](#)] [[PubMed](#)]
56. Lalli, C.M.; Gilmer, R.W. *Pelagic Snails: The Biology of Holoplanktonic Gastropod Mollusks*; Stanford University Press: Stanford, CA, USA, 1989.
57. Hunt, B.; Pakhomov, E.; Hosie, G.W.; Siegel, V.; Ward, P.; Bernard, K. Pteropods in Southern Ocean ecosystems. *Prog. Oceanogr.* **2008**, *78*, 193–221. [[CrossRef](#)]

58. Lochte, K.; Pfannkuche, O. Processes driven by the small sized organisms at the water-sediment interface. In *Ocean Margin Systems*; Wefer, G., Billet, D., Hebbeln, D., Jørgensen, B.B., Schluter, M., Weering, T.C., Eds.; Springer: Berlin/Heidelberg, Germany, 2003.
59. Vinogradov, M. Food sources for the deep water fauna. Speed of decomposition of dead Pteropoda. *Dokl. Akad. Nauk SSSR* **1961**, *138*, 1439–1442.
60. Herman, Y. Vertical and horizontal distribution of pteropods in Quaternary sequences. In *The Micropalaeontology of Oceans*; Funnell, B.M., Reidel, W.R., Eds.; Cambridge University Press: Cambridge, UK, 1971; pp. 463–486.
61. Buccheri, G. Pteropods as climatic indicators in Quaternary sequences: A Lower-Middle Pleistocene sequence outcropping in Cava Puleo (Ficarazzi, Palermo, Sicilia). *Palaeogeogr. Palaeoclim. Palaeoecol.* **1984**, *45*, 75–86. [[CrossRef](#)]
62. Almogi-Labin, A.; Hemleben, C.; Meischner, D.; Erlenkeuser, H. Paleoenvironmental events during the last 13,000 years in the central Red Sea as recorded by pteropoda. *Paleoceanography* **1991**, *6*, 83–98. [[CrossRef](#)]
63. Almogi-Labin, A.; Hemleben, C.; Meischner, D. Carbonate preservation and climatic changes in the central Red Sea during the last 380 kyr as recorded by pteropods. *Mar. Micropaleontol.* **1998**, *33*, 87–107. [[CrossRef](#)]
64. Almogi-Labin, A.; Bar-Matthews, M.; Shriki, D.; Kolosovsky, E.; Paterne, M.; Schilman, B.; Ayalon, A.; Aizenshtat, Z.; Matthews, A. Climatic variability during the last ~90 ka of the southern and northern Levantine Basin as evident from marine records and speleothems. *Quat. Sci. Rev.* **2009**, *28*, 2882–2896. [[CrossRef](#)]
65. Singh, A.D.; Nisha, N.R.; Joydas, T.V. Distribution patterns of Recent pteropods in surface sediments of the western continental shelf of India. *J. Micropalaeontol.* **2005**, *24*, 39. [[CrossRef](#)]
66. Almogi-Labin, A.; Edelman-Furstenberg, Y.; Hemleben, C. Variations in the biodiversity of thecosomatous pteropods during the Late Quaternary as a response to environmental changes in the Gulf of Aden—Red Sea—Gulf of Aqaba ecosystem. In *Aqaba—Eliat, the Improbable Gulf—Environment, Biodiversity and Preservation*; Por, F.D., Ed.; The Hebrew University Magnes Press: Jerusalem, Israel, 2008; pp. 31–48.
67. Johnson, R.; Manno, C.; Ziveri, P. Spring distribution of shelled pteropods across the Mediterranean Sea. *Biogeosci. Discuss.* **2020**, 1–23. [[CrossRef](#)]
68. Howes, E.L.; Stemann, L.; Assailly, C.; Irisson, J.O.; Dima, M.; Bijma, J.; Gattuso, J.P. Pteropod time series from the North Western Mediterranean (1967–2003): Impacts of pH and climate variability. *Mar. Ecol. Prog. Ser.* **2015**, *531*, 193–206. [[CrossRef](#)]
69. Lykousis, V. Subaqueous bedforms on the Cyclades Plateau (NE Mediterranean)—Evidence of Cretan Deep Water Formation? *Cont. Shelf Res.* **2001**, *21*, 495–507. [[CrossRef](#)]
70. Karageorgis, A.P.; Ioakim, C.; Rousakis, G.; Sakellariou, D.; Vougioukalakis, G.; Panagiotopoulos, I.P.; Zimianitis, E.; Koutsopoulou, E.; Kanellopoulos, T.; Papatrechas, C. Geomorphology, sedimentology and geochemistry in the marine area between Sifnos and Kimolos Islands, Greece. *Bull. Geol. Soc. Greece* **2016**, *50*, 334–344. [[CrossRef](#)]
71. Piper, D.; Perissoratis, C. Quaternary neotectonics of the South Aegean arc. *Mar. Geol.* **2003**, *198*, 259–288. [[CrossRef](#)]
72. Antonarakou, A.; Kontakiotis, G.; Vasilatos, C.; Besiou, E.; Zarkogiannis, S.; Drinia, H.; Mortyn, P.; Tsaparas, N.; Makri, P.; Karakitsios, V. Evaluating the Effect of Marine Diagenesis on Late Miocene Pre-Evaporitic Sedimentary Successions of Eastern Mediterranean Sea. *IOP Conf. Ser. Earth Environ. Sci.* **2019**, *221*, 012051. [[CrossRef](#)]
73. Hemleben, C.; Spindler, M.; Anderson, O. *Modern Planktic Foraminifera*; Springer-Verlag: New York, NY, USA, 1989; Volume 22.
74. Rohling, E.J.; Jorissen, F.; Grazzini, C.V.; Zachariasse, W.J. Northern Levantine and Adriatic Quaternary planktic foraminifera; Reconstruction of paleoenvironmental gradients. *Mar. Micropaleontol.* **1993**, *21*, 191–218. [[CrossRef](#)]
75. Aurahs, R.; Grimm, G.; Hemleben, V.; Hemleben, C.; Kucera, M. Geographical distribution of cryptic genetic types in the planktonic foraminifer *Globigerinoides ruber*. *Mol. Ecol.* **2009**, *18*, 1692–1706. [[CrossRef](#)]
76. Walkley, A.; Black, I.A. An examination of the Degtjareff Method for determining soil organic matter, and a proposed modification of the chromic acid titration method. *Soil Sci.* **1934**, *37*, 29–38. [[CrossRef](#)]
77. Angelova, V.; Akova, V.; Ivanov, K.; Licheva, P.A. Comparative study of titrimetric methods for determination of organic carbon in soils, compost and sludge. *J. Int. Sci. Publ. Ecol. Saf.* **2014**, *8*, 430–440. [[CrossRef](#)]

78. Wang, B.; Wu, R.; Fu, X. Pacific–East Asian Teleconnection: How Does ENSO Affect East Asian Climate? *J. Clim.* **2000**, *13*, 1517–1536. [CrossRef]
79. Löwemark, L.; Hong, W.-L.; Yui, T.-F.; Hugn, G.-W. A test of different factors influencing the isotopic signal of planktonic foraminifera in surface sediments from the northern South China Sea. *Mar. Micropaleontol.* **2005**, *55*, 49–62. [CrossRef]
80. Spero, H.J.; Mielke, K.M.; Kalve, E.M.; Lea, D.W.; Pak, D.K. Multispecies approach to reconstructing eastern equatorial Pacific thermocline hydrography during the past 360 kyr. *Paleoceanography* **2003**, *18*. [CrossRef]
81. Stuiver, M.; Reimer, P.J. Extended ^{14}C data base and revised CALIB 3.0 ^{14}C age calibration program. *Radiocarbon* **1993**, *35*, 215–320. [CrossRef]
82. Facorellis, Y.; Maniatis, Y. Apparent ^{14}C ages of marine mollusk shells from a Greek Island: Calculation of the marine reservoir effect in the Aegean Sea. *Radiocarbon* **1998**, *40*, 963–973. [CrossRef]
83. Reimer, P.; Bard, E.; Bayliss, A.; Beck, J.; Blackwell, P.; Ramsey, C.; Buck, C.; Cheng, H.; Edwards, R.; Friedrich, M.; et al. IntCal13 and MARINE13 radiocarbon age calibration curves 0–50,000 years cal BP. *Radiocarbon* **2013**, *55*, 1869–1887. [CrossRef]
84. Jorissen, F.J.; Asioli, A.; Borsetti, A.M.; Capotondi, L.; de Visser, J.P.; Hilgen, F.J.; Rohling, E.J.; van der Borg, K.; Vergnaud Grazzini, C.; Zachariasse, W.J. Late Quaternary central Mediterranean biochronology. *Mar. Micropaleontol.* **1993**, *21*, 169–189. [CrossRef]
85. Hammer, Ø.; Harper, D.A.T.; Ryan, P.D. PAST: Paleontological Statistics software package for education and data analysis. *Palaeontol. Electron.* **2001**, *4*, 9. Available online: http://palaeo-electronica.org/2001_1/past/issue1_01.htm (accessed on 21 June 2001).
86. Sbaffi, L.; Wezel, F.C.; Curzi, G.; Zoppi, U. Millennial- to centennial-scale palaeoclimatic variations during Termination I and the Holocene in the central Mediterranean Sea. *Global Planet. Change* **2004**, *40*, 201. [CrossRef]
87. Anastasakis, G.C.; Stanley, D.J. Sapropels and organic-rich variants in the Mediterranean: Sequence development and classification. *Geol. Soc. Spec. Publ.* **1984**, *15*, 497. [CrossRef]
88. Mercone, D.; Thomson, J.; Croudace, I.W.; Siani, G.; Paterne, M.; Troelstra, S. Duration of S1, the most recent sapropel in the eastern Mediterranean Sea, as indicated by accelerator mass spectrometry radiocarbon and geochemical evidence. *Paleoceanography* **2000**, *15*, 336–347. [CrossRef]
89. Zachariasse, W.; Jorissen, F.; Perissoratis, C.; Rohling, E.; Tsapralis, V. Late Quaternary foraminiferal changes and the nature of sapropel S1 in Skopelos Basin. In Proceedings of the 5th Hellenic Symposium of Oceanography and Fisheries, Kavala, Greece, 15–18 April 1997; pp. 391–394.
90. Capotondi, L.; Maria Borsetti, A.; Morigi, C. Foraminiferal ecozones, a high resolution proxy for the late Quaternary biochronology in the central Mediterranean Sea. *Mar. Geol.* **1999**, *153*, 253–274. [CrossRef]
91. Hayes, A.; Rohling, E.J.; De Rijk, S.; Kroon, D.; Zachariasse, W.J. Mediterranean planktonic foraminiferal faunas during the last glacial cycle. *Mar. Geol.* **1999**, *153*, 239–252. [CrossRef]
92. Casford, J.; Rohling, E.J.; Abu-Zied, R.; Cooke, S.; Boessenkool, K.P.; Brinkhuis, H.; Vries, C.; Wefer, G.; Geraga, M.; Papatheodorou, G.; et al. Mediterranean climate variability during the Holocene. *Mediterr. Mar. Sci.* **2001**, *2*, 45–55. [CrossRef]
93. Schneider, A.; Wallace, W.R.D.; Kortzinger, A. Alkalinity of the Mediterranean Sea. *Geophys. Res. Lett.* **2007**, *34*. [CrossRef]
94. Wilke, I.; Meggers, H.; Bickert, T. Depth habitats and seasonal distributions of recent planktic foraminifers in the Canary Islands region (29 °N) based on oxygen isotopes. *Deep Sea Res. Part I Oceanogr. Res. Pap.* **2009**, *56*, 89. [CrossRef]
95. Wit, J.C.; Reichert, G.-J.; Jung, S.J.A.; Kroon, D. Approaches to unravel seasonality in sea surface temperatures using paired single-specimen foraminiferal $\delta^{18}\text{O}$ and Mg/Ca analyses. *Paleoceanography* **2010**, *25*. [CrossRef]
96. Goudeau, M.L.S. Seasonality variations in the Central Mediterranean during climate change events in the Late Holocene. *Palaeogeogr. Palaeoclim. Palaeoecol.* **2015**, *418*, 304–318. [CrossRef]
97. Kucera, M.; Weinelt, M.; Kiefer, T.; Pflaumann, U.; Hayes, A.; Weinelt, M.; Chen, M.-T.; Mix, A.C.; Barrows, T.T.; Cortijo, E.; et al. Reconstruction of sea-surface temperatures from assemblages of planktonic foraminifera: Multi-technique approach based on geographically constrained calibration data sets and its application to glacial Atlantic and Pacific Oceans. *Quat. Sci. Rev.* **2005**, *24*, 951–998. [CrossRef]

98. Žarić, S.; Donner, B.; Fischer, G.; Mulitza, S.; Wefer, G. Sensitivity of planktic foraminifera to sea surface temperature and export production as derived from sediment trap data. *Mar. Micropaleontol.* **2005**, *55*, 75–105. [[CrossRef](#)]
99. Fraile, I.; Schulz, M.; Mulitza, S.; Kucera, M. Predicting the global distribution of planktonic foraminifera using a dynamic ecosystem model. *Biogeosciences* **2008**, *5*, 891–911. [[CrossRef](#)]
100. Fraile, I.; Mulitza, S.; Schulz, M. Modeling planktonic foraminiferal seasonality: Implications for sea-surface temperature reconstructions. *Mar. Micropaleontol.* **2009**, *72*, 1–9. [[CrossRef](#)]
101. Sprovieri, R.; Stefano, E.; Incarbona, A.; Gargano, M. A high-resolution record of the last deglaciation in the Sicily Channel based on foraminifera and calcareous nannofossil quantitative distribution. *Palaeogeogr. Palaeoclim. Palaeoecol.* **2003**, *202*, 119–142. [[CrossRef](#)]
102. Di Donato, V.; Esposito, P.; Russo-Ermolli, E.; Scarano, A.; Cheddadi, R. Coupled atmospheric and marine palaeoclimatic reconstruction for the last 35 ka in the Sele Plain—Gulf of Salerno area (southern Italy). *Quat. Int.* **2008**, *190*, 146–157. [[CrossRef](#)]
103. Biekart, W.J. Euthecosomatous pteropods as paleohydrological and paleoecological indicators in a Tyrrhenian deep-sea core. *Palaeogeogr. Palaeoclim. Palaeoecol.* **1989**, *71*, 205–224. [[CrossRef](#)]
104. Kutzbach, J.E.; Guetter, P.J. The Influence of Changing Orbital Parameters and Surface Boundary Conditions on Climate Simulations for the Past 18,000 Years. *J. Atmos. Sci.* **1986**, *43*, 1726–1759. [[CrossRef](#)]
105. Kotthoff, U.; Koutsodendris, A.; Pross, J.; Schmiedl, G.; Bornemann, A.; Kaul, C.; Marino, G.; Peyron, O.; Schiebel, R. Impact of Lateglacial cold events on the northern Aegean region reconstructed from marine and terrestrial proxy data. *J. Quat. Sci.* **2011**, *26*, 86–96. [[CrossRef](#)]
106. Dormoy, I.; Peyron, O.; Combourieu Nebout, N.; Goring, S.; Kotthoff, U.; Magny, M.; Pross, J. Terrestrial climate variability and seasonality changes in the Mediterranean region between 15,000 and 4000 years BP deduced from marine pollen records. *Clim. Past* **2009**, *5*, 615–632. [[CrossRef](#)]
107. Björck, S.; Walker, M.; Cwynar, L.; Johnsen, S.; Knudsen, K.; Lowe, J.; Wohlfarth, B. An event stratigraphy for the Last Termination in the North Atlantic region based on the Greenland ice-core record: A proposal by the INTIMATE group. *J. Quat. Sci.* **1998**, *13*, 283–292. [[CrossRef](#)]
108. Rasmussen, S.O.; Vinther, B.M.; Clausen, H.B.; Andersen, K.K. Early Holocene climate oscillations recorded in three Greenland ice cores. *Quat. Sci. Rev.* **2007**, *26*, 1907–1914. [[CrossRef](#)]
109. Peyron, O.; Bégeot, C.; Brewer, S.; Heiri, O.; Magny, M.; Millet, L.; Ruffaldi, P.; Campo, E.; Yu, G. Lateglacial climate in the Jura mountains (France) based on different quantitative reconstruction approaches from pollen, lake-levels, and chironomids. *Quat. Res.* **2005**, *64*, 197–211. [[CrossRef](#)]
110. Bordon, A.; Peyron, O.; Lezine, A.-M.; Brewer, S.; Fouache, E. Pollen-inferred Late-Glacial and Holocene climate in southern Balkans (Lake Maliq). *Quat. Int.* **2009**, *200*, 19–30. [[CrossRef](#)]
111. Larocque, I.; Finsinger, W. Late-glacial chironomid-based temperature reconstructions for Lago Piccolo di Avigliana in the southwestern Alps (Italy). *Palaeogeogr. Palaeoclim. Palaeoecol.* **2008**, *257*, 207–223. [[CrossRef](#)]
112. Sijinkumar, A.V.; Bejugam, N.; Guptha, M.V.S. Late Quaternary record of pteropod preservation from the Andaman Sea. *Mar. Geol.* **2010**, *275*. [[CrossRef](#)]
113. Rottman, M.L. Net tow and surface sediment distributions of pteropods in the South China Sea region: Comparison and oceanographic implications. *Mar. Micropaleontol.* **1980**, *5*, 71–110. [[CrossRef](#)]
114. Rossignol-Strick, M. Sea-land correlation of pollen records in the Eastern Mediterranean for the glacial-interglacial transition: Biostratigraphy versus radiometric time-scale. *Quat. Sci. Rev.* **1995**, *14*, 893. [[CrossRef](#)]
115. Laskar, J.; Robutel, P.; Joutel, F.; Gastineau, M.; Correia, A.C.M.; Levrard, B. A long-term numerical solution for the insolation quantities of the Earth. *A&A* **2004**, *428*, 261–285.
116. Rossignol-Strick, M. African monsoons, an immediate climate response to orbital insolation. *Nature* **1983**, *304*, 46–49. [[CrossRef](#)]
117. Rohling, E.J. Glacial conditions in the Red Sea. *Paleoceanography* **1994**, *9*, 653–660. [[CrossRef](#)]
118. Weikert, H.G.; Cederbaum, L.S. Particle-number-dependent theory of few-and many-body systems. *Few Body Syst.* **1987**, *2*, 33–51. [[CrossRef](#)]
119. Weikert, H. The vertical distribution of zooplankton in relation to habitat zones in the area of the Atlantis II Deep, central Red Sea. *Mar. Ecol. Prog. Ser.* **1982**, *8*, 129–143. [[CrossRef](#)]
120. Wormuth, J. Vertical distributions and diel migrations of Euthecosomata in the northwest Sargasso Sea. *Deep Sea Res. Part I Oceanogr. Res. Pap.* **1981**, *28*, 1493–1515. [[CrossRef](#)]

121. Bé, A.W.H.; Gilmer, R.W. A zoogeographic and taxonomic review of euthecosomatous Pteropoda. *Ocean. Micropaleontol.* **1977**, *1*, 733–808.
122. Sakthivel, M. A preliminary report on the distribution and relative abundance of Euthecosomata with a note on the seasonal variation of Limacina species in the Indian Ocean. *Bull. Nat. Inst. Sci. India* **1969**, *38*, 700–717.
123. Almogi-Labin, A.; Hemleben, C.; Deuser, W.G. Seasonal variation in the flux of euthecosomatous pteropods collected in a deep sediment trap in the Sargasso Sea. *Deep Sea Res. Part I Oceanogr. Res. Pap.* **1988**, *35*, 441–464. [[CrossRef](#)]



© 2020 by the authors. Licensee MDPI, Basel, Switzerland. This article is an open access article distributed under the terms and conditions of the Creative Commons Attribution (CC BY) license (<http://creativecommons.org/licenses/by/4.0/>).

Article

Evidence of Stable Foraminifera Biomineralization during the Last Two Climate Cycles in the Tropical Atlantic Ocean

Stergios D. Zarkogiannis ^{1,*}, Assimina Antonarakou ¹, Vincent Fernandez ²,
P. Graham Mortyn ^{3,4}, George Kontakiotis ¹, Hara Drinia ¹ and Mervyn Greaves ⁵

¹ Department of Historical Geology-Paleontology, Faculty of Geology & Geoenvironment, School of Earth Sciences, National & Kapodistrian University of Athens, Zografou University Hill, 157 84 Athens, Greece; aantonar@geol.uoa.gr (A.A.); gkontak@geol.uoa.gr (G.K.); cntrinia@geol.uoa.gr (H.D.)

² Imaging and Analysis Centre, Natural History Museum, London SW7 5BD, UK; v.fernandez@nhm.ac.uk

³ Institute of Environmental Science and Technology (ICTA), Universitat Autònoma de Barcelona, 08193 Barcelona, Spain; graham.mortyn@uab.cat

⁴ Department of Geography, Universitat Autònoma de Barcelona, 08193 Barcelona, Spain

⁵ Department of Earth Sciences, University of Cambridge, Cambridge CB2 3EQ, UK; mg109@cam.ac.uk

* Correspondence: stergiosz@geol.uoa.gr

Received: 13 August 2020; Accepted: 21 September 2020; Published: 24 September 2020



Abstract: Planktonic foraminiferal biomineralization intensity, reflected by the weight of their shell calcite mass, affects global carbonate deposition and is known to follow climatic cycles by being increased during glacial stages and decreased during interglacial stages. Here, we measure the dissolution state and the mass of the shells of the planktonic foraminifera species *Globigerina bulloides* from a Tropical Eastern North Atlantic site over the last two glacial–interglacial climatic transitions, and we report no major changes in plankton calcite production with the atmospheric $p\text{CO}_2$ variations. We attribute this consistency in foraminifera calcification to the climatic and hydrological stability of the tropical regions. However, we recorded increased shell masses midway through the penultimate deglaciation (Termination II). In order to elucidate the cause of the increased shell weights, we performed $\delta^{18}\text{O}$, Mg/Ca, and μCT measurements on the same shells from a number of samples surrounding this event. Compared with the lighter ones, we find that the foraminifera of increased weight are internally contaminated by sediment infilling and that their shell masses respond to local surface seawater density changes.

Keywords: planktonic foraminifera; shell weight; climate variability; sea surface density; carbonate production; X-ray microscopy (μCT); $\delta^{18}\text{O}$ and Mg/Ca analyses

1. Introduction

Planktonic foraminifera are important marine calcifiers, and the ongoing change in the oceanic carbon system makes it essential to understand the influence of environmental factors on the biomineralization of their shells [1]. Although shell weight is a prominent, easily measured feature of foraminiferal tests that has direct implications for the carbon cycle and carbonate budgets, it is currently not being widely recorded or discussed because its exact environmental meaning is unclear. The amount of calcite deposited by planktonic foraminifera during calcification has been hypothesized to reflect a range of environmental factors. Through the years, changes in planktonic foraminifera shell weights have been linked to different biotic and abiotic parameters such as dissolution [2], carbonate ion concentration [3], optimum growth conditions [4], phosphate concentrations [5], temperature [6], or salinity [1], and thus the various studies have used foraminifera shell weights each time as a different

proxy. Recent studies have shown that planktonic foraminifera can alter their shell mass according to ambient seawater density [7] and that the degree of this alteration in time is a function of latitude [8].

Planktonic organisms are able to biosynthesize out of equilibrium with their ambient environment by maintaining chemical gradients. However, as passive floaters, they must always retain equilibrium with the seawater in order to remain afloat at certain depths. It can thus be argued that plankton physiology is more sensitive to the physical rather than chemical characteristics of seawater. Because planktonic organisms lack active floatation devices, their only inert way to counterbalance seawater buoyancy changes and remain at certain depths is to modify their shell mass [9]. Shell biomineralization must thus be a function of both chemical and physical seawater properties. Although the effects of ocean chemistry on plankton have been extensively studied, there is currently a lack of literature on the effects of physical oceanic properties such as buoyancy, density, or pressure, which very likely affect foraminifera physiology and morphology [10]. Here, we examine the shell mass of the planktonic foraminifera species *Globigerina bulloides* (NCBI:txid69025) from a sediment core of the northeastern tropical Atlantic Ocean through the two most recent climatic cycles. After assessing the preservation of the foraminifera tests, we report consistent shell weights, and thus steady foraminiferal calcification, independent of atmospheric $p\text{CO}_2$, in agreement with a Pliocene Caribbean record [11]. We thus attribute this consistency to the stability of the hydrological conditions over time at the tropics, because the tropical environment is strongly associated with the notion of physical and chemical stability [12,13].

The stability in the foraminifera shell weights is briefly interrupted midway through Termination II, where elevated weights are recorded. In order to understand this feature, we used standard geochemical analyses ($\delta^{18}\text{O}$, Mg/Ca) for a set of samples that we combined with high resolution X-ray computed tomography (CT) to evaluate potential changes in the thickness of foraminifera shells [14] along with other biometric characteristics. The geochemical analyses confirmed a relationship between shell mass and water density, which is further supported by the μCT data that indicate clay contamination as the cause of the elevated shell weights. The μCT analysis also allowed the determination of cell volumes, volume normalized weights (i.e., shell density), or porosities, and has proven a valuable tool in the study of foraminifera shells. The present record provides new evidence on the response of planktonic calcifiers to ocean acidification that will help to better constrain the role that shell mass variations have on the sedimentary calcite budget and the carbon cycle.

2. Location and Oceanographic Setting

GeoB 8502 (19°13.27' N, 18°56.04' W) is a Tropical North Atlantic pelagic site at the lower reaches of the Cap Timiris Canyon, approximately 250 km offshore the Mauritanian coast (Figure 1). The canyon head abuts the Tamanrasset River System, which, although not discharging under present-day climate conditions, ranks among the largest river systems worldwide. The mouth of this potential river system is located off Cap Timiris, but its flow pathways are at present covered by extensive Saharan sand dunes [15]. Presently, the Senegal River is the northernmost active drainage system of West Africa. Core GeoB 8502-2 was retrieved from 2956 m water depth on the lower Northwestern (NW) African continental rise and consists of levee sediments that are predominantly hemipelagic deposits.

Modern climate over the NW African margin is governed by the dynamics of the West African Monsoon, which is associated with the seasonal latitudinal shifts of the intertropical convergence zone (ITCZ) [16]. In winter, the equatorward displacement of the ITCZ (5° N) causes a southward shift of dry subtropical air masses and is associated with the development of strong easterly Saharan Air Layer winds. The southward shift of the ITCZ and wind development cause dust transport from the Sahara [17]. The dust plume is generally located between 15 and 25° N along an E–W axis over the tropical Atlantic Ocean [18]. During boreal summer, dry subtropical air is shifted northward as the ITCZ is located around 20° N (Figure 1). This represents the onset of the rainy season (summer monsoon), with heavy rainfall and changes in atmospheric circulation [19]. Trade winds

from the southern hemisphere, loaded with water vapor, penetrate north to the West African continent. The moisture-laden air spreads over the ocean and continent, permitting heavy rains over the area.

As part of the Eastern Boundary Current system, the Mauritanian upwelling region is one of the major upwelling areas in the Atlantic Ocean [20]. Along the NW African margin, the temporal dynamics of the coastal upwelling is driven basically by the intensity of the northeast trade-winds, itself dependent on the seasonal intertropical convergence zone (ITCZ) migration [21,22] on a perennial basis, producing cold nutrient-rich surface waters with modern sea surface temperatures (SSTs) as low as 16 °C. The studied area is under the influence of the major return branch of the subtropical gyre, the Canary Current (CC), flowing southward along the north-west African coast, then becoming the North Equatorial Current (NEC) when turning southwestward and leaving the African continent. Further south, the westward flowing North Equatorial Counter Current (NECC) is encountered, which transports low salinity water in the area and is known to show a strong seasonal cycle position with maximum velocities when the ITCZ is located at the northernmost position and weak velocities in northern spring [22].

The main water masses encountered in the upwelling region are the Tropical Surface Water (TSW), the North and South Atlantic Central Waters (NACW and SACW), and the Antarctic Intermediate Water (AAIW) [22]. Because of the Cape Verde frontal zone (CVFZ), which is the transition boundary zone between NACW and SACW, the upwelling is fed by two different subsurface water masses depending on latitude [23]. The CVFZ is located at about 20° N off Africa oriented southwestward to about 16° N in the central tropical Atlantic. The front is associated with a convergence at the coast between the CC conveying NACW southward and a northward flow of SACW. With SACW and NACW occupying the same density range, the front is density-compensated and results in a multitude of intrusions, filaments, and lenses [24]. The NACW is warmer and more saline compared with the SACW. Both central water masses appear in the permanent pycnocline between depths of 150 m and 600 m at temperatures greater than about 8 °C, below which lies the AAIW [22]. At greater depths, the core sediments are currently bathed in the carbonate saturated North Atlantic Deep Water (NADW) and may have remained so during the glacials [25].

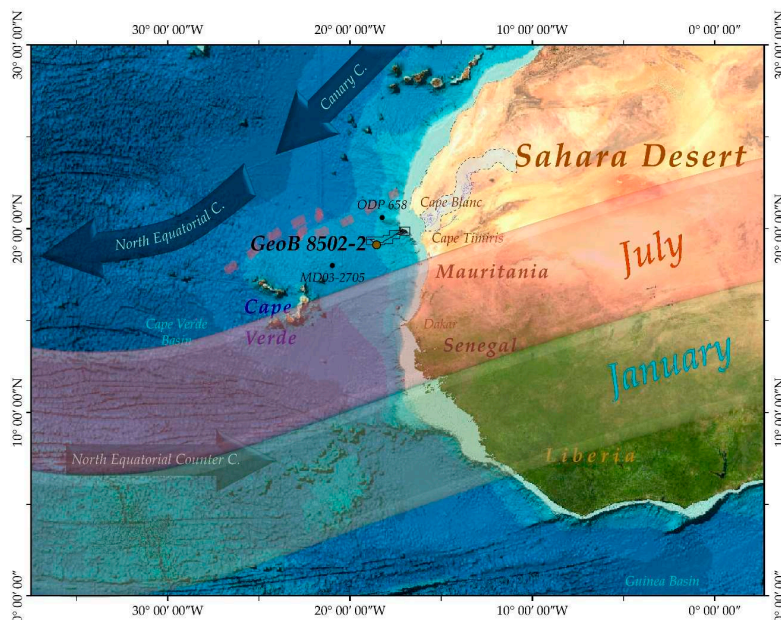


Figure 1. Location of the studied core GeoB 8502-2 along the north-western African margin compared with the atmospheric and oceanographic regional settings. The Cap Timiris Canyon pathway is marked. The arrows show the pathway of the modern dominant surface currents in the area. Red and blue bands identify the migration domains of the summer and winter intertropical convergence zone (ITCZ), respectively. The dashed red band close to the core position denotes the Cape Verde frontal zone (CVFZ) location. The Tamanrasset River paleodrainage valley is indicated, as suggested by [15].

3. Materials and Methods

GeoB 8502-2 is 14.78 m long with an average sedimentation rate of ≈ 6 cm/ky and extends back 200 ky to Marine Isotope Stage (MIS) 6. Samples were taken at a resolution of ~ 1700 years (10 cm sampling interval) by extracting a slice of material, 1 cm in thickness, which corresponds approximately to an average of 170 years of sedimentation. All samples were freeze-dried, weighed, and washed through a $63 \mu\text{m}$ sieve. They were subsequently dry-sieved into several sieve fractions and non-fragmented *G. bulloides* shells from the 315–355 μm size fraction were picked for mass analysis. The very narrow size interval ($40 \mu\text{m}$) should be sufficient to overcome the greater proportion of natural size variability without further normalization [26]. Furthermore, this size fraction is widely used in paleoceanographic studies and can allow comparisons. However, any record of shell weight is a composite signal of dissolution superimposed upon initial shell weight variability.

In order to assess whether the influence of dissolution is responsible for the observed shell weights, the preservation state of the specimens underwent multiproxy assessment. Moreover, to better understand the increase in *G. bulloides* shell mass during Termination II (T-II), the selected specimens were analyzed both geochemically and by high resolution X-ray microcomputed tomography (μCT). μCT was used to inspect the interior and the internal structure of the foraminiferal tests, and apart from addressing the test's integrity (manifestation of dissolution), we were also able to assess to what degree the increased recorded masses are the result of interference from shell inclusions or of changes in test thickness. Finally, the XMCT analysis led to total shell volume estimates that allowed the calculation for the first time of volume normalized shell weights or *G. bulloides* shell densities, presenting a more precise method of eliminating the contribution of shell size to shell weight.

3.1. Weight Analysis

Where available, ideally, 50 (minimum 38) *G. bulloides* shells were weighed in a preweighed aluminum carrier using a Sartorius CP2P microbalance with a precision of $\pm 1 \mu\text{g}$. Average shell masses were calculated by dividing the recorded mass by the total number of foraminifera weighed. Subsequently, for each sample, each shell was weighed separately, in order to estimate standard shell mass deviations. As explained above, performing shell weight analyses on a narrow size fraction of foraminifera constrains the ontogenic stage of the specimens to a certain number of chambers, and thus minimizes size-related weight differences [26–28]). The analytical error, estimated by triplicate measurements of 50 random specimens, ranged from 0.42 to 0.58 μg , which is in accordance with the error of the balance.

3.2. Dissolution Assessment

Because of the immediate impact of dissolution on shell mass, a multiproxy approach was applied to determine the preservation state of the foraminiferal carbonate because indirect dissolution proxies may respond to influences other than dissolution alone. First, the conventional fragmentation index (F.I.) was counted in a sub-split of (~ 300) particles from the 315–355 μm sieve fraction. Subsequently, 30 of the weighed specimens was mounted for ultrastructural examination under the SEM using the *G. bulloides* dissolution index (BDX'). As this species has a high dissolution susceptibility ranking [29], it is a reliable indicator of the foraminiferal carbonate preservation state. The BDX' [30] is based on the direct assessment of corrosion of the specimen's surface and consists of distinct dissolution stages that are determined by the decreasing preservation state of the four ultrastructural test features: pores, interpore space, spines, and ridges. As dissolution proceeds, pores are widened, the interpore areas are etched, and ridges and spines become denuded until the specimen is finally broken down. It thus consists of six stages worsening from 0 to 5, with severe dissolution starting above stage 3. The SEM analysis was performed with a Zeiss DSM 940A SEM in the Department of Geosciences at the University of Bremen.

3.3. X-ray Micro-Computed Tomography (μ CT)

For X-ray microscopic analysis, in total, 27 specimens were scanned from 3 samples (9 specimens per sample) that correspond to the time interval of the increased mass event (132.2 ka), the penultimate glacial maximum (139.1 ka) prior to the event, and a time interval of increased shell weights that followed (122.5 ka). Each batch of shells was poured into a quartz cylindrical carrier 1 mm in diameter [31]. They were stabilized with diluted tragacanth glue and left to dry prior to scanning. The specimens were subsequently retrieved for the geochemical analyses. The micro-CT (μ CT) scanning was carried out with a Zeiss Versa 520 at the X-ray Microscopy laboratory of London Natural History Museum. X-ray source and detector geometry were kept constant throughout the scans. Anode voltage was set at 100 kV, the X-ray tube current was 90 μ A, and the exposure time was 2 s at an optical magnification of 4 \times . By processing approximately 1024 images per sample, a scan resolution voxel size of $\sim 1.2 \mu\text{m}^3$ was typically achieved using this set up in order to maximize the number of specimens that could be analysed in a single scan. The images were combined to build a 3D rendering using Avizo software, which was also used for segmentation. The segmentation resulted in the separation of the tomographs into shell area, area occupied by clay infillings (dirt), and internal shell (protoplasm) voids (Figure 2).

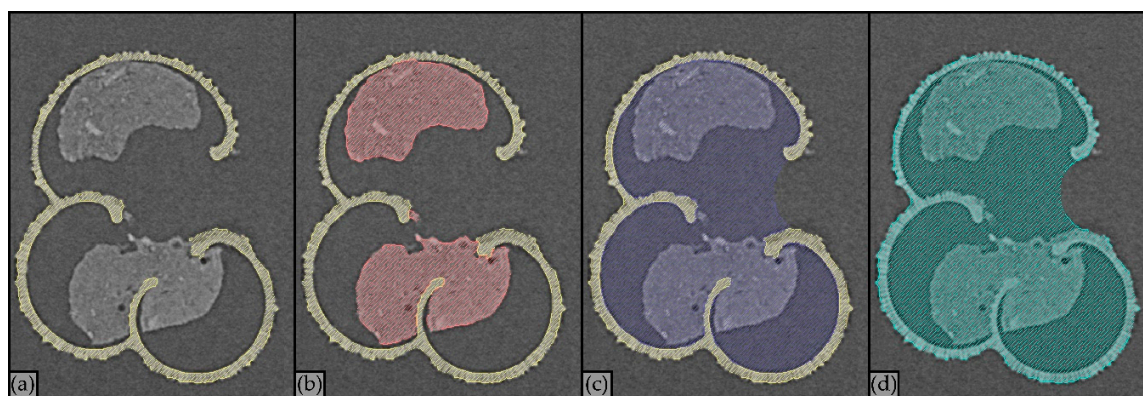


Figure 2. Example of tomograph segmentation using computed tomography (CT) data visualization software, where (a) in yellow, the foraminifera test is solely segmented; (b) in red, the area covered by dirt was also segmented; (c) dirt and internal (chamber) voids were considered together to calculate the area that was occupied by protoplasm (in blue); and (d) protoplasm and shell areas were merged together (in cyan) to calculate the total volume occupied by a foraminifer.

Subject to the degree of segmentation, the X-ray microscopic analysis allows the determination and study of a number of biometric characteristics of the foraminifera shells, such as total shell volume (Figure 2d), thus shell density (volume normalized weight) and calcite (test) volume, and thus test density [32] and calcite (test) surface (Figure 2a). The ratio of calcite volume/calcite surface provides a linear unidimensional quantity in length units and can thus serve as a measure of average test thickness. In this study, in addition to shell density, that is, the ratio of shell volume to shell mass, we use the “specific surface area”, that is, the ratio of test volume/test surface, as a measure of average test thickness [32] and the test density, that is, the ratio of test volume to shell mass, as an indication of test porosity. Furthermore, by segmenting the area occupied by clay infillings, we were able to calculate by volume percent the degree of contamination in weight measurements.

3.4. Geochemical Analysis

In order to reconstruct the oceanographic regime of the time interval surrounding the increased shell mass event during T-II, 12 adjacent down core samples, covering the period of $\sim 22,000$ years between 119 and 140 ka, were geochemically analysed to determine shell Mg/Ca ratios for seawater temperature estimations and $\delta^{18}\text{O}$ isotope ($\delta^{18}\text{O}_{\text{shell}}$). Mg-derived temperatures and foraminiferal

$\delta^{18}\text{O}_{\text{shell}}$ were used together to assess changes in seawater $\delta^{18}\text{O}$ ($\delta^{18}\text{O}_{\text{sw}}$) composition. Mg/Ca ratios were converted to temperatures using an equation for temperate ranges [33]. $\delta^{18}\text{O}_{\text{sw}}$ was calculated using a published paleotemperature equation [34], and a VPDB-to-SMOW $\delta^{18}\text{O}$ conversion of 0.27‰ [35]. Salinity estimates were derived from $\delta^{18}\text{O}_{\text{sw}}$ using the tropical Atlantic salinity- $\delta^{18}\text{O}_{\text{sw}}$ relationship [36] and corrected for deglacial whole ocean salinity changes using a 120 m scaled sea-level curve [37] and an average ocean depth of 3800 m. Seawater densities were calculated from temperature and salinity estimates using the equation of state of the water [38] at a (*G. bulloides* calcification) depth of 100 m. In order to test the correlation between shell mass and the different environmental and oceanographic data, two-tailed regression analyses were performed using the reduced major axis model, at $n - 1$ degrees of freedom (n representing sample size).

3.4.1. Oxygen Stable Isotope Determination

For oxygen isotopes determination, on average, five *G. bulloides* tests from each sample were transferred into sample vials, crushed, and then dried in an oven at 50 °C. The vials were loaded into the carousel and analysed using a Thermo Kiel device attached to a Thermo MAT253 Mass Spectrometer in dual inlet mode at The Godwin Laboratory for Paleoclimate Research, Department of Earth Sciences, University of Cambridge. The preparation system operates automatically, analysing samples in sequence. Then, 100% orthophosphoric acid is dropped onto the evacuated vial and reacts with the calcium carbonate sample. The evolved carbon dioxide is cryogenically dried and then admitted to the dual inlet mass spectrometer for isotopic analysis by comparison with a reference gas. Each run of 30 samples was accompanied by 10 reference carbonates and 2 control samples. The results are reported with reference to the international standard VPDB and the precision is better than ± 0.06 per mil for $\delta^{13}\text{C}$ and ± 0.08 per mil for $\delta^{18}\text{O}$.

3.4.2. Mg/Ca Determination

On average, 15 *G. bulloides* tests from each sample were used for Mg/Ca determination. The specimens were cleaned using the standard protocol [39], omitting the reductive treatment, and were analysed for Mg/Ca ratios by inductively coupled plasma optical emission spectrometry (ICP-OES) using an Agilent 5100 instrument at the Godwin Laboratory for Paleoclimate Research, Department of Earth Sciences, University of Cambridge. Samples were dissolved in 0.1 M HNO_3 and centrifuged to remove any undissolved material. After an initial run to determine Ca concentration, samples were diluted to constant [Ca] (100 ppm). Mg/Ca ratios were determined by the intensity ratio method of [40] using calibration standards prepared according to [41]. Cleaning efficiency and diagenetic effects were monitored by measuring Fe/Ca, Mn/Ca, Al/Ca, Si/Ca, and Ba/Ca ratios.

The instrumental precision for the Mg/Ca ratios is $\pm 0.51\%$, determined by replicate analyses of a standard solution containing Mg/Ca ratios of 1.3 mmol mol^{-1} and a Ca concentration of 100 ppm. The accuracy of Mg/Ca ratios has been established by interlaboratory calibration [42]. Sample heterogeneity for Mg/Ca ratios has been shown to be much greater than instrumental precision [39,43]. We estimate the reproducibility of planktonic foraminiferal Mg/Ca ratios as $\sim 8\%$ from replicate analyses of *G. bulloides* picked from an Atlantic core-top sample.

4. Results

The record of *G. bulloides* shell mass attained from GeoB 8502-2 for the last 200 ky shows no distinct mode of variability (Figure 3a). In general, shell weights are stable, fluctuating only on a small scale ($\pm 1.1 \mu\text{g}$, 1σ) around an average of 13.4 μg . They thus do not exhibit any glacial–interglacial cyclicity or follow the atmospheric $p\text{CO}_2$ fluctuations (Figure 3d). Lower shell mass weights are found within MIS 6, while values almost increase progressively after MIS 5.2. Superimposed on this pattern is a broad maximum in shell weight centred on the MIS 5/6 boundary of T-II with a duration of approximately 2300 yr, during which shell masses increase by 30% above average.

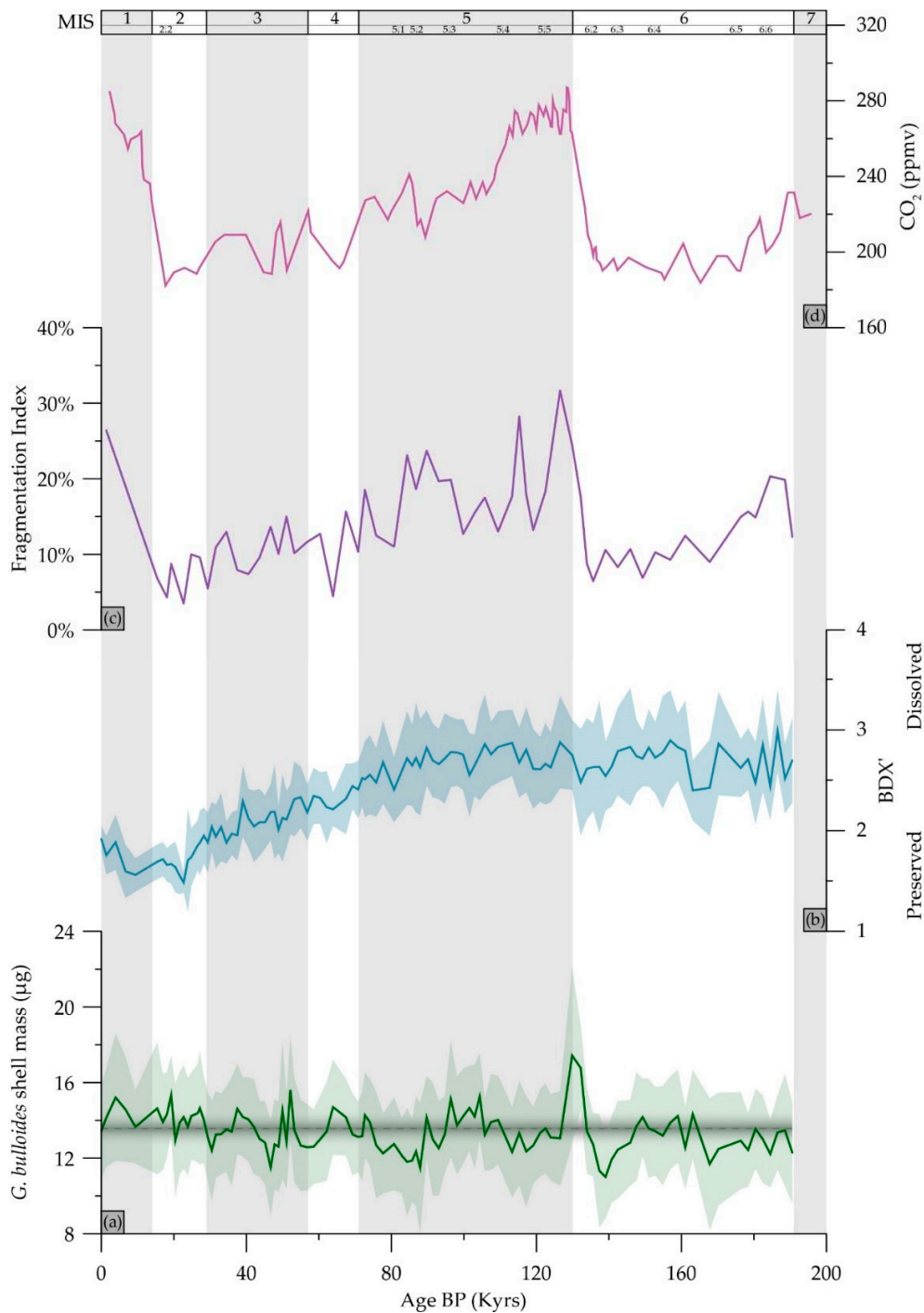


Figure 3. Climatic records of the last 200 ky (before present; BP): (a) *G. bulloides* average shell mass record from GeoB 8502-2. The grey line denotes the record’s mean shell mass and the 1 σ confidence interval is indicated by the shading; (b) specimen’s preservation assessment using the Bulloides dissolution index (BDX’); (c) the fragmentation index of the coarse fraction; and (d) the record of atmospheric CO₂ from Vostok [44] is shown for comparison. The 1 σ confidence interval for the shell mass and BDX’ plots shown as transparent polygons. Numbers refer to Marine Isotopic Stages (MIS) or sub-stages and grey shaded areas interglacial periods. Data are available in Supplementary Tables.

The multiproxy carbonate preservation assessment of the studied core is shown in Figures 2c and 3b. The record of fragmentation strikingly parallels that of the atmospheric $p\text{CO}_2$, indicating the influence of carbonate chemistry changes on the study samples. Nonetheless, this influence does not prove

sufficient to severely alter foraminifera shell mass. In general, foraminiferal carbonate is found to be well preserved (Figures 2c and 3b), because any severe dissolution takes place after BDX' values of 3 [30]. The BDX' and the F.I. assessments (Figures 2c and 3b respectively) are in agreement, indicating that the preservation becomes better during the course of the last glacial period. However, regardless of the increase in foraminifera fragmentation after the Last Glacial Maximum, the *G. bulloides* specimens' ultrastructure was not found to be corroded. A similar disagreement between the dissolution proxies exists for MIS 6, where, although the surface ultrastructure of *G. bulloides* specimens shows signs of corrosion, overall foraminiferal breakage is found to be limited. The deteriorated shell preservation state during MIS 6, as suggested by the BDX', might be adequate to explain to some extent the slightly decreased *G. bulloides* shell weight values of this period, but on the other hand, the gradual decrease of the BDX' values towards the present may explain a gradual increase in mass.

The results of the geochemical analyses of the samples surrounding T-II are summarized in Figure 4 together with a focused record of *G. bulloides* shell weights, atmospheric $p\text{CO}_2$, and relative sea level. $\delta^{18}\text{O}$ ranges from -0.09 to 0.71‰ and, with the exception of the first sample in MIS 6, in general, they are found to be more depleted within the glacial period. The most depleted value is found near MIS 6.2 (133.9 ka), after which values start to increase and become heavier during the Eemian. Mg/Ca ratios range from 2.33 to 4.15 mmol/mol, but are in general consistent around 2.8 mmol/mol during this period. However, they are slightly more depleted prior to the termination and exhibit a spike with a $\sim 46\%$ increase in their values during the MIS 6.1 interstadial. This increase should indicate an environmental signal as all the contamination indicators (Fe, Al, and so on) were low for this sample.

The results of the μCT analysis of the samples covering the 22 ky interval surrounding the 30% increase in shell weight event during T-II are summarized in Table 1. Shells are on average $\sim 16\%$ thicker during the time that they are heavier (132.2 ka), with a mean thickness of $5.7\ \mu\text{m}$. They are also $\sim 32\%$ more voluminous/larger within the same sieve fraction during the same time, but with the highest size variability. Apart from being larger and thicker, they are also found to be more than threefold contaminated by clay infillings (19% of their interior void), thus the observed increase in weight is a result of both enhanced biomineralization and contamination. Shell densities or volume normalized weights do not change significantly (up to 7% from the densest during the time of the highest masses to the lightest during the interglacial), but values show high variability. In terms of test density or porosity, the heaviest and densest shells are only intermediate porous.

Table 1. Average biometric data of foraminifera from weighing and μCT (computed tomography) analysis. Test thickness is the ratio of calcite volume to calcite surface, and shell and test density are the ratio of the average shell weight to test and shell volume, respectively (see Section 3.3 for details). Sediment infilling is the specimen's internal volume percentage occupied by sediment impurities. The μCT analysis results for individual specimens are published in an accompanying paper [31].

Sample	Age (kyrs)	Test Mass (μg)	Test Thickness (μm)	Cell Volume (μm^3)	Sediment Infilling	Shell Density (g/cm^3)	Test Density (g/cm^3)
785	122.5	13.6 ± 2.4	5.0 ± 0.4	$22,326,089 \pm 11\%$	5%	0.61 ± 0.12	35 ± 7
825	132.2	16.8 ± 2.2	5.7 ± 0.5	$24,126,844 \pm 22\%$	19%	0.69 ± 0.18	21 ± 6
865	139.1	11.0 ± 2.2	4.8 ± 0.5	$19,091,400 \pm 17\%$	4%	0.58 ± 0.15	17 ± 4

Sample 865 at 139.1 ka should record the Penultimate Glacial Maximum (PGM) in the present archive, which, in the northern hemisphere, is placed at ~ 140 ka BP [45], because after that, the sea level and atmospheric CO_2 rise continuously (Figure 4). The low shell weights recorded during this period indicate reduced calcification, which is further supported by the μCT scans, which reveal small, thin, and highly porous shells of low density. The scanned shells closest to the peak of the Eemian interglacial period were found to be of average mass, intermediate size, thickness, and density, but were also the least porous. The interior of the Eemian and PGM specimens was found to be filled with sediment by only 5% and 4%, respectively, thus with minimum distortions to the weight measurements.

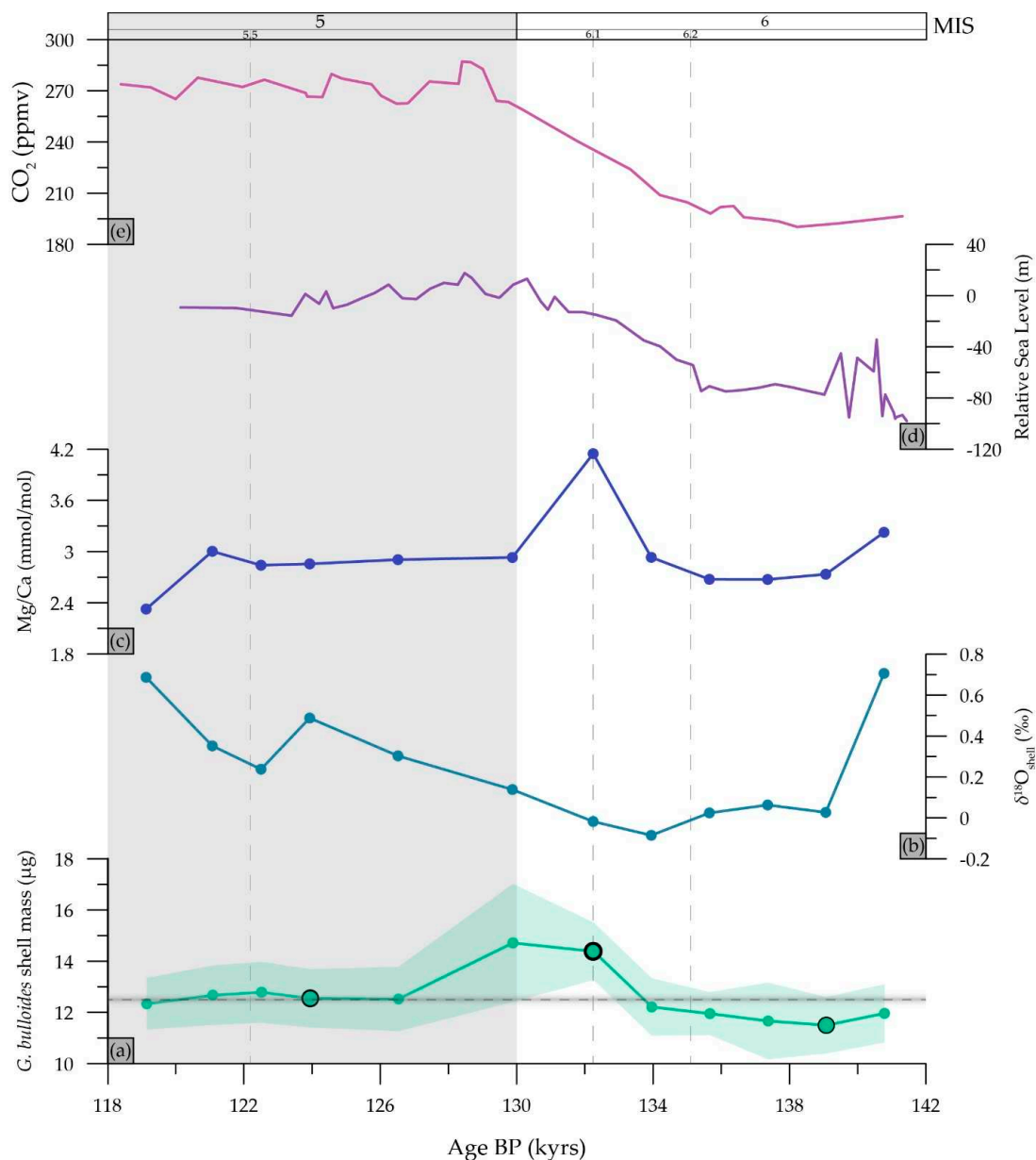


Figure 4. Climatic and geochemical records of the period surrounding the increased *G. bulloides* shell mass events during T-II: (a) average *G. bulloides* shell mass from GeoB 8502-2. The grey line denotes the mean shell mass of this period and the shading is the 1 σ confidence interval. Enlarged circles denote the samples that have been X-ray microscopically analysed. The thickness of their envelope line is proportional to the average shell wall thickness shown in Table 1; (b) $\delta^{18}\text{O}_{\text{shell}}$ of the foraminiferal calcite; (c) Mg/Ca ratios of the foraminiferal calcite; (d) the relative sea level record [46] is shown for comparison and (e) the record of atmospheric CO_2 from Vostok [44] is also shown for comparison. The 1 σ confidence interval for the shell mass plot is shown as transparent polygons. Numbers refer to Marine Isotopic Stages and substages. Geochemical and shell mass data are available in the Supplementary Tables.

The geochemical analyses allow the reconstruction of the physical oceanographic parameters that characterize the period surrounding T-II at the study area and are shown in Figure 5a–c. Temperatures are relatively stable at around 17 °C and they are only slightly lower, in comparison with during MIS 5.5, for most of the late MIS 6 glacial. During the MIS 6.1 interstadial peak, the temperature rises to 20.3 °C, while after the Eemian peak, it drops to 14.8 °C. The salinity reconstructions show

strong changes in the salt content during this time, with a drop in salinity from ~34 to 29 psu for 3400 years between 139.1 and 135.7 ka, and then a ~24% increase to ~38 psu after the PGM before decreasing back to 34 at the peak interglacial. The same applies with the reconstructed densities of the water column that reveal lighter waters during the glacial and denser waters after MIS 6.1. Following the previous study [7], shell weights were plotted against the reconstructed seawater density values and a significant ($R^2 = 0.43$, $p < 0.05$, $n = 12$) relationship between these parameters was verified (Figure 5d), which becomes even more significant ($R^2 = 0.74$, $p < 0.01$, $n = 12$) if the (upper right) two heaviest (most contaminated by clay infillings) samples are omitted. It is evident that these two samples of excessive shell weights deviate from the resulting regression line. If this regression line dictates shell mass according to the shell's geochemical signal, then we can infer that these two samples are contaminated with 2–3 μg of sediment.

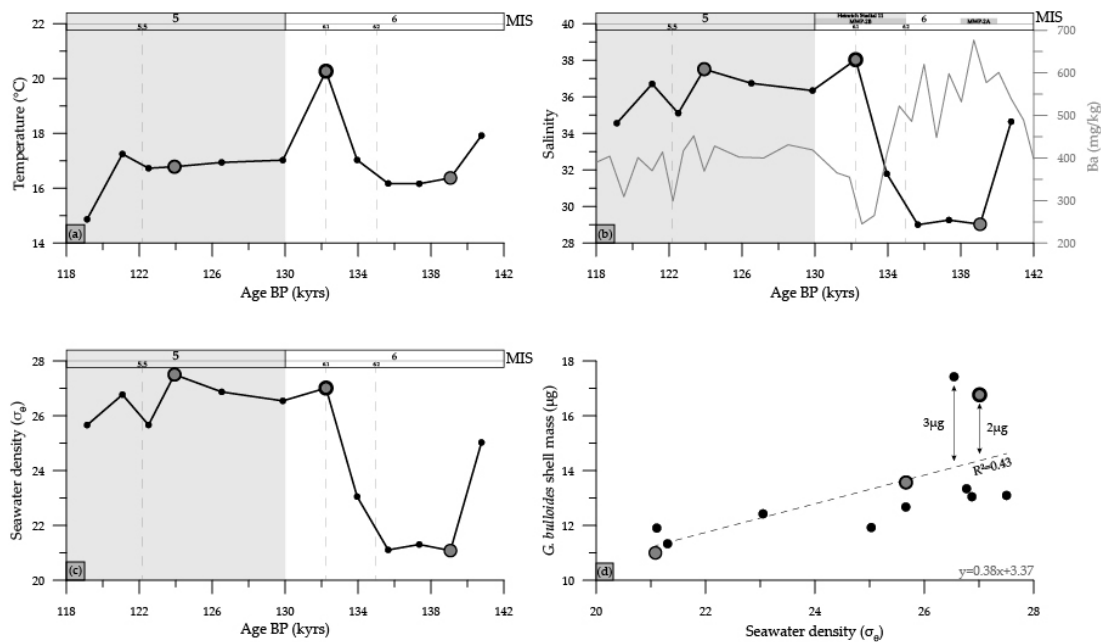


Figure 5. Geochemically reconstructed physical oceanographic parameters for the period surrounding T-II and their relation to average *G. bulloides* shell weights: (a) temperature estimates based on Mg/Ca ratios; (b) salinity reconstructions based on coupled Mg/Ca and $\delta^{18}\text{O}$ measurements together with Barium (Ba) X-ray fluorescence (XRF) counts; (c) ambient seawater density reconstructions based on the preceding temperature and salinity estimates; (d) shell mass and seawater density regression plot. The two upper right points are the increased shell mass samples that deviate from the regression line by 2 and 3 μg , respectively. At the lower right, the contamination corrected regression equation is shown. Enlarged circles denote the samples that have been X-ray microscopically analysed. The thickness of their envelope line is proportional to the average shell wall thickness shown in Table 1. Data are available in the Supplementary Tables and XRF data from [47].

5. Discussion

The sieved based weight analysis of *G. bulloides* shells from the tropical Atlantic core GeoB8502-2 revealed a typical value of 13.4 μg and only small variability in the average mass throughout the last two climatic cycles, which does not follow the atmospheric $p\text{CO}_2$ record. This stability in planktonic foraminifera shell masses despite changes in atmospheric $p\text{CO}_2$ has also been reported in similar latitudes for the Pliocene [48], and may be the result of the environmental stability of the tropical regions. The tropics are generally an environment in which the physicochemical factors are not undergoing major changes through time [12] and this hydrological stability can explain the observed stability in the foraminifera shell weight record that we report here. The incoming solar energy varies considerably from tropical to polar latitudes. At the equatorial region, the average insolation is the highest with

only minor peak energy changes, while at middle and high latitudes, the regular periodicities in the Earth's orbit and tilt influence the amount and distribution of incoming energy and temporal changes are greater [49].

Test weights and the range of test weights in North Atlantic Pliocene and Pleistocene *G. bulloides* are similar despite the higher $p\text{CO}_2$ during the Pliocene [11]. However, the absolute *G. bulloides* shell mass values for specimens 300–350 μm in size reported here for a tropical Atlantic site are low compared with the North Atlantic records [48,50]. This is consistent with the influence of seawater densities on shell weights [7], as the lowest sea surface density values are found in the tropical waters, where salinity is lowest due to excess rainfall associated with the intertropical convergence zone, and increases toward the poles [51]. At higher latitudes, *G. bulloides* shell weight changes by around one-third over glacial–interglacial cycles [3,50,52], and a similar variability in test weight is seen through the Pliocene glacial–interglacial cycles at a similar location [48]. At these higher latitudes that are more sensitive to (latitudinal) changes in solar radiation through time, foraminifera shell weights follow the pronounced hydrological changes between the climatic cycles, with the most sensitive latitudes for explaining the glacial/interglacial ice-dynamics around 65° [53], leaving the tropical shell mass records almost invariable. The consistency in foraminifera shell mass may reflect hydrological stability in the study area, and thus stability of the ITCZ locations during the last 200 ky.

Both dissolution proxies (F.I. and BDX') agree that the biogenic carbonate preservation is generally good to very good. There is a clear match in the trends of both proxies for deterioration in the preservation of foraminifera specimens from MIS 2 to MIS 5.5. Increased specimen dissolution is also evident in the tomographs of the mid T-II sample [54]. This deteriorating trend, however, is not sufficient to cause obvious reductions in the weights of *G. bulloides* shells during this time interval. The two proxies disagree within MIS 6, where the degree of ultrastructural corrosion does not parallel the degree of specimens' fragmentation. This discrepancy points either to the application limits of the proxies or is the result of different test architecture. The F.I. is an indirect measure of shell dissolution and may be the result of ecologic factors like shell initial thickness or different environmental ones (e.g., degree of bioturbation), but in this case, it closely follows the atmospheric $p\text{CO}_2$, implying an influence of carbonate chemistry. On the other hand, the BDX' assesses specimen dissolution directly, but it is more subjective than F.I. as a proxy. However, if specimens are smaller during the late MIS 6, as suggested by the CT analysis (Sample 865; Table 1), then they would have been less prone to fragmentation [55] even at a higher degree of corrosion, and this could explain the offset in the indices.

Carbonate dissolution in the equatorial Atlantic was traditionally believed to be greater during interglacial periods, mainly because of lower carbonate contents in the glacial sequences that fluctuated in response to Quaternary climatic oscillations [56–59]. However, Broecker, et al. [60] showed, in a core from the north Atlantic, that net carbonate input actually increased in the last glacial, but a proportionately higher detrital terrigenous influx diluted the carbonate, in accordance with later studies [61–63] showing that large glacial–interglacial differences in carbonate concentration are caused mainly by increased dilution by non-carbonate material during low sea levels. On the basis of the multiproxy dissolution assessment and the consistency of foraminifera shell weight, the present analysis shows that biogenic carbonate dissolution has overall been minimal in the eastern tropical north Atlantic, with a slight increase towards the peak interglacial. Slightly increased dissolution of fossil shells is to be expected during interglacials as a result of the biomineralization of dissolution susceptible higher-Mg calcite. Together with findings from the western equatorial Atlantic [63], the present study indicates that the average carbonate productivity in the tropical Atlantic has been constant during the last two climatic cycles. Furthermore, the strong carbonate preservation in the study site suggests that the Cape Verde plateau has remained under the influence of the non-corrosive NADW during the past 200 ky, the carbonate chemistry of which closely followed the atmospheric $p\text{CO}_2$.

The homogeneity of the *G. bulloides* shell mass record is interrupted by a spike in the mass values during T-II, where weights increase by 30% above average. In order to explain this abnormality, a series of geochemical and tomographic analyses were performed that point to sediment contamination as

the cause of the increase of the measured weights. The first elevated masses are recorded at 132.2 ka during MIS 6.1, where high Mg/Ca temperatures are also recorded, and persisted for approximately 2400 years. With the exception of MIS 6.1, when 20.3 °C was reconstructed, temperatures in the area are relatively stable around 16–17 °C and only slightly reduced during glacial times. For comparison, in the upwelling region of the area, the full range of glacial to interglacial temperature changes amounted to more than 6 °C [64], and such variations in SST most probably result from changes in the intensity of coastal upwelling, and in turn the consequence of fluctuations in trade-wind strength [65]. Peak warm stages, accordingly, correspond to a cessation of upwelling and trade winds. Indeed, temperatures of 25 °C are characteristic of the subtropical Atlantic outside the upwelling region [66]. T-II is defined by the fairly gradual $\delta^{18}\text{O}_{\text{shell}}$ decrease between substages 6.2 and 5.5, as has been manifested for the study area before [67]. Coupled $\delta^{18}\text{O}_{\text{shell}}$ – Mg/Ca derived salinities and densities reveal that, because temperatures are relatively stable during this time interval, it is salinity that dictates the sea surface density (SSD) and major hydrological changes in the area take place after MIS 6.1, when salinities return to normal marine conditions.

During the late MIS 6, the geochemical data suggest salinities as low as 29 for ~3500 years. The presence of a less-saline water surface layer will most often lead to reduced production, as higher density differences will slow down the upwelling system. T-II contains two major meltwater pulses [68] (MWP-2A and MWP-2B) that, on one hand, can explain low salinities, which are centered on 139 ± 1 and 133 ± 1 ka [69], and coincided within uncertainties with two North Atlantic cooling episodes [70]. MWP-2A indicates an early phase of ice-sheet retreat. MWP-2B is more convincingly resolved and marks a steep ~70 m sea-level rise (~70% of the glacial–interglacial change) at rates of 28 ± 8 m ky^{-1} [68,69]. Although small scale perturbations in SSSs and SSDs such as during MIS 5.5 may have been explained by changes in the position of CVFZ and, accordingly, shifts in the influence of NACW and SACW, salinities in the order of 29 indicate the influence of continental discharge, as similar values are found at sites closest to the river mouth in western Africa [71–73]. Fluvial delivery is also suggested by the increase in Ba^{2+} core X-ray fluorescence (XRF) data (Figure 5b), which are used to infer freshwater inputs [72,74]. Seawater Ba concentrations at oceanic sites influenced by riverine runoff have a notably high inverse correlation to salinity, because dissolved Ba is high in riverine water [75]. Saharan aquifers were found to be recharged during glacials [76] and such humid periods trigger the reactivation of the Tamanrasset river system in Western Sahara [15], part of which is the Cap Timiris canyon.

Shell weights closely follow SSD changes ($R^2 = 0.43$, $p < 0.05$, $n = 12$) during the time interval analyzed (Figure 5d). The two samples that exhibit abnormally elevated shell masses within the record are also shown to be outliers in Figure 5d plot and, according to the CT analysis performed in one of them, the specimens were four times more contaminated by clay impurities than the rest of the scanned samples. If these two contaminated samples are omitted, the correlation between weighed shell mass and geochemically reconstructed seawater densities becomes more significant ($R^2 = 0.74$, $p < 0.01$, $n = 10$). There is a weaker correlation with salinity ($R^2 = 0.41$, $p < 0.05$, $n = 10$), while there is no significant correlation between shell weights and atmospheric $p\text{CO}_2$ ($R^2 = 0.16$, $p < 0.10$, $n = 12$) during this period. Using the shell mass–density regression line to correct the elevated weights, a contamination of 2–3 μg is found. If these corrections are applied then the slope of the regression line (0.38; Figure 5d) matches that of Zarkogiannis, et al. [7] (0.39), which appears to be characteristic for *G. bulloides*. On the basis of this relationship, the low shell weights recorded prior to MIS 6.1 (Figure 4a) can be explained by the freshening of Mauritanian waters. Furthermore, during this time interval, the μCT analysis showed that foraminifera shells have the lowest volume normalized weights and they are smaller, thinner, and of highest porosity (Table 1). The lowest porosities are found close to the peak interglacial, when all other shell characteristics are intermediate. The heaviest, thickest, and densest shells are indeed recorded during the increased shell mass event (132.2 ka), when specimens are also largest, but of intermediate porosity (test density). Increased shell wall thicknesses and shell and

test densities are characteristics of increased biomineralization efforts and play a partial role in the observed increased shell masses.

Shell mass is an easy to measure, central feature of fossil planktonic foraminifera that reflects their physiology and provides clues regarding the ocean carbon cycle. Furthermore, the whole-shell weights of planktonic foraminifera picked from a narrow size range can provide a measure of the extent of surface ocean density changes. The consistency of the different shell mass records from Pliocene core material [11] to Miocene land section samples [77] proves that foraminifera weighing is a robust method for assessing the extent of pelagic biomineralization. However, the present study has shown that the degree of shell cleanliness can greatly affect weight measurements, imposing distortions to paleoceanographic interpretations. Nonetheless, the cleaning procedure remains unstandardized, and different laboratories currently use a variety of treatment methods. It becomes apparent that, in studies of planktonic foraminifera shell weight variations, it is of particular importance to ensure the removal of the detritus trapped within shell chambers and μ CT scanning should complement such studies. Except for the degree of contamination, CT provides a wealth of information on the biometry and the preservation of the tests.

6. Conclusions

On the basis of a record of planktonic foraminifera shell weights from a sediment core in the eastern tropical north Atlantic, we provide evidence of steady carbonate productivity in the equatorial Atlantic Ocean during the last two climatic cycles. A multiproxy dissolution assessment found foraminiferal carbonate to be well preserved, and the consistency in the measured shell masses is a reliable indication of stable foraminifera biomineralization strength, independent of changes in atmospheric $p\text{CO}_2$. We attribute this invariability in the mass of *G. bulloides* shells to the stability of the local hydrologic conditions, which also reveals stability in the position of the ITCZ during the last two glacial–interglacial stages. Furthermore, the enhanced preservation of the foraminiferal record indicates that the Cape Verde plateau remained under the influence of the non-corrosive NADW during the study interval.

The geochemical analysis of the samples surrounding the termination revealed a freshening of the surface waters prior to PGM, which coincided with freshwater pulses or the reactivation of a sub-Saharan drainage system. Furthermore, the reported relationship between *G. bulloides* shell weight and ambient seawater densities was verified, reinforcing the use of foraminifera shell weight as a hydrological indicator. The X-ray tomographic analysis of selected samples allowed the determination of volume normalized weights and revealed that the spike observed in the *G. bulloides* shell weight record during T-II is an artifact of specimen contamination by clay infillings. Overall, the tomographic analysis proved to be a very powerful micropaleontological tool for the determination of key shell characteristics (e.g., cell volume, shell thickness, porosity), which are important for paleoclimatic studies.

Supplementary Materials: The following are available online at <http://www.mdpi.com/2077-1312/8/10/737/s1>.

Author Contributions: Conceptualization and original draft preparation, S.D.Z.; Geochemical analyses and data curation, M.G.; X-ray micro computed tomographic analyses, V.F.; review and editing, P.G.M., G.K., V.F., H.D., A.A., and M.G.; supervision, A.A. All authors have read and agreed to the published version of the manuscript.

Funding: This research received no external funding. The article processing charges for this open-access publication were covered by the University of Athens.

Acknowledgments: We would like to thank the Geosciences department of the University of Bremen for providing sediment core material and scanning electron microscope facilities. We would also like to thank the three anonymous reviewers and the handling editorial team for their constructive comments, which helped to considerably improve this manuscript.

Conflicts of Interest: The authors declare no conflict of interest.

Availability of Supporting Data: Supporting micro-CT data of the scanned specimens used in the paper are available for inspection from the GigaScience database (GigaDB) repository [54]. The acquired geochemical and micropaleontological data are available in the Supplementary Tables.

References

1. Weinkauf, M.F.G.; Moller, T.; Koch, M.C.; Kučera, M. Calcification intensity in planktonic Foraminifera reflects ambient conditions irrespective of environmental stress. *Biogeosciences* **2013**, *10*, 6639–6655. [[CrossRef](#)]
2. Lohmann, G.P. A model for variation in the chemistry of planktonic foraminifera due to secondary calcification and selective dissolution. *Paleoceanography* **1995**, *10*, 445–457. [[CrossRef](#)]
3. Barker, S.; Elderfield, H. Foraminiferal calcification response to glacial-interglacial changes in atmospheric CO₂. *Science* **2002**, *297*, 833–836. [[CrossRef](#)] [[PubMed](#)]
4. De Villiers, S. Optimum growth conditions as opposed to calcite saturation as a control on the calcification rate and shell-weight of marine foraminifera. *Mar. Biol.* **2004**, *144*, 45–49. [[CrossRef](#)]
5. Aldridge, D.; Beer, C.J.; Purdie, D.A. Calcification in the planktonic foraminifera *Globigerina bulloides* linked to phosphate concentrations in surface waters of the North Atlantic Ocean. *Biogeosciences* **2012**, *9*, 1725–1739. [[CrossRef](#)]
6. Qin, B.; Li, T.; Xiong, Z.; Algeo, T.J.; Jia, Q. Calcification of planktonic foraminifer *Pulleniatina obliquiloculata* controlled by seawater temperature rather than ocean acidification. *Glob. Planet. Chang.* **2020**, *193*, 103256. [[CrossRef](#)]
7. Zarkogiannis, S.D.; Antonarakou, A.; Tripathi, A.; Kontakiotis, G.; Mortyn, P.G.; Drinia, H.; Greaves, M. Influence of surface ocean density on planktonic foraminifera calcification. *Sci. Rep.* **2019**, *9*, 533. [[CrossRef](#)]
8. Zarkogiannis, S.D.; Kontakiotis, G.; Antonarakou, A.; Mortyn, P.G.; Drinia, H. Latitudinal Variation of Planktonic Foraminifera Shell Masses During Termination I. *IOP Conf. Ser. Earth Environ. Sci.* **2019**, *221*, 12052. [[CrossRef](#)]
9. Marszalek, D.S. The role of heavy skeletons in vertical movements of non-motile zooplankton. *Mar. Behav. Physiol.* **1982**, *8*, 295–303. [[CrossRef](#)]
10. Lipps, J.H. Ecology and paleoecology of planktic foraminifera. In *Foraminiferal Ecology and Paleoecology*; Lipps, J.H., Berger, W.H., Buzas, M.A., Douglas, R.G., Ross, C.A., Eds.; SEPM Society for Sedimentary Geology: Broken Arrow, OK, USA, 1979; Volume 6, pp. 62–104.
11. Davis, C.V.; Badger, M.P.S.; Bown, P.R.; Schmidt, D.N. The response of calcifying plankton to climate change in the Pliocene. *Biogeosciences* **2013**, *10*, 6131–6139. [[CrossRef](#)]
12. Barron, E.J. Tropical climate stability and implications for the distribution of life. In *Effects of Past Global Change on Life*; National Research Council, Ed.; The National Academies Press: Washington, DC, USA, 1995; pp. 108–117. [[CrossRef](#)]
13. Newell, R.E.; Navato, A.R.; Hsiung, J. Long-term global sea surface temperature fluctuations and their possible influence on atmospheric CO₂ concentrations. *Pure Appl. Geophys.* **1978**, *116*, 351–371. [[CrossRef](#)]
14. Fox, L.; Stukins, S.; Hill, T.; Miller, C.G. Quantifying the Effect of Anthropogenic Climate Change on Calcifying Plankton. *Sci. Rep.* **2020**, *10*, 1620. [[CrossRef](#)] [[PubMed](#)]
15. Skonieczny, C.; Paillou, P.; Bory, A.; Bayon, G.; Biscara, L.; Crosta, X.; Eynaud, F.; Malaizé, B.; Revel, M.; Aleman, N.; et al. African humid periods triggered the reactivation of a large river system in Western Sahara. *Nat. Commun.* **2015**, *6*, 8751. [[CrossRef](#)]
16. Nicholson, S. A revised picture of the structure of the ‘monsoon’ and land ITCZ over West Africa. *Clim. Dyn.* **2009**, *32*, 1155–1171. [[CrossRef](#)]
17. Tulet, P.; Mallet, M.; Pont, V.; Pelon, J.; Boone, A. The 7–13 March 2006 dust storm over West Africa: Generation, transport, and vertical stratification. *J. Geophys. Res. Atmos.* **2008**, *113*. [[CrossRef](#)]
18. Holz, C.; Stuut, J.-B.W.; Henrich, R.; Meggers, H. Variability in terrigenous sedimentation processes off northwest Africa and its relation to climate changes: Inferences from grain-size distributions of a Holocene marine sediment record. *Sediment. Geol.* **2007**, *202*, 499–508. [[CrossRef](#)]
19. Peyrillé, P.; Lafore, J.-P.; Redelsperger, J.-L. An Idealized Two-Dimensional Framework to Study the West African Monsoon. Part I: Validation and Key Controlling Factors. *J. Atmos. Sci.* **2007**, *64*, 2765–2782. [[CrossRef](#)]
20. Aouni, A.E.; Daoudi, K.; Yahia, H.; Minaoui, K.; Benazzouz, A. Surface mixing and biological activity in the North-West African upwelling. *Chaos Interdiscip. J. Nonlinear Sci.* **2019**, *29*, 011104. [[CrossRef](#)] [[PubMed](#)]
21. Mittelstaedt, E. The ocean boundary along the northwest African coast: Circulation and oceanographic properties at the sea surface. *Prog. Oceanogr.* **1991**, *26*, 307–355. [[CrossRef](#)]

22. Stramma, L.; Hóttl, S.; Schafstall, J. Water masses and currents in the upper tropical northeast Atlantic off northwest Africa. *J. Geophys. Res.* **2005**, *110*, C12006. [[CrossRef](#)]
23. Tomczak, M. An analysis of mixing in the frontal zone of South and North Atlantic Central Water off North-West Africa. *Prog. Oceanogr.* **1981**, *10*, 173–192. [[CrossRef](#)]
24. Tomczak, M.; Godfrey, J.S. *Regional Oceanography: Introduction*; Elsevier: New York, NY, USA, 1994; p. 422.
25. Howe, J.N.W.; Piotrowski, A.M.; Noble, T.L.; Mulitza, S.; Chiessi, C.M.; Bayon, G. North Atlantic Deep Water Production during the Last Glacial Maximum. *Nat. Commun.* **2016**, *7*, 11765. [[CrossRef](#)] [[PubMed](#)]
26. Barker, S.; Kiefer, T.; Elderfield, H. Temporal changes in North Atlantic circulation constrained by planktonic foraminiferal shell weights. *Paleoceanography* **2004**, *19*, PA3008. [[CrossRef](#)]
27. Beer, C.J.; Schiebel, R.; Wilson, P.A. Technical Note: On methodologies for determining the size-normalised weight of planktic foraminifera. *Biogeosciences* **2010**, *7*, 2193–2198. [[CrossRef](#)]
28. Broecker, W.; Clark, E. An evaluation of Lohmann's Foraminifera weight dissolution index. *Paleoceanography* **2001**, *16*, 531–534. [[CrossRef](#)]
29. Thunell, R.C.; Honjo, S. Calcite dissolution and the modification of planktonic foraminiferal assemblages. *Mar. Micropaleontol.* **1981**, *6*, 169–182. [[CrossRef](#)]
30. Volbers, A.N.A.; Henrich, R. Present water mass calcium carbonate corrosiveness in the eastern South Atlantic inferred from ultrastructural breakdown of *Globigerina bulloides* in surface sediments. *Mar. Geol.* **2002**, *186*, 471–486. [[CrossRef](#)]
31. Zarkogiannis, S.; Fernandez, V.; Greaves, M.; Mortyn, P.G.; Kontakiotis, G.; Antonarakou, A. X-ray tomographic data of planktonic foraminifera species *Globigerina bulloides* from the Eastern Tropical Atlantic across Termination II. *Gigabyte* **2020**, *1*. [[CrossRef](#)]
32. Iwasaki, S.; Kimoto, K.; Sasaki, O.; Kano, H.; Uchida, H. Sensitivity of planktic foraminiferal test bulk density to ocean acidification. *Sci. Rep.* **2019**, *9*, 9803. [[CrossRef](#)]
33. Mashiotto, T.A.; Lea, D.W.; Spero, H.J. Glacial–interglacial changes in Subantarctic sea surface temperature and $\delta^{18}\text{O}$ -water using foraminiferal Mg. *Earth Planet. Sci. Lett.* **1999**, *170*, 417–432. [[CrossRef](#)]
34. Kim, S.-T.; O'Neil, J.R. Equilibrium and non-equilibrium oxygen isotope effects in synthetic carbonates. *Geochim. Cosmochim. Acta* **1997**, *61*, 3461–3475. [[CrossRef](#)]
35. Hut, G. Consultants group meeting on stable isotope reference samples for geochemical and hydrological investigations. In Proceedings of the Report to the Director General of the International Atomic Energy Agency, Vienna, Austria, 16–18 September 1985; p. 42.
36. LeGrande, A.N.; Schmidt, G.A. Global gridded data set of the oxygen isotopic composition in seawater. *Geophys. Res. Lett.* **2006**, *33*, L12604. [[CrossRef](#)]
37. Fairbanks, R.G. A 17,000-year glacio-eustatic sea level record: Influence of glacial melting rates on the Younger Dryas event and deep-ocean circulation. *Nature* **1989**, *342*, 637–642. [[CrossRef](#)]
38. UNESCO. *The International Thermodynamic Equation of Seawater—2010: Calculation and Use of Thermodynamic Properties*; UNESCO: Paris, France, 2010; p. 196.
39. Barker, S.; Greaves, M.; Elderfield, H. A study of cleaning procedures used for foraminiferal Mg/Ca paleothermometry. *Geochem. Geophys. Geosyst.* **2003**, *4*. [[CrossRef](#)]
40. De Villiers, S.; Greaves, M.; Elderfield, H. An intensity ratio calibration method for the accurate determination of Mg/Ca and Sr/Ca of marine carbonates by ICP-AES. *Geochem. Geophys. Geosyst.* **2002**, *3*. [[CrossRef](#)]
41. Greaves, M.; Barker, S.; Daunt, C.; Elderfield, H. Accuracy, standardization, and interlaboratory calibration standards for foraminiferal Mg/Ca thermometry. *Geochem. Geophys. Geosyst.* **2005**, *6*. [[CrossRef](#)]
42. Greaves, M.; Caillon, N.; Rebaubier, H.; Bartoli, G.; Bohaty, S.; Cacho, I.; Clarke, L.; Cooper, M.; Daunt, C.; Delaney, M.; et al. Interlaboratory comparison study of calibration standards for foraminiferal Mg/Ca thermometry. *Geochem. Geophys. Geosyst.* **2008**, *9*. [[CrossRef](#)]
43. Rosenthal, Y.; Perron-Cashman, S.; Lear, C.H.; Bard, E.; Barker, S.; Billups, K.; Bryan, M.; Delaney, M.L.; de Menocal, P.B.; Dwyer, G.S.; et al. Interlaboratory comparison study of Mg/Ca and Sr/Ca measurements in planktonic foraminifera for paleoceanographic research. *Geochem. Geophys. Geosyst.* **2004**, *5*. [[CrossRef](#)]
44. Petit, J.R.; Jouzel, J.; Raynaud, D.; Barkov, N.I.; Barnola, J.M.; Basile, I.; Bender, M.; Chappellaz, J.; Davis, M.; Delaygue, G.; et al. Climate and atmospheric history of the past 420,000 years from the Vostok ice core, Antarctica. *Nature* **1999**, *399*, 429–436.
45. Colleoni, F.; Wekerle, C.; Näslund, J.-O.; Brandefelt, J.; Masina, S. Constraint on the penultimate glacial maximum Northern Hemisphere ice topography (≈ 140 kyrs BP). *Quat. Sci. Rev.* **2016**, *137*, 97–112. [[CrossRef](#)]

46. Siddall, M.; Rohling, E.J.; Almogi-Labin, A.; Hemleben, C.; Meischner, D.; Schmelzer, I.; Smeed, D.A. Sea-level fluctuations during the last glacial cycle. *Nature* **2003**, *423*, 853–858. [[CrossRef](#)] [[PubMed](#)]
47. Wien, K.; Holz, C.; Kölling, M.; Schulz, H.D. Geochemical data (solid phase) of sediment core GeoB8502-2. *Pangaea* **2006**. [[CrossRef](#)]
48. Davis, C.V.; Rivest, E.B.; Hill, T.M.; Gaylord, B.; Russell, A.D.; Sanford, E. Ocean acidification compromises a planktic calcifier with implications for global carbon cycling. *Sci. Rep.* **2017**, *7*, 2225. [[CrossRef](#)]
49. Liou, K.-N. Radiation climatology. In *International Geophysics*; Academic Press: Cambridge, MA, USA, 1980; Volume 26, pp. 293–348.
50. Barker, S.; Archer, D.; Booth, L.; Elderfield, H.; Henderiks, J.; Rickaby, R.E.M. Globally increased pelagic carbonate production during the Mid-Brunhes dissolution interval and the CO₂ paradox of MIS 11. *Quat. Sci. Rev.* **2006**, *25*, 3278–3293. [[CrossRef](#)]
51. Johnson, G.C.; Schmidtko, S.; Lyman, J.M. Relative contributions of temperature and salinity to seasonal mixed layer density changes and horizontal density gradients. *J. Geophys. Res. Oceans* **2012**, *117*. [[CrossRef](#)]
52. Moy, A.D.; Howard, W.R.; Bray, S.G.; Trull, T.W. Reduced calcification in modern Southern Ocean planktonic foraminifera. *Nat. Geosci.* **2009**, *2*, 276–280. [[CrossRef](#)]
53. Berger, A. Milankovitch Theory and climate. *Rev. Geophys.* **1988**, *26*, 624–657. [[CrossRef](#)]
54. Zarkogiannis, S.; Fernandez, V.; Greaves, M.; Mortyn, P.G.; Kontakiotis, G.; Antonarakou, A. Supporting data for “X-ray tomographic data of planktonic foraminifera species *Globigerina bulloides* from the Eastern Tropical Atlantic across Termination II”. *GigaScience Database* **2020**. [[CrossRef](#)]
55. Berger, W.H.; Bonneau, M.C.; Parker, F.L. Foraminifera on the deep-sea floor: Lysocline and dissolution rate. *Oceanol. Acta* **1982**, *5*, 249–258.
56. Ruddiman, W.F. Pleistocene Sedimentation in the Equatorial Atlantic: Stratigraphy and Faunal Paleoclimatology. *Geol. Soc. Am. Bull.* **1971**, *82*, 283–302. [[CrossRef](#)]
57. Curry, W.B.; Lohmann, G.P. Late Quaternary carbonate sedimentation at the Sierra Leone Rise (eastern equatorial Atlantic Ocean). *Mar. Geol.* **1986**, *70*, 223–250. [[CrossRef](#)]
58. Prell, W.L. *Late Pleistocene Faunal, Sedimentary and Temperature History of the Columbia Basin, Caribbean Sea*; Columbia University: New York, NY, USA, 1974.
59. Damuth, J.E. *The Western Equatorial Atlantic Morphology, Quaternary Sediments, and Climatic Cycles*; Columbia University: New York, NY, USA, 1973.
60. Broecker, W.S.; Turekian, K.K.; Heezen, B.C. The relation of deep sea [Atlantic Ocean] sedimentation rates to variations in climate. *Am. J. Sci.* **1958**, *256*, 503–517. [[CrossRef](#)]
61. Hays, J.D.; Perruzza, A. The Significance of Calcium Carbonate Oscillations in Eastern Equatorial Atlantic deep-Sea Sediments for the End of the Holocene Warm Interval. *Quat. Res.* **1972**, *2*, 355–362. [[CrossRef](#)]
62. Bacon, M.P. Glacial to interglacial changes in carbonate and clay sedimentation in the Atlantic Ocean estimated from ²³⁰Th measurements. *Chem. Geol.* **1984**, *46*, 97–111. [[CrossRef](#)]
63. Curry, W.B.; Cullen, J.L. Carbonate production and dissolution in the western equatorial Atlantic during the last 1 MY. In *Proceedings of the Ocean Drilling Program, Scientific Results*, Charleston, SC, USA, 8 January–14 February 1997; Volume 154, p. 189. [[CrossRef](#)]
64. Eglinton, G.; Bradshaw, S.; Resell, A.; Sarnthein, M.; Pflaumann, U.; Tiedemann, R. Molecular record of secular sea surface temperature changes on 100-year timescales for glacial terminations I, II and IV. *Nature* **1992**, *356*, 423–426. [[CrossRef](#)]
65. Speth, P.; Detlefsen, H.; Sierks, H.-W. Meteorological influence on upwelling off Northwest Africa. *Ocean Dyn.* **1978**, *31*, 95–104. [[CrossRef](#)]
66. CLIMAP-Project-Members. The last interglacial ocean. *Quat. Res.* **1984**, *21*, 123–224. [[CrossRef](#)]
67. Sarnthein, M.; Tiedemann, R. Younger Dryas-style cooling events at glacial Terminations I–VI at ODP Site 658: Associated benthic $\delta^{13}\text{C}$ anomalies constrain meltwater hypothesis. *Paleoceanography* **1990**, *5*, 1041–1055. [[CrossRef](#)]
68. Grant, K.M.; Rohling, E.J.; Ramsey, C.B.; Cheng, H.; Edwards, R.L.; Florindo, F.; Heslop, D.; Marra, F.; Roberts, A.P.; Tamisiea, M.E.; et al. Sea-level variability over five glacial cycles. *Nat. Commun.* **2014**, *5*, 5076. [[CrossRef](#)]
69. Grant, K.M.; Rohling, E.J.; Bar-Matthews, M.; Ayalon, A.; Medina-Elizalde, M.; Ramsey, C.B.; Satow, C.; Roberts, A.P. Rapid coupling between ice volume and polar temperature over the past 150,000 years. *Nature* **2012**, *491*, 744–747. [[CrossRef](#)]




70. Marino, G.; Rohling, E.J.; Rodríguez-Sanz, L.; Grant, K.M.; Heslop, D.; Roberts, A.P.; Stanford, J.D.; Yu, J. Bipolar seesaw control on last interglacial sea level. *Nature* **2015**, *522*, 197–201. [[CrossRef](#)] [[PubMed](#)]
71. Dupont, L.M.; Weinelt, M. Vegetation history of the savanna corridor between the Guinean and the Congolian rain forest during the last 150,000 years. *Vegetat. Hist. Archaeobot.* **1996**, *5*, 273–292. [[CrossRef](#)]
72. Weldeab, S.; Lea, D.W.; Schneider, R.R.; Andersen, N. 155,000 years of West African monsoon and ocean thermal evolution. *Science* **2007**, *316*, 1303–1307. [[CrossRef](#)] [[PubMed](#)]
73. Sierro, F.J.; Hodell, D.A.; Andersen, N.; Azibeiro, L.A.; Jimenez-Espejo, F.J.; Bahr, A.; Flores, J.A.; Ausin, B.; Rogerson, M.; Lozano-Luz, R.; et al. Mediterranean Overflow over the Last 250 kyr: Freshwater Forcing from the Tropics to the Ice Sheets. *Paleoceanogr. Paleoclimatol.* **2020**, *35*, e2020PA003931. [[CrossRef](#)]
74. Grant, K.M.; Grimm, R.; Mikolajewicz, U.; Marino, G.; Ziegler, M.; Rohling, E.J. The timing of Mediterranean sapropel deposition relative to insolation, sea-level and African monsoon changes. *Quat. Sci. Rev.* **2016**, *140*, 125–141. [[CrossRef](#)]
75. Coffey, M.; Dehairs, F.; Collette, O.; Luther, G.; Church, T.; Jickells, T. The Behaviour of Dissolved Barium in Estuaries. *Estuar. Coast. Shelf Sci.* **1997**, *45*, 113–121. [[CrossRef](#)]
76. Abouelmagd, A.; Sultan, M.; Milewski, A.; Kehew, A.E.; Sturchio, N.C.; Soliman, F.; Krishnamurthy, R.V.; Cutrim, E. Toward a better understanding of palaeoclimatic regimes that recharged the fossil aquifers in North Africa: Inferences from stable isotope and remote sensing data. *Palaeogeogr. Palaeoclimatol. Palaeoecol.* **2012**, *329–330*, 137–149. [[CrossRef](#)]
77. Kontakiotis, G.; Besiou, E.; Antonarakou, A.; Zarkogiannis, S.D.; Kostis, A.; Mortyn, P.G.; Moissette, P.; Cornée, J.J.; Schulbert, C.; Drinia, H.; et al. Decoding sea surface and paleoclimate conditions in the eastern Mediterranean over the Tortonian-Messinian Transition. *Palaeogeogr. Palaeoclimatol. Palaeoecol.* **2019**, *534*, 109312. [[CrossRef](#)]



© 2020 by the authors. Licensee MDPI, Basel, Switzerland. This article is an open access article distributed under the terms and conditions of the Creative Commons Attribution (CC BY) license (<http://creativecommons.org/licenses/by/4.0/>).

Article

An Improved Cleaning Protocol for Foraminiferal Calcite from Unconsolidated Core Sediments: HyPerCal—A New Practice for Micropaleontological and Paleoclimatic Proxies

Stergios D. Zarkogiannis ^{1,2,*} , George Kontakiotis ² , Georgia Gkaniatsa ², Venkata S. C. Kuppili ^{3,4}, Shashidhara Marathe ³, Kazimir Wanelik ³, Vasiliki Lianou ², Evaggelia Besiou ², Panayiota Makri ² and Assimina Antonarakou ² 

¹ Department of Earth Sciences, University of Oxford, Oxford OX1 3AN, UK

² Faculty of Geology & Geoenvironment, Department of Historical Geology-Paleontology, School of Earth Sciences, National & Kapodistrian University of Athens, Zografou University Campus, 157 84 Athens, Greece; gkontak@geol.uoa.gr (G.K.); gorgiagkan@gmail.com (G.G.); vlianou@geol.uoa.gr (V.L.); wwwuea@hotmail.com (E.B.); pmakri@geol.uoa.gr (P.M.); aantonar@geol.uoa.gr (A.A.)

³ Diamond Light Source, Harwell Science and Innovation Campus, Oxford OX11 0DE, UK; charan.kuppili@lightsource.ca (V.S.C.K.); shashidhara.marathe@diamond.ac.uk (S.M.); kaz.wanelik@diamond.ac.uk (K.W.)

⁴ Canadian Light Source, Spectromicroscopy (SM) beamline, Saskatoon, SK S7N 2V3, Canada

* Correspondence: stergiosz@geol.uoa.gr

Received: 11 November 2020; Accepted: 1 December 2020; Published: 7 December 2020



Abstract: Paleoclimatic and paleoceanographic studies routinely rely on the usage of foraminiferal calcite through faunal, morphometric and physico-chemical proxies. The application of such proxies presupposes the extraction and cleaning of these biomineralized components from ocean sediments in the most efficient way, a process which is often labor intensive and time consuming. In this respect, in this study we performed a systematic experiment for planktonic foraminiferal specimen cleaning using different chemical treatments and evaluated the resulting data of a Late Quaternary gravity core sample from the Aegean Sea. All cleaning procedures adopted here were made on the basis of their minimum potential bias upon foraminiferal proxies, such as the faunal assemblages, degree of fragmentation, stable isotope composition ($\delta^{18}\text{O}$ and $\delta^{13}\text{C}$) and/or Mg/Ca ratios that are frequently used as proxies for surface-ocean climate parameters (e.g., sea surface temperature, sea surface salinity). Six different protocols were tested, involving washing, sieving, and chemical treatment of the samples with hydrogen peroxide and/or sodium hexametaphosphate (Calgon[®]). Single species foraminifera shell weighing was combined with high-resolution scanning electron microscopy (SEM) and synchrotron X-ray microtomography ($\text{S}\mu\text{CT}$) of the material processed by each of the cleaning protocols, in order to assess the decontamination degree of specimen's ultrastructure and interior. It appeared that a good compromise between time and cleaning efficiency is the simultaneous treatment of samples with a mixed hydrogen peroxide and Calgon solution, while the most effective way to almost completely decontaminate the calcareous components from undesirable sedimentary material is a two-step treatment—initially with hydrogen peroxide and subsequently with Calgon solutions.

Keywords: cleaning protocol; unconsolidated core sediments; shell weight; climate reconstruction; synchrotron X-ray microtomography ($\text{S}\mu\text{CT}$); foraminiferal-based proxies

1. Introduction

Foraminifera shells (tests) are widely used in paleoceanographic and paleoclimatic studies as biostratigraphic or ecological indicators and through physicochemical analyses as proxies of past oceanic conditions [1]. The tests of different foraminifera species can provide environmental information by means of both physical and chemical analyses. Despite the main focus for environmental reconstructions based on stable isotope [2,3] and trace metal geochemistry [4–6] of foraminifera tests a wealth of information can be attained by their physical analyses that include the study of shell fragmentation [7], abundancies for ecological [8] or biostratigraphic purposes [9] and shell biometry [10–12] including size [13,14] and weight [15,16].

A necessary preliminary step for the use of foraminifera tests in paleoenvironmental studies is the isolation of the test specimens from the muddy sedimentary matrices, that consists of several components. A number of methodologies have been employed to transform the bulk sediment samples into useable micropaleontological material [17,18] as a first level treatment. Although the additional cleaning protocols to isolate primary calcite for geochemical analyses are advanced and several cleaning experiments have sought to quantify the effects of each of these methods on measured elements [19–22], there are only a few studies that assess the efficiency of different treatment procedures on the physical properties of the foraminifera shells such as their weight [21,23].

Studies that focus on foraminifera shell weight measurements are particularly vulnerable to the degree of test contamination, due to their foraminous nature, these specimens have the potential to include contaminants (i.e., sedimentary residuals), which can alter or skew the record toward heavier values [24]. Residual clays or nano-ooze in poral spaces and shell surface obstruct the study of test ultrastructure that yield information about the degree of carbonate dissolution [25] or test porosity [26]. Furthermore, such coatings or infillings (in apertures) often precludes automated recognition software, which is based on morphological features of foraminifera shells [27], from classifying their images correctly [28] and greatly complicate specimen segmentation when using high resolution X-ray tomographic techniques [29]. In the present study, by using light microscope imaging, SEM and X-ray tomography to assess the cleanliness of tests treated with reagents that are established not to alter the fossil geochemical signal, we propose a methodology that effectively diminishes surface and internal specimen contamination.

2. Materials and Methods

For the cleaning test, *Globigerinoides ruber albus* (NCBI:txid2606480) sensu stricto specimens were used, from the 45 cm interval of unconsolidated sediments from the North Aegean Sea core M22-67 (245 m water depth; 38°21.87' N, 25°56.96' E) with a radiocarbon date (AMS ¹⁴C) of 14.5 ka before present. The core consisted mainly of fine-grained hemipelagic muds and clays and represents a sedimentary archive of the last 85 kyr. The predominant clay minerals in the area are [30] and have been during the study interval [31] illite and smectite. The carbonate content of the sample was measured to be ~42% and since it was not from a sapropel or sapropelic layer its organic content is estimated to be less than 0.6% [32]. *G. ruber albus* s.s. was chosen for species under investigation because of its high abundance in the sample and its importance in paleoclimatic studies. It is likely that foraminiferal tests from different settings, and possibly different foraminifera species of different size, will respond differently to cleaning.

The sample was oven-dried overnight at 50 °C and was weighed unprocessed 24 g. Subsequently, it was divided into six aliquots (~4.10 g each) that were transferred into different 50 mL glass beakers and underwent treatment for 20 min at room temperature before wet sieving over a 63 µm mesh, using six processing methods: (1) addition of Calgon® (sodium hexametaphosphate, (NaPO₃)₆); (2) 2.5% hydrogen peroxide (H₂O₂); (3) 2.5% hydrogen peroxide and subsequent treatment with Calgon; (4) simultaneous treatment with 2.5% hydrogen peroxide and Calgon; (5) 4% hydrogen peroxide (H₂O₂); and (6) distilled water without chemical additions (see Table 1 for procedures). Hydrogen peroxide tends to acidify the solution by oxidizing the organic residuals, while Calgon is an alkaline dispersant

that neutralizes the charge of clay particles. Both reagents have traditionally been used in sediment or rock processing methods and in the present study they are applied in a specific order that aims to best use their effects.

Beaker 1 received treatment with Calgon by filling up the beaker with 5% Calgon solution (50 g $\text{Na}_6\text{P}_6\text{O}_{18}$ diluted in 950 mL distilled water) as proposed by [23]. Beaker 2 received treatment with 30% hydrogen peroxide by adding 4 mL of the reagent and filling up the beaker to 50 mL with distilled water, producing a 2.5% hydrogen peroxide solution. Beaker 3 received a “two step treatment”. The sample was initially treated with 2.5% hydrogen peroxide solution, like beaker 2, and after washed through a 63- μm sieve the remaining coarse fraction was transferred back to the beaker and treated with 5% Calgon solution, similar to beaker 1 (HyPerCal treatment). Beaker 4 received simultaneous treatment with hydrogen peroxide and Calgon by adding 4 mL of 30% hydrogen peroxide in 46 mL of 5% Calgon solution. Beaker 5 received treatment with 4% hydrogen peroxide solution by diluting 4 mL of 49.5% hydrogen peroxide in 46 mL distilled water, and beaker 6 only received treatment with distilled water. All beakers were gently agitated periodically sonicated every 2 min for 4 s, since a 4 s sonication step has been found to provide a greater detritus cleaning effect and minimize test breakage [23].

After their treatment the sample aliquots were thoroughly washed with tap water over a 63 μm wire mesh sieve and left overnight in the oven to dry at 50 °C. They were subsequently dry-sieved and the first random 15 non-fragmented *G. ruber albus* s.s. specimens from the 300–355 μm sieve fraction were picked from each aliquot for further analyses. In order to minimize the effect of specimen size (i.e., size of apertural openings, chamber size) in the cleaning efficiency tests from a narrow size fraction were used. This particular sieve fraction was chosen because of its frequent use in paleoceanographic studies. For assessing the effect that each treatment had on the surface ultrastructure of the foraminifera specimens, 5 specimens from each sample were mounted and gold-coated for SEM imaging. The samples were examined with a JEOL JSM-6390 instrument at a 1100 \times magnification, a working distance of 2.1 mm and an accelerating voltage of 20 kV in the Department of Geology and Geoscience of the National Kapodistrian University of Athens. In order to evaluate the extent of detritus removal from the interior of the specimens and quantify weight loss from each chemical treatment method, 5 additional specimens from each sample were weighed and subsequently scanned using X-ray computed tomography. The tests were initially weighed as a group of five individuals to obtain their average mass and subsequently in three groups of two individuals in order to record the weight variation in each sample. After weighing the tests were oriented and photographed (Figure 1) using a Leica M165 C stereo microscope with an integrated camera at the Department of Geology and Geoscience of the National Kapodistrian University of Athens. The weight analysis took place using a Sartorius microbalance (1 mg precision) also at the University of Athens.

The specimens were subsequently tomographically scanned using Synchrotron X-ray radiation at the Diamond Manchester Imaging Branchline (I13-2) at Diamond Light Source. The tests were transferred into quartz capillaries of 1 mm inner diameter (similar to [29]) that were subsequently attached to magnetic cryo-cap holders and mounted on to a goniometer. The data was acquired with partially coherent, pink X-ray beam which has broader energy spectrum centered around 27 keV. For each of the sessions exposure time of 0.5 s were used, at a 0.09 degree rotation step size producing an acquisition of 2000 projections with 2560 \times 2160 pixel resolution using a pco.edge 5.5 camera at a 4 \times magnification, which resulted in an effective pixel size of 0.8125 μm . The reconstruction of the acquisition data and their downsampling to 8bit tomographic images were performed with Savu package [33]. Links to the raw tomographic data are given the Appendix A below. The images were subsequently analyzed in Avizo software, where the test and sedimentary infilled areas were segmented and discriminated as described in Section 3.3 of [24].

Table 1. Table summarizing the different cleaning methods followed.

Method	Method Name	Chemical Treatment			Treatment Time	Processing	
		Step 1	Step 2	Step 3		Step 4	Step 5
1	“Calgon”	50 mL Calgon 5%	-	-	20 min sonicated every 2 min for 4 s	Wet sieving over >63 µm mesh	Dried overnight
2	“30% Peroxide”	2.5% hydrogen peroxide (4 mL of H ₂ O ₂ were added to 46 mL distilled water)	-	-	20 min sonicated every 2 min for 4 s	Wet sieving over >63 µm mesh	Dried overnight
3	“HyPerCal treatment”	4 mL of 30% H ₂ O ₂ added to 46 mL distilled water (2.5% hydrogen peroxide)	Wet sieving over >63 µm mesh	4 mL 5% Calgon were added in 46 mL distilled water	20 + 20 min sonicated every 2 min for 4 s	Wet sieving over >63 µm mesh	Dried overnight
4	“Mixed Calgon and peroxide”	4 mL of 30% H ₂ O ₂ added in 46 mL of 5% Calgon solution	-	-	20 min sonicated every 2 min for 4 s	Wet sieving over >63 µm mesh	Dried overnight
5	“4% Peroxide”	4 mL of 49.5% H ₂ O ₂ added to 46 mL distilled water (4% hydrogen peroxide)	-	-	20 min sonicated every 2 min for 4 s	Wet sieving over >63 µm mesh	Dried overnight
6	“Control”	Treatment only with distilled water	-	-	20 min sonicated every 2 min for 4 s	Wet sieving over >63 µm mesh	Dried overnight

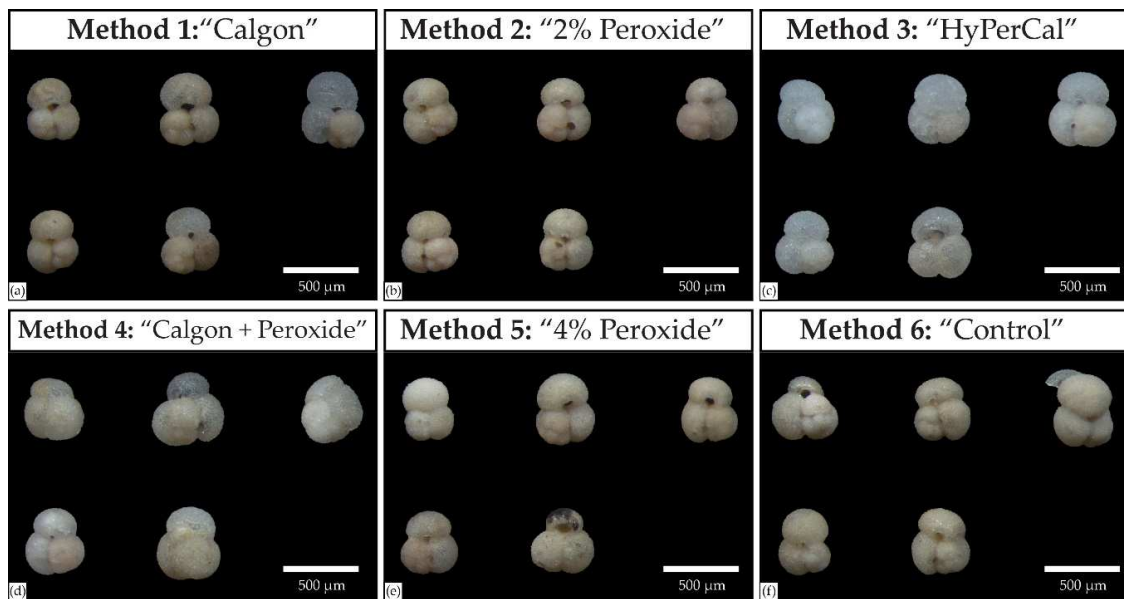


Figure 1. Images of the analyzed specimens after their treatment with the different cleaning protocols.

3. Results

There are some general observations of the behavior of the different sample solutions that deserve to be noted here. Due to the cohesion degree of the core sample not all treatment solutions were capable to completely disintegrate the sample's mass. The most effective reagent to turn the sample solution into homogeneous mud slurry was H_2O_2 regardless of its concentration or admixture. The sample aliquots that were treated with water or $Na_6O_{18}P_6$ solution did not completely disintegrate and small chunks of sediment were left still standing in the beaker that required some extra mechanical effort to dissolve better. Finally, beaker 4 which contained simultaneously both H_2O_2 and $Na_6O_{18}P_6$ exhibited strong foaming during treatment time.

3.1. Scanning Electron Microscopic Analysis

The results of the SEM analysis are shown in Figure 2. It can be seen that the surface ultrastructure of the tests that underwent HyPerCal treatment, initially with H_2O_2 and subsequently with $Na_6O_{18}P_6$, is almost completely free from detrital particles and clay impurities (Figure 2k–o). This treatment method removed detritus from all the different ultrastructural test features such as pores, ridges, interpore area and spine bases, even in the case of dissolved and etched interpore surfaces (Figure 2n). The treatment with H_2O_2 of diverse concentrations (Methods 2 and 5) showed that the different ultrastructural features of all the specimens were covered to some degree with detritus. Treatment with $Na_6O_{18}P_6$ or water had some better cleaning effects especially for some of the specimens (Figure 2a–e,z–ad) and the same is true for Method 4, of simultaneous treatment with hydrogen H_2O_2 and $Na_6O_{18}P_6$.

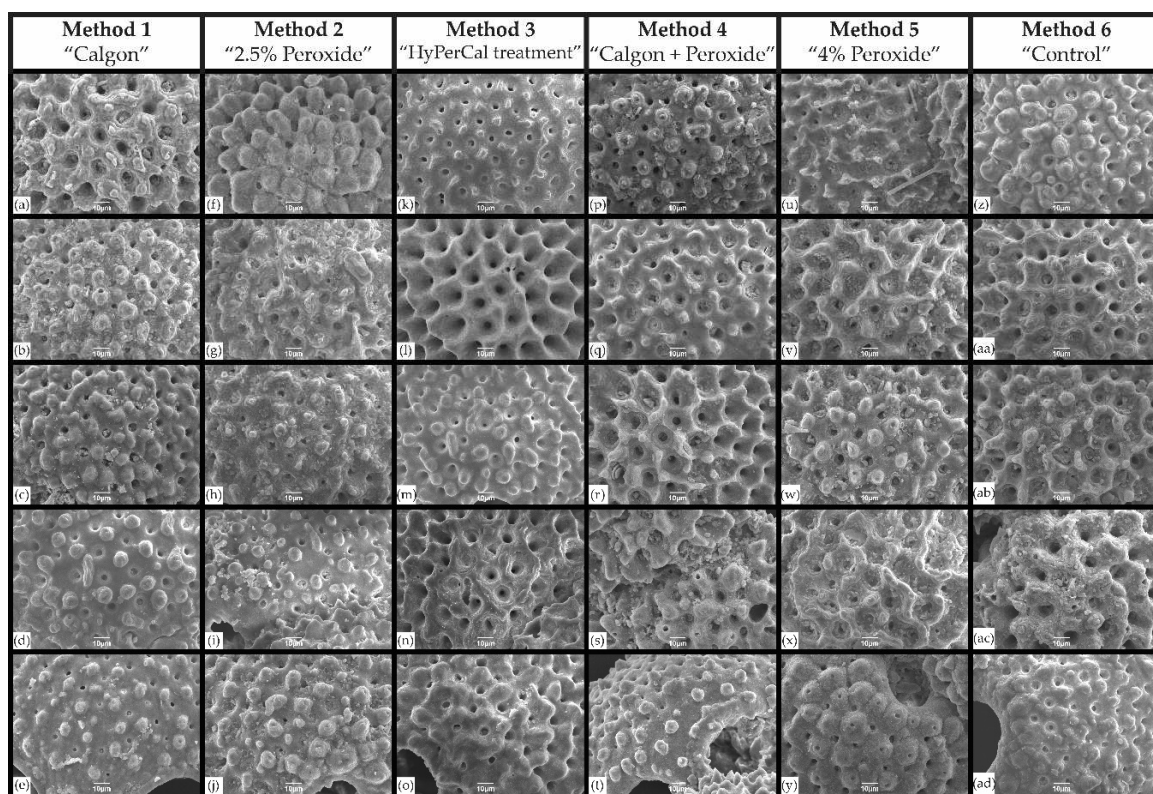


Figure 2. Scanning electron microscope images of the ultrastructure of the specimens after their treatment with the different cleaning methods: (a–e) tomographs of specimens after treatment with $\text{Na}_6\text{O}_{18}\text{P}_6$, (f–j) images of specimens after treatment with 2.5% H_2O_2 solution; (k–o) images after treatment first with 2.5% H_2O_2 and subsequently with $\text{Na}_6\text{O}_{18}\text{P}_6$ solution (HyPerCal); (p–t) images after treatment simultaneously with 2.5% H_2O_2 and $\text{Na}_6\text{O}_{18}\text{P}_6$ solution; (u–y) images after treatment with 4% H_2O_2 , and (z–ad) images after treatment with only with distilled water.

3.2. Synchrotron X-ray Absorption and Weight Analysis

Tomographic slices of the scanned specimens that underwent different treatment are shown in Figure 3 and the results of the tomographic analysis together with the weight measurements are summarized in Table 2. The visual inspection of the tomographs clearly shows that the HyPerCal treatment of Method 3 is the most effective way to eliminate contamination from the internal tests cavities of foraminifera. As it can be seen in Figure 3k–o even the smallest chambers or the secondary apertures and pores are free from detrital material. The two-step treatment with H_2O_2 and subsequently with $\text{Na}_6\text{O}_{18}\text{P}_6$ shows also reduced contamination in the smaller chambers but there is still sedimentary material attached to the interior of the larger chamber walls. $\text{Na}_6\text{O}_{18}\text{P}_6$ alone is less effective in removing contamination, especially in the smaller chambers, while treatment only with water leaves the test infilling in an aggregated form. Treatment with H_2O_2 has left the tests with considerable amounts of detritus and the cohesion of this remaining detrital mass seems to increase with H_2O_2 concentration.

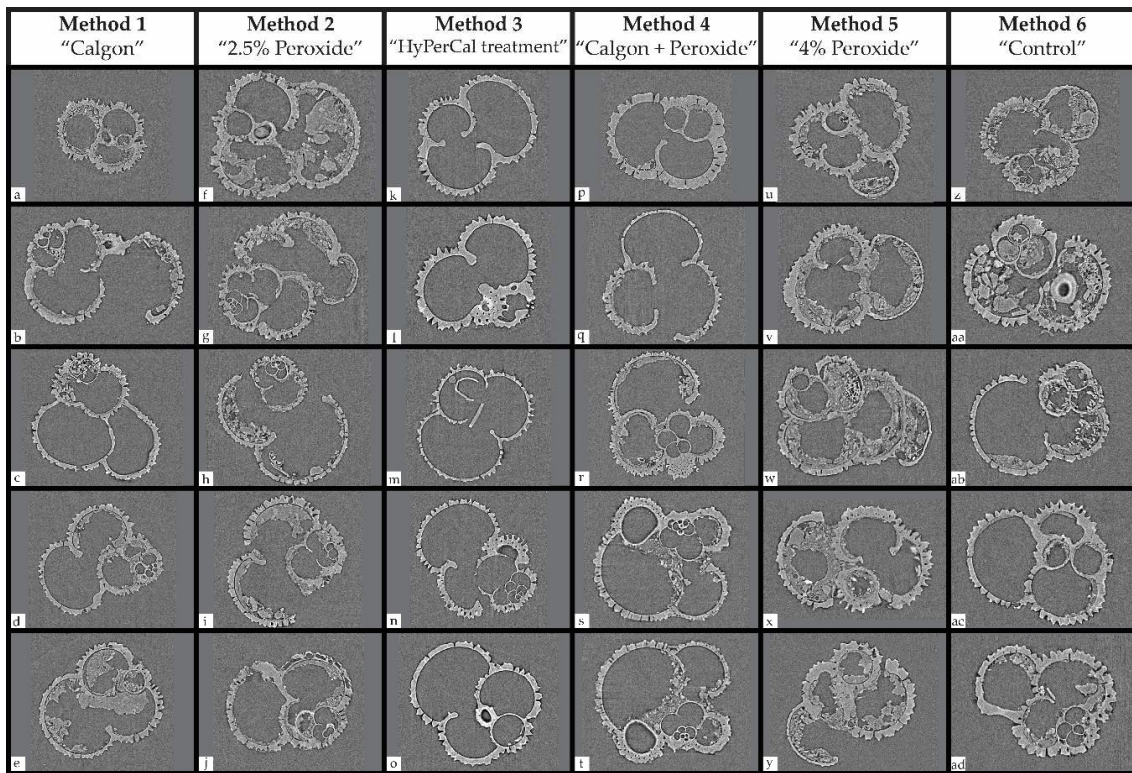


Figure 3. X-ray tomographic images of the interior of the specimens after their treatment with the different cleaning methods: (a–e) tomographs of specimens after treatment with $\text{Na}_6\text{O}_{18}\text{P}_6$, (f–j) tomographs of specimens after treatment with 2.5% H_2O_2 solution, (k–o) tomographs after treatment first with 2.5% H_2O_2 and subsequently with $\text{Na}_6\text{O}_{18}\text{P}_6$ solution (HyPerCal), (p–t) tomographs after treatment simultaneously with 2.5% H_2O_2 and $\text{Na}_6\text{O}_{18}\text{P}_6$ solution, (u–y) tomographs after treatment with 4% H_2O_2 , and (z–ad) tomographs after treatment with only with distilled water.

Table 2. Table showing the results of the X-ray tomographic and weight analyses. The degree of contamination is given as a percentage of cell’s volume. Furthermore, the difference in the measured weights in regard to the average shell weight of the least contaminated tests.

Method	Method Name	Nº of Tests	Contamination (%)	Weight (μg)	Weight Diff.
1	“Calgon”	5	14 (± 12)	23.8 (± 1.6)	21%
2	“2.5% Peroxide”	5	18 (± 6)	28.2 (± 2.8)	44%
3	“PerCal treatment”	5	0 (± 1)	19.6 (± 1.4)	-
4	“Mixed Calgon and peroxide”	5	5 (± 5)	22.0 (± 2.0)	12%
5	“4% Peroxide”	5	21 (± 6)	24.4 (± 0.9)	25%
6	“Control”	5	12 (± 6)	26.4 (± 3.8)	35%

Apart from the visual inspection, the X-ray analysis allowed the determination of the total foraminifera cell volume and that of the area in the interior of the test, which is occupied by sedimentary infill. Thus the degree of contamination of each test is presented in Table 2 as the percentage of detritus within the cell’s volume. It can be seen that the HyPerCal treatment of the sample with H_2O_2 and $\text{Na}_6\text{O}_{18}\text{P}_6$ in two steps has almost completely removed the sediment infill (0%, Table 2) from the test’s interior, as this is also evident in Figure 3k–o. The simultaneous treatment with H_2O_2 and $\text{Na}_6\text{O}_{18}\text{P}_6$ within the same solution had adequate results since detrital contamination was reduced to only 5% by volume. Treatment with $\text{Na}_6\text{O}_{18}\text{P}_6$ or water had a similar effect on detrital removal by reducing

contamination to 14% and 12% respectively, while treatment with H₂O₂ (of different concentrations) had the minimum efficiency in specimen cleaning.

Shell weight is found to be a function of the degree of contamination as shown in Figure 4. It can be seen that samples treated with hydrogen peroxide solution group in the right corner of the graph, while samples treated with aqueous solutions (i.e., water or Calgon) group in its middle. The heaviest tests were the ones that were treated with 2.5% hydrogen peroxide (Method 2). Their average shell weight was 44% greater than that measured for the least contaminated tests. Although treatment with 4% hydrogen peroxide produced consistently lower shell weights its effect on contamination removal was the lowest, suggesting possibly calcite dissolution by the unbuffered solution [34]. Treatment with water produced weights increased by 35% compared to the actual/uncontaminated ones. From the single-constituent solutions Calgon was the one to have the greatest effect on shell weight but also with the greatest variability (12%) in the extent of sediment detrital removal. The simultaneous treatment of the sample with Calgon and hydrogen peroxide is found to be an effective method for specimen cleaning since contamination was found consistently reduced to 5%. Finally, the most effective method that almost completely removed contamination (0% ± 1%) was the HyPerCal treatment.

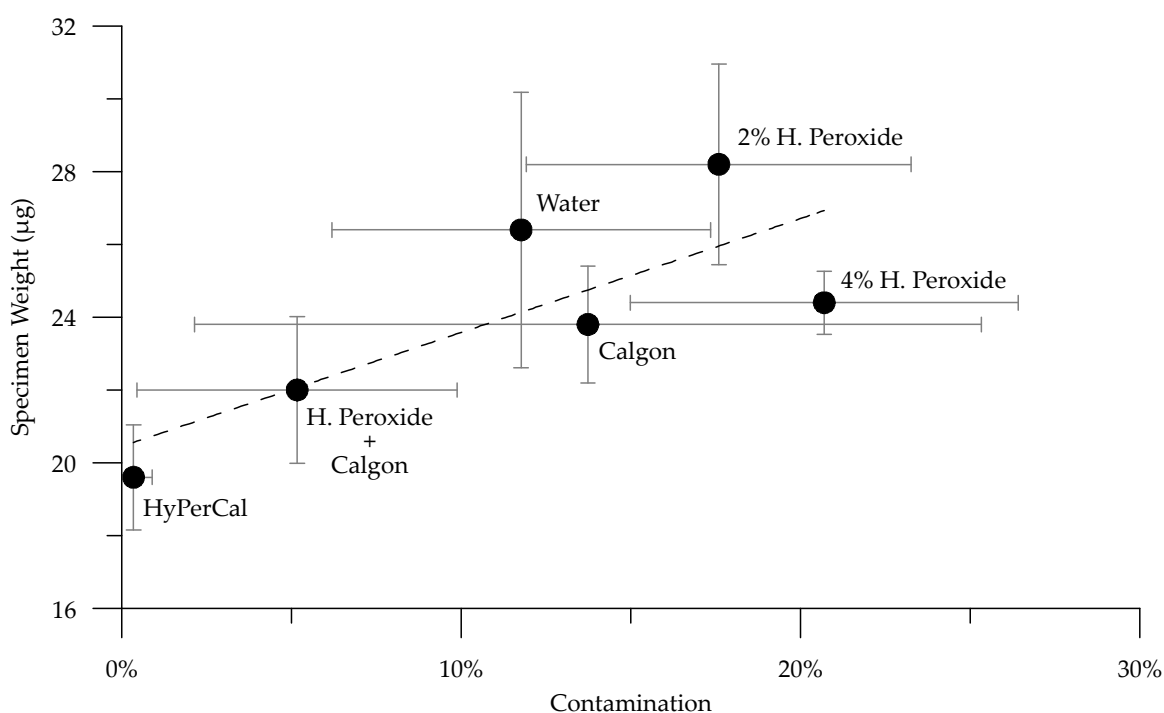


Figure 4. Plot of *G. ruber albus* s.s. shell weights after treatment with the different cleaning methods against their contamination as per volume percentage.

4. Discussion

We performed a systematic experiment with chemical treatments commonly utilized to disaggregate marine sediment and which are known to not significantly affect foraminiferal based proxies, such as species abundance, shell fragmentation, $\delta^{18}\text{O}$, $\delta^{13}\text{C}$, and Mg/Ca. The chemical agents used in solutions were hydrogen peroxide (H₂O₂) in two different concentrations, 5% Calgon (sodium hexametaphosphate, Na₆P₆O₁₈), a swap and a combination of them. We find that the most effective way for preparing foraminifera samples for their subsequent micropaleontological or geochemical analyses is the initial cleaning of the sedimentary material with H₂O₂ followed by treatment of the sieved sample residual with Na₆O₁₈P₆ solution and we refer to this procedure as HyPerCal. In the present experiment the samples were treated for 20 min in every solution and were sonicated every 2 min for 4 s in order to minimize shell breakage [23] but duration of treatment may

vary depending on the cohesion of the sedimentary mass. After cleaning, single-species specimens from a certain sieve fraction were picked, weighed, and subsequently inspected using light microscope, SEM and μ CT. The analyses showed that the different procedures had a variable effect in contamination removal (Figure 4) from the surface and the interior of the examined specimens and that the HyPerCal treatment left the specimens free of (surface or internal) sedimentary residuals, shiny and translucent (Figure 1c).

Sodium hexametaphosphate is a common dispersing agent in research of marine sediments and is more effective than water in removing clay clumps from tests interiors [35], while foraminifera shell weight loss has been previously reported with [21] and without [23] the use of it during cleaning. Our tomographic analysis supports previous studies and confirms that weight differences are the result of sediment contamination removal. The initial treatment with H_2O_2 promotes the degradation of organic matter, which is the major binding agent in benthic sediments [36] and thus minimizing the adhesive forces within the medium. Cohesive forces are at molecular scale the result of the attractive interactions in vacuum between contiguous particles of the same medium, while the adhesive forces are defined as the additional binding forces between particles, due to the presence of a second, interparticle medium [37]. The dispersing action of $\text{Na}_6\text{O}_{18}\text{P}_6$, as a second treatment step, helps to neutralize the attraction electrostatic forces between (clay) particles [38] and is thus reducing particle cohesion. The use of only one of these two reagents alone ($\text{Na}_6\text{O}_{18}\text{P}_6$, H_2O_2) in specimen cleaning did not produce satisfying results both under the SEM and μ CT analyses. The use of both reagents in the same solution, compared to HyPerCal, produced fairly satisfactory results by reducing contamination to only 5%. The high efficiency, however, of the HyPerCal treatment can also stem from the fact that during a two-step treatment the sample processed and sonicated twice as much or from the fact that $\text{Na}_6\text{O}_{18}\text{P}_6$ is only applied on the coarse fraction of sample, free of a substantial amount of material.

Due to the highly reactive nature of the used reagents, there is number of studies that accuse them for foraminifera specimen dissolution [21,34,39]. The release of CO_2 during organic matter oxidation by the unbuffered H_2O_2 increases ambient pH and raises dissolution concerns, while $\text{Na}_6\text{O}_{18}\text{P}_6$ is known to react with calcite [40]. Nevertheless, both of our imaging analyses do not reveal signs of foraminifera calcite dissolution. Dissolution can be assessed by the preservation state of four ultrastructural test features such as pores, interpore space, spines, and ridges [25]. As dissolution proceeds, pores get widened, the interpore areas is etched, ridges and spines become denuded. However, such features are not observed on the well decontaminated ultrastructural surface of most of the tests that were cleaned with HyPerCal (Figure 2k–o) that have thus undergone treatment with both reagents. Further evidence of negligible dissolution can be found by the examination of the μ C-tomographs that show intact chamber walls and well defined initial juvenile chambers (Figure 3k–o), since dissolution first attacks the high-Mg calcite parts of the test. The first signs of dissolution apparent in CT images is that chamber walls become blurred and paler in color, especially in the middle, while the smallest inner chambers start to vanish [41]. Such alterations are not here observed possibly also due to the low organic content of the oligotrophic in nature Mediterranean Sea.

The effectiveness of sediment cleaning procedures is a function sediment matrix mineralogy, grain size and degree of consolidation. The present sediment core material consists of fine-grained (hemipelagic) sediment and originates from the Southeastern Mediterranean basin, which is known for the fine particle size of its clay minerals [42]. The chemical treatment tested here has proved appropriate for removal of the fine material that are usually found in sedimentary basins and should remain so for recent sediment, where the depth of burial is not considered important to initiate diagenetic alteration of the clay minerals [43]. The efficiency of the HyPerCal procedure in the cleaning of calcitic microfossils makes it complementary for foraminifera shell weight studies since it was shown to bring the measured weight closer to that of an “original” shell. Furthermore, it paves the way for its use in modern analytical techniques that require some degree of automatization, such as image recognition software that are unable to recognize a lot of foraminifera images, whose umbilical aperture is not fully cleaned and is infilled with remaining nannofossil ooze [28]. On the other hand, it has proved

beneficial for the upcoming practice of microfossil X-ray tomography, since CT image analysis software cannot easily discriminate between contaminated areas and areas referring to the foraminifera tests unless (subjective) manual labor intensive segmentation is employed [24].

5. Conclusions

In the present study a sediment core sample of late Quaternary age was divided in six aliquots each of which was treated with reagents that do not alter foraminifera calcite geochemistry following different cleaning procedures and the efficiency of each method in specimen cleaning was assessed using SEM and X-ray tomography. The results of the visualization analyses were combined with shell weight measurements and allowed us to conclude that the method that has proven the most effective in removing fine detritus trapped within foraminiferal tests is a two-step treatment of the sedimentary material, named here HyPerCal treatment, initially with 2.5% hydrogen peroxide and subsequently with 5% Calgon solutions. The proposed protocol minimizes discrepancies in foraminifera shell weight measurements and greatly facilitates microfossil X-ray imaging analyses.

Author Contributions: Conceptualization, S.D.Z.; original draft preparation, G.K. and S.D.Z.; laboratory analyses, G.G., S.D.Z. and P.M.; SEM data acquisition, E.B. and V.L.; synchrotron data acquisition, V.S.C.K. and S.M., synchrotron data scientific computing and analysis, K.W. and S.D.Z.; writing—review and editing, G.K., S.D.Z. and A.A.; supervision, A.A. All authors have read and agreed to the published version of the manuscript.

Funding: This research received no external funding.

Acknowledgments: We would like to acknowledge Efterpi Koskeridou and Danae Thivaïou for access to the camera light stereomicroscope and photograph acquisition. This synchrotron X-ray scanning work was carried out with the support of Diamond Light Source, instrument I13-2 (part of proposal MG23868).

Conflicts of Interest: The authors declare no conflict of interest.

Appendix A

The μ CT reconstructed data of (individual) specimens that were cleaned with the different cleaning methods are available online at: (1) <https://doi.org/10.6084/m9.figshare.13333772> for those treated with 5% $\text{Na}_6\text{P}_6\text{O}_{18}$, (2) <https://doi.org/10.6084/m9.figshare.13335002> for those treated with 2.5% H_2O_2 , (3) <https://doi.org/10.6084/m9.figshare.13335833> for those that underwent HyPerCal treatment, (4) <https://doi.org/10.6084/m9.figshare.13335890> for those that treated simultaneously with 2.5% H_2O_2 and 5% $\text{Na}_6\text{P}_6\text{O}_{18}$, (5) <https://doi.org/10.6084/m9.figshare.13335908> for those treated with 4% H_2O_2 , and (6) <https://doi.org/10.6084/m9.figshare.13335935> for those treated only with distilled water.

References

1. Kucera, M. Planktonic Foraminifera as Tracers of Past Oceanic Environments. In *Developments in Marine Geology*; Hillaire-Marcel, C., De Vernal, A., Eds.; Elsevier: Amsterdam, The Netherlands, 2007; Volume 1, pp. 213–262.
2. Shackleton, N.J. Oxygen isotopes, ice volume and sea level. *Quat. Sci. Rev.* **1987**, *6*, 183–190. [[CrossRef](#)]
3. Emiliani, C. Depth habitats of some species of pelagic foraminifera as indicated by oxygen isotope ratios. *Am. J. Sci.* **1954**, *252*, 149–158. [[CrossRef](#)]
4. Anand, P.; Elderfield, H.; Conte, M.H. Calibration of Mg/Ca thermometry in planktonic foraminifera from a sediment trap time series. *Paleoceanography* **2003**, *18*, 1050. [[CrossRef](#)]
5. Brown, S.J.; Elderfield, H. Variations in Mg/Ca and Sr/Ca ratios of planktonic foraminifera caused by postdepositional dissolution: Evidence of shallow Mg-dependent dissolution. *Paleoceanography* **1996**, *11*, 543–551. [[CrossRef](#)]
6. Hönisch, B.; Hemming, N.G. Surface ocean pH response to variations in $p\text{CO}_2$ through two full glacial cycles. *Earth Planet. Sci. Lett.* **2005**, *236*, 305–314. [[CrossRef](#)]
7. Berger, W.H. Planktonic Foraminifera: Selective solution and the lysocline. *Mar. Geol.* **1970**, *8*, 111–138. [[CrossRef](#)]

8. Kucera, M.; Weinelt, M.; Kiefer, T.; Pflaumann, U.; Hayes, A.; Weinelt, M.; Chen, M.-T.; Mix, A.C.; Barrows, T.T.; Cortijo, E.; et al. Reconstruction of sea-surface temperatures from assemblages of planktonic foraminifera: Multi-technique approach based on geographically constrained calibration data sets and its application to glacial Atlantic and Pacific Oceans. *Quat. Sci. Rev.* **2005**, *24*, 951–998. [[CrossRef](#)]
9. Antonarakou, A.; Kontakiotis, G.; Karageorgis, A.P.; Besiou, E.; Zarkogiannis, S.; Drinia, H.; Mortyn, G.P.; Tripsanas, E. Eco-biostratigraphic advances on late Quaternary geochronology and palaeoclimate: The marginal Gulf of Mexico analogue. *Geol. Q.* **2019**, *63*, 178–191. [[CrossRef](#)]
10. Speijer, R.P.; Van Loo, D.; Masschaele, B.; Vlassenbroeck, J.; Cnudde, V.; Jacobs, P. Quantifying foraminiferal growth with high-resolution X-ray computed tomography: New opportunities in foraminiferal ontogeny, phylogeny, and paleoceanographic applications. *Geosphere* **2008**, *4*, 760–763. [[CrossRef](#)]
11. Zarkogiannis, S.; Kontakiotis, G.; Antonarakou, A. Logarithmic expression of *Globigerina bulloides* shell evolution through the biometric analysis: Paleoceanographic implications for the late Quaternary. *IOP Conf. Ser. Earth Environ. Sci.* **2019**, *362*, 012100. [[CrossRef](#)]
12. Caromel, A.G.M.; Schmidt, D.N.; Phillips, J.C.; Rayfield, E.J. Hydrodynamic constraints on the evolution and ecology of planktic foraminifera. *Mar. Micropaleontol.* **2014**, *106*, 69–78. [[CrossRef](#)]
13. Schmidt, D.N.; Thierstein, H.R.; Bollmann, J.; Schiebel, R. Abiotic forcing of plankton evolution in the Cenozoic. *Science* **2004**, *303*, 207–210. [[CrossRef](#)] [[PubMed](#)]
14. Zarkogiannis, S.; Kontakiotis, G.; Antonarakou, A. Recent planktonic foraminifera population and size response to Eastern Mediterranean hydrography. *Rev. Micropaléontologie* **2020**, *69*, 100450. [[CrossRef](#)]
15. Barker, S.; Elderfield, H. Foraminiferal calcification response to glacial-interglacial changes in atmospheric CO₂. *Science* **2002**, *297*, 833–836. [[CrossRef](#)]
16. Zarkogiannis, S.D.; Antonarakou, A.; Tripathi, A.; Kontakiotis, G.; Mortyn, P.G.; Drinia, H.; Greaves, M. Influence of surface ocean density on planktonic foraminifera calcification. *Sci. Rep.* **2019**, *9*, 533. [[CrossRef](#)]
17. Lohmann, G.P. A model for variation in the chemistry of planktonic foraminifera due to secondary calcification and selective dissolution. *Paleoceanography* **1995**, *10*, 445–457. [[CrossRef](#)]
18. Broecker, W.; Clark, E. An evaluation of Lohmann's Foraminifera weight dissolution index. *Paleoceanography* **2001**, *16*, 531–534. [[CrossRef](#)]
19. Vetter, L.; Spero, H.J.; Russell, A.D.; Fehrenbacher, J.S. LA-ICP-MS depth profiling perspective on cleaning protocols for elemental analyses in planktic foraminifers. *Geochem. Geophys. Geosyst.* **2013**, *14*, 2916–2931. [[CrossRef](#)]
20. Barker, S.; Greaves, M.; Elderfield, H. A study of cleaning procedures used for foraminiferal Mg/Ca paleothermometry. *Geochem. Geophys. Geosyst.* **2003**, *4*, 8407. [[CrossRef](#)]
21. Feldmeijer, W.; Metcalfe, B.; Scussolini, P.; Arthur, K. The effect of chemical pretreatment of sediment upon foraminiferal-based proxies. *Geochem. Geophys. Geosyst.* **2013**, *14*, 3996–4014. [[CrossRef](#)]
22. Rosenthal, Y.; Perron-Cashman, S.; Lear, C.H.; Bard, E.; Barker, S.; Billups, K.; Bryan, M.; Delaney, M.L.; deMenocal, P.B.; Dwyer, G.S.; et al. Interlaboratory comparison study of Mg/Ca and Sr/Ca measurements in planktonic foraminifera for paleoceanographic research. *Geochem. Geophys. Geosyst.* **2004**, *5*, Q04D09. [[CrossRef](#)]
23. Qin, B.; Li, T.; Chang, F.; Xiong, Z.; Algeo, T.J. An Improved Protocol For Cleaning of Planktonic Foraminifera For Shell Weight Measurement. *J. Sediment. Res.* **2016**, *86*, 431–437. [[CrossRef](#)]
24. Zarkogiannis, S.D.; Antonarakou, A.; Fernandez, V.; Mortyn, P.G.; Kontakiotis, G.; Drinia, H.; Greaves, M. Evidence of stable foraminifera biomineralization during the last two climate cycles in the tropical Atlantic Ocean. *J. Mar. Sci. Eng.* **2020**, *8*, 737. [[CrossRef](#)]
25. Volbers, A.N.A.; Henrich, R. Late Quaternary variations in calcium carbonate preservation of deep-sea sediments in the northern Cape Basin: Results from a multiproxy approach. *Mar. Geol.* **2002**, *180*, 203–220. [[CrossRef](#)]
26. Weinkauf, M.F.G.; Zwick, M.M.; Kučera, M. Constraining the Role of Shell Porosity in the Regulation of Shell Calcification Intensity in the Modern Planktonic Foraminifer *Orbulina Universa* d'Orbigny. *J. Foraminifer. Res.* **2020**, *50*, 195–203. [[CrossRef](#)]
27. Hsiang, A.Y.; Brombacher, A.; Rillo, M.C.; Mleneck-Vautravers, M.J.; Conn, S.; Lordsmith, S.; Jentzen, A.; Henehan, M.J.; Metcalfe, B.; Fenton, I.S.; et al. Endless Forams: >34,000 Modern Planktonic Foraminiferal Images for Taxonomic Training and Automated Species Recognition Using Convolutional Neural Networks. *Paleoceanogr. Paleoclimatol.* **2019**, *34*, 1157–1177. [[CrossRef](#)]

28. Marchant, R.; Tetard, M.; Pratiwi, A.; Adebayo, M.; de Garidel-Thoron, T. Automated analysis of foraminifera fossil records by image classification using a convolutional neural network. *J. Micropalaeontol.* **2020**, *39*, 183–202. [[CrossRef](#)]
29. Zarkogiannis, S.; Fernandez, V.; Greaves, M.; Mortyn, P.G.; Kontakiotis, G.; Antonarakou, A. X-ray tomographic data of planktonic foraminifera species *Globigerina bulloides* from the Eastern Tropical Atlantic across Termination II. *Gigabyte* **2020**, *1*, 1–10. [[CrossRef](#)]
30. Ehrmann, W.; Schmiedl, G.; Hamann, Y.; Kuhnt, T. Distribution of clay minerals in surface sediments of the Aegean Sea: A compilation. *Int. J. Earth Sci.* **2006**, *96*, 769. [[CrossRef](#)]
31. Ehrmann, W.; Schmiedl, G.; Hamann, Y.; Kuhnt, T.; Hemleben, C.; Siebel, W. Clay minerals in late glacial and Holocene sediments of the northern and southern Aegean Sea. *Palaeogeogr. Palaeoclimatol. Palaeoecol.* **2007**, *249*, 36–57. [[CrossRef](#)]
32. Kidd, R.B.; Cita, M.B.; Ryan, W.B.F. Stratigraphy of eastern Mediterranean sapropel sequences recovered during DSDP Leg 42A and their paleoenvironmental significance. In *Initial Reports of the Deep Sea Drilling Project/1975/Malaga*; Government Printing Office: Washington, DC, USA, 1978; pp. 421–443.
33. Atwood, R.C.; Bodey, A.J.; Price, S.W.T.; Basham, M.; Drakopoulos, M. A high-throughput system for high-quality tomographic reconstruction of large datasets at Diamond Light Source. *Philos. Trans. R. Soc. A Math. Phys. Eng. Sci.* **2015**, *373*, 20140398. [[CrossRef](#)] [[PubMed](#)]
34. D’Onofrio, R.; Luciani, V. Do different extraction techniques impact planktic foraminiferal assemblages? An early Eocene case study. *Mar. Micropaleontol.* **2020**, *155*, 101795. [[CrossRef](#)]
35. Kilmer, V.J.; Alexander, L.T. Methods of making mechanical analyses of soils. *Soil Sci.* **1949**, *68*, 15–24. [[CrossRef](#)]
36. Righetti, M.; Lucarelli, C. May the Shields theory be extended to cohesive and adhesive benthic sediments? *J. Geophys. Res. Ocean.* **2007**, *112*, C05039. [[CrossRef](#)]
37. Israelachvili, J.N. *Intermolecular and Surface Forces*; Academic Press: San Diego, CA, USA, 2011; p. 674. [[CrossRef](#)]
38. Castellini, E.; Lusvardi, G.; Malavasi, G.; Menabue, L. Thermodynamic aspects of the adsorption of hexametaphosphate on kaolinite. *J. Colloid Interface Sci.* **2005**, *292*, 322–329. [[CrossRef](#)]
39. Green, O.R. Extraction Techniques for Calcareous Microfossils from Argillaceous Sediments. In *A Manual of Practical Laboratory and Field Techniques in Palaeobiology*; Springer: Dordrecht, The Netherlands, 2001; pp. 334–341. [[CrossRef](#)]
40. Thomson, R.T. Some properties of sodium hexametaphosphate. *Analyst* **1936**, *61*, 320–323. [[CrossRef](#)]
41. Johnstone, H.J.H.; Schulz, M.; Barker, S.; Elderfield, H. Inside story: An X-ray computed tomography method for assessing dissolution in the tests of planktonic foraminifera. *Mar. Micropaleontol.* **2010**, *77*, 58–70. [[CrossRef](#)]
42. Weir, A.H.; Ormerod, E.C.; El Mansey, I.M.I. Clay mineralogy of sediments of the western Nile Delta. *Clay Miner.* **2018**, *10*, 369–386. [[CrossRef](#)]
43. Rostási, Á.; Raucsik, B.; Varga, A. Palaeoenvironmental controls on the clay mineralogy of Carnian sections from the Transdanubian Range (Hungary). *Palaeogeogr. Palaeoclimatol. Palaeoecol.* **2011**, *300*, 101–112. [[CrossRef](#)]




Publisher’s Note: MDPI stays neutral with regard to jurisdictional claims in published maps and institutional affiliations.



© 2020 by the authors. Licensee MDPI, Basel, Switzerland. This article is an open access article distributed under the terms and conditions of the Creative Commons Attribution (CC BY) license (<http://creativecommons.org/licenses/by/4.0/>).

Article

Latitudinal Differentiation among Modern Planktonic Foraminiferal Populations of Central Mediterranean: Species–Specific Distribution Patterns and Size Variability

George Kontakiotis ^{1,*}, Eirini Efstathiou ¹, Stergios D. Zarkogiannis ², Evangelia Besiou ¹
and Assimina Antonarakou ²

¹ Department of Historical Geology-Paleontology, Faculty of Geology and Geoenvironment, School of Earth Sciences, National and Kapodistrian University of Athens, Panepistimiopolis, Zografou, 15784 Athens, Greece; euirini@gmail.com (E.E.); evabesiou@geol.uoa.gr (E.B.)

² Department of Earth Sciences, University of Oxford, Oxford OX1 3AN, UK; stergios.zarkogiannis@earth.ox.ac.uk (S.D.Z.); aantonar@geol.uoa.gr (A.A.)

* Correspondence: gkontak@geol.uoa.gr; Tel.: +30-21-0727-4804

Abstract: Studies of the spatial distribution and size of modern planktonic foraminifera are still lacking in the Mediterranean Sea. In this study, 17 core-top sediments collected from a north-south transect along the central Mediterranean have been analyzed for planktonic foraminiferal content, in terms of their distributional pattern and intraspecific size variability. Among the analyzed planktonic foraminiferal species, *Globigerina bulloides* and *Globigerinoides ruber* (w) were the most abundant, presenting an antagonistic behavior and an overall decreasing trend in their average size values from Adriatic to Ionian sub-basins. Intraspecific differences have been also documented for *G. ruber* (w), with the dominant sensu stricto morphotype to present generally higher frequencies and more constant shell sizes than sensu lato. The greater size variability of the latter is possibly related to its adaptation in particular hydrographic conditions based on its depth habitat preference and ecological characteristics to reach the (sub)optimum growth conditions. The rest of the species occur in minor percentages and show on average 11% increase with decreasing latitude characterized by distinct species-specific size variations along the transect. Our results show that the relationship between planktonic foraminifera shell size and abundance or sea surface temperature are either absent or weaker than previously reported for other regions and that in central Mediterranean assemblages' size may be mainly related to nutrient availability. Besides the environmental parameters (sea surface temperature, primary productivity, water depth, stratification), the possible hidden cryptic diversity, still lingers to be consistently determined, could give a better understanding of the geographic and morphological differentiation within the Mediterranean planktonic populations.

Keywords: planktonic foraminiferal biogeography; surface sediments; morphometrics; shell size; environmental biomonitoring; ecological optimum conditions; primary productivity; depth habitat preference; cryptic speciation; central Mediterranean hydrodynamics



Citation: Kontakiotis, G.; Efstathiou, E.; Zarkogiannis, S.D.; Besiou, E.; Antonarakou, A. Latitudinal Differentiation among Modern Planktonic Foraminiferal Populations of Central Mediterranean: Species–Specific Distribution Patterns and Size Variability. *J. Mar. Sci. Eng.* **2021**, *9*, 551. <https://doi.org/10.3390/jmse9050551>

Academic Editor: Wonho Yih

Received: 28 April 2021

Accepted: 18 May 2021

Published: 20 May 2021

Publisher's Note: MDPI stays neutral with regard to jurisdictional claims in published maps and institutional affiliations.



Copyright: © 2021 by the authors. Licensee MDPI, Basel, Switzerland. This article is an open access article distributed under the terms and conditions of the Creative Commons Attribution (CC BY) license (<https://creativecommons.org/licenses/by/4.0/>).

1. Introduction

Foraminifera are one of the most abundant and diverse heterotrophic protists in the oceans consisting of a major group of calcareous marine microplankton [1]. Due to their great abundance and their good fossilization potential, foraminifera are commonly used for bio-ecostratigraphic [2–7], paleoceanographic/paleoclimatic [8–19], and/or paleobiogeographic [20–24] studies. Particularly, planktonic foraminifera are the most frequently applied microfossil group in this manner because they have an excellent fossil record with global distribution, high abundance in sedimentary archives, and further present an enhanced sensitivity to varying sea surface conditions [25,26]. The geographic ranges and abundance of these organisms can also provide valuable quantitative and qualitative proxy

data through the estimation of several paleoceanographic and paleoclimatic indices for reconstructing paleoenvironments [27–29]. Both their abundance and shape-size-related changes are strongly related to surface ocean physico-chemical properties, most notably temperature, but also nutrient and oxygen availability, water column stratification, salinity, turbidity, and carbonate saturation [8,25,30–38]. Elucidation of the factors governing their distribution, and processes involved in their ontogenetic development are therefore essential for reconstructing paleoceanographic conditions.

Compared to the large body of knowledge on the taxonomy, physiology, and ecology of planktonic foraminiferal species, their spatial distribution and size response to hydroclimate remains poorly studied, especially for the oceanic sub-basins and/or marginal seas, which are often more responsive to paleoceanographic and paleoclimatic changes than global oceans. Moreover, as a significant constituent of microzooplankton, they are key components of pelagic food webs and the main predators of phytoplankton in (sub)tropical oligotrophic waters regulating thus the carbon flux in such environments [39–43]. Although at a global scale, their abundance follows the overall pattern of primary productivity (PP; [44]), at a regional scale this relationship is weaker possibly due to the omnivorous diet of the planktonic foraminifera in the marine food web, and phase shifts in the production of phytoplankton and zooplankton [1]. Species abundance varies with season, water mass, and water depth [36]. Both the highest horizontal and vertical separation of species are recorded from temperate to subtropical waters, owing to a wider diversity of meso-scale local hydrographic features and biotic variables, which make their distribution patchy on temporal and spatial scales [45,46].

Based on the species-specific ecological tolerance limits of modern planktonic foraminifera [1,47], the potential reduction in abundance is related to their departure from optimum conditions [48], and the subsequent size-related and/or weight-related changes on the planktonic fauna [49], since planktonic foraminifera must compensate for their greater shell weight to maintain buoyancy [50]. Changes in size can be attributed to different processes (volume or surface area dependent) linked to the ecology of each species [51–53]. Particularly, isometric features increase with the cube of linear dimensions, while surface area-related features increase merely with the square of linear dimensions. Consequently, surface area-dependent processes, such as feeding, respiration, and skeletal support of foraminifera have to keep up with volume and weight changes.

The main goal of this study is to evaluate and further quantify the spatial and size-related distribution of modern planktonic foraminifera from the central Mediterranean Sea. In our attempt to better understand the paleoecological and paleobiogeographical significance of size variability in planktonic foraminiferal fauna of Adriatic and Ionian basins, the relative importance of environmental factors controlling rates, magnitudes, spatial scale, and biotic change are also examined. This allows for the establishment of a detailed reference record for the central Mediterranean in terms of planktonic foraminiferal ecosystem functioning (including species composition, diversity, and size variability), providing, on the one hand, a solid eco-morphological microplankton response to environmental conditions for the study area, and facilitating, on the other hand, paleoceanographic correlations at a local (e.g., eastern Mediterranean—Aegean and Levantine basins; [24]) and a global, e.g., [37], scale.

2. Study Area

2.1. Regional Oceanographic Setting

The Mediterranean Sea is a land-locked Sea characterized by an anti-estuarine circulation pattern which is forced by negative hydrological balance and density gradient compared to the open Atlantic Ocean [54]. Particularly, the central Mediterranean basin consists of the Adriatic and Ionian Seas (Figure 1), which are characterized by complex geomorphology and oceanography, as well as different productivity regimes. The Adriatic Sea is a small semi-enclosed shelf area connected to the eastern Mediterranean through the Otranto Strait. According to its topography, it presents strong bathymetric contrasts from north to south with its northernmost part being the shallowest (~50 m), the middle Adriatic deeper (~270 m) and the southern Adriatic the deepest (up to 1250 m) [55]. The same exists for the Ionian Sea, which constitutes distinct sub-basins with different bathymetric and hydrological characteristics. For instance, the Salerno area is characterized by a broad continental shelf with rocky bottoms, the Calabrian sector by numerous narrow submarine canyons [56], while the central Ionian by the homonymous abyssal plain. Overall, the Ionian Sea is affected by the inflow of water from the Levantine, Aegean, Adriatic and western Mediterranean basins and therefore different water masses propagate into the Ionian Sea and mixing between them can occur. The general hydrographic conditions determine substantial differences in temperature and salinity values within the study area and the large-scale circulation pattern undergoes seasonal changes resulting in diverse physical, biogeochemical, and ecological conditions [57,58].

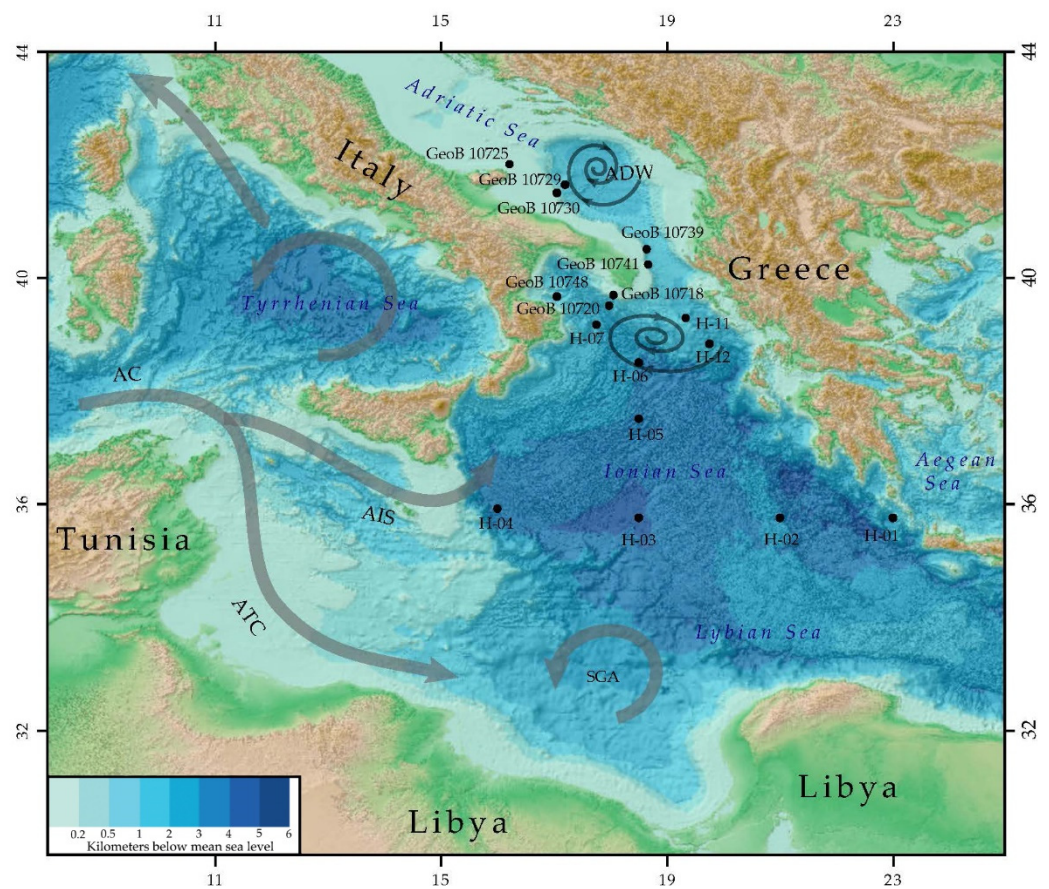


Figure 1. Bathymetric map of the central Mediterranean depicting the sampling locations in the Adriatic and Ionian sub-basins along with the upper ocean current system in the study area.

2.2. Water Masses and Circulation

The Ionian Sea is affected by the inflow of diverse water masses from the Levantine, Aegean, Adriatic, and western Mediterranean. At the entrance of the Sicily Strait, inflowing surface waters occupying the upper 200 m (Modified Atlantic Water; MAW) flow eastward along the north African coast and separate into two branches: one turns northward along the Sicilian coast into a broad anticyclonic pattern, while the other continues in an easterly direction along the African coast with increasing salinity, following a large-scale counter-clockwise pathway [59,60] (Figure 1). The northern branch, called the Atlantic Ionian Stream (AIS; [61]), is complicated by quasi-permanent mesoscale gyres and their spatial variable in terms of shape, position and strength lobes, meanders and transient eddies contributing to the MAW transport into the eastern Mediterranean off the southern coast of Sicily [59,62]. Such meso-scale eddies are often very efficient in transferring particles and passive tracers vertically or horizontally, contributing in this way to the propagation and mixing of water masses. The eastern-most MAW, termed Atlantic Tunisian Current (ATC; [63]), shows a marked path in winter when it cools and undergoes a severe salt enrichment forming the Levantine Intermediate Water (LIW). The LIW, enriched by Cretan intermediate water, flows westward into the Tyrrhenian Sea at 200–600 m depth as the salty outflow waters. Its role is particularly important since it is the preconditioning agent for the dense water formation of both the Adriatic Deep Water (AdDW) and Aegean Deep Water (AeDW) below 800 m [60,64–66] and their communication to the western Mediterranean basin [67].

The surface circulation of the Adriatic Sea consists of a basin-wide and seasonal variable cyclonic gyre with a northward flow along the eastern side, the Eastern Adriatic Current (EAC; [68]), and a southward return flow along the Italian coast on the western side (Western Adriatic Current; WAC; [69]) which flushes the nutrient-rich water out of the northern Adriatic [70]. During autumn and winter, a cold and relatively fresh dense water mass (AdDW) is also formed in the northern and central Adriatic Sea. Outflowing AdDW is accompanied by inflowing warmer LIW from the Ionian Sea, and this thermal circulation is driven by winter cooling of the Adriatic [71]. Overall, there are three main forcing factors affecting the circulation pattern: (a) river runoff causing heat loss and low-salinity water gain; (b) atmospheric forcing responsible for dense water formation and seasonal differences in circulation; and (c) exchange via the Strait of Otranto balancing the water budget by the intrusion of warm and salty waters from the Ionian Sea. As a result, temperature, salinity and circulation display marked spatial and temporal variations [72]. Moreover, the Adriatic Sea typically presents lower surface salinities than the rest of the central Mediterranean, mostly due to large freshwater inputs from rivers, acting as a dilution basin [73].

2.3. Productivity Regimes

River runoff affects the circulation through freshwater input and impacts the marine ecosystem by introducing large amounts of organic matter, nutrients, and sediments. Particularly, Po and Apennine rivers play a major role in freshwater supply for the northern Adriatic. Beyond the seasonal character of river discharges, the long-term changes of nutrient concentrations in the northern Adriatic are also strongly influenced by atmospheric conditions and therefore connected with climatic fluctuations, which can modify the water column dynamics (e.g., vertical mixing, horizontal advection, water exchange rate between north-central Adriatic; [74]). The southern Adriatic open waters show oligotrophic characteristics comparable to the Ionian Sea, with nutrient supply to the euphotic zone strongly depending on vertical stratification and mixing processes [75]. However, higher phytoplankton densities have been observed in the surface waters along the south Italian coasts driven by intensified freshwater inputs [76,77]. Horizontal or vertical advection of nutrient-rich LIW from the Ionian Sea is also an important productivity factor [78] for specific locations within the southern Adriatic Sea where phytoplankton blooms follow deep convection events [79]. Physical and chemical parameters of these blooms [80] have

shown a switch from typical Mediterranean phosphorous- to nitrogen-limited conditions for this setting.

3. Materials and Methods

3.1. Sediment Sampling Strategy and Site Selection

The study is based on the micropaleontological analysis of the distribution abundance pattern and size variability of the planktonic foraminiferal fauna in a series of modern core-tops derived from 17 surface sediment sites across the central Mediterranean Sea. The samples were collected by multicores during various expeditions (POSEIDON cruise “CAPPUCCINO” in June 2006, Meteor cruise M71/3 in January 2007) and cover a latitudinal NW-SE transect from the north Adriatic to the south Ionian Sea, spanning variable sea surface parameters, different productivity regimes, and a wide depth range between 94 and 4088 m (Table 1 and Figure 1). Their chronology is based on ^{210}Pb and ^{137}Cs radiometric dating applied on some of the present samples [81] and surrounding core-tops [82,83]. Although generally the core-top samples provide integrated information on a longer time scale (decades, centuries or millennia depending on the sedimentation rate of the selected sites) compared to the water column (e.g., plankton tow, sediment traps) derived samples, the relatively low ($0.06\text{--}0.91\text{ cm yr}^{-1}$, avg. 0.19 cm yr^{-1} ; [77]) sedimentation rates (likely decrease with distance from the shore) in conjunction with the constant sediment accumulation rate over the last century that characterizes the central Mediterranean surface sediments [84] corroborate the recent character of the analyzed samples. Accordingly, all studied core tops are suggested to have a modern age and in accordance with other core-top studies within the Mediterranean Sea [18,20,24,77,85,86]. Thus, our dataset represents an integrated record of some yr to 50 yr or a few 100 yr at most, depending on the core location. The multicore provided topmost (0–1 cm) sediments with an undisturbed sediment–water interface. More explicitly, we use 6 core-top samples along the south Adriatic Sea from the Gargano Promontory to the Strait of Otranto, supplemented by additional 11 samples from the entire Ionian basin (from the Gulf of Taranto to the Mediterranean Ridge offshore Crete Island).

Given the availability of processed sediment samples with well-preserved foraminifera, the analyzed core-tops are further carefully selected based on the major circulation features in Adriatic and Ionian basins as well as the Italian river influences. Therefore, they are strategically positioned to check the sensitivity of environmental parameters and the subsequent planktonic foraminiferal fauna responses by assessing the adaptability of each species, including both species-specific distribution patterns and size variations, to different environmental regimes. For this reason, relative abundances and size offsets have been interpreted in regard to upper water chlorophyll-a (Chl-a) concentrations and mean annual sea surface temperature (SST), salinity (SSS), and density values of the central Mediterranean water masses. SST and SSS data were derived from the Emodnet database (<https://portal.emodnet-physics.eu/>) (15 December 2020) of the years 1900–2013, while density data obtained from the National oceanic and atmospheric administration dataset (<https://www.ncei.noaa.gov/access/world-ocean-atlas-2018/bin/woa18.pl>) (15 December 2020) on a 0.1° grid resolution. The Chl-a concentrations at each core location were used as satellite data retrieved from OBPG MODIS-Aqua Monthly Global 4 km database (<http://oceancolor.gsfc.nasa.gov>) (15 December 2020) for the time period 4 September 2002 to 30 June 2020 (Table 1).

Table 1. Core-top locations, coordinates, scientific expeditions, seafloor water depths, lithology, and mean annual SST, SSS and density data along with Chl-a concentrations.

Cruise	Station	Latitude	Longitude	Basin (Region)	Water Depth	Lithology	SST	SSS	Ch-a	Density
		(°N)	(°E)		(m)		°C	psu	kgCm ⁻² yr ⁻¹	(kg/m ³)
Poseidon P339	#17. GeoB 10725	42.001	16.217	Gargano Promontory (S. Adriatic Sea)	94	Mud	14.40	38.29	0.42	28.65
Poseidon P339	#16. GeoB 10729	41.647	17.191	Gargano Promontory (S. Adriatic Sea)	708	Sandy mud	13.40	38.60	0.19	29.10
Poseidon P339	#15. GeoB 10730	41.500	17.050	Gargano Promontory (S. Adriatic Sea)	179	Sandy mud	13.90	38.70	0.21	29.07
Poseidon P339	#14. GeoB 10739	40.500	18.642	Strait of Otranto (S. Adriatic Sea)	561	Mud	13.80	38.73	0.24	29.12
Poseidon P339	#13. GeoB 10741	40.234	18.667	Strait of Otranto (S. Adriatic Sea)	286	Sandy mud	14.00	38.67	0.28	29.03
Poseidon P339	#12. GeoB 10718	39.693	18.058	Gulf of Taranto (NW Ionian Sea)	214	Sandy mud	14.20	38.32	0.27	28.71
Poseidon P339	#11. GeoB 10748	39.667	17.050	Strait of Otranto (S. Adriatic Sea)	284	Mud	13.80	38.73	0.25	29.12
Poseidon P339	#10. GeoB 10720	39.507	17.979	Gulf of Taranto (NW Ionian Sea)	1384	Mud	13.60	38.69	0.19	29.13
Meteor M 71-3	#9. H-11	39.283	19.333	Offshore Kerkyra basin (NE. Ionian Sea)	1032	Muddy sand	13.60	38.70	0.15	29.14
Meteor M 71-3	#8. H-07	39.167	17.750	External Calabrian Arc (NW. Ionian Sea)	1663	Mud	13.60	38.69	0.18	29.13
Meteor M 71-3	#7. H-12	38.833	19.750	Offshore Kerkyra basin (NE. Ionian Sea)	1459	Clay	13.60	38.70	0.14	29.14
Meteor M 71-3	#6. H-06	38.500	18.500	Ionian Bathyal Plain (N. Ionian Sea)	3018	Clay	13.80	38.71	0.14	29.10
Meteor M 71-3	#5. H-05	37.500	18.500	Ionian Bathyal Plain (C. Ionian Sea)	3157	Mud	13.90	38.72	0.12	29.09
Meteor M 71-3	#4. H-04	35.917	16.000	External Calabrian Arc (W. Ionian Sea)	3747	Muddy sand	13.80	38.67	0.14	29.07
Meteor M 71-3	#3. H-01	35.750	23.000	Offshore Cretan basin (E. Ionian Sea)	2121	Clay	14.10	38.83	0.11	29.13
Meteor M 71-3	#2. H-02	35.750	21.000	Mediterranean Ridge (C. Ionian Sea)	3005	Clay	13.90	38.74	0.09	29.10
Meteor M 71-3	#1. H-03	35.750	18.500	Ionian Bathyal Plain (C. Ionian Sea)	4088	Clay	13.80	38.67	0.10	29.07

3.2. Micropaleontological Quantitative Analysis

The planktonic foraminiferal assemblages for the studied core-tops were picked from 10 cm³ of wet sediment after washing through a 125 µm mesh sieve and cleaning using the HyPerCal protocol [87]. The 125 µm size fraction was selected in order to increase the reliability of studied planktonic foraminiferal assemblages that derived from such a subtropical oligotrophic-to-mesotrophic region with relatively low planktonic foraminiferal abundance [22,88,89] by avoiding over/under-estimations in the percentages of smaller (e.g., *Turborotalita quinqueloba*) or larger (e.g., *Trilobatus trilobus*) in size than the usual mean size of other species. The adopted size fraction is commonly used in relevant investigations within and beyond the Mediterranean Sea, which analyze the modern foraminiferal record [21,24,90–92] and implement a paleoclimatic analysis [8,9,93,94]. The dry residues (~3 g) were split using an Otto micro-splitter into aliquots of at least 300 planktonic foraminiferal specimens, which were identified to the species level according to the taxonomic concepts of Hemleben et al. [1] and Schiebel and Hemleben [95]. Raw data were transformed into percentages of the total absolute abundance, and relative percentage abundance curves were plotted versus latitude. Following Aurahs et al. [96], we distinguish *Globigerinoides ruber* pink (var. *rosea*) as a distinct morphotype, whereas for the white variety (var. *alba*), we follow the concept of Wang [97] by distinguishing *G. ruber* sensu stricto (s.s.) and *G. ruber* sensu lato (s.l.) morphotypes which have different depth preferences [98] and reflect distinctive environmental parameters [99,100]. We further note that *G. ruber* s.s. is equivalent to Morphotype A (type “Normal”), while those specimens

are grouped as *G. ruber* s.l. correspond to the Morphotypes B and C (type “Platys” and “Elongate”) of Kontakiotis et al. [21] from the Mediterranean Sea. The *Globigerina bulloides* group includes the species *G. bulloides* and *G. falconensis* due to their similar ecological preferences [95]. Finally, the ecological interpretations and biogeographic implications for the studied species were based on the reference of [22,24,101–103].

3.3. Morphometric Analysis

For morphometric analysis, the picked specimens were transferred with a brush on a chapman micro-slide, where each species positioned in separate cells. Given the minimized difference in average areas for the umbilical or spiral sides for several species [104], we oriented the foraminiferal shells in umbilical or spiral position (species dependent) to capture the maximum silhouette area of each individual. The fixed specimens were photographed in transmitted light under a 50-fold magnification by a modular Leica M165 C fully apochromatic stereo microscope equipped with an integrated 10 megapixel (MP) Leica IC90 E color camera and processed using ImageJ software (version 1.50i). The derived images were parsed into objects by thresholding and their shape and size parameters were automatically extracted. Automated recognition of multiple foraminifera in the images was succeeded due to the contrast between the bright background and the dark silhouettes of the specimens. Following the pioneer work of Kucera and Kennett [105] and in accordance with a recent study of Zarkogiannis et al. [24] for the eastern Mediterranean, the Equivalent Circular Diameter (ECD) was measured as an aspect of the size of the species analyzed. Calibration for the silhouette area and diameter measurements was performed using a microscale image taken at the same magnification as the foraminiferal images optimizing the reproducibility and accuracy of the measurements. Additional to size analysis, image processing automatically performs planktonic foraminiferal counting, as well for each site, resulting in the overall changes in their assemblages for the study area during recent times.

4. Results

4.1. Relative Abundance Data

Thirteen planktonic foraminiferal species were identified at the studied core-tops along the N-S transect of the central Mediterranean Sea. The overall changes in their abundances are illustrated in Figure 2. Overall, the planktonic assemblages are dominated by *G. bulloides*, followed by *G. ruber* (including var. *alba* and *rosea*), while the species *Globigerinella siphonifera*, *Neogloboquadrina pachyderma*, *Orbulina universa*, *Globoturborotalita rubescens*, and *Globigerinita glutinata* are common. *Globorotalia inflata*, *Globorotalia truncatulinoides* and *Turborotalita quinqueloba* display a more sporadic faunal pattern with lower percentages.

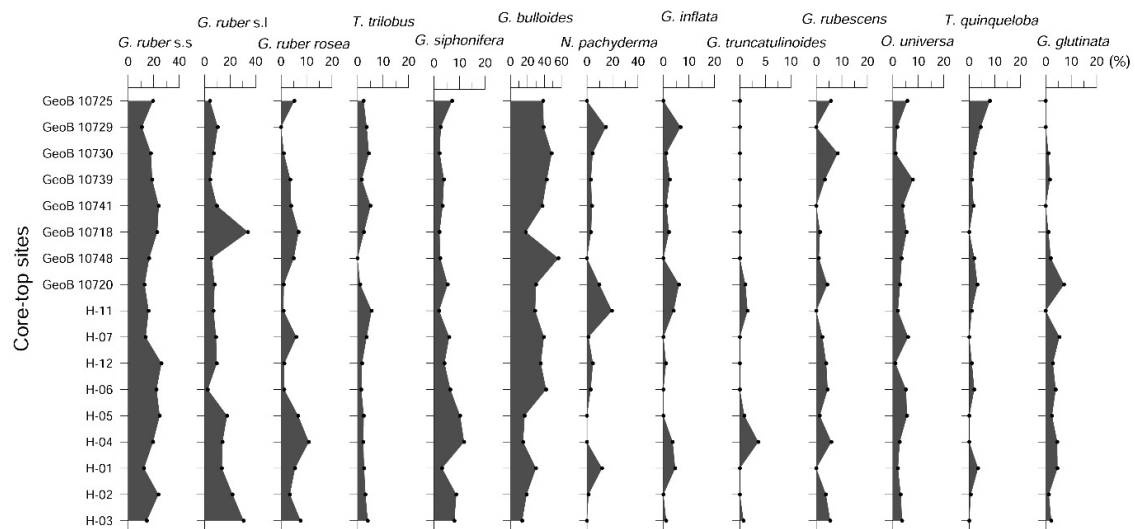


Figure 2. Planktonic foraminifera species abundances in core-top samples from the eastern Mediterranean. The labels in the vertical axis are representative of the core-top locations presented in Table 1.

G. bulloides is the major contributor in the planktonic fauna in all samples with percentages up to 57%. However, the average contribution of this species significantly differs between the two study regions with a clear geographic signal to have emerged in its distribution. More explicitly, a sharp decrease in the abundance of *G. bulloides* with latitude is marked with the average values of 43.9% for the Adriatic to be diminished to 26.3% for the Ionian basin, respectively. It reaches high abundance values, constantly higher than 35% within the south Adriatic Sea, while its distributional pattern displays minor (almost half) percentages in the Ionian basin. *Globigerinoides ruber* (w) is the second ubiquitous and more abundant species showing an average abundance of 29.8% in the central Mediterranean. This species is continuously present throughout the transect, displaying almost an opposite distributional pattern compared to *G. bulloides*. Such an antagonistic pattern is documented for both s.s. and s.l. morphotypes. Except for two samples (H-03 and GeoB 10718), the s.s. morphotype is the main constituent in the *G. ruber* (w) morphospace. This intra-specific trend is more pronounced in the Adriatic basin, where the dominant morphotype presents higher frequencies (i.e., at least the double percentages) compared to *G. ruber* s.l. in most of the samples. *Globigerinoides ruber rosea* is present in lower percentages up to 11% being more abundant in the southern part of the Ionian basin. *Globigerinella siphonifera* is present in almost all locations, but its percentages become important by exceeded 10% only in the westernmost sites (H-04, H-05) within the Ionian basin. *Neogloboquadrina pachyderma* presents a highly variable distributional pattern, occasionally reaching significant percentages up to 20% (i.e., site H-11 at the northernmost part of the Ionian basin). *Orbulina universa*, *G. rubescens*, and *T. trilobus* show comparable patterns with continuous although limited presence (<8%) in both basins. *Globigerinita glutinata* is mostly found within the Ionian basin with restricted occurrence in relatively small percentages (<7%), and it is almost absent in the southern Adriatic Sea. *Turborotalita quinqueloba*, where present, exists with very small percentages around 3%. *Globorotalia inflata* shows a geographically sporadic distribution pattern with percentages stably less than 10% and the deep-dweller *G. truncatulinoides* is nearby absent from all regions, since it occasionally occurred at very low percentages (maximum 4%).

4.2. Preservation Regime and Size Variability

The presence of pristine specimens of the tiny thin-walled species reinforces the recent character of the analyzed material and further indicates the excellent preservation of the samples, suggesting that the reported assemblages are not biased by dissolution. The absence of differential preservation of thin-walled specimens of the analyzed species along with the strong carbonate preservation potential of the study area [106] indicate minimized modifications on the size spectrum of the planktonic association.

The mean population size of the identified planktonic foraminifera along with the standard deviation values of species-specific sizes reflecting the overall variability per basin analyzed are summarized in Table 2, while the species-specific size variations along the study transect are shown in Figure 3. The number of individuals measured per species varied from 2 to 170, averaging 21 individuals per species per sample. Generally, the mean population size of the analyzed planktonic foraminiferal assemblages is skewed toward larger sizes from north to south. Our dataset reports a 4–16% increase (avg ~11%) for all species from Adriatic to Ionian settings, except for *G. ruber* (including both chromotypes and morphotypes) and *G. bulloides*, which support the opposite pattern (Table 2). The most consistent in size within the central Mediterranean sub-basins with the smallest standard deviation between analyzed samples are the populations of *G. bulloides*, *G. ruber* (s.s. and s.l.), and *G. rubescens* based on the number of specimens measured.

Table 2. Intraspecific ECD ranges and their average values (in μm) per basin analyzed. nd: not determined.

Species	ECD Range		Average ECD	
	Adriatic Sea	Ionian Sea	Adriatic Sea	Ionian Sea
<i>Globigerinoides ruber</i> s.s.	125–419	130–377	229	223
<i>Globigerinoides ruber</i> s.l.	162–417	157–469	308	269
<i>Globigerinoides ruber rosea</i>	135–574	126–579	344	302
<i>Trilobatus trilobus</i>	129–561	127–569	273	284
<i>Globigerinella siphonifera</i>	125–544	125–689	273	306
<i>Globigerina bulloides</i>	135–414	126–364	227	217
<i>Neogloboquadrina pachyderma</i>	130–392	127–400	213	234
<i>Globorotalia inflata</i>	162–551	171–612	303	357
<i>Globorotalia truncatulinoides</i>	nd	153–818	nd	435
<i>Globigerina rubescens</i>	130–207	128–259	169	191
<i>Orbulina universa</i>	153–814	174–905	414	496
<i>Turborotalita quinqueloba</i>	126–199	127–252	166	175
<i>Globigerinita glutinata</i>	126–211	125–315	165	197

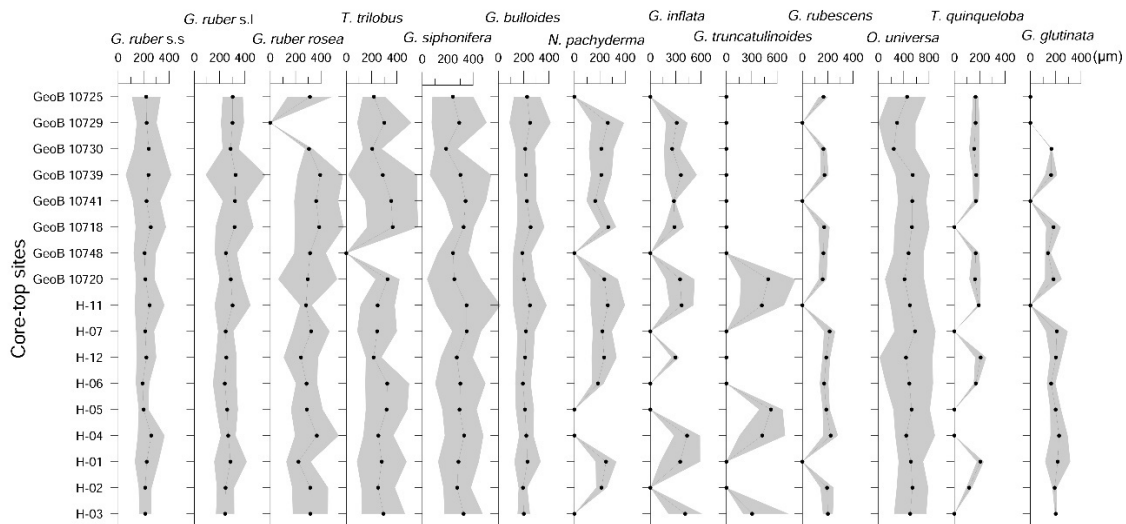


Figure 3. Average population size of the planktonic foraminifera species identified together with their overall population size. The gray shaded areas denote one standard deviation. The labels in the vertical axis are representative of the core-top locations presented in Table 1.

Orbulina universa population is the largest one in both study basins, even more than *G. truncatulinoides* and *G. inflata* which are followed (Table 2). Spherical shells of *O. universa* reflected by their ultimate chamber that covers all the previous ones of the pre-adult trochospiral stages seem to be very voluminous in the Ionian as well as in Adriatic basins. Our results from the central Mediterranean show an inverse correlation between shell size and latitudinal occurrence since their average shell diameters increase from the Adriatic (414 μm) to the Ionian Sea (496 μm). A closer view of the central Mediterranean dataset, regarding this species, indicates an intra-basin latitudinal relationship to the shell size, with the smallest specimens (avg. = 414 μm) occurring in the south Adriatic basin, intermediate values (avg. = 491 μm) are recorded in the north Ionian sub-basin and the largest specimens (avg. = 503 μm) are found in the south Ionian sub-basin. Next in size is *G. ruber rosea*, which is significantly larger than the white variety of the same species, similar to what was found in the Aegean and Levantine sub-basins [24].

The oligotrophic, symbiont-bearing species *T. trilobus* and *G. siphonifera* present similar shell sizes, indicating that they thrive in the same water masses constrained mostly by the same productivity regime of the surface waters. Within *G. ruber* (w) morphospace, the

sensu lato appears larger (by ~20%) than the sensu stricto populations. This seems reliable since the former includes the mixing of Platys and Elongate specimens (morphotypes B and C of Kontakiotis et al. [21]). *Neogloboquadrina pachyderma* and *G. bulloides* present quite similar intermediate-sized average values of about 220–230 μm , probably correlating with the same levels of primary productivity of the sub-surface waters. Finally, the species *T. quinqueloba*, *G. glutinata* and *G. rubescens* are the smallest ones recording ECD values less than 200 μm . Although the two first species are known from the literature as small-sized foraminifera, our results show that *G. rubescens* can also be added to this group confirming the previous observations of Al-Sabouni et al. [82] and Zarkogiannis et al. [24] from the Atlantic Ocean and the eastern Mediterranean Sea regarding its small size.

5. Discussion

5.1. Ecological and Oceanographic Context of the Planktonic Foraminiferal Biogeographic Distribution in Adriatic and Ionian Basins

Changes in oceanographic parameters could lead to a geographic offset among modern planktonic associations that may lead to differential abundance patterns and/or shell mass variability towards the optimum growth conditions, modifying the size spectrum of the entire population [20,21,24,49,89,107]. Therefore, the assessment of the dominant environmental parameters controlling the planktonic foraminiferal communities within the Mediterranean Sea, such as SST, SSS, and PP [8,28,89,108,109], along with their correlation with the ecological characteristics of the identified species are crucial for explaining the offsets mentioned above.

Although the Adriatic and the Ionian sub-basins are quite similar from the faunistic point of view, some differences seem to exist regarding the abundance of the most significant species. Both sub-basins are dominated by *G. bulloides* and *G. ruber* (w), which exhibit an antagonistic faunal pattern. The maximum abundance peaks of *G. ruber* (s.s. and s.l.) are coincident with minimum relative peaks of *G. bulloides* in the Ionian basin, while the opposite trend is recorded for the Adriatic Sea (Figure 3), indicating the partly replacement between these species in the planktonic fauna. The high percentages of the opportunistic species *G. bulloides* are controlled by phyto- and zoo-plankton blooms [22] mainly attributed to the fertilizing effect to the Po River discharge waters and additional local eastern Italian freshwater inputs in the south Adriatic Sea. On the contrary, relative abundance of this species gradually decreases within the Ionian Sea, where the plume waters lose their characteristic features when mixed with other south-eastern Mediterranean surface waters. *Globigerinoides ruber* is evenly abundant by showing a continuous presence throughout the study transect, due to its ability to withstand large fluctuations in temperature and salinity of the water column [22,110]. Its slightly higher contribution (including both morphotypes) in the Ionian basin (Figure 3) could be attributed to more favorable (compared to those of the Adriatic Sea) conditions for its flourishing in the more oligotrophic water column. We highlight that such growth optimum conditions based on depth habitat preference and environmental parameters would certainly help to explain the observed regionally variable abundance patterns of the analyzed morphotypes.

The observed dominance of the normal morphotype in central Mediterranean sub-basins possibly is due to its depth and ecological characteristics. *G. ruber* s.s. has a very constant depth habitat (top 30–50 m; [99,111,112]) and prefers a temperature- and salinity-stratified environment [113], which in the study area is attained by the halocline due to riverine inputs and/or the seasonal thermocline due to surface warming during late spring to early fall. The less abundant *G. ruber* s.l. reaches its highest percentages in sample GeoB 10,718 south of the strait of Otranto and at sites H02, H03, and H-05 in the central-eastern part of the Ionian basin, where recurrent or transient small-scale cyclonic and anticyclonic gyres are formed and enhance the primary productivity (eastern Ionian bloom of D’Ortenzio, et al. [114]), which primarily controls its distribution [21,100]. The intermittent nature of these localized blooms (known as “intermittently blooming areas” of D’Ortenzio and Ribera d’Alcalà [115]) due to their pronounced interannual variability in the spatial shape and timing [114], in combination with the seasonal control of primary

production trapped at the subsurface Deep Chlorophyll Maximum (DCM) layer [116], which is estimated to be at times even more important than surface production in such oligotrophic setting [117], could be considered the most plausible explanations for their slight record in the satellite-sensed Chl-a data in the study area [114,115]. Moreover, satellite data provide no information on subsurface production, which is known to be important in the eastern part of the Mediterranean and does not always match the timing of surface Chl-a peaks [118] (Figure 4).

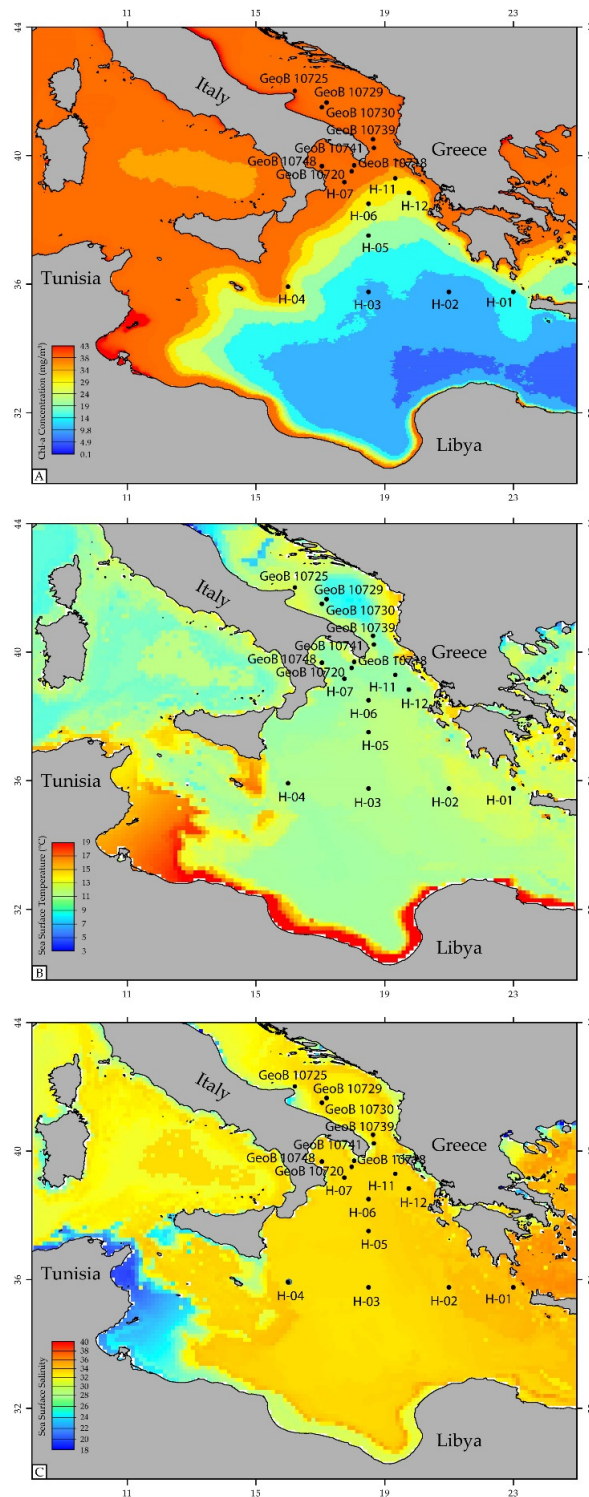


Figure 4. (A) Chlorophyll-a (Chl-a), (B) sea surface temperature (SST), and (C) sea surface salinity (SSS) distribution map for the study area.

However, the additional factors of heterogeneous bathymetry and distance from the coast could not be omitted as they have a large influence on the distributional abundance pattern of this morphotype, as have already been indicated for the Adriatic [85] and the Aegean Sea [21]. Given the above factors, the observed distributional pattern of *G. ruber* s.l. could be correlated with a relevant trend to deeper habitats at these sites. As the nutrient content decreases offshore [77,119], this regime causes unfavorable conditions for this species, reflected by even more reduced percentages of the most productivity-sensitive morphotype Elongate (belonging to *G. ruber* s.l.). Consequently, the representatives of *G. ruber* s.l. are adapted to a different depth habitat, possibly beneath the halocline or deeper in the mixed layer to avoid the highly stratified and oligotrophic surface waters.

Besides the two abundant aforementioned species, most of the species that live in the central Mediterranean are surface/sub-surface symbiont bearing species (e.g., *G. ruber rosea*, *G. rubescens*, *O. universa*, *G. siphonifera*, *T. trilobus*) each one displaying percentages up to ~10%, while important components in some places are also the productivity- and stratification-related indicators, such as *N. pachyderma*, *G. inflata*, *T. quinqueloba*, and *G. glutinata* [1,120]. The significant cumulative percentage (up to 30%) of symbiont-bearing species seems to reflect the ability of this group to cope with the oligotrophy of the study area. Particularly, *G. ruber rosea* and *G. rubescens* thrive in a warmer and overall, more oligotrophic and stratified water column [28,103,121], and *T. trilobus* dwells in warm, oligotrophic to mesotrophic waters but prefers less salty superficial waters [95,122]. *Orbulina universa* is usually abundant in (sub)tropical to temperate waters and tolerates a wide range of salinity and temperature [47,95]. Its increased percentages in the Adriatic and Ionian sites could be interpreted as an increase in depth and possibly the extent of the thermocline. In only some locations (e.g., samples H-11, GeoB 10729), these species are replaced by asymbionts (e.g., *T. quinqueloba*, *G. bulloides*) and some deeper dwellers, mostly by *N. pachyderma* and *G. inflata*, that are associated with deep winter mixing and generally more productive environments [22,95,123]. The relatively low percentages of *G. inflata* and its general displacement from the Ionian to the Adriatic basin could be explained by the fact that this species is less frequent or absent in warmer, stratified, and nutrient-depleted regions of the Mediterranean than in more productive areas (e.g., western Mediterranean; [22,109]). The same applies to *T. quinqueloba*, which maintains a residual presence in the study area, since its ecological preferences are mostly linked to cold and very productive surface waters [103,124]. The cosmopolitan species *G. glutinata* comprises significant percentages up to ~10% of the assemblage composition since it is able to survive both in oligotrophic and mesotrophic environments [125] due to its dual behavior related to diet requirements, being thus very sensitive to changes in productivity [42,126], while it is not dependent on temperature, salinity or depth [1]. Its presence in the Mediterranean Sea has been attributed to the spring bloom, triggered by the increased nutrients at the end of the winter mixing and increased solar irradiation [22,127].

5.2. On the Environmental Component on the Latitudinal Size Variability

The average maximum diameter (282 μm) of the central Mediterranean (excluding the Tyrrhenian Sea) assemblages is comparable with that of the eastern Mediterranean (279 μm ; [24]), but slightly lower than that reported for subtropical assemblages on a global scale (309 μm ; [37]). The ~8% offset in planktonic size could be considered reliable due to the more oligotrophic nature of higher water density in the marginal Mediterranean Sea compared to the global open ocean. Although tolerance limits of modern foraminifera are not completely defined, the progressive increase in test size is initially believed to be related to ecological optimum conditions [37,128–130]. Nevertheless, we note that the majority (apart from Schmidt et al. [37] who analyzed 69 Holocene samples worldwide) of the studies supports the optimum-size hypothesis focused on sediment samples collected within a single oceanic basin [31,131–135], reflecting a limited part of the biogeographical range of each species.

Most shell-mass-related studies have shown that the planktonic foraminiferal shell size increase with seawater temperature (e.g., [38]). In the case of the central Mediterranean basin, the increase in sea surface temperature from the Adriatic to the southernmost Ionian sites (Figure 4) could partly explain the average 11% increase observed in most of the species. However, this trend does not exist for the most dominant species, since both *G. bulloides* and *G. ruber* (w; s.s. and s.l.) present larger tests at higher latitudes. The decreasing trend with latitude of these two species is quite similar to that (~10% decrease towards the Levantine basin) reported by Zarkogiannis et al. [24] for the eastern sector of the Mediterranean Sea, indicating the latitudinal influence on these species within the entire Mediterranean Sea. This finding is also supplemented by the recent observations of Mallo et al. [81] showing a W-E difference in size of the same species (more extreme in *G. ruber* than *G. bulloides*, as similarly observed in our N-S transect), with the western basin hosting the largest individuals, while the gradual decrease in shell size occurs in the Tyrrhenian, eastern Ionian and finally in Levantine basin. Both latitudinal and longitudinal trends clearly reveal that the most abundant and paleoceanographically significant species for the Mediterranean Sea are possibly driven by environmental forces, beyond the SST, in terms of the specific hydrographic dynamics of each sub-basin within the Mediterranean Sea. Our findings are consistent with the observations of Rillo et al. [136] highlighting that SST does not always explain shell size variations, and further show that contrasting results can be obtained when analyzing intra-specific size patterns, even in a narrower geographical range as that one adopted here. Furthermore, given the species-specific size variability presented for the first time here, this study could be considered as a pioneer since it fills the gap characterized by the lack of studies testing the intraspecific consistency of the optimum-size hypothesis.

Nutrient availability can mediate the temperature-size relationships observed in the plankton communities and has been shown to affect planktonic foraminifera size [136,137]. More explicitly, enhanced food availability in the water column facilitates faster cell growth and larger final shell size [138,139]. On a global scale, surface primary productivity is strongly correlated with plankton size. Below the value of $150 \text{ g C m}^{-2} \text{ yr}^{-1}$ there is a positive relationship, while above this threshold the cell size decreases with increasing primary productivity [37]. Within the low-productivity ecosystem of the Mediterranean Sea ($<150 \text{ g C m}^{-2} \text{ yr}^{-1}$; [140]) it would be expected shell size to be increased with productivity. According to the current and the already known from the literature's Mediterranean dataset, the above size-productivity relationship is evident for several species, mostly the symbiont-barren taxa, and is more pronounced in a longitudinal way. For instance, *O. universa* presents larger size fractions in the eutrophic upwelling areas from the Atlantic to the Strait of Sicily [89], relatively intermediate-sized shells in mesotrophic-to-oligotrophic Adriatic and Ionian basins (this study) and lowermost sizes into the ultra-oligotrophic eastern Mediterranean basin [24]. Into the general oligotrophic Adriatic and Ionian settings, *G. ruber* and other photosymbiotic species seem to have an advantage due to their symbionts which they use as an ecological strategy to survive in nutrient-limited environments [141]. The relatively stable shell sizes reported between Adriatic and Ionian domains of the most abundant species *G. ruber* s.s. (229 vs. 223 μm ; Table 2) and *G. bulloides* (227 vs. 217 μm ; Table 2) clearly support this concept. Moreover, the fact that these species were developed almost equally in size, presenting size structure values around roughly 220 μm , indicates that they possibly reach the optimum environmental conditions for the study area. The less abundant species (e.g., *G. ruber* s.l., *G. ruber rosea*, and *G. rubescens*), which are usually influenced by the competition with more abundant co-occurring species, present significant size variability and thereby reach their highest shell sizes in sub-optimal conditions. The comparison between the average intraspecific shell sizes for the central and the eastern basins (Table 3) points toward which species reaches the optimum or sub-optimum conditions and in which basin exactly within the Mediterranean setting. We nonetheless note that an additional N-S transect in the western Mediterranean, where the

eutrophic species dominate, is needed to complete full geographic coverage of the shell differentiation into the entire Mediterranean Sea.

Table 3. Average population size of the identified planktonic foraminifera species within the Central Mediterranean (this study) and comparison with the Eastern Mediterranean basin [24]. The number of sampling locations that each species was encountered is also shown together with the total number of specimens counted. nd: not determined.

Species	ECD (μm)		St. Dev. (%)	No of Sites	No of Specimens
	Central Mediterranean	Eastern Mediterranean			
<i>Globigerinoides ruber</i> s.s.	224	218	8	17	897
<i>Globigerinoides ruber</i> s.l.	279	259	11	17	592
<i>Globigerinoides ruber rosea</i>	313	338	15	16	192
<i>Trilobatus trilobus</i>	280	315	18	16	122
<i>Globigerinella siphonifera</i>	292	305	15	17	260
<i>Globigerina bulloides</i>	218	207	9	17	1463
<i>Neogloboquadrina pachyderma</i>	227	220	14	12	211
<i>Globorotalia inflata</i>	337	266	17	11	90
<i>Globorotalia truncatulinoides</i>	435	nd	20	5	20
<i>Globigerina rubescens</i>	184	189	11	13	140
<i>Orbulina universa</i>	471	427	19	17	180
<i>Turborotalita quinqueloba</i>	171	192	14	12	79
<i>Globigerinita glutinata</i>	188	189	13	13	118

5.3. The Possible Role of a Hidden Biological Diversity in Mediterranean Assemblages

Numerous studies have shown that many planktonic foraminiferal species display multiple genotypes, which are genetically independent but morphologically similar [142–144]. These cryptic species may also have different geographical distributions exhibiting possible morphological gradients with latitude [145] or longitude [107], occupy different niches [142], and display different relationships between abundance, size patterns, and environmental parameters [146–148]. Among the identified species, variable relationships have been discovered between their cryptic species and depth-, and/or environmental (SST, stratification, productivity)-related specializations whose abundance, shell size, and porosity vary with latitude. For instance, the size-abundance-environmental relationship has been documented for species with cryptic diversity, namely *O. universa* [131,146,149–151], *G. inflata* [152], *G. ruber* [144,146,153], *G. siphonifera* [148,154,155], *G. truncatulinoides* [156,157], *G. bulloides* [144,146,158,159] and *N. pachyderma* [160–164]. For most of them, both spinose and non-spinose species, it is premature to invoke cryptic diversity and ecophenotypy relationships due to the lack of large-scale inter-basin analysis within the Mediterranean Sea. However, some of them, especially those presenting the greatest variability in shell size ranges (*G. truncatulinoides*, *G. inflata*, and *O. universa*) could constitute good candidates for better explaining the observed geographic differentiation in the study area. Therefore, we interpret the documented latitudinal divergent trends among the fauna as the consequence of a hidden biological diversity with different mean sizes within these taxa, adapted to particular hydrographic conditions. We further note that there may be additional undiscovered genotypes in different lineages, especially in small and neglected species [165], possibly due to their relatively low number of specimens that have been surveyed so far.

5.4. Potential Depth Preferred Regulating Mechanism

We did not find any relationship between population shell size and abundance, caution thus against the concept of intraspecific size variation in parallel with population abundances, in accordance with previous studies [38,166]. In the present study, species richness which previously has been positively correlated with assemblage size [37] is found constant along our transect, indicating that the population size variation cannot be explained by assemblage changes. The relatively constant number of 13 species identified in the majority of the studied core-top samples is by ~40% lower than that of the low productivity oceanic gyre centers (>20 species; [167–169]), but similar to that of the marginal seas [22,89,170]. The slightly higher number in species richness reported here, compared to the number of 10 that characterizes the ultra-oligotrophic regions (e.g., Levantine Sea [20], Red Sea [171]), results mainly from the presence of cold- and deep-water dwellers that are associated with enhanced seasonal primary productivity [109,172]. The mechanism that could explain the expected ecological optimum pattern of simultaneous large sizes and high abundances involves higher feeding frequency (higher nutrient availability) leading to higher individual growth and finally to higher population growth [130]. However, it also implies that populations in different productive regimes have different generation times, with the more generations at optimum conditions to lead in higher abundance in the sediment, but relative to other populations of the same species, and not relative to the local assemblage [136]. In the local basin-wide abundance, nutrient availability is the same for all co-occurring species. Both satellite and in situ productivity data measured across the central Mediterranean reveal an increasing N-S oligotrophy gradient, mainly due to the limiting Chl-a concentrations from the Adriatic to Ionian Sea [115]. As would be expected, it is not followed by a relevant decrease in abundance for several species (e.g., *G. ruber*, *G. siphonifera*, *G. glutinata*), which means that the above mechanism cannot be applied here, since the primary production pattern of the region cannot explain sufficiently the observed decrease in mean foraminiferal size with latitude for the most abundant species either the opposite trend for the rest of the species in accordance also with their abundances. To understand the observed trends, we need to consider the effects of vertical instability on planktonic assemblages. The mesotrophic to oligotrophic character of the central Mediterranean basin is reflected by surface-dwelling oligotrophic and deeper eutrophic faunas, both of which are growing outside their ecologically optimum ranges (eastern and western Mediterranean respectively). In this setting, the overall assemblage is thus characterized by many species with almost overlapping shell sizes (Table 2). The species with a constant depth habitat such as *G. ruber* s.s., *T. quinqueloba*, and *T. trilobus* obviously are within optimal conditions and therefore present the lowest size variability. On the contrary, the species presenting a more variable depth habitat (e.g., *G. bulloides*, *G. ruber* s.l., *O. universa*) in their attempt to find plentiful food should be adapted to greater depths, representing sub-optimal ecological conditions for their survival.

6. Conclusions

In the present work, we studied the abundance and size distribution of recent planktonic foraminiferal populations derived by 17 surface sediment samples spanning from the mesotrophic Adriatic to the oligotrophic Ionian Sea. The fauna consists of subtropical species, mostly symbiont-bearing spinose species indicative of the mesotrophic-to-oligotrophic nature of the study area. Even though the most abundant species *G. bulloides* and *G. ruber* (w) show an antagonistic distributional pattern, both present the opposite trend compared to the rest of the species with their average size decreasing with latitude. The recent fluctuations in the relative abundance along with morphospecies-specific shell size trends of the dominating species may reflect the current adjustment to ongoing sea surface warming and a decrease in primary productivity in certain depth levels along the N-S transect. Overall, our findings are consistent with previous studies, which suggest that sea surface temperature, depth habitat, and food availability are the main controlling factors for their latitudinal distributional differentiation in the central Mediterranean. Moreover, shell

size variation in planktonic foraminiferal species analyzed cannot be consistently predicted by the environment, with a hidden biological diversity with different mean sizes within these taxa to be possibly appeared, as an adaptation to ecological (sub)optimum conditions.

Author Contributions: Conceptualization, G.K., S.D.Z.; methodology, G.K., S.D.Z.; software, G.K., S.D.Z., E.E.; validation, G.K., S.D.Z., E.E.; formal analysis, G.K., S.D.Z., E.E.; investigation, G.K., S.D.Z., E.E., E.B., A.A.; resources, G.K.; data curation, G.K., S.D.Z., E.E., A.A.; writing—Original draft preparation, G.K.; writing—Review and editing, G.K., S.D.Z., E.E., E.B., A.A.; visualization, G.K., S.D.Z.; supervision, A.A.; project administration, G.K., A.A.; funding acquisition, G.K. All authors have read and agreed to the published version of the manuscript.

Funding: This research received no external funding.

Institutional Review Board Statement: Not applicable.

Informed Consent Statement: Not applicable.

Data Availability Statement: Data that support the findings of this study are available from the corresponding author upon reasonable request.

Acknowledgments: The authors are grateful to Jurgen Möbius for providing part of the study material. The constructive and thorough reviews of two anonymous reviewers are warmly acknowledged.

Conflicts of Interest: The authors declare no conflict of interest.

References

1. Hemleben, C.; Anderson, O.R.; Spindler, M. *Modern Planktonic Foraminifera*; Springer: New York, NY, USA, 1989.
2. Tsiolakis, E.; Tsaila-Monopoli, S.; Kontakiotis, G.; Antonarakou, A.; Sprovieri, M.; Geraga, M.; Ferentinos, G.; Zissimos, A. Integrated paleohydrology reconstruction and Pliocene climate variability in Cyprus Island (eastern Mediterranean). *Iop Conf. Ser. Earth Environ. Sci.* **2019**, *362*, 012103. [\[CrossRef\]](#)
3. Antonarakou, A.; Kontakiotis, G.; Karageorgis, A.P.; Besiou, E.; Zarkogiannis, S.; Drinia, H.; Mortyn, G.P.; Tripsanas, E. Eco-biostratigraphic advances on late Quaternary geochronology and palaeoclimate: The marginal Gulf of Mexico analogue. *Geol. Q.* **2019**, *63*, 178–191. [\[CrossRef\]](#)
4. Budillon, F.; Lirer, F.; Iorio, M.; Macrì, P.; Sagnotti, L.; Vallefucio, M.; Ferraro, L.; Garziglia, S.; Innangi, S.; Sahabi, M.; et al. Integrated stratigraphic reconstruction for the last 80 kyr in a deep sector of the Sardinia Channel (Western Mediterranean). *Deep Sea Res. II* **2009**, *56*, 725–737. [\[CrossRef\]](#)
5. Drinia, H.; Antonarakou, A.; Tsourou, T.; Kontakiotis, G.; Psychogiou, M.; Anastasakis, G. Foraminifera eco-biostratigraphy of the southern Evoikos outer shelf, central Aegean Sea, during MIS 5 to present. *Cont. Shelf Res.* **2016**, *126*, 36–49. [\[CrossRef\]](#)
6. Lirer, F.; Luca, M.; Iaccarino, S.; Gianfranco, S.; Turco, E.; Claudia, C.; Sierro, F.; Caruso, A. Mediterranean Neogene planktonic foraminifer biozonation and biochronology. *Earth-Sci. Rev.* **2019**, *196*. [\[CrossRef\]](#)
7. Triantaphyllou, M.V.; Antonarakou, A.; Kouli, K.; Dimiza, M.; Kontakiotis, G.; Papanikolaou, M.D.; Ziveri, P.; Mortyn, P.G.; Lianou, V.; Lykousis, V.; et al. Late Glacial–Holocene ecostratigraphy of the south-eastern Aegean Sea, based on plankton and pollen assemblages. *Geo-Mar. Lett.* **2009**, *29*, 249–267. [\[CrossRef\]](#)
8. Giamali, C.; Kontakiotis, G.; Koskeridou, E.; Ioakim, C.; Antonarakou, A. Key Environmental Factors Controlling Planktonic Foraminiferal and Pteropod Community’s Response to Late Quaternary Hydroclimate Changes in the South Aegean Sea (Eastern Mediterranean). *J. Mar. Sci. Eng.* **2020**, *8*, 709. [\[CrossRef\]](#)
9. Giamali, C.; Koskeridou, E.; Antonarakou, A.; Kontakiotis, G.; Ioakim, C.; Karageorgis, A.; Roussakis, G.; Karakitsios, V. Multiproxy marine ecosystem response of abrupt Holocene climatic changes in the northeastern Mediterranean sedimentary archive. *Quat. Res.* **2019**, *92*, 665–685. [\[CrossRef\]](#)
10. Kontakiotis, G.; Besiou, E.; Antonarakou, A.; Zarkogiannis, S.D.; Kostis, A.; Mortyn, P.G.; Moissette, P.; Cornée, J.J.; Schulbert, C.; Drinia, H.; et al. Decoding sea surface and paleoclimate conditions in the eastern Mediterranean over the Tortonian-Messinian Transition. *Palaeogeogr. Palaeoclimatol. Palaeoecol.* **2019**, *534*, 109312. [\[CrossRef\]](#)
11. Kontakiotis, G.; Karakitsios, V.; Mortyn, P.G.; Antonarakou, A.; Drinia, H.; Anastasakis, G.; Agiadi, K.; Kafousia, N.; De Rafelis, M. New insights into the early Pliocene hydrographic dynamics and their relationship to the climatic evolution of the Mediterranean Sea. *Palaeogeogr. Palaeoclimatol. Palaeoecol.* **2016**, *459*, 348–364. [\[CrossRef\]](#)
12. Le Houedec, S.; Mojtahid, M.; Bicchi, E.; de Lange, G.J.; Hennekam, R. Suborbital Hydrological Variability Inferred From Coupled Benthic and Planktic Foraminiferal-Based Proxies in the Southeastern Mediterranean During the Last 19 ka. *Paleoceanogr. Paleoclimatol.* **2020**, *35*, e2019PA003827. [\[CrossRef\]](#)
13. Louvari, M.A.; Drinia, H.; Kontakiotis, G.; Di Bella, L.; Antonarakou, A.; Anastasakis, G. Impact of latest-glacial to Holocene sea-level oscillations on central Aegean shelf ecosystems: A benthic foraminiferal palaeoenvironmental assessment of South Evoikos Gulf, Greece. *J. Mar. Syst.* **2019**. [\[CrossRef\]](#)

14. Margaritelli, G.; Cacho, I.; Català, A.; Barra, M.; Bellucci, L.G.; Lubritto, C.; Rettori, R.; Lirer, F. Persistent warm Mediterranean surface waters during the Roman period. *Sci. Rep.* **2020**, *10*, 10431. [\[CrossRef\]](#)
15. Margaritelli, G.; Vallefucio, M.; Di Rita, F.; Capotondi, L.; Bellucci, L.G.; Insinga, D.D.; Petrosino, P.; Bonomo, S.; Cacho, I.; Cascella, A.; et al. Marine response to climate changes during the last five millennia in the central Mediterranean Sea. *Glob. Planet. Chang.* **2016**, *142*, 53–72. [\[CrossRef\]](#)
16. Quillévéré, F.; Nouailhat, N.; Joannin, S.; Cornée, J.-J.; Moissette, P.; Lécuyer, C.; Fourel, F.; Agiadi, K.; Koskeridou, E.; Escarguel, G. An onshore bathyal record of tectonics and climate cycles at the onset of the Early-Middle Pleistocene Transition in the eastern Mediterranean. *Quat. Sci. Rev.* **2019**, *209*, 23–39. [\[CrossRef\]](#)
17. Siani, G.; Paterne, M.; Colin, C. Late glacial to Holocene planktic foraminifera bioevents and climatic record in the South Adriatic Sea. *J. Quat. Sci.* **2010**, *25*, 808–821. [\[CrossRef\]](#)
18. Kontakiotis, G.; Mortyn, P.G.; Antonarakou, A.; Martínez-Botí, M.A.; Triantaphyllou, M.V. Field-based validation of a diagenetic effect on *G. ruber* Mg/Ca paleothermometry: Core top results from the Aegean Sea (eastern Mediterranean). *Geochem. Geophys. Geosyst.* **2011**, *12*, Q09004. [\[CrossRef\]](#)
19. Vasiliev, I.; Karakitsios, V.; Bouloubassi, I.; Agiadi, K.; Kontakiotis, G.; Antonarakou, A.; Triantaphyllou, M.; Gogou, A.; Kafousia, N.; de Rafélis, M.; et al. Large Sea Surface Temperature, Salinity, and Productivity-Preservation Changes Preceding the Onset of the Messinian Salinity Crisis in the Eastern Mediterranean Sea. *Paleoceanogr. Paleoclimatol.* **2019**, *34*, 182–202. [\[CrossRef\]](#)
20. Avnaim-Katav, S.; Herut, B.; Rahav, E.; Katz, T.; Weinstein, Y.; Alkalay, R.; Berman-Frank, I.; Zlatkin, O.; Almogi-Labin, A. Sediment trap and deep sea coretop sediments as tracers of recent changes in planktonic foraminifera assemblages in the southeastern ultra-oligotrophic Levantine Basin. *Deep Sea Res. Part II Top. Stud. Oceanogr.* **2020**, *171*, 104669. [\[CrossRef\]](#)
21. Kontakiotis, G.; Antonarakou, A.; Mortyn, P.G.; Drinia, H.; Anastasakis, G.; Zarkogiannis, S.; Möbius, J. Morphological recognition of *Globigerinoides ruber* morphotypes and their susceptibility to diagenetic alteration in the eastern Mediterranean Sea. *J. Mar. Syst.* **2017**, *174*, 12–24. [\[CrossRef\]](#)
22. Pujol, C.; Grazzini, C.V. Distribution patterns of live planktic foraminifera as related to regional hydrography and productive systems of the Mediterranean Sea. *Mar. Micropaleontol.* **1995**, *25*, 187–217. [\[CrossRef\]](#)
23. Wilson, B. Biogeography and ecostratigraphy of Late Quaternary planktonic foraminiferal taphocoenoses in the Leeward Islands, Lesser Antilles, NE Caribbean Sea. *Mar. Micropaleontol.* **2012**, *86–87*, 1–10. [\[CrossRef\]](#)
24. Zarkogiannis, S.; Kontakiotis, G.; Antonarakou, A. Recent planktonic foraminifera population and size response to Eastern Mediterranean hydrography. *Rev. Micropaleontol.* **2020**, *69*, 100450. [\[CrossRef\]](#)
25. Bé, A.W.H.; Tolderlund, D.S. Distribution and ecology of living planktonic foraminifera in surface waters of the Atlantic and Indian Oceans. In *The Micropaleontology of Oceans*; Funnel, B.M., Riedel, W.R., Eds.; Cambridge University Press: Cambridge, UK, 1971; pp. 105–149.
26. Kucera, M. Chapter Six Planktonic Foraminifera as Tracers of Past Oceanic Environments. In *Developments in Marine Geology*; Hillaire-Marcel, C., De Vernal, A., Eds.; Elsevier: Amsterdam, The Netherlands, 2007; Volume 1, pp. 213–262.
27. Imbrie, J.; Kipp, N. A new micropaleontological method for quantitative paleoclimatology: Application to a late pleistocene Caribbean core. In *The Late Cenozoic Glacial Ages*; Turekian, K.K., Ed.; Yale University Press: New Haven, CT, USA, 1971; pp. 71–181.
28. Kontakiotis, G. Late Quaternary paleoenvironmental reconstruction and paleoclimatic implications of the Aegean Sea (eastern Mediterranean) based on paleoceanographic indexes and stable isotopes. *Quat. Int.* **2016**, *401*, 28–42. [\[CrossRef\]](#)
29. Kucera, M.; Weinelt, M.; Kiefer, T.; Pflaumann, U.; Hayes, A.; Weinelt, M.; Chen, M.-T.; Mix, A.C.; Barrows, T.T.; Cortijo, E.; et al. Reconstruction of sea-surface temperatures from assemblages of planktonic foraminifera: Multi-technique approach based on geographically constrained calibration data sets and its application to glacial Atlantic and Pacific Oceans. *Quat. Sci. Rev.* **2005**, *24*, 951–998. [\[CrossRef\]](#)
30. Berger, W.H. Kummerform foraminifera as clues to Oceanic environments: Abstract. *Am. Assoc. Pet. Geol. Bull.* **1969**, *53*. [\[CrossRef\]](#)
31. Moller, T.; Schulz, H.; Kucera, M. The effect of sea surface properties on shell morphology and size of the planktonic foraminifer *Neogloboquadrina pachyderma* in the North Atlantic. *Palaeogeogr. Palaeoclimatol. Palaeoecol.* **2013**, *391*, 34–48. [\[CrossRef\]](#)
32. Morey, A.; Mix, A.; Pisias, N. Planktonic foraminiferal assemblages preserved in surface sediments correspond to multiple environment variables. *Quat. Sci. Rev.* **2005**, *24*, 925–950. [\[CrossRef\]](#)
33. Ortiz, J.D.; Mix, A.C.; Collier, R.W. Environmental control of living symbiotic and asymbiotic foraminifera of the California Current. *Paleoceanography* **1995**, *10*, 987–1009. [\[CrossRef\]](#)
34. Rebotim, A.; Voelker, A.H.L.; Jonkers, L.; Waniek, J.J.; Meggers, H.; Schiebel, R.; Fraile, I.; Schulz, M.; Kucera, M. Factors controlling the depth habitat of planktonic foraminifera in the subtropical eastern North Atlantic. *Biogeosci. Discuss.* **2016**, *2016*, 1–48. [\[CrossRef\]](#)
35. Renaud, S.; Schmidt, D. Habitat tracking as a response of the planktic foraminifer *Globorotalia truncatulinoides* to environmental fluctuations during the last 140 kyr. *Mar. Micropaleontol.* **2003**, *49*, 97–122. [\[CrossRef\]](#)
36. Schiebel, R.; Waniek, J.; Bork, M.; Hemleben, C. Planktic foraminiferal production stimulated by chlorophyll redistribution and entrainment of nutrients. *Deep Sea Res. Part I Oceanogr. Res. Pap.* **2001**, *48*, 721–740. [\[CrossRef\]](#)
37. Schmidt, D.N.; Renaud, S.; Bollmann, J.; Schiebel, R.; Thierstein, H.R. Size distribution of Holocene planktic foraminifer assemblages: Biogeography, ecology and adaptation. *Mar. Micropaleontol.* **2004**, *50*, 319–338. [\[CrossRef\]](#)

38. Weinkauf, M.F.G.; Kunze, J.G.; Waniek, J.J.; Kučera, M. Seasonal variation in shell calcification of planktonic foraminifera in the NE Atlantic reveals species-specific response to temperature, productivity, and optimum growth conditions. *PLoS ONE* **2016**, *11*, e0148363. [[CrossRef](#)] [[PubMed](#)]
39. Siokou-Frangou, I.; Bianchi, M.; Christaki, U.; Christou, E.D.; Giannakourou, A.; Gotsis, O.; Ignatiades, L.; Pagou, K.; Pitta, P.; Psarra, S.; et al. Carbon flow in the planktonic food web along a gradient of oligotrophy in the Aegean Sea (Mediterranean Sea). *J. Mar. Syst.* **2002**, *33–34*, 335–353. [[CrossRef](#)]
40. Siokou-Frangou, I.; Christaki, U.; Mazzocchi, M.G.; Montresor, M.; Ribera d'Alcalá, M.; Vaqué, D.; Zingone, A. Plankton in the open Mediterranean Sea: A review. *Biogeosciences* **2010**, *7*, 1543–1586. [[CrossRef](#)]
41. Wassmann, P.; Ypma, J.E.; Tselepidis, A. Vertical flux of faecal pellets and microplankton on the shelf of the oligotrophic Cretan Sea (NE Mediterranean Sea). *Prog. Oceanogr.* **2000**, *46*, 241–258. [[CrossRef](#)]
42. Schmuker, B.; Schiebel, R. Planktic foraminifers and hydrography of the eastern and northern Caribbean Sea. *Mar. Micropaleontol.* **2002**, *46*, 387–403. [[CrossRef](#)]
43. Lykousis, V.; Chronis, G.; Tselepidis, A.; Price, N.B.; Theocharis, A.; Siokou-Frangou, I.; Van Wambeke, F.; Danovaro, R.; Stavrakakis, S.; Duineveld, G.; et al. Major outputs of the recent multidisciplinary biogeochemical researches undertaken in the Aegean Sea. *J. Mar. Syst.* **2002**, *33–34*, 313–334. [[CrossRef](#)]
44. Schiebel, R. Planktic foraminiferal sedimentation and the marine calcite budget. *Glob. Biogeochem. Cycles* **2002**, *16*, 1065. [[CrossRef](#)]
45. Schiebel, R.; Hemleben, C. Modern planktic foraminifera. *Palaontol. Z.* **2005**, *79*, 135–148. [[CrossRef](#)]
46. Siccha, M.; Schiebel, R.; Schmidt, S.; Howa, H. Short-term and small-scale variability in planktic foraminifera test flux in the Bay of Biscay. *Deep Sea Res. Part I Oceanogr. Res. Pap.* **2012**, *64*, 146–156. [[CrossRef](#)]
47. Bijma, J.; Faber, W.W.; Hemleben, C. Temperature and salinity limits for growth and survival of some planktonic foraminifers in laboratory cultures. *J. Foraminifer. Res.* **1990**, *20*, 95–116. [[CrossRef](#)]
48. Arnold, A.J.; Parker, W.C. *Biogeography of Planktonic Foraminifera*; Springer: Dordrecht, The Netherlands; Boston, MA, USA; London, UK, 1999.
49. Zarkogiannis, S.; Kontakiotis, G.; Antonarakou, A.; Mortyn, P.; Drinia, H. Latitudinal Variation of Planktonic Foraminifera Shell Masses During Termination I. *Iop Conf. Ser. Earth Environ. Sci.* **2019**, *221*, 012052. [[CrossRef](#)]
50. Zarkogiannis, S.D.; Antonarakou, A.; Tripathi, A.; Kontakiotis, G.; Mortyn, P.G.; Drinia, H.; Greaves, M. Influence of surface ocean density on planktonic foraminifera calcification. *Sci. Rep.* **2019**, *9*, 533. [[CrossRef](#)]
51. Caromel, A.G.M.; Schmidt, D.N.; Phillips, J.C.; Rayfield, E.J. Hydrodynamic constraints on the evolution and ecology of planktic foraminifera. *Mar. Micropaleontol.* **2014**, *106*, 69–78. [[CrossRef](#)]
52. Caromel, A.G.M.; Schmidt, D.N.; Rayfield, E.J. Ontogenetic constraints on foraminiferal test construction. *Evol. Dev.* **2017**, *19*, 157–168. [[CrossRef](#)]
53. Zarkogiannis, S.; Kontakiotis, G.; Antonarakou, A. Logarithmic expression of *Globigerina bulloides* shell evolution through the biometric analysis: Paleoceanographic implications for the late Quaternary. *Iop Conf. Ser. Earth Environ. Sci.* **2019**, *362*, 012100. [[CrossRef](#)]
54. Robinson, A.R.; Golnaraghi, M. The Physical and Dynamical Oceanography of the Mediterranean Sea. In *Ocean Processes in Climate Dynamics: Global and Mediterranean Examples*; Malanotte-Rizzoli, P., Robinson, A.R., Eds.; Springer: Dordrecht, The Netherlands, 1994; pp. 255–306.
55. Cushman-Roisin, B.; Gacic, M.; Poulain, P.-M.; Artegiani, A. *Physical Oceanography of the Adriatic Sea: Past, Present and Future*; Springer: Dordrecht, The Netherlands, 2001.
56. Ricci, P.; Libralato, S.; Capezzuto, F.; D'Onghia, G.; Maiorano, P.; Sion, L.; Tursi, A.; Solidoro, C.; Carlucci, R. Ecosystem functioning of two marine food webs in the North-Western Ionian Sea (Central Mediterranean Sea). *Ecol. Evol.* **2019**, *9*, 10198–10212. [[CrossRef](#)]
57. Civitarese, G.; Gacic, M.; Lipizer, M.; Eusebi Borzelli, G.L. On the impact of the Bimodal Oscillating System (BiOS) on the biogeochemistry and biology of the Adriatic and Ionian Seas (Eastern Mediterranean). *Biogeosciences* **2010**, *7*, 3987–3997. [[CrossRef](#)]
58. Specchiulli, A.; Bignami, F.; Marini, M.; Fabbrocini, A.; Scirocco, T.; Campanelli, A.; Penna, P.; Santucci, A.; D'Adamo, R. The role of forcing agents on biogeochemical variability along the southwestern Adriatic coast: The Gulf of Manfredonia case study. *Estuar. Coast. Shelf Sci.* **2016**, *183*, 136–149. [[CrossRef](#)]
59. Béranger, K.; Mortier, L.; Crépon, M. Seasonal variability of water transport through the Straits of Gibraltar, Sicily and Corsica, derived from a high-resolution model of the Mediterranean circulation. *Prog. Oceanogr.* **2005**, *66*, 341–364. [[CrossRef](#)]
60. Pinardi, N.; Masetti, E. Variability of the large scale general circulation of the Mediterranean Sea from observations and modelling: A review. *Palaeogeogr. Palaeoclimatol. Palaeoecol.* **2000**, *158*, 153–173. [[CrossRef](#)]
61. Robinson, A.R.; Sellschopp, J.; Warn-Varnas, A.; Leslie, W.G.; Lozano, C.J.; Haley, P.J.; Anderson, L.A.; Lermusiaux, P.F.J. The Atlantic Ionian Stream. *J. Mar. Syst.* **1999**, *20*, 129–156. [[CrossRef](#)]
62. Bonanno, A.; Placenti, F.; Basilone, G.; Mifsud, R.; Genovese, S.; Patti, B.; Di Bitetto, M.; Aronica, S.; Barra, M.; Giacalone, G.; et al. Variability of water mass properties in the Strait of Sicily in summer period of 1998–2013. *Ocean Sci. Discuss.* **2014**, *11*. [[CrossRef](#)]
63. Sammari, C.; Millot, C.; Taupier-Letage, I.; Stefani, A.; Brahim, M. Hydrological characteristics in the Tunisia–Sardinia–Sicily area during spring 1995. *Deep Sea Res. Part I Oceanogr. Res. Pap.* **1999**, *46*, 1671–1703. [[CrossRef](#)]

64. Gačić, M.; Schroeder, K.; Civitarese, G.; Cosoli, S.; Vetrano, A.; Eusebi Borzelli, G.L. Salinity in the Sicily Channel corroborates the role of the Adriatic–Ionian Bimodal Oscillating System (BiOS) in shaping the decadal variability of the Mediterranean overturning circulation. *Ocean Sci.* **2013**, *9*, 83–90. [[CrossRef](#)]
65. Pinardi, N.; Zavatarelli, M.; Adani, M.; Coppini, G.; Fratianni, C.; Oddo, P.; Simoncelli, S.; Tonani, M.; Lyubartsev, V.; Dobricic, S.; et al. Mediterranean Sea large-scale low-frequency ocean variability and water mass formation rates from 1987 to 2007: A retrospective analysis. *Prog. Oceanogr.* **2015**, *132*, 318–332. [[CrossRef](#)]
66. Roether, W.; Manca, B.B.; Klein, B.; Bregant, D.; Georgopoulos, D.; Beitzel, V.; Kovačević, V.; Luchetta, A. Recent Changes in Eastern Mediterranean Deep Waters. *Science* **1996**, *271*, 333. [[CrossRef](#)]
67. Gasparini, G.P.; Ortona, A.; Budillon, G.; Astraldi, M.; Sansone, E. The effect of the Eastern Mediterranean Transient on the hydrographic characteristics in the Strait of Sicily and in the Tyrrhenian Sea. *Deep Sea Res. Part I Oceanogr. Res. Pap.* **2005**, *52*, 915–935. [[CrossRef](#)]
68. Marini, M.; Grilli, F.; Guarnieri, A.; Jones, B.; Klajic, Z.; Nadia, P.; Sanxhaku, M. Is the southeastern Adriatic Sea coastal strip an eutrophic area? *Estuar. Coast. Shelf Sci.* **2010**, 395–406. [[CrossRef](#)]
69. Artegiani, A.; Paschini, E.; Russo, A.; Bregant, D.; Raicich, F.; Pinardi, N. The Adriatic Sea General Circulation. Part II: Baroclinic Circulation Structure. *J. Phys. Oceanogr.* **1997**, *27*, 1515–1532. [[CrossRef](#)]
70. Marini, M.; Jones, B.H.; Campanelli, A.; Grilli, F.; Lee, C.M. Seasonal variability and Po River plume influence on biochemical properties along western Adriatic coast. *J. Geophys. Res. Ocean.* **2008**, 113. [[CrossRef](#)]
71. Orlic, M.; Dadić, V.; Grbec, B.; Leder, N.; Marki, A.; Matić, F.; Mihanovic, H.; Beg Paklar, G.; Pasaric, M.; Pasarić, Z.; et al. Wintertime buoyancy forcing, changing seawater properties, and two different circulation systems produced in the Adriatic. *J. Geophys. Res.* **2006**, 112. [[CrossRef](#)]
72. Giani, M.; Djakovac, T.; Degobbi, D.; Cozzi, S.; Solidoro, C.; Umani, S.F. Recent changes in the marine ecosystems of the northern Adriatic Sea. *Estuar. Coast. Shelf Sci.* **2012**, *115*, 1–13. [[CrossRef](#)]
73. Manca, B.; Budillon, G.; Scarazzato, P.; Ursella, L. Evolution of dynamics in the eastern Mediterranean affecting water mass structures and properties in the Ionian and Adriatic Seas. *J. Geophys. Res.* **2003**, 108. [[CrossRef](#)]
74. Degobbi, D.; Precali, R.; Ivančić, I.; Smodlaka, N.; Fuks, D.; Kveder, S. Long-term Changes in the northern Adriatic ecosystem related to anthropogenic eutrophication. *Int. J. Environ. Pollut.* **2000**, *13*, 495–533. [[CrossRef](#)]
75. Viličić, D.; Vučak, Z.; Škrivanić, A.; Grzetić, Z. Phytoplankton blooms in the oligotrophic open South Adriatic waters. *Mar. Chem.* **1989**, *28*, 89–107. [[CrossRef](#)]
76. Totti, C.; Civitarese, G.; Acri, F.; Barletta, D.; Candelari, G.; Paschini, E.; Solazzi, A. Seasonal variability of phytoplankton populations in the middle Adriatic sub-basin. *J. Plankton Res.* **2000**, *22*, 1735–1756. [[CrossRef](#)]
77. Zonneveld, K.; Chen, L.; Moebius, J.; Mahmoud, M. Environmental significance of dinoflagellate cysts from the proximal part of the Po-river discharge plume (off southern Italy, Eastern Mediterranean). *J. Sea Res.* **2009**, *62*, 189–213. [[CrossRef](#)]
78. Marasović, I.; Grbec, B.; Morović, M. Long-term production changes in the Adriatic. *Neth. J. Sea Res.* **1995**, *34*, 267–273. [[CrossRef](#)]
79. Vilibić, I.; Šantić, D. Deep water ventilation traced by *Synechococcus* cyanobacteria. *Ocean Dyn.* **2008**, *58*, 119–125. [[CrossRef](#)]
80. Vilibić, I.; Matijević, S.; Šepić, J.; Kušpilić, G. Changes in the Adriatic oceanographic properties induced by the Eastern Mediterranean Transient. *Biogeosciences* **2012**, *9*, 2085–2097. [[CrossRef](#)]
81. Palinkas, C.M.; Nittrouer, C.A. Clinoform sedimentation along the Apennine shelf, Adriatic Sea. *Mar. Geol.* **2006**, *234*, 245–260. [[CrossRef](#)]
82. Boudena, M. Sea Surface Temperature of the Central Mediterranean during the Last Millenium. Ph.D. Thesis, Università degli Studi di Torino, Turin, Italy, 2004; p. 64.
83. Frignani, M.; Langone, L.; Ravaioli, M.; Sorgente, D.; Alvisi, F.; Albertazzi, S. Fine-sediment mass balance in the western Adriatic continental shelf over a century time scale. *Mar. Geol.* **2005**, *222–223*, 113–133. [[CrossRef](#)]
84. Incarbona, A.; Ziveri, P.; Di Stefano, E.; Lirer, F.; Mortyn, G.; Patti, B.; Pelosi, N.; Sprovieri, M.; Tranchida, G.; Vallefucio, M.; et al. The Impact of the Little Ice Age on Coccolithophores in the Central Mediterranean Sea. *Clim. Past* **2010**, *6*, 795–805. [[CrossRef](#)]
85. Grauel, A.L.; Bernasconi, S.M. Core-top calibration of $\delta^{18}\text{O}$ and $\delta^{13}\text{C}$ of *G. ruber* (white) and *U. mediterranea* along the southern Adriatic coast of Italy. *Mar. Micropaleontol.* **2010**, *77*, 175–186. [[CrossRef](#)]
86. Thunell, R.C. Distribution of recent planktonic foraminifera in surface sediments of the Mediterranean Sea. *Mar. Micropaleontol.* **1978**, *3*, 147–173. [[CrossRef](#)]
87. Zarkogiannis, S.D.; Kontakiotis, G.; Gkaniatsa, G.; Kuppili, V.S.C.; Marathe, S.; Wanelik, K.; Lianou, V.; Besiou, E.; Makri, P.; Antonarakou, A. An Improved Cleaning Protocol for Foraminiferal Calcite from Unconsolidated Core Sediments: HyPerCal—A New Practice for Micropaleontological and Paleoclimatic Proxies. *J. Mar. Sci. Eng.* **2020**, *8*, 998. [[CrossRef](#)]
88. Incarbona, A.; Stefano, E.; Sprovieri, R.; Ferraro, S. The Uniqueness of Planktonic Ecosystems in the Mediterranean Sea: The Response to Orbital- and Suborbital-Climatic Forcing over the Last 130,000 Years. *Open Geosci.* **2016**, *8*. [[CrossRef](#)]
89. Mallo, M.; Ziveri, P.; Mortyn, P.G.; Schiebel, R.; Grelaud, M. Low planktic foraminiferal diversity and abundance observed in a spring 2013 west–east Mediterranean Sea plankton tow transect. *Biogeosciences* **2017**, *14*, 2245–2266. [[CrossRef](#)]
90. Al-Sabouni, N.; Kucera, M.; Schmidt, D.N. Vertical niche separation control of diversity and size disparity in planktonic foraminifera. *Mar. Micropaleontol.* **2007**, *63*, 75–90. [[CrossRef](#)]

91. Antonarakou, A.; Kontakiotis, G.; Zarkogiannis, S.; Mortyn, P.G.; Drinia, H.; Koskeridou, E.; Anastasakis, G. Planktonic foraminiferal abnormalities in coastal and open marine eastern Mediterranean environments: A natural stress monitoring approach in recent and early Holocene marine systems. *J. Mar. Syst.* **2018**, *181*, 63–78. [[CrossRef](#)]
92. Capotondi, L.; Erica, S.; Speranza, P.; Corselli, C. Late Quaternary planktonic foraminiferal distributions: Problems related to size fraction. In *Proceedings of the First Italian Meeting on Environmental Micropaleontology Edition*; Coccioni, R., Galeotti, S., Lirer, F., Eds.; Grzybowski Foundation Special Publication: Krakow, Poland, 2004; Volume 9, pp. 1–6.
93. Cisneros, M.; Cacho, I.; Frigola, J.; Canals, M.; Masqué, P.; Martrat, B.; Casado, M.; Grimalt, J.O.; Pena, L.D.; Margaritelli, G.; et al. Sea surface temperature variability in the central-western Mediterranean Sea during the last 2700 years: A multi-proxy and multi-record approach. *Clim. Past* **2016**, *12*, 849–869. [[CrossRef](#)]
94. Margaritelli, G.; Cisneros, M.; Cacho, I.; Capotondi, L.; Vallefucio, M.; Rettori, R.; Lirer, F. Climatic variability over the last 3000 years in the central- western Mediterranean Sea (Menorca Basin) detected by planktonic foraminifera and stable isotope records. *Glob. Planet. Chang.* **2018**, *169*, 179–187. [[CrossRef](#)]
95. Schiebel, R.; Hemleben, C. *Planktic Foraminifers in the Modern Ocean*; Springer: Berlin/Heidelberg, Germany, 2017; p. 358.
96. Aurahs, R.; Grimm, G.W.; Hemleben, V.; Hemleben, C.; Kucera, M. Geographical distribution of cryptic genetic types in the planktonic foraminifer *Globigerinoides ruber*. *Mol. Ecol.* **2009**, *18*, 1692–1706. [[CrossRef](#)]
97. Wang, L. Isotopic signals in two morphotypes of *Globigerinoides ruber* (white) from the South China Sea: Implications for monsoon climate change during the last glacial cycle. *Palaeogeogr. Palaeoclimatol. Palaeoecol.* **2000**, *161*, 381–394. [[CrossRef](#)]
98. Kuroyanagi, A.; Kawahata, H. Vertical distribution of living planktonic foraminifera in the seas around Japan. *Mar. Micropaleontol.* **2004**, *53*, 173–196. [[CrossRef](#)]
99. Antonarakou, A.; Kontakiotis, G.; Mortyn, P.G.; Drinia, H.; Sprovieri, M.; Besiou, E.; Tripsanas, E. Biotic and geochemical ($\delta^{18}\text{O}$, $\delta^{13}\text{C}$, Mg/Ca, Ba/Ca) responses of *Globigerinoides ruber* morphotypes to upper water column variations during the last deglaciation, Gulf of Mexico. *Geochim. Cosmochim. Acta* **2015**, *170*. [[CrossRef](#)]
100. Kuroyanagi, A.; Tsuchiya, M.; Kawahata, H.; Kitazato, H. The occurrence of two genotypes of the planktonic foraminifer *Globigerinoides ruber* (white) and paleo-environmental implications. *Mar. Micropaleontol.* **2008**, *68*, 236–243. [[CrossRef](#)]
101. Kontakiotis, G.; Antonarakou, A.; Zachariasse, W.J. Late Quaternary palaeoenvironmental changes in the Aegean Sea: Interrelations and interactions between North and South Aegean Sea. *Bull. Geol. Soc. Greece* **2013**, *47*, 167–177. [[CrossRef](#)]
102. Lirer, F.; Sprovieri, M.; Vallefucio, M.; Ferraro, L.; Pelosi, N.; Giordano, L.; Capotondi, L. Planktonic foraminifera as bio-indicators for monitoring the climatic changes that have occurred over the past 2000 years in the southeastern Tyrrhenian Sea. *Integr. Zool.* **2014**, *9*, 542–554. [[CrossRef](#)]
103. Rohling, E.J.; Jorissen, F.J.; Grazzini, C.V.; Zachariasse, W.J. Northern Levantine and Adriatic Quaternary planktic foraminifera; Reconstruction of paleoenvironmental gradients. *Mar. Micropaleontol.* **1993**, *21*, 191–218. [[CrossRef](#)]
104. Marshall, B.J.; Thunell, R.C.; Henehan, M.J.; Astor, Y.; Wejnert, K.E. Planktonic foraminiferal area density as a proxy for carbonate ion concentration: A calibration study using the Cariaco Basin ocean time series. *Paleoceanography* **2013**, *28*, 363–376. [[CrossRef](#)]
105. Kucera, M.; Kennett, J. Causes and consequences of a Middle Pleistocene origin of the modern planktonic foraminifer *Neoglobobulimina papyroderma* sinistral. *Geology* **2002**, *30*, 539–542. [[CrossRef](#)]
106. Schneider, A.; Wallace, D.W.R.; Körtzinger, A. Alkalinity of the Mediterranean Sea. *Geophys. Res. Lett.* **2007**, *34*, L15608. [[CrossRef](#)]
107. Ujiie, Y.; Asami, T.; de Garidel-Thoron, T.; Liu, H.; Ishitani, Y.; de Vargas, C. Longitudinal differentiation among pelagic populations in a planktic foraminifer. *Ecol. Evol.* **2012**, *2*, 1725–1737. [[CrossRef](#)]
108. Kontakiotis, G. Palaeoceanographic and Palaeoclimatic Study of Eastern Mediterranean During Late Quaternary, Based on Planktonic Foraminiferal Assemblages. Ph.D. Thesis, National and Kapodistrian University of Athens, Athens, Greece, 2012. (In Greek, with English extended abstract).
109. Rigual-Hernández, A.S.; Sierro, F.J.; Bárcena, M.A.; Flores, J.A.; Heussner, S. Seasonal and interannual changes of planktic foraminiferal fluxes in the Gulf of Lions (NW Mediterranean) and their implications for paleoceanographic studies: Two 12-year sediment trap records. *Deep Sea Res. Part I Oceanogr. Res. Pap.* **2012**, *66*, 26–40. [[CrossRef](#)]
110. Tolderlund, D.S.; Allan, W.H.B. Seasonal Distribution of Planktonic Foraminifera in the Western North Atlantic. *Micropaleontology* **1971**, *17*, 297–329. [[CrossRef](#)]
111. Numberger, L.; Hemleben, C.; Hoffmann, R.; Mackensen, A.; Schulz, H.; Wunderlich, J.-M.; Kucera, M. Habitats, abundance patterns and isotopic signals of morphotypes of the planktonic foraminifer *Globigerinoides ruber* (d’Orbigny) in the eastern Mediterranean Sea since the Marine Isotopic Stage 12. *Mar. Micropaleontol.* **2009**, *73*, 90–104. [[CrossRef](#)]
112. Richey, J.N.; Poore, R.Z.; Flower, B.P.; Hollander, D.J. Ecological controls on the shell geochemistry of pink and white *Globigerinoides ruber* in the northern Gulf of Mexico: Implications for paleoceanographic reconstruction. *Mar. Micropaleontol.* **2012**, *82–83*, 28–37. [[CrossRef](#)]
113. Wejnert, K.E.; Pride, C.J.; Thunell, R.C. The oxygen isotope composition of planktonic foraminifera from the Guaymas Basin, Gulf of California: Seasonal, annual, and interspecies variability. *Mar. Micropaleontol.* **2010**, *74*, 29–37. [[CrossRef](#)]
114. D’Ortenzio, F.; Ragni, M.; Marullo, S.; Ribera d’Alcalà, M. Did biological activity in the Ionian Sea change after the Eastern Mediterranean Transient? Results from the analysis of remote sensing observations. *J. Geophys. Res. Ocean.* **2003**, *108*. [[CrossRef](#)]
115. D’Ortenzio, F.; Ribera d’Alcalà, M. On the trophic regimes of the Mediterranean Sea: A satellite analysis. *Biogeosciences* **2009**, *6*, 139–148. [[CrossRef](#)]

116. Lavigne, H.; D’Ortenzio, F.; Ribera D’Alcalà, M.; Claustre, H.; Sauzède, R.; Gacic, M. On the vertical distribution of the chlorophyll a concentration in the Mediterranean Sea: A basin-scale and seasonal approach. *Biogeosciences* **2015**, *12*, 5021–5039. [\[CrossRef\]](#)
117. Gotsis-Skretas, O.; Pagou, K.; Moraitou-Apostolopoulou, M.; Ignatiades, L. Seasonal horizontal and vertical variability in primary production and standing stocks of phytoplankton and zooplankton in the Cretan Sea and the Straits of the Cretan Arc (March 1994–January 1995). *Prog. Oceanogr.* **1999**, *44*, 625–649. [\[CrossRef\]](#)
118. Malinverno, E.; Maffioli, P.; Corselli, C.; De Lange, G.J. Present-day fluxes of coccolithophores and diatoms in the pelagic Ionian Sea. *J. Mar. Syst.* **2014**, *132*, 13–27. [\[CrossRef\]](#)
119. Grilli, F.; Marini, M.; Book, J.W.; Campanelli, A.; Paschini, E.; Russo, A. Flux of nutrients between the middle and southern Adriatic Sea (Gargano-Split section). *Mar. Chem.* **2013**, *153*, 1–14. [\[CrossRef\]](#)
120. Takagi, H.; Kimoto, K.; Fujiki, T.; Saito, H.; Schmidt, C.; Kucera, M.; Moriya, K. Characterizing photosymbiosis in modern planktonic foraminifera. *Biogeosciences* **2019**, *16*, 3377–3396. [\[CrossRef\]](#)
121. Rohling, E.J.; Jorissen, F.J.; De Stigter, H.C. 200 Year interruption of Holocene sapropel formation in the Adriatic Sea. *J. Micropalaeontol.* **1997**, *16*, 97–108. [\[CrossRef\]](#)
122. Žarić, S.; Donner, B.; Fischer, G.; Mulitza, S.; Wefer, G. Sensitivity of planktic foraminifera to sea surface temperature and export production as derived from sediment trap data. *Mar. Micropaleontol.* **2005**, *55*, 75–105. [\[CrossRef\]](#)
123. Rohling, E.J.; Sprovieri, M.; Cane, T.; Casford, J.S.L.; Cooke, S.; Bouloubassi, I.; Emeis, K.C.; Schiebel, R.; Rogerson, M.; Hayes, A.; et al. Reconstructing past planktic foraminiferal habitats using stable isotope data: A case history for Mediterranean sapropel S5. *Mar. Micropaleontol.* **2004**, *50*, 89–123. [\[CrossRef\]](#)
124. Rasmussen, T.L.; Thomsen, E. Changes in planktic foraminiferal faunas, temperature and salinity in the Gulf Stream during the last 30,000 years: Influence of meltwater via the Mississippi River. *Quat. Sci. Rev.* **2012**, *33*, 42–54. [\[CrossRef\]](#)
125. Schiebel, R.; Hemleben, C. Interannual variability of planktic foraminiferal populations and test flux in the eastern North Atlantic Ocean (JGOFS). *Deep Sea Res. Part II Top. Stud. Oceanogr.* **2000**, *47*, 1809–1852. [\[CrossRef\]](#)
126. Machain, M.; Monreal-Gomez, M.; Arellano-Torres, E.; Merino-Ibarra, M.; Gonzalez-Chavez, G. Recent planktonic foraminiferal distribution patterns and their relation to hydrographic conditions of the Gulf of Tehuantepec, Mexican Pacific. *Mar. Micropaleontol.* **2008**, *66*, 103–119. [\[CrossRef\]](#)
127. Casford, J.S.L.; Rohling, E.J.; Abu-Zied, R.; Cooke, S.; Fontanier, C.; Leng, M.; Lykousis, V. Circulation changes and nutrient concentrations in the late Quaternary Aegean Sea: A nonsteady state concept for sapropel formation. *Paleoceanography* **2002**, *17*, 14-1–14-11. [\[CrossRef\]](#)
128. Hecht, A.D. Size variations in planktonic foraminifera: Implications for quantitative paleoclimatic analysis. *Science* **1976**, *192*, 1330–1332. [\[CrossRef\]](#)
129. Schmidt, D.N.; Lazarus, D.; Young, J.R.; Kucera, M. Biogeography and evolution of body size in marine plankton. *Earth-Sci. Rev.* **2006**, *78*, 239–266. [\[CrossRef\]](#)
130. Schmidt, D.N.; Thierstein, H.R.; Bollmann, J.; Schiebel, R. Abiotic forcing of plankton evolution in the Cenozoic. *Science* **2004**, *303*, 207–210. [\[CrossRef\]](#)
131. Bé, A.W.H.; Harrison, S.M.; Lott, L. *Orbulina universa* d’Orbigny in the Indian Ocean. *Micropaleontology* **1973**, *19*, 150–192. [\[CrossRef\]](#)
132. Hecht, A.D. An ecologic model for test size variation in recent planktonic foraminifera: Applications to the fossil record. *J. Foraminifer. Res.* **1976**, *6*, 295–311. [\[CrossRef\]](#)
133. Kennett, J.P. Phenotypic variation in some recent and late Cenozoic planktonic foraminifera. In *Foraminifera*; Hedley, R.H., Adams, C.G., Eds.; Academic Press: New York, NY, USA, 1976; Volume 2, pp. 111–170.
134. Malmgren, B.A.; Kennett, J.P. Size variations in *Globigerina bulloides* d’Orbigny as a Quaternary paleoclimatic index in the Southern Ocean. *Antarct. J.* **1976**, 177–178.
135. Malmgren, B.A.; Kennett, J.P. Biometric differentiation between recent *Globigerina bulloides* and *Globigerina falconensis* in the southern Indian Ocean. *J. Foraminifer. Res.* **1977**, *7*, 130–148. [\[CrossRef\]](#)
136. Rillo, M.C.; Miller, C.G.; Kučera, M.; Ezard, T.H.G. Predictability of intraspecific size variation in extant planktonic foraminifera. *bioRxiv* **2018**, 468165. [\[CrossRef\]](#)
137. Peter, K.; Sommer, U. Phytoplankton Cell Size Reduction in Response to Warming Mediated by Nutrient Limitation. *PLoS ONE* **2013**, *8*, e71528. [\[CrossRef\]](#)
138. Bé, A.W.H.; Caron, D.A.; Anderson, O.R. Effects of feeding frequency on life processes of the planktonic foraminifer *Globigerinoides sacculifer* in laboratory culture. *J. Mar. Biol. Assoc. UK* **1981**, *61*, 257–277. [\[CrossRef\]](#)
139. Takagi, H.; Kimoto, K.; Fujiki, T.; Moriya, K. Effect of nutritional condition on photosymbiotic consortium of cultured *Globigerinoides sacculifer* (Rhizaria, Foraminifera). *Symbiosis* **2018**, *76*, 25–39. [\[CrossRef\]](#)
140. Stambler, N. The Mediterranean Sea—Primary Productivity. In *The Mediterranean Sea: Its History and Present Challenges*; Goffredo, S., Dubinsky, Z., Eds.; Springer: Dordrecht, The Netherlands, 2014; pp. 113–121.
141. Bé, A.W.H.; Hutson, W.H. Ecology of Planktonic Foraminifera and Biogeographic Patterns of Life and Fossil Assemblages in the Indian Ocean. *Micropaleontology* **1977**, *23*, 369. [\[CrossRef\]](#)
142. Darling, K.F.; Wade, C.M. The genetic diversity of planktic foraminifera and the global distribution of ribosomal RNA genotypes. *Mar. Micropaleontol.* **2008**, *67*, 216–238. [\[CrossRef\]](#)

143. de Vargas, C.; Zaninetti, L.; Hilbrecht, H.; Pawlowski, J. Phylogeny and rates of molecular evolution of planktonic Foraminifera: SSU rDNA sequences compared to the fossil record. *J. Mol. Evol.* **1997**, *45*, 285–294. [[CrossRef](#)]
144. Kucera, M.; Darling, K.F. Cryptic species of planktonic foraminifera: Their effect on palaeoceanographic reconstructions. *Philos. Trans. Ser. A Math. Phys. Eng. Sci.* **2002**, *360*, 695–718. [[CrossRef](#)] [[PubMed](#)]
145. Parker, F.L. Planktonic Foraminiferal Species in Pacific Sediments. *Micropaleontology* **1962**, *8*, 219–254. [[CrossRef](#)]
146. Darling, K.F.; Wade, C.M.; Kroon, D.; Brown, A.J.L.; Bijma, J. The Diversity and Distribution of Modern Planktic Foraminiferal Small Subunit Ribosomal RNA Genotypes and their Potential as Tracers of Present and Past Ocean Circulations. *Paleoceanography* **1999**, *14*, 3–12. [[CrossRef](#)]
147. de Vargas, C.; Bonzon, M.; Rees, N.W.; Pawlowski, J.; Zaninetti, L. A molecular approach to biodiversity and biogeography in the planktonic foraminifer *Globigerinella siphonifera* (d’Orbigny). *Mar. Micropaleontol.* **2002**, *45*, 101–116. [[CrossRef](#)]
148. Huber, R.; van Staaden, M.J.; Kaufman, L.S.; Liem, K.F. Microhabitat use, trophic patterns, and the evolution of brain structure in African cichlids. *Brain Behav. Evol.* **1997**, *50*, 167–182. [[CrossRef](#)] [[PubMed](#)]
149. Darling, K.F.; Wade, C.M.; Kroon, D.; Brown, A.J.L. Planktic foraminiferal molecular evolution and their polyphyletic origins from benthic taxa. *Mar. Micropaleontol.* **1997**, *30*, 251–266. [[CrossRef](#)]
150. Morard, R.; Quillévéré, F.; Escarguel, G.; Ujiie, Y.; de Garidel-Thoron, T.; Norris, R.D.; de Vargas, C. Morphological recognition of cryptic species in the planktonic foraminifer *Orbulina universa*. *Mar. Micropaleontol.* **2009**, *71*, 148–165. [[CrossRef](#)]
151. Vargas, C.d.; Norris, R.; Zaninetti, L.; Gibb, S.; Pawlowski, J. Molecular evidence of cryptic speciation in planktonic foraminifers and their relation to oceanic provinces. *Proc. Natl. Acad. Sci. USA* **1999**, *96*, 2864–2868. [[CrossRef](#)]
152. Morard, R.; Quillévéré, F.; Douady, C.J.; de Vargas, C.; de Garidel-Thoron, T.; Escarguel, G. Worldwide genotyping in the planktonic foraminifer *Globoconella inflata*: Implications for life history and paleoceanography. *PLoS ONE* **2011**, *6*, e26665. [[CrossRef](#)]
153. Aurahs, R.; Treis, Y.; Darling, K.; Kucera, M. A revised taxonomic and phylogenetic concept for the planktonic foraminifer species *Globigerinoides ruber* based on molecular and morphometric evidence. *Mar. Micropaleontol.* **2011**, *79*, 1–14. [[CrossRef](#)]
154. Sears, H.A.; Darling, K.F.; Wade, C.M. Ecological partitioning and diversity in tropical planktonic foraminifera. *BMC Evol. Biol.* **2012**, *12*, 54. [[CrossRef](#)] [[PubMed](#)]
155. Weiner, A.K.; Weinkauff, M.F.; Kurasawa, A.; Darling, K.F.; Kucera, M.; Grimm, G.W. Phylogeography of the tropical planktonic foraminifera lineage *globigerinella* reveals isolation inconsistent with passive dispersal by ocean currents. *PLoS ONE* **2014**, *9*, e92148. [[CrossRef](#)] [[PubMed](#)]
156. de Vargas, C.; Renaud, S.; Hilbrecht, H.; Pawlowski, J. Pleistocene Adaptive Radiation in *Globorotalia truncatulinoides*: Genetic, Morphologic, and Environmental Evidence. *Paleobiology* **2001**, *27*, 104–125. [[CrossRef](#)]
157. Quillévéré, F.; Morard, R.; Escarguel, G.; Douady, C.J.; Ujiie, Y.; de Garidel-Thoron, T.; de Vargas, C. Global scale same-specimen morpho-genetic analysis of *Truncorotalia truncatulinoides*: A perspective on the morphological species concept in planktonic foraminifera. *Palaeogeogr. Palaeoclimatol. Palaeoecol.* **2013**, *391*, 2–12. [[CrossRef](#)]
158. Darling, K.F.; Wade, C.M.; Stewart, I.A.; Kroon, D.; Dingle, R.; Brown, A.J. Molecular evidence for genetic mixing of Arctic and Antarctic subpolar populations of planktonic foraminifers. *Nature* **2000**, *405*, 43–47. [[CrossRef](#)]
159. Stewart, I.A.; Darling, K.F.; Kroon, D.; Wade, C.M.; Troelstra, S.R. Genotypic variability in subarctic Atlantic planktic foraminifera. *Mar. Micropaleontol.* **2001**, *43*, 143–153. [[CrossRef](#)]
160. André, A.; Quillévéré, F.; Schiebel, R.; Morard, R.; Howa, H.; Meilland, J.; Douady, C.J. Disconnection between genetic and morphological diversity in the planktonic foraminifer *Neogloboquadrina pachyderma* from the Indian sector of the Southern Ocean. *Mar. Micropaleontol.* **2018**, *144*, 14–24. [[CrossRef](#)]
161. Bauch, D.; Darling, K.; Simstich, J.; Bauch, H.A.; Erlenkeuser, H.; Kroon, D. Palaeoceanographic implications of genetic variation in living North Atlantic *Neogloboquadrina pachyderma*. *Nature* **2003**, *424*, 299–302. [[CrossRef](#)]
162. Darling, K.F.; Kucera, M.; Kroon, D.; Wade, C.M. A resolution for the coiling direction paradox in *Neogloboquadrina pachyderma*. *Paleoceanography* **2006**, *21*, PA2011. [[CrossRef](#)]
163. Darling, K.F.; Kucera, M.; Pudsey, C.J.; Wade, C.M. Molecular evidence links cryptic diversification in polar planktonic protists to Quaternary climate dynamics. *Proc. Natl. Acad. Sci. USA* **2004**, *101*, 7657. [[CrossRef](#)]
164. Darling, K.F.; Kucera, M.; Wade, C.M. Global molecular phylogeography reveals persistent Arctic circumpolar isolation in a marine planktonic protist. *Proc. Natl. Acad. Sci. USA* **2007**, *104*, 5002. [[CrossRef](#)] [[PubMed](#)]
165. Morard, R.; Vollmar, N.M.; Greco, M.; Kucera, M. Unassigned diversity of planktonic foraminifera from environmental sequencing revealed as known but neglected species. *PLoS ONE* **2019**, *14*, e0213936. [[CrossRef](#)] [[PubMed](#)]
166. Beer, C.J.; Schiebel, R.; Wilson, P.A. Testing planktic foraminiferal shell weight as a surface water [CO₃²⁻] proxy using plankton net samples. *Geology* **2010**, *38*, 103–106. [[CrossRef](#)]
167. Deuser, W.G.; Ross, E.H.; Hemleben, C.; Spindler, M. Seasonal changes in species composition, numbers, mass, size, and isotopic composition of planktonic foraminifera settling into the deep sargasso sea. *Palaeogeogr. Palaeoclimatol. Palaeoecol.* **1981**, *33*, 103–127. [[CrossRef](#)]
168. Ortiz, J.D.; Mix, A.C. The spatial distribution and seasonal succession of planktonic foraminifera in the California Current off Oregon, September 1987–September 1988. *Geol. Soc. Lond. Spec. Publ.* **1992**, *64*, 197–213. [[CrossRef](#)]
169. Salmon, K.H.; Anand, P.; Sexton, P.F.; Conte, M. Upper ocean mixing controls the seasonality of planktonic foraminifer fluxes and associated strength of the carbonate pump in the oligotrophic North Atlantic. *Biogeosciences* **2015**, *12*, 223–235. [[CrossRef](#)]

170. Poore, R.Z.; Spear, J.W.; Tedesco, K.A. Seasonal flux and assemblage composition of planktic foraminifers from a sediment-trap study in the northern Gulf of Mexico. *J. Coast. Res.* **2013**, 6–19. [[CrossRef](#)]
171. Chernihovsky, N.; Torfstein, A.; Almogi-Labin, A. Seasonal flux patterns of planktonic foraminifera in a deep, oligotrophic, marginal sea: Sediment trap time series from the Gulf of Aqaba, northern Red Sea. *Deep Sea Res. Part I Oceanogr. Res. Pap.* **2018**, *140*, 78–94. [[CrossRef](#)]
172. Jonkers, L.; Kučera, M. Global analysis of seasonality in the shell flux of extant planktonic Foraminifera. *Biogeosciences* **2015**, *12*, 2207–2226. [[CrossRef](#)]

Article

Disruption of the Atlantic Meridional Circulation during Deglacial Climates Inferred from Planktonic Foraminiferal Shell Weights

Stergios D. Zarkogiannis 

Department of Earth Sciences, University of Oxford, South Parks Road, OX1 3AN Oxford, UK;
stergios.zarkogiannis@earth.ox.ac.uk

Abstract: Changes in the density structure of the upper oceanic water masses are an important forcing of changes in the Atlantic Meridional Overturning Circulation (AMOC), which is believed to widely affect Earth's climate. However, very little is known about past changes in the density structure of the Atlantic Ocean, despite being extensively studied. The physical controls on planktonic foraminifera calcification are explored here, to obtain a first-order approximation of the horizontal density gradient in the eastern Atlantic during the last 200,000 years. Published records of *Globigerina bulloides* shells from the North and Tropical eastern Atlantic were complemented by the analysis of a South Atlantic core. The masses of the same species shells from three different dissolution assessed sediment cores along the eastern Atlantic Ocean were converted to seawater density values using a calibration equation. Foraminifera, as planktonic organisms, are subject to the physical properties of the seawater and thus their shells are sensitive to buoyancy forcing through surface temperature and salinity perturbations. By using planktonic foraminifera shell weight as an upper ocean density proxy, two intervals of convergence of the shell masses are identified during cold intervals of the last two deglaciations that may be interpreted as weak ocean density gradients, indicating nearly or completely eliminated meridional circulation, while interhemispheric Atlantic density differences appear to alleviate with the onset of the last interglacial. The results confirm the significance of variations in the density of Atlantic surface waters for meridional circulation changes.

Keywords: planktonic foraminifera; shell weight; ocean paleodensity; Atlantic Meridional Circulation (AMOC); climate variability



Citation: Zarkogiannis, S.D. Disruption of the Atlantic Meridional Circulation during Deglacial Climates Inferred from Planktonic Foraminiferal Shell Weights. *J. Mar. Sci. Eng.* **2021**, *9*, 519. <https://doi.org/10.3390/jmse9050519>

Academic Editor: Christos Stefanakos

Received: 16 April 2021

Accepted: 7 May 2021

Published: 11 May 2021

Publisher's Note: MDPI stays neutral with regard to jurisdictional claims in published maps and institutional affiliations.



Copyright: © 2021 by the author. Licensee MDPI, Basel, Switzerland. This article is an open access article distributed under the terms and conditions of the Creative Commons Attribution (CC BY) license (<https://creativecommons.org/licenses/by/4.0/>).

1. Introduction

The Atlantic Meridional Overturning Circulation (AMOC) is a system of ocean currents that has an essential role in Earth's climate, redistributing heat and influencing the carbon cycle [1,2]. It is a basin-scale baroclinic ocean circulation with a northward flow of warm water and a cold return flow at depth [3]. During its northward travel, the surface water exchanges heat with the atmosphere, modifying the climate of the Northern Atlantic region and contributing to the relatively mild climate in Europe. This overturning circulation is a meridional plane portrait of a much more complex three-dimensional circulation in the Atlantic, which can be conditionally split into wind-driven and thermohaline circulations [4]. This latter circulation depends in part on oceanic density gradients and hence on temperature and salinity gradients controlled by warming/cooling and evaporation/precipitation at the surface of the ocean.

Progress in the reconstruction of past Atlantic circulation changes has revealed that AMOC reductions coincided with colder episodes within the Last Glacial, especially Heinrich Events [5,6]. Additionally, a prominent chemocline has been identified in the North Atlantic during the Last Glacial Maximum (LGM) and Heinrich Event 1 (H1) [6], which suggests an altered deep-water circulation state. However, so far hardly anything is known about the past subsurface density structure in the North Atlantic [7], while it is still

poorly constrained beyond the LGM. As this structure is fundamental for understanding deep-water circulation [8], it is critically important that new means are established for assessing changes in oceanic vertical density structures. I present new insight into this structure in the eastern Atlantic from a novel approach that centers on the physical controls on planktonic foraminifera biomineralization through time.

Although the effects of ocean chemistry on plankton are being extensively studied, there is a lack in the literature about the effects of physical oceanic properties such as buoyancy or pressure, which very likely affect foraminifera physiology and morphology [9]. Different foraminifera species have different optimum living depth habitats [10,11], to which they adapt according to the oceanic inhomogeneity. These organisms are able to biosynthesize out of equilibrium with their ambient environment by maintaining chemical gradients [12–14]; however, as plankton they must thus always retain equilibrium with the seawater to remain floating. It can thus be argued that plankton physiology is more sensitive to the physical rather than the chemical characteristics of seawater. In order to inhabit certain depths, planktonic foraminifera should regulate their (cell) density to match that of the surrounding liquid in which they are immersed. Should this not be the case, then the organisms must relocate until they reach a particular density horizon to equilibrate.

Foraminifera may have different strategies (e.g., storage of metabolic gases) for short-term displacement or micro-positioning in the water column, such as diurnal migrations, but compared to gasses and lipids the most inert way for non-motile plankton to regulate buoyancy in the long term is by biomineralization [15,16]. Based on the foraminiferal need for certain habitat acquisition and recent findings on the influence of surface ocean density on their calcification [17], the application of foraminifera shell weights as a (paleo)seawater density proxy is introduced here as a means to reconstruct paleoseawater density and stratification of the surface Atlantic Ocean and thus the rigorousness of its meridional overturning circulation. For this purpose, synchronous sieve-based shell weights of the planktonic foraminifera species *G. bulloides* are compared across three Atlantic locations. *G. bulloides* is a subsurface, cosmopolitan foraminifera species with a wide use in paleoceanographic studies that thus allowed for the comparison of the results of a new S. Atlantic core with two more shell weight records from the bibliography.

2. Oceanographic Setting of the Core Locations

The present study involves the analyses of three sediment cores from the eastern margins of the Atlantic Ocean (Figure 1). The southernmost one is GeoB 1710-3 from the northern Cape Basin and was taken from the southwestern African lower continental slope (2987 m). The Cape Basin, located in the subtropical eastern South Atlantic Ocean, is bordered to the east by the African continent, to the north and west by the Walvis Ridge and the Mid-Atlantic Ridge, respectively, and to the south by the Agulhas Ridge (Figure 1). The wind system is almost entirely dominated by the southeast trade winds [18]. Surface waters in the Cape basin may be derived from three different regions: the Indian Ocean's Agulhas current, the South Atlantic current, and the Subantarctic Surface Waters [19–21]. Below the surface currents lies the Antarctic Intermediate Water (AAIW), which spreads to the north between 500 and 1000 m water depth. The dominant modern deep water mass, in the Cape Basin, is a mixture of ~60% Circumpolar Deep Water (CPDW) and ~40% North Atlantic Deep Water (NADW) from the western South Atlantic [22,23]. The relatively warm, saline, southward-flowing NADW is injected in the equatorward-flowing CPDW and extends between about 1700 and 3900 m water depth [24]. Between 1000 and 1700 m, the NADW is overlain by Upper Circumpolar Deep Water (UCPDW) and underlain by Lower Circumpolar Deep Water (LCPDW) [25]. The LCPDW is formed when Antarctic Bottom Water (AABW) is mixed with the slightly less dense overlying water [26]. The extremely cold, oxygen-depleted, nutrient-enriched, of low CO_3^{2-} and high CO_2 content AABW is encountered below 4000 m [27]. During glacial times, the conveyor circulation was weak, and the abyssal Cape Basin was filled with less corrosive and aged

deep waters [28]. The core location is currently bathed in NADW [27] and must have been so for the last 245 Kyrs [29].

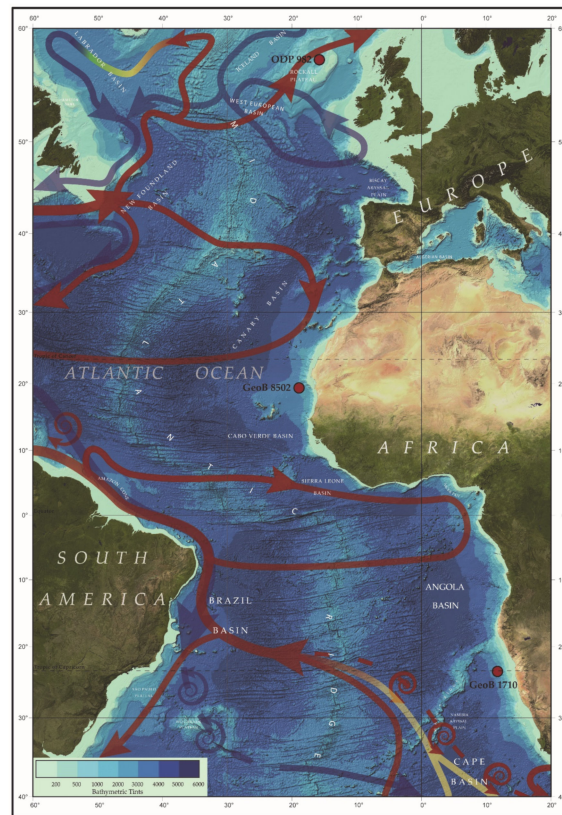


Figure 1. Location of the sediment cores and schematic of the Atlantic Meridional Overturning Circulation. Red is the surface flow, blue the deep one, and yellow and green represent transition flows between depths. Terrain after the general bathymetric chart of the Ocean.

GeoB 8502 (19°13.27' N, 18°56.04' W) is a Tropical North Atlantic pelagic site at the lower reaches of the Cap Timiris Canyon, approximately 250 km offshore the Mauritanian coast (Figure 1), and was retrieved from 2956 m water depth on the lower Northwestern African continental rise and consists of levee sediments that are predominantly hemipelagic deposits. As part of the Eastern Boundary Current system, the Mauritanian upwelling region is one of the major upwelling areas in the Atlantic Ocean [30]. Along the NW African margin, the temporal dynamics of the coastal upwelling are driven basically by the intensity of the northeast trade-winds, itself dependent on the seasonal Intertropical Convergence Zone (ITCZ) migration [31,32] on a perennial basis, producing cold nutrient-rich surface waters with modern sea surface temperatures (SSTs) as low as 16°C. The main water masses encountered in the upwelling region are the Tropical Surface Water (TSW), the North and South Atlantic Central Waters (NACW and SACW), and AAIW. Both central water masses appear in the permanent pycnocline between depths of 150 m and 600 m at temperatures greater than about 8°C, below which lies the AAIW [32]. At greater depths, the core sediments are currently bathed in the carbonate-saturated NADW and may have remained so during the glacials [33].

Core ODP 982 was retrieved from the Rockall Plateau, which is an extensive shallow water (~2000 m) area located south of Iceland and west of the British Isles (Figure 1). The surface circulation in the Rockall area is characterized by warm, highly saline water of the North Atlantic Drift Current (NADC), which forms the continuation of the Gulf Stream heading to the Nordic Seas [34]. The NADC is the major surface water component of the AMOC, which is one driving factors behind the global conveyor belt and NADW formation [35,36]. The NADW may be divided into two main components: the upper

NADW, in the intermediate depths, and the lower NADW (deeper than 2000 m). Intermediate depths in the North Atlantic, near the Rockall Plateau, contain three principal water masses between the AAIW, Mediterranean Overflow Water (MOW), and Labrador Sea Water (LSW). The upper NADW consists of a mixture of LSW, MOW, and overflows from the Nordic Seas and is the densest of the intermediate water masses, occupying depths between 1500 and 1600 m in the interior ocean. The lower NADW is composed of a mixture of the dense overflows from the Nordic Seas and LSW [37]. The deepest water mass in the Rockall area (≥ 3500 m) consists of modified AABW, which is characterized by lower salinity than the waters above [38].

3. Material and Methods

3.1. Sediment Core Locations and Methodological Overview

The present study is based on the weight analyses of foraminifer shells from three sediment cores (Table 1). *G. bulloides* shell weights from the 300–355 μm sieve fraction existed for cores ODP 982 [39] in the North Atlantic and GeoB 8502-2 [40] in the Tropical Atlantic and thus the weight analysis was extended to specimens from core GeoB 1710-3 in the South Atlantic. GeoB 1710-3 is 10.45 m long with an average sedimentation rate of ≈ 5 cm/ky [41] and extends back 245 kyr to Marine Isotope Stage (MIS) 7, yet the present analysis was restricted to the last 200 kyr to match the extent of GeoB 8502-2. Samples from GeoB 1710-3 were taken at a resolution of ~ 2000 years (10 cm sampling interval) by extracting a slice of material, 1 cm in thickness, which corresponds approximately to an average of 200 years of sedimentation. The coarse fraction of all samples was already available from a previous study [42] and was subsequently dry-sieved into several sieve fractions. Non-fragmented *G. bulloides* shells from the 315–355 μm size fraction were picked for mass analysis. The very narrow size interval (40 μm) should be sufficient to overcome the greater proportion of natural size variability without further normalization [43]. Since any record of shell weight is a composite signal of dissolution superimposed upon the initial shell weight variability, the cores considered here were already assessed for carbonate dissolution using the same method (ODP 982 [17], GeoB 8502-2 [40], GeoB 1710-3 [44]) and their foraminiferal carbonate is reported to be well preserved. The coarse fraction from the studied cores was disaggregated with deionized water and then wet-sieved through a 63 μm mesh. Since all samples underwent the same washing process, any offset due to residual fine debris would be constant among samples. Although treatment solely with water is not a very efficient cleaning method for weighing analyses [45], the examined specimens did not show increased contamination (see Section 4).

Table 1. List of the core sites.

Core	Latitude	Longitude	Depth (m)
ODP 982A	57°30.99' N	15°52.00' W	1135
GeoB 8502-2	19°13.27' N	18°56.04' W	2956
GeoB 1710-3	23°25.9' S	11°41.9' E	2987

The weight analyses revealed two instances where *G. bulloides* shell masses between the studied cores converge and these convergence intervals were termed Shell Mass Convergence Event (SMCE) I and II, during the last (~ 18.4 ka) and the penultimate (~ 122.4 ka) deglaciations, respectively. In order to better understand the physiology of the shells during these intervals, the selected specimens from GeoB cores were analyzed by high resolution X-ray microcomputed tomography (X μ CT). The tomographic analysis was extended to the shells that mark the Last Glacial Maximum (LGM) in core GeoB 1710-3, which were the heaviest found in all three records during the last 200 kyr. μ CT was used to inspect the interior and the internal structure of the foraminiferal tests. Apart from addressing the test's integrity, X μ CT allowed for the assessment of the degree to which the recorded masses are the result of interference from shell inclusions or of changes in test thickness. Finally, the μ CT analysis led to total shell volume estimates that allowed for the calculation

of volume-normalized shell weights or *G. bulloides* shell densities, presenting a more precise method of eliminating the contribution of shell size to shell weight.

3.2. Weight Analysis

Where available, ideally, 50 (minimum 31) *G. bulloides* shells were weighed in a preweighed aluminum carrier in the Department of Earth Sciences at the University of Oxford using a Sartorius SE 2 ultra-microbalance with a precision of $\pm 0.1 \mu\text{g}$. Replicate weight measurements of specimens from core ODP 982 were performed in the Godwin laboratory at the University of Cambridge using a UMX2 Mettler Toledo ultra-microbalance at the same precision. Average shell masses were calculated by dividing the recorded mass by the total number of foraminifera weighed. Subsequently, for each sample, the average shell weights of batches of five individuals (minimum four, maximum eight) were determined, in order to estimate standard shell mass deviations. As explained above, performing shell weight analyses on a narrow size fraction of foraminifera constrains the ontogenic stage of the specimens to a certain number of chambers, and thus minimizes size-related weight differences [43,46]. The analytical error, estimated by triplicate measurements of 50 random specimens, ranged from 0.04 to 0.06 μg for both balances, which is in accordance with their analytical error.

3.3. Determination of Atlantic Seawater Paleodensity

The acquired shell weight measurements were converted to paleoseawater densities using Equation (1) that was derived by correlating weight and geochemical analyses of equally sized *G. bulloides* specimens between both 250–315 and 300–355 μm from the Atlantic Ocean [17]:

$$\text{Seawater density} = 0.29(\pm 0.01) * G. \text{bulloides shell mass} + 1022.78(\pm 0.11) \quad (1)$$

This equation is based on the hypothesis that foraminifera shell masses can be used as a direct (paleo)seawater density proxy and is considered to describe the ocean density at 100 m depths. When *G. bulloides* shell weights approach zero, like the smallest juvenile tests, the density approaches 1023 kg/m^3 , thus describing well the modern average surface ocean density. The weight-derived ocean densities were also compared to published geochemically derived seawater densities for the penultimate deglaciation from core GeoB 8502-2. The propagated error from the transformation of shell mass to seawater density is $\pm 0.23 \text{ kg}/\text{m}^3$.

3.4. X-ray Micro-Computed Tomography (μCT)

For X-ray microscopic analysis, in total, 28 specimens were scanned from four samples of cores GeoB 8502-2 and GeoB 1710-3 that correspond to the time intervals of shell mass convergence during the last and penultimate deglaciations (SMCE I and II), and a sample from the last glacial maximum in core GeoB 1710-3, where the highest shell weights of all the studied records were recorded. The dataset was complemented with CT data previously published in Zarkogiannis, et al. [40] that refer to the time-slice of SMCE II in core GeoB 8502-2. On average, seven (min four, max five) specimens were scanned from each of the studied intervals. Each batch of shells was poured into a quartz cylindrical carrier 1 mm in diameter [47]. They were stabilized with diluted tragacanth glue and left to dry prior to scanning. The micro-CT (μCT) scanning was carried out with a Zeiss Xradia 510 Versa at the Maxwell Centre of the University of Cambridge. X-ray source and detector geometry were kept constant throughout the scans. The anode voltage was set at 100 kV, the X-ray tube current was 90 μA , and the exposure time was 2 s at an optical magnification of $4\times$. By processing approximately 1024 images per sample, a scan resolution voxel size of $\sim 1.2 \mu\text{m}^3$ was typically achieved using this setup in order to maximize the number of specimens that could be analyzed in a single scan. The images were combined to build a 3D rendering using Avizo software, which was also used for segmentation. The segmentation resulted in

the separation of the tomographs into shell area, area occupied by clay infillings (dirt), and internal shell (protoplasm) voids.

Subject to the degree of segmentation, the X-ray microscopic analysis allows for the determination and study of a number of biometric characteristics of the foraminifera shells, such as total shell volume, thus shell density (volume-normalized weight) and calcite (test) volume, and thus test density and calcite (test) surface [40]. The calculation of the total cell volume and the volume of shell calcite allowed for the determination of the percentage that the shell occupies within the cell. The ratio of calcite volume/calcite surface provides a linear unidimensional quantity in length units and can thus serve as a measure of average test thickness. In this study, in addition to shell density, that is, the ratio of shell volume to shell mass, we used the “specific surface area”, that is, the ratio of test volume/test surface, as a measure of average test thickness [48] and the test density, that is, the ratio of test volume to shell mass, as an indication of test porosity. Furthermore, by segmenting the area occupied by clay infillings, the degree of contamination in weight measurements was calculated as percent by volume. Links to raw tomographic data can be found in the data availability statement section below.

4. Results

The record of *G. bulloides* shell mass attained from GeoB 1710-3 for the last 200 kyr shows enhanced climatic cyclicity (Figure 2a) and variability between mass values of more than 100%, but shell weights were consistent between replicates. During the cold MIS 6 interval, shell weights were generally increased but with considerable variation, of up to 80% since some of the lowest mass values in the record are at 148 and 180 ka. During MIS 5e, shell masses are low and they gradually increase after MIS 5d. The lowest shell mass values followed MIS 5b, after which shell weights increase until they reach their maximum value at 20 ka, which possibly marks the LGM interval for this core. During the last deglaciation, mass values drop abruptly and they remained low during the Holocene.

In contrast to GeoB 1710-3, the shell weight record of the lower latitude core GeoB 8502-2 shows no cyclicity between glacial and interglacial periods the last 200 kyr. *G. bulloides* shell masses are stable, fluctuating only on a small scale ($\pm 1.1 \mu\text{g}$, 1σ) around an average of $13.4 \mu\text{g}$. Lower shell mass weights are found within MIS 6, while values almost increase progressively after MIS 5b. The broad maximum in shell weight centered at the MIS 5/6 boundary of Termination II recorded for approximately 2300 yr, during which shell masses increase by 30% above average, was attributed to contamination clay infillings. In core ODP 982A, shell weights show again a clearer glacial/interglacial pattern, which is less “nervous” than that of GeoB 1710-3. Here, *G. bulloides* shell masses consistently increased at around $17.3 (\pm 1.3) \mu\text{g}$ during the cold MIS 6 interval. Low mass values are recorded during the warmest MIS 5e interval, after which weights increase gradually during the course of the last glaciation until around 21 ka. At this age, the highest mass values are recorded, denoting the LGM period in this core, after which values drop and decrease even further during the late Holocene.

By using Equation (1), the planktonic foraminifera shell weights were converted to ocean density values and the results for the three records are summarized in Figure 3. The superposition of the three records reveals a convergence in Atlantic Ocean densities for two instances during the last 200 kyr. The first convergence event (SMCE I) takes place after the onset of the last deglaciation around 18.4 ka and the second (SMCE II) around 122.4 ka within the peak of the penultimate deglaciation. During both of these instances, the water densities convergence to the same value of $\sim 1026.82 \text{ kg/m}^3$ and this value is similar to seawater densities reconstructed for the modern core-top samples. It also appears that most of the time the South Atlantic is densest. Prior to SMCE II, density gradients are more or less constant between the different Atlantic localities, while after this convergence event densities start to diverge between the tropical site and the sites at higher latitudes until the LGM when the divergence becomes the maximum between the sites. After SMCE I,

seawater density gradients between the different eastern margins of the ocean alleviate considerably until today.

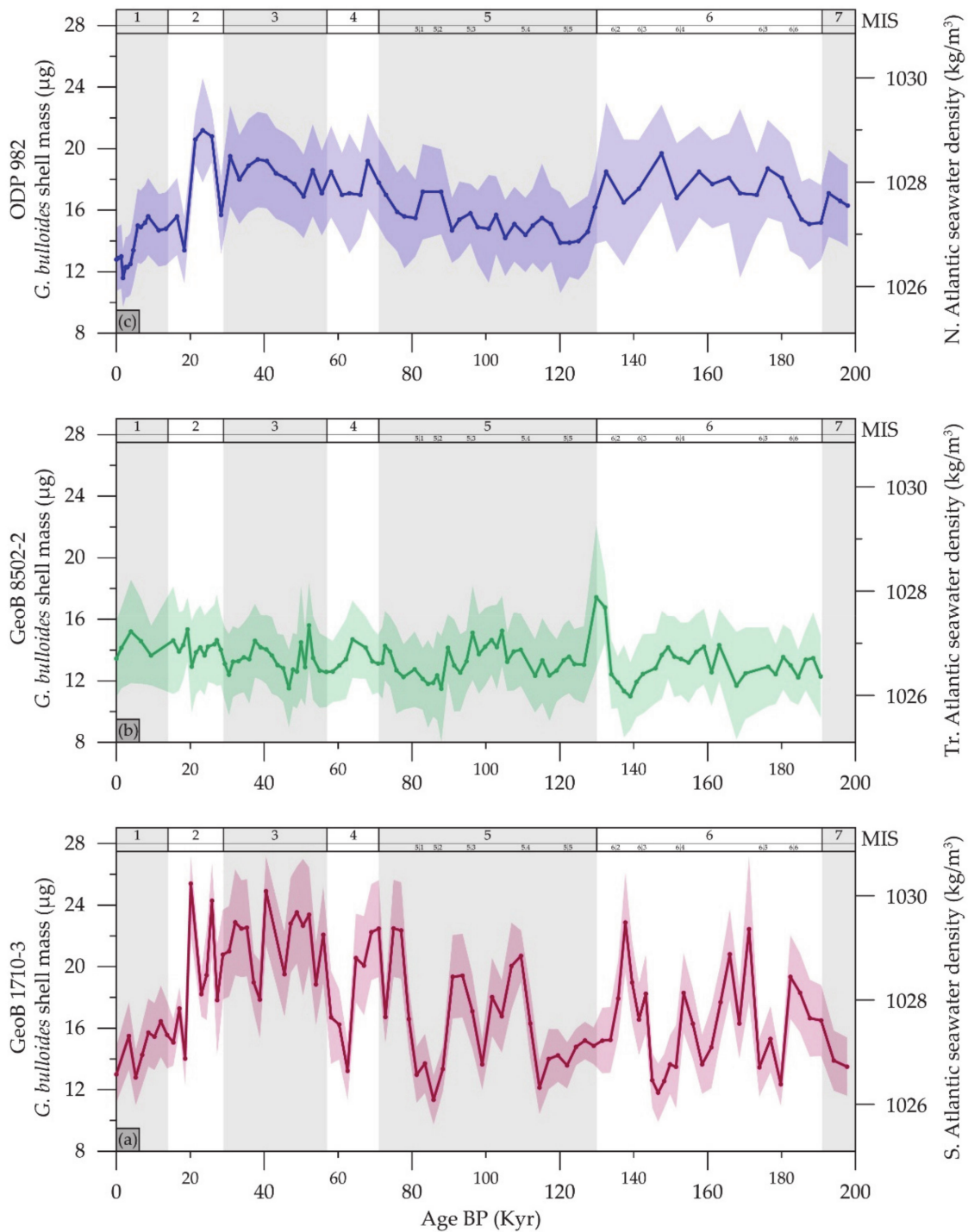


Figure 2. Shell weight records of the last 200 kyr (before present, BP) for: (a) core GeoB 1710-3 from the eastern South Atlantic; (b) core GeoB 8502-2 from the eastern Equatorial Atlantic [40]; and (c) core ODP 982 from the eastern North Atlantic. The 1σ confidence interval for each shell mass plot is shown as a color-shaded area. Numbers refer to Marine Isotopic Stages (MIS) or substages and grey-shaded areas interglacial periods. Data are available in Supplementary Table S1.

The results from the intervals that surround the two SMCE events are summarized in Table 2. The average *G. bulloides* shell masses during SMCE I across the different sites are $13.9 (\pm 0.5) \mu\text{g}$ and $13.7 (\pm 0.2) \mu\text{g}$ during SMCE II, which equal to almost identical

Atlantic seawater densities (1026.86 and 1026.79 kg/m³, respectively) also between the two intervals. The density value of ~1026.8 kg/m³ to which Atlantic seawater densities converged on average during the two SMCEs resembles that of the modern ocean. The weight-derived Atlantic seawater densities are comparable within error to geochemically reconstructed seawater density values from combined Mg/Ca and δ¹⁸O measurements on the weighed *G. bulloides* specimens from core GoeB 8502-2 for this interval.

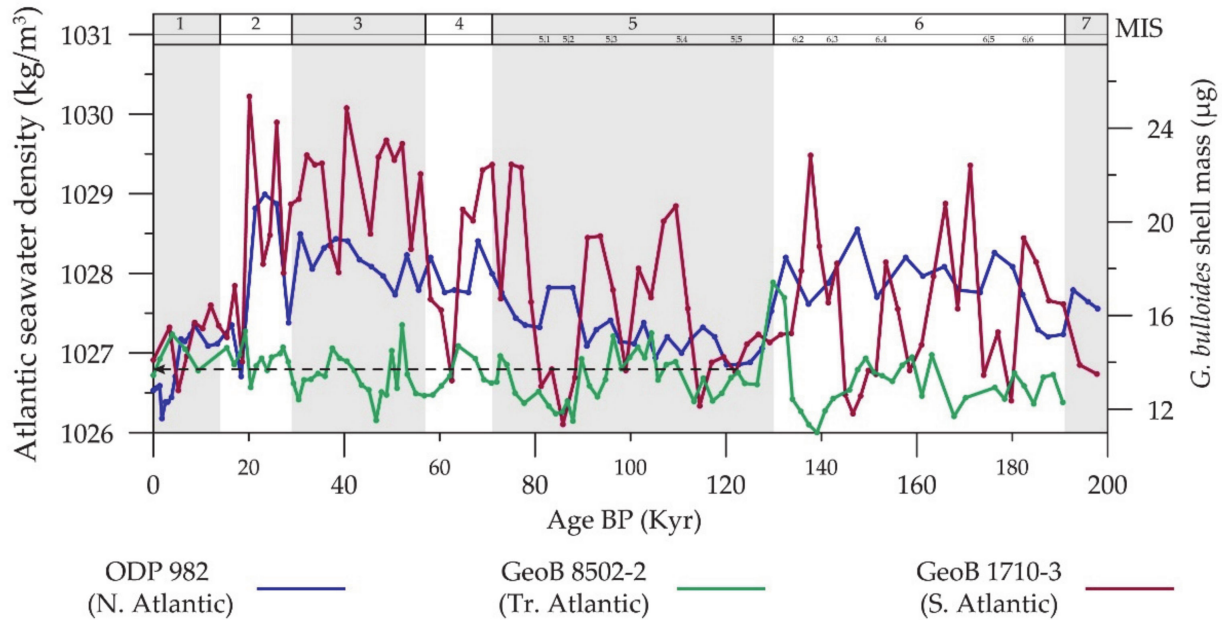


Figure 3. Atlantic Ocean density reconstructions for the last 200 kyr based on planktonic foraminifera shell weights from three different sites. Note the convergence in seawater density/planktonic foraminifera shell mass values for two instances in the records and how these values match the modern seawater densities.

Table 2. Summary of *G. bulloides* shell masses and the mass-derived seawater densities for the three different Atlantic sites across the two SMCEs during the last two deglaciations. The reconstructed densities presented in the last column are geochemically reconstructed seawater densities during SMCE II published in Zarkogiannis, et al. [40] for core GeoB 8502-2.

Sites	SMCE I—Last Deglaciation			SMCE II—Penultimate Deglaciation			
	Age (ka)	Weight (µg)	Derived Density (kg/m ³)	Age (ka)	Weight (µg)	Derived Density (kg/m ³)	Reconstructed Density (kg/m ³)
ODP 982A	16.42	15.6	1027.35	120.12	13.9	1026.85	
	18.40	13.4	1026.71	122.60	13.9	1026.85	
	21.38	20.6	1028.82	125.08	14.0	1026.88	
GeoB 8502-2	16.95	13.9	1026.85	121.08	13.3	1026.69	1027.21
	18.10	14.3	1026.98	122.51	13.6	1026.76	1026.10
	19.26	15.3	1027.28	123.93	13.1	1026.62	1027.14
GeoB 1710-3	17.08	17.3	1027.84	119.49	14.2	1026.95	
	18.65	14.0	1026.89	121.96	13.6	1026.76	
	20.15	25.4	1030.22	124.40	14.8	1027.11	

The results from the CT analyses are summarized in Table 3. The specimens that were available for CT scanning are from the GeoB cores. The analysis mainly focused on the specimens from SMCE I and II intervals and reveal other physical characteristics of the specimens with the same mass across the Atlantic basins and time intervals. In addition to these intervals, LGM specimens from core GeoB 1710-3 displayed the highest shell mass in the studied records. The CT analyses showed that contamination by sediment infilling of specimens is minimal (only ~5% by volume) and thus the reported shell mass values are

not artifacts. Furthermore, the inspection of the tomographs (found in the data availability statement section below) verified the good preservation of the specimens and thus the shell weight variation due to dissolution can be considered minimal too.

Table 3. Biometric data of foraminifera from weighing and $\chi\mu$ CT analysis. Test thickness is the ratio of calcite volume to calcite surface, and shell and test density are the ratio of the average shell weight to test and shell volume, respectively. Sediment infilling is the specimen’s internal volume percentage occupied by sediment impurities. The μ CT analysis results for individual specimens are given in Supplementary Table S2.

Period	Site	Age (kyrs)	Test Mass (μ g)	Test Thickness (μ m)	Cell Volume (μ m ³)	Sediment Infilling (%)	Test %	Shell Density (g/cm ³)	Test Density (g/cm ³)
Last Deglaciation	GeoB 8502	18.10	14.3 ± 2.2	5.1 ± 0.7	21,737,763 ± 15%	4%	23%	0.66	2.71
	GeoB 1710	18.65	14.0 ± 1.7	4.7 ± 0.5	24,155,433 ± 7%	2%	22%	0.58	2.69
Penultimate Deglaciation	GeoB 8502	122.51	13.6 ± 2.4	5.0 ± 0.4	22,326,089 ± 9%	5%	23%	0.61	2.62
	GeoB 1710	121.96	13.6 ± 1.5	5.2 ± 0.7	21,270,578 ± 10%	7%	25%	0.64	2.60
Last Glacial Maximum	GeoB 1710	20.15	25.4 ± 0.5	11.0 ± 17%	27,088,617 ± 6%	6%	42%	0.94	2.24

The merging of shell masses is also reflected in a convergence in the mean wall thickness of the shells at ~5 μ m (Figure 4a–h). Although the shell thickness is similar, during SMCE I shell masses are slightly more elevated than during SMCE II but the shells are found to be more voluminous. Thus, the shell thickness remains the same because mass changes are compensated for by changes in total volume, and this is reflected in the shell density values of Table 3. Furthermore, during convergence events the foraminifera shell comprise 23% of the total cell, while the overall shell density (i.e., volume-normalized weight) varies only by a little and is on average 0.62 g/cm³. The test porosity (an indication of test porosity) of SMCE I individuals is slightly increased compared with that of SMCE II. Test density values vary around the values of the calcite’s density.

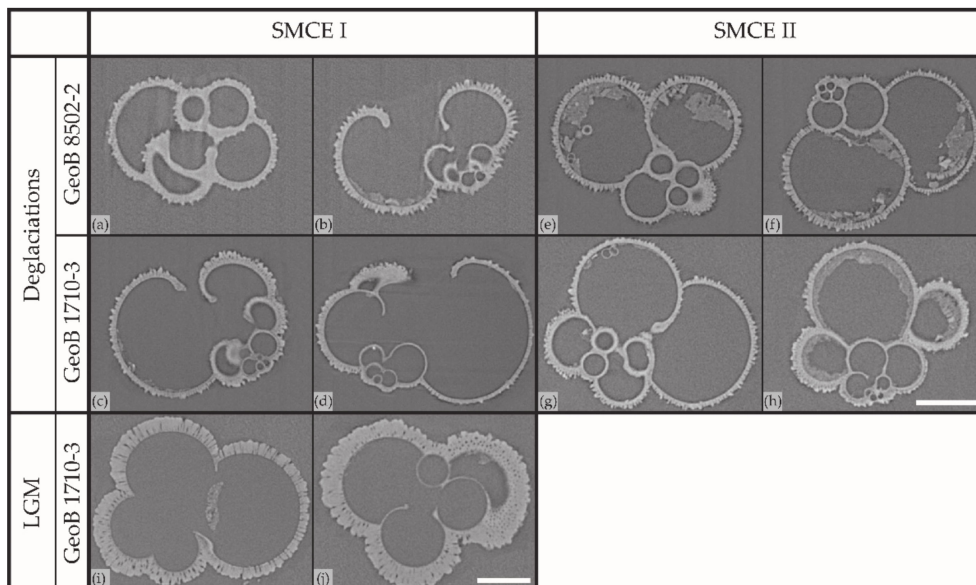


Figure 4. X-ray tomographs of *G. bulloides* specimens of cores GeoB 8502-2 and GeoB 1710-3; (a–d) specimens from shell mass convergence event SMCE I; (e–h) specimens from SMCE II; and (i–j) Last Glacial Maximum specimens from core GeoB 1710-3.

The LGM specimens of GeoB 17010-3 exhibit different characteristics to those of the SMCEs (Table 3). Their mass almost doubles and so does their shell wall thickness. This is also visually evident in their tomographs of Figure 4i,j, where the specimens are found to be heavily encrusted. Internal chamber walls are very delicate and thin (Figure 4j), while in most of the cases these chamber walls are completely dissolved and are thus not evident within the shell (Figure 4i). LGM shells are ~20% more voluminous than the others and this extra volume is due to the increase in their shell calcite, which now comprises the 42% of the total cell volume (Table 3), while the total volume of the cavities that are filled with protoplasm is similar to the SMCE specimens (Supplementary Table S2). The overall shell density during the LGM is increased by more than 50%, while the test itself is found to be less dense and thus more porous (Table 3).

5. Discussion

5.1. Foraminifera Shell Weights Are Tracers of Past Oceanic Circulation

The sieved-based weight analysis of *G. bulloides* shells from the South Atlantic core GeoB 1710-3 during the last 200 kyr was combined with two additional eastern Atlantic shell weight records and revealed reorganizations in the meridional circulation of the Atlantic Ocean. The measured foraminifera shell masses were converted to seawater density values using a lineal relationship that was calibrated for the Atlantic Ocean using geochemical data [17]. The mass-based reconstructed seawater densities from the three different eastern Atlantic localities describe their hydrography and unveil two occasions, SMCE I and SMCE II, when the seawater densities between these regions appear similar (Figure 3). Interhemispheric convergence of surface Atlantic densities denotes the absence of seawater density gradients across the basins and thus momentary cessation of the Atlantic Meridional Overturning Circulation (AMOC), which implies an increase in surface ocean stratification [49] and abrupt, large changes in climate [50].

The basin-scale reconstructions of seawater densities using planktonic foraminifera shell mass measurements have enabled the consideration of several aspects of the Atlantic hydrography. Figure 3 showed that planktonic foraminifera can alter their shell mass considerably and verifies that the degree of this alteration in time is a function of latitude [51] with no overall response to atmospheric $p\text{CO}_2$. The water from the S. Atlantic site is generally found to be denser than the other two eastern areas. This illustrates the northward water movement towards less dense regions, which is known to feed the northern Atlantic latitudes with southern-sourced waters [52]. The high S. Atlantic densities of enhanced variability may be the result of the site's location offshore the Kalahari Desert, which as a hyper-arid area would favor the development of high salinity in the sea water, while pulses of leaking warmer and thus lighter Agulhas waters may contribute to abrupt density variabilities (see Section 5.2). Seawater densities at the tropical Atlantic site GeoB 8502-2 are stable throughout the studied interval and *G. bulloides* specimens were the lightest between records. As discussed in Zarkogiannis, et al. [40], this is a tropical region of insolation and climatic stability, under the influence of the ITCZ, which is a zone of enhanced precipitation and of low-density surface waters [53].

Planktonic foraminifera shell weights start recording the glacial/interglacial cyclicity signal at mid-latitudes or at latitudes that are more sensitive to insolation changes. That seawater densities are here reconstructed higher for the site at 23° S (GeoB 1710-3) than that of 57° N (ODP 982A) might imply that the overturning circulation and oceanic density gradients may not respond directly to the amount of summer insolation falling across northern high-latitude regions. They are possibly dictated by moisture fluxes from Hadley cells, driven by the Earth's latitudinal insolation gradient (LIG) [54] and the latitudinal temperature gradient (LTG) that it creates, which drives the poleward energy flux via the atmospheric and ocean circulation [55]. Site GeoB 1710-3, where the highest shell weights were recorded, is located directly at the descending limb of the Hadley cell. Furthermore, since the LGM is an arid period [56,57] and may have been more arid than the penultimate glacial maximum [58], the highest-density waters (of increased salinity and decreased

temperature) were to be expected in the Atlantic basins of the mid-latitudes (Figure 5a). The response of planktonic calcification to high-density waters is notably manifested in Figure 4i,j.

Furthermore, Figure 3 suggests that the Atlantic Ocean was slightly lighter during MIS 6 than the subsequent glaciation as it can be seen in all three records. The penultimate glacial, MIS 6, appears to have been approximately as extreme as the last ice age in terms of global ice volume and sea level [59,60]. Yet, unlike the last glacial interval, no major ice-rafted debris (IRD) deposits, known as Heinrich events [61,62] that suggest increased iceberg formation, were recorded prior to the penultimate deglaciation in the Atlantic [63,64], while on the Iberian margin, MIS 6 has been described as a warmer glacial interval compared with the last ice age [63,65]. Thus, for occupying the same volume at higher temperatures, its density should have been reduced. Except for this glacial interval, which raises arguments that the interocean salt leakage is not as straightforward as previously suggested [66], the South Atlantic has most of the time been the densest of the three basins as it is today [67]. Furthermore, its record appears to be “nervous” with increased variability.

The most important outcome of Figure 3 in terms of abrupt Atlantic hydroclimate changes may however be the identification of intervals of surface seawater density convergence. Independent indications of a collapse of the Atlantic meridional circulation during SMCE I and SMCE II are provided by geochemical evidence of $^{231}\text{Pa}/^{230}\text{Th}$ records from N. Atlantic cores. $^{231}\text{Pa}/^{230}\text{Th}$ is a kinematic proxy for the meridional overturning circulation. For a given scavenging rate, lower rates of AMOC in the past would result in comparatively less ^{231}Pa export from the Atlantic and in higher sedimentary $^{231}\text{Pa}/^{230}\text{Th}$, reaching a maximum of 0.093 for a total cessation [68]. In the present study, the first instance of surface ocean density gradient attenuation is recorded at ~122.4 ka (SMCE II), shortly after the peak in the last interglacial (MIS 5.5) within a cold climatic phase [69,70]. During the same interval, the sedimentary record of core MD95-2037 from the north central Atlantic shows increased $^{231}\text{Pa}/^{230}\text{Th}$ values that also indicate cessation of the overturning circulation in the region (Figure 2 in [71]).

According to the density differences between the Atlantic regions of Figure 3 and in line with previous findings, the overturning rate at the ocean surface was weak during MIS 5e, and a change to a more vigorous circulation pattern occurred mostly during the glacial inception, i.e., the transition from MIS 5.5 to MIS 5.4 [71–73]. Hence, during the warm optimum of MIS 5.5, the structure of the AMOC was similar to the modern one (Figure 5b). The records are also in agreement for a sluggish Atlantic circulation at ~100 ka, since the weak density gradients that appear in Figure 3 are synchronous with an increase in the $^{231}\text{Pa}/^{230}\text{Th}$ records [71]. Nevertheless, the weight-based reconstructed density gradients show that the glacial Atlantic circulation mode started after 120,000 years ago with an increase in the overturning rate [71] and thus a more vigorous behavior of the AMOC [74,75] following the decrease in Northern Hemisphere summer insolation, which favored the initiation of ice-sheet growth [76].

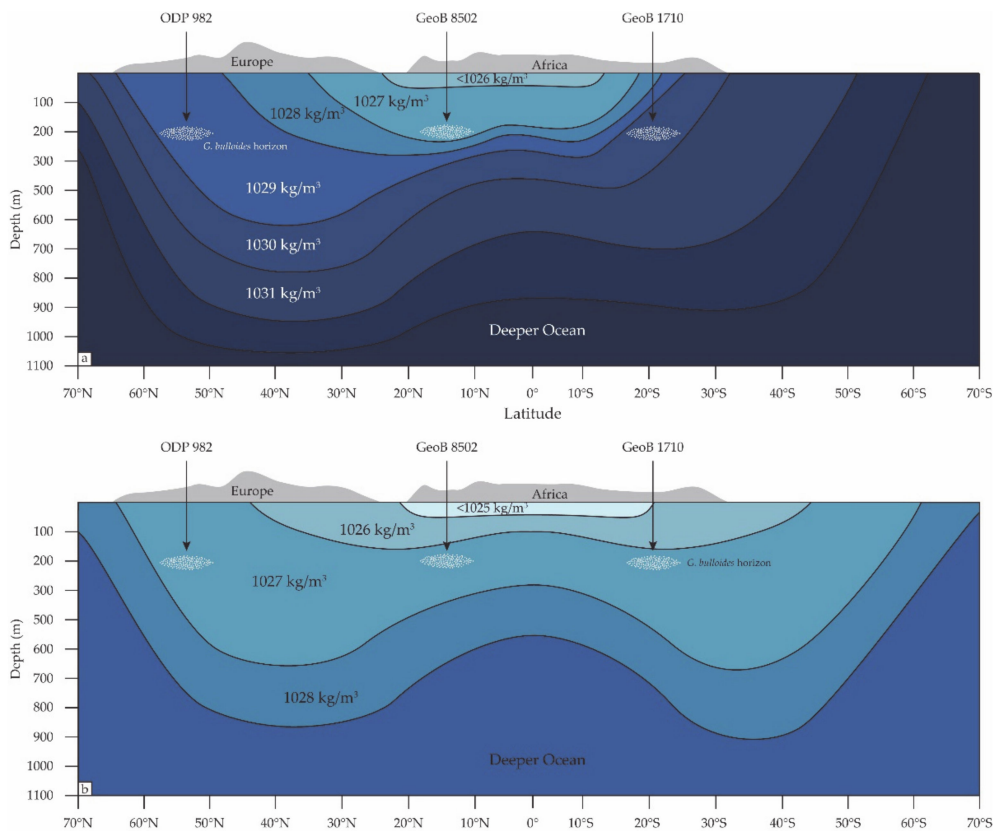


Figure 5. The hydrographic properties of water parcels are strongly influenced by the atmosphere through air–sea interaction and once subducted from the surface layer the density (temperature and salinity) of a water parcel is conserved and remains constant since mixing across isopycnal surfaces is generally much weaker than mixing on isopycnal surfaces [77]. In oceanic regions of normal salinity conditions, the latitudinal temperature changes determine the density of the subducted waters. (a) During extreme glacial conditions, such as the LGM, enhanced atmospheric thermal gradients increase the number of seawater subduction zones that lead to enhanced oceanic density gradients (Figure 3) and thus more vigorous oceanic circulation; (b) during deglacial times of relaxed thermal gradients, surface ocean stratification prevails that can lead to the cessation of the oceanic circulation (SMCEs). Note the density difference between the glacial and interglacial ocean, which can be up to $\sim 3.5 \text{ kg/m}^3$ [78] due to ice cap buildup. However, the seawater density of tropical regions under the influence of the ITCZ is expected to be stable with perhaps only small glacial/interglacial variations.

The surface ocean density values during MIS 5e ($\sim 1026.8 \text{ kg/m}^3$) were found to be remarkably similar to the values recorded for SMCE I during Termination I ($\sim 18.4 \text{ ka}$) and for most of the Holocene. $^{231}\text{Pa}/^{230}\text{Th}$ radiochemical data from sediment core OCE326-GGC5 from the western subtropical Atlantic also provide independent evidence of a collapse and rapid resumption of the AMOC [5]. In that $^{231}\text{Pa}/^{230}\text{Th}$ record, the circulation is found to momentarily cease at 17.5 kyr ago, during the H1 stadial. This is a few hundred years later than suggested from the convergence of the planktonic foraminifera shell weight records. This discrepancy may be due to the difference in the resolution of the records and/or because the response time of sediment $^{231}\text{Pa}/^{230}\text{Th}$ to changes in circulation is $\sim 500 \text{ yr}$ [68,79]. Thus, the $^{231}\text{Pa}/^{230}\text{Th}$ profiles lag the information of surface ocean circulation changes that is provided by the foraminifera proxy.

The two records also agree in the duration of the shutdown of the AMOC, which appears to last 2000 yr by the $^{231}\text{Pa}/^{230}\text{Th}$ signal and 1600 to 2000 years in the foraminiferal records. The synchrony between changes in $^{231}\text{Pa}/^{230}\text{Th}$ and foraminifera weights suggests a connection between the AMOC and local surface hydrography, and the inferred near-cessation of AMOC during early deglaciation appears to be directly linked to the freshening and increased buoyancy of Northern Atlantic surface water during the H1 [80–82]. During this event, decreasing *G. bulloides* shell weights were recorded in three additional cores from

the N. Atlantic, all converging towards the beginning of the Holocene [43]. These findings thus support earlier suggestions that melt water associated with catastrophic iceberg discharge freshened the high-latitude surface ocean, stabilized the water column, and weakened the AMOC [83,84]. The results indicate that the effect was dramatic, resulting in a near-total collapse of the AMOC possibly during periods of substantial regional cooling.

Present planktonic foraminifera shell weight records reveal an attenuation of surface Atlantic density gradients after SMCE 1 (~18.4 ka), and this is supported by investigations that provide ample evidence for large-scale glacial and deglacial AMOC reorganizations [85–87]. While discrepancies remain between the different studies regarding the timing, overall tendency, and amplitude of circulation variations [88], there is a general consensus that AMOC variability was subdued during the Holocene compared with the last glacial termination [89,90]. This is also supported by the present record, where similar shell weight values are shown to characterize entire Holocene sections ($14.1 \pm 0.6 \mu\text{g}$), suggesting no major changes in AMOC during at least the past 18 kyr (Figure 3). The slightly steeper gradients during the early Holocene imply a weakly increased rate of AMOC, supporting previous findings [5], but the convergence of shell mass values in the most recent sediment samples supports recent studies that suggest a decline in the AMOC strength during the past centuries [91–93]. However, these results must be confirmed with additional high-resolution analyses.

5.2. Assessing Atlantic Planktonic Foraminifera Shell Mass Records as Seawater Density and AMOC Proxies

The use of planktonic foraminifera shell mass as a seawater paleodensity proxy has revealed changes in the circulation mode of the Atlantic Ocean and has provided estimates of absolute past density values of the seawater column at the depths where *G. bulloides* live when they attain a cell size of 300–355 μm . The average Atlantic Ocean density during the periods of quasi-total cessation of the AMOC was found to be $\sim 1026.82 \text{ kg/m}^3$. This value is similar to 1026.72 kg/m^3 , which is the average density reconstructed for the modern ocean by the three core top samples and refers to a depth of 130–170 m in the study area today [94]. Such depths are in the range of the calcification depths reported for *G. bulloides* for the southern Atlantic [95], the Indian [96] and Southern Ocean [97], and the Atlantic [98,99], although for the N. Atlantic shallower depths have also been reported [100]. Since calcification depths change with ontogeny and thus with size [99,101], it is reasonable to assume that specimens as large as 355 μm calcify at greater depths and so the proposed reconstructions are plausible. However, like many applications of transfer functions on fossil foraminifera to reconstruct past environments, the shell-weight-based seawater density reconstructions fundamentally rely on the assumption of stable environmental niches in both space and time. Niche stability in environmental space is found to be greatest for subpolar species such as *G. bulloides* across glacial and interglacial intervals [102].

Planktonic foraminifera shell mass biomineralization responds very differently to atmospheric $p\text{CO}_2$ with latitude (Figure 2a,c) if at all (Figure 2b). Shell weight variability is greater at intermediate latitudes and especially at those related to the descending limb of the Hadley circulation, such as the region of core GeoB 1710-3. The increased shell masses recorded during the last glacial maximum could also have been attributed to enhanced upwelling, a wind-driven oceanic circulation, of denser water masses during the LGM but this is definitely not the case for core GeoB 8502-2, which is beneath one of the major upwelling areas in the Atlantic Ocean [30]. Furthermore, the intervals of shell weight convergence between the records would suggest an instantaneous decline in the wind-driven circulation and its attenuation of 18 ka for which no evidence exists. Alternatively, the shell weight variations are overall better explained by changes in the thermohaline circulation that match the $^{231}\text{Pa}/^{230}\text{Th}$ geochemical indications of AMOC cessation and thus increased shell masses are related to densification of the Atlantic waters. The geochemically reconstructed density estimates for SMCE II from GeoB 8502-2 in Table 2 agree within error (which is $\pm 1.73 \text{ kg/m}^3$ [17]) with the weight-based density estimates;

however, more geochemical analyses of the present records are required to confirm the accuracy of the results.

6. Conclusions

Species-specific planktonic foraminifera shell weights have the potential to be a valuable tool for the determination of surface ocean paleoseawater circulation and thus a powerful proxy for physical paleoceanographic applications in paleoclimatology. The use of planktonic foraminifera shell weight as a direct seawater paleodensity proxy has revealed two intervals in the Atlantic Ocean during the past 200 kyr, when the meridional circulation may have been disrupted momentarily due to the absence of interhemispheric seawater density gradients in the Atlantic. Shell-weight-based seawater density values not only converge in the three studied cores within these extraordinary intervals but they also converge between both of these intervals to the same value, which also characterizes the modern Atlantic Ocean density at the same depth horizons. After the convergence at 18 ka, the Atlantic seawater density gradients alleviate and this weakening suggests a decline in the AMOC strength with only small variability thereafter.

Furthermore, it confirms that the surface South Atlantic has always been denser [67] and that, after the last convergence (at ~18.4 Ka) towards the Holocene, the interhemispheric surface Atlantic density gradients alleviate, possibly suggesting an attenuated AMOC thereafter.

Supplementary Materials: The following are available online at <https://www.mdpi.com/article/10.3390/jmse9050519/s1>, Table S1: *G. bulloides* sieve (300–355 μm) based shell weights from core GeoB 1710-3, Table S2: Biometric analyses of X μ CT scanned *G. bulloides* specimens.

Funding: This research was published during my research fellowship at the University of Oxford funded by the Royal Society.

Data Availability Statement: The raw tomographic data from the X μ CT scanning of *G. bulloides* specimens from core GeoB 8502-2 can be found at 10.6084/m9.figshare.14370959 and for core GeoB 1710-3 at 10.6084/m9.figshare.14397884.

Acknowledgments: I would like to thank the University of Bremen in Germany and the University of Cambridge in the United Kingdom for providing sample materials and resources. I would also like to thank the Maxwell Institute at the University of Cambridge for providing the X-ray facilities. This research was completed during my research fellowship in the University of Oxford, funded by the Royal Society under the Newton International Fellowships scheme.

Conflicts of Interest: The author declares no conflict of interest.

References

1. Sigman, D.M.; Hain, M.P.; Haug, G.H. The polar ocean and glacial cycles in atmospheric CO₂ concentration. *Nature* **2010**, *466*, 47–55. [[CrossRef](#)] [[PubMed](#)]
2. Srokosz, M.A.; Bryden, H.L. Observing the Atlantic Meridional Overturning Circulation yields a decade of inevitable surprises. *Science* **2015**, *348*, 1255575. [[CrossRef](#)] [[PubMed](#)]
3. Wunsch, C. What Is the Thermohaline Circulation? *Science* **2002**, *298*, 1179–1181. [[CrossRef](#)] [[PubMed](#)]
4. Fedorov, A.; Barreiro, M.; Boccaletti, G.; Pacanowski, R.; Philander, S.G. The Freshening of Surface Waters in High Latitudes: Effects on the Thermohaline and Wind-Driven Circulations. *J. Phys. Oceanogr.* **2007**, *37*, 896–907. [[CrossRef](#)]
5. McManus, J.F.; Francois, R.; Gherardi, J.M.; Keigwin, L.D.; Brown-Leger, S. Collapse and rapid resumption of Atlantic meridional circulation linked to deglacial climate changes. *Nature* **2004**, *428*, 834–837. [[CrossRef](#)]
6. Robinson, L.F.; Adkins, J.F.; Keigwin, L.D.; Southon, J.; Fernandez, D.P.; Wang, S.-L.; Scheirer, D.S. Radiocarbon Variability in the Western North Atlantic During the Last Deglaciation. *Science* **2005**, *310*, 1469–1473. [[CrossRef](#)]
7. Rogerson, M.; Bigg, G.R.; Rohling, E.J.; Ramirez, J. Vertical density gradient in the eastern North Atlantic during the last 30,000 years. *Clim. Dyn.* **2012**, *39*, 589–598. [[CrossRef](#)]
8. Lynch-Stieglitz, J.; Adkins, J.F.; Curry, W.B.; Dokken, T.; Hall, I.R.; Herguera, J.C.; Hirschi, J.J.-M.; Ivanova, E.V.; Kissel, C.; Marchal, O.; et al. Atlantic Meridional Overturning Circulation During the Last Glacial Maximum. *Science* **2007**, *316*, 66–69. [[CrossRef](#)]
9. Lipps, J.H. Ecology and Paleoecology of Planktic Foraminifera. In *Foraminiferal Ecology and Paleoecology*; Lipps, J.H., Berger, W.H., Buzas, M.A., Douglas, R.G., Ross, C.A., Eds.; SEPM Society for Sedimentary Geology: Tulsa, OK, USA, 1979; Volume 6, pp. 62–104.

10. Hemleben, C.; Anderson, O.R.; Spindler, M. *Modern Planktonic Foraminifera*; Springer: New York, NY, USA, 1989.
11. Emiliani, C. Depth habitats of some species of pelagic foraminifera as indicated by oxygen isotope ratios. *Am. J. Sci.* **1954**, *252*, 149–158. [[CrossRef](#)]
12. de Nooijer, L.J.; Toyofuku, T.; Kitazato, H. Foraminifera promote calcification by elevating their intracellular pH. *Proc. Natl. Acad. Sci. USA* **2009**, *106*, 15374–15378. [[CrossRef](#)]
13. Toyofuku, T.; Matsuo, M.Y.; de Nooijer, L.J.; Nagai, Y.; Kawada, S.; Fujita, K.; Reichart, G.-J.; Nomaki, H.; Tsuchiya, M.; Sakaguchi, H.; et al. Proton pumping accompanies calcification in foraminifera. *Nat. Commun.* **2017**, *8*, 14145. [[CrossRef](#)]
14. Erez, J. Vital effect on stable-isotope composition seen in foraminifera and coral skeletons. *Nature* **1978**, *273*, 199–202. [[CrossRef](#)]
15. Marszalek, D.S. The role of heavy skeletons in vertical movements of non-motile zooplankton. *Mar. Behav. Physiol.* **1982**, *8*, 295–303. [[CrossRef](#)]
16. Campbell, R.W.; Dower, J.F. Role of lipids in the maintenance of neutral buoyancy by zooplankton. *Mar. Ecol. Prog. Ser.* **2003**, *263*, 93–99. [[CrossRef](#)]
17. Zarkogiannis, S.D.; Antonarakou, A.; Tripathi, A.; Kontakiotis, G.; Mortyn, P.G.; Drinia, H.; Greaves, M. Influence of surface ocean density on planktonic foraminifera calcification. *Sci. Rep.* **2019**, *9*, 533. [[CrossRef](#)]
18. Embley, R.W.; Morley, J.J. Quaternary sedimentation and paleoenvironmental studies off Namibia (South-West Africa). *Mar. Geol.* **1980**, *36*, 183–204. [[CrossRef](#)]
19. De Ruijter, W.P.M.; Biastoch, A.; Drijfhout, S.S.; Lutjeharms, J.R.E.; Matano, R.P.; Pichevin, T.; van Leeuwen, P.J.; Weijer, W. Indian-Atlantic interocean exchange: Dynamics, estimation and impact. *J. Geophys. Res.* **1999**, *104*, 20885–20910. [[CrossRef](#)]
20. Garzoli, S.L.; Gordon, A.L. Origins and variability of the Benguela Current. *J. Geophys. Res.* **1996**, *101*, 897–906. [[CrossRef](#)]
21. Lutjeharms, J.R.E. The exchange of water between the South Indian and South Atlantic Oceans. In *The South Atlantic: Present and Past Circulation*; Wefer, G., Berger, W.H., Siedler, G., Webb, D.J., Eds.; Springer: Berlin/Heidelberg, Germany, 1996; pp. 125–162.
22. Bainbridge, A.E. *GEOSECS Atlantic Expedition: Sections and Profiles*; National Science Foundation: Washington, DC, USA, 1980.
23. Broecker, W.; Blanton, S.; Smethie, W.M., Jr.; Ostlund, G. Radiocarbon decay and oxygen utilization in the Deep Atlantic Ocean. *Glob. Biogeochem. Cycles* **1991**, *5*, 87–117. [[CrossRef](#)]
24. Stramma, L.; England, M. On the water masses and mean circulation of the South Atlantic Ocean. *J. Geophys. Res.* **1999**, *104*, 20863–20883. [[CrossRef](#)]
25. Reid, J.L. On the total geostrophic circulation of the South Atlantic Ocean: Flow patterns, tracers, and transports. *Prog. Oceanogr.* **1989**, *23*, 149–244. [[CrossRef](#)]
26. Sloyan, B.M. Antarctic bottom and lower circumpolar deep water circulation in the eastern Indian Ocean. *J. Geophys. Res.* **2006**, *111*, C02006. [[CrossRef](#)]
27. Dittert, N.; Henrich, R. Carbonate dissolution in the South Atlantic Ocean: Evidence from ultrastructure breakdown in *Globigerina bulloides*. *Deep Sea Res. Part 1 Oceanogr. Res. Pap.* **2000**, *47*, 603–620. [[CrossRef](#)]
28. Christl, M.; Mangini, A. Water mass properties and circulation in the Cape Basin. A multiproxy approach. *Geochim. Cosmochim. Acta* **2009**, *73*, A224.
29. Volbers, A.N.A.; Henrich, R. Late Quaternary variations in calcium carbonate preservation of deep-sea sediments in the northern Cape Basin: Results from a multiproxy approach. *Mar. Geol.* **2002**, *180*, 203–220. [[CrossRef](#)]
30. Aouni, A.E.; Daoudi, K.; Yahia, H.; Minaoui, K.; Benazzouz, A. Surface mixing and biological activity in the North-West African upwelling. *Chaos Interdiscip. J. Nonlinear Sci.* **2019**, *29*, 011104. [[CrossRef](#)]
31. Mittelstaedt, E. The ocean boundary along the northwest African coast: Circulation and oceanographic properties at the sea surface. *Prog. Oceanogr.* **1991**, *26*, 307–355. [[CrossRef](#)]
32. Stramma, L.; Hóttl, S.; Schafstall, J. Water masses and currents in the upper tropical northeast Atlantic off northwest Africa. *J. Geophys. Res.* **2005**, *110*, C12006. [[CrossRef](#)]
33. Howe, J.N.W.; Piotrowski, A.M.; Noble, T.L.; Mulitza, S.; Chiessi, C.M.; Bayon, G. North Atlantic Deep Water Production during the Last Glacial Maximum. *Nat. Commun.* **2016**, *7*, 11765. [[CrossRef](#)]
34. Didié, C.; Bauch, H.A. Species composition and glacial-interglacial variations in the ostracode fauna of the northeast Atlantic during the past 200,000 years. *Mar. Micropaleontol.* **2000**, *40*, 105–129. [[CrossRef](#)]
35. Broecker, W.S. Thermohaline circulation, the Achilles heel of our climate system: Will man-made CO₂ upset the current balance? *Science* **1997**, *278*, 1582–1588. [[CrossRef](#)] [[PubMed](#)]
36. Hansen, B.; Østerhus, S.; Quadfasel, D.; Turrell, W. Already the day after tomorrow? *Science* **2004**, *305*, 953–954. [[CrossRef](#)] [[PubMed](#)]
37. Kawase, M.; Sarmiento, J.L. Circulation and nutrients in middepth Atlantic waters. *J. Geophys. Res.* **1986**, *91*, 9749–9770. [[CrossRef](#)]
38. Manighetti, B.; McCave, I.N. Late glacial and Holocene palaeocurrents around Rockall Bank, NE Atlantic Ocean. *Paleoceanography* **1995**, *10*, 611–626. [[CrossRef](#)]
39. Barker, S.; Archer, D.; Booth, L.; Elderfield, H.; Henderiks, J.; Rickaby, R.E.M. Globally increased pelagic carbonate production during the Mid-Brunhes dissolution interval and the CO₂ paradox of MIS 11. *Quat. Sci. Rev.* **2006**, *25*, 3278–3293. [[CrossRef](#)]
40. Zarkogiannis, S.D.; Antonarakou, A.; Fernandez, V.; Mortyn, P.G.; Kontakiotis, G.; Drinia, H.; Greaves, M. Evidence of stable foraminifera biomineralization during the last two climate cycles in the tropical Atlantic Ocean. *J. Mar. Sci. Eng.* **2020**, *8*, 737. [[CrossRef](#)]
41. Schmiedl, G.; Mackensen, A. Age model of sediment core GeoB1710-3. *PANGAEA* **1997**. [[CrossRef](#)]






42. Volbers, A.N.A.; Niebler, H.S.; Giraudeau, J.; Schmidt, H.; Henrich, R. Paleooceanographic changes in the northern Benguela upwelling system over the last 245,000 years as derived from planktic foraminifera assemblages. In *The South Atlantic in the Late Quaternary: Reconstruction of Material Budget and Current Systems*; Wefer, G., Mulitza, S., Ratmeyer, V., Eds.; Springer: Berlin/Heidelberg, Germany; New York, NY, USA, 2004; pp. 601–622.
43. Barker, S.; Kiefer, T.; Elderfield, H. Temporal changes in North Atlantic circulation constrained by planktonic foraminiferal shell weights. *Paleoceanography* **2004**, *19*, PA3008. [[CrossRef](#)]
44. Volbers, A.N.A.; Henrich, R. Present water mass calcium carbonate corrosiveness in the eastern South Atlantic inferred from ultrastructural breakdown of *Globigerina bulloides* in surface sediments. *Mar. Geol.* **2002**, *186*, 471–486. [[CrossRef](#)]
45. Zarkogiannis, S.D.; Kontakiotis, G.; Gkaniatsa, G.; Kuppili, V.S.C.; Marathe, S.; Wanelik, K.; Lianou, V.; Besiou, E.; Makri, P.; Antonarakou, A. An Improved Cleaning Protocol for Foraminiferal Calcite from Unconsolidated Core Sediments: HyPerCal—A New Practice for Micropaleontological and Paleoclimatic Proxies. *J. Mar. Sci. Eng.* **2020**, *8*, 998. [[CrossRef](#)]
46. Broecker, W.; Clark, E. An evaluation of Lohmann’s Foraminifera weight dissolution index. *Paleoceanography* **2001**, *16*, 531–534. [[CrossRef](#)]
47. Zarkogiannis, S.; Fernandez, V.; Greaves, M.; Mortyn, P.G.; Kontakiotis, G.; Antonarakou, A. X-ray tomographic data of planktonic foraminifera species *Globigerina bulloides* from the Eastern Tropical Atlantic across Termination II. *Gigabyte* **2020**, *1*. [[CrossRef](#)]
48. Iwasaki, S.; Kimoto, K.; Sasaki, O.; Kano, H.; Uchida, H. Sensitivity of planktic foraminiferal test bulk density to ocean acidification. *Sci. Rep.* **2019**, *9*, 9803. [[CrossRef](#)]
49. Cheng, J.; Liu, Z.; Zhang, S.; Liu, W.; Dong, L.; Liu, P.; Li, H. Reduced interdecadal variability of Atlantic Meridional Overturning Circulation under global warming. *Proc. Natl. Acad. Sci. USA* **2016**, *113*, 3175–3178. [[CrossRef](#)]
50. Schenk, F.; Välranta, M.; Muschitiello, F.; Tarasov, L.; Heikkilä, M.; Björck, S.; Brandefelt, J.; Johansson, A.V.; Näslund, J.-O.; Wohlfarth, B. Warm summers during the Younger Dryas cold reversal. *Nat. Commun.* **2018**, *9*, 1634. [[CrossRef](#)]
51. Zarkogiannis, S.D.; Kontakiotis, G.; Antonarakou, A.; Mortyn, P.G.; Drinia, H. Latitudinal Variation of Planktonic Foraminifera Shell Masses During Termination I. *IOP Conf. Ser. Earth Environ. Sci.* **2019**, *221*, 12052. [[CrossRef](#)]
52. Gordon, A.L.; Piola, A.R. Atlantic Ocean Upper Layer Salinity Budget. *J. Phys. Oceanogr.* **1983**, *13*, 1293–1300. [[CrossRef](#)]
53. Johnson, G.C.; Schmidtko, S.; Lyman, J.M. Relative contributions of temperature and salinity to seasonal mixed layer density changes and horizontal density gradients. *J. Geophys. Res. Ocean.* **2012**, *117*. [[CrossRef](#)]
54. Deininger, M.; McDermott, F.; Cruz, F.W.; Bernal, J.P.; Mudelsee, M.; Vonhof, H.; Millo, C.; Spötl, C.; Treble, P.C.; Pickering, R.; et al. Inter-Hemispheric synchronicity of Holocene precipitation anomalies controlled by Earth’s latitudinal insolation gradients. *Nat. Commun.* **2020**, *11*, 5447. [[CrossRef](#)]
55. Davis, B.A.S.; Brewer, S. Orbital forcing and role of the latitudinal insolation/temperature gradient. *Clim. Dyn.* **2009**, *32*, 143–165. [[CrossRef](#)]
56. Stokes, S.; Haynes, G.; Thomas, D.S.G.; Horrocks, J.L.; Higginson, M.; Malifa, M. Punctuated aridity in southern Africa during the last glacial cycle: The chronology of linear dune construction in the northeastern Kalahari. *Palaeogeogr. Palaeoclimatol. Palaeoecol.* **1998**, *137*, 305–322. [[CrossRef](#)]
57. Fuhrmann, F.; Diensberg, B.; Gong, X.; Lohmann, G.; Sirocko, F. Aridity synthesis for eight selected key regions of the global climate system during the last 60,000 years. *Clim. Past* **2020**, *16*, 2221–2238. [[CrossRef](#)]
58. Tierney, J.E.; deMenocal, P.B.; Zander, P.D. A climatic context for the out-of-Africa migration. *Geology* **2017**, *45*, 1023–1026. [[CrossRef](#)]
59. Lisiecki, L.E.; Raymo, M.E. A Pliocene-Pleistocene stack of 57 globally distributed benthic $\delta^{18}\text{O}$ records. *Paleoceanography* **2005**, *20*, PA1003. [[CrossRef](#)]
60. Rohling, E.J.; Fenton, M.; Jorissen, F.J.; Bertrand, P.; Ganssen, G.; Caulet, J.P. Magnitudes of sea-level lowstands of the past 500,000 years. *Nature* **1998**, *394*, 162–165. [[CrossRef](#)]
61. Heinrich, H. Origin and consequences of cyclic ice rafting in the Northeast Atlantic Ocean during the past 130,000 years. *Quat. Res.* **1988**, *29*, 142–152. [[CrossRef](#)]
62. McManus, J.F.; Oppo, D.W.; Cullen, J.L. A 0.5-Million-Year Record of Millennial-Scale Climate Variability in the North Atlantic. *Science* **1999**, *283*, 971–975. [[CrossRef](#)]
63. Margari, V.; Skinner, L.C.; Tzedakis, P.C.; Ganopolski, A.; Vautravers, M.; Shackleton, N.J. The nature of millennial-scale climate variability during the past two glacial periods. *Nat. Geosci.* **2010**, *3*, 127–131. [[CrossRef](#)]
64. Hodell, D.A.; Channell, J.E.T.; Curtis, J.H.; Romero, O.E.; Röhl, U. Onset of “Hudson Strait” Heinrich events in the eastern North Atlantic at the end of the middle Pleistocene transition (~640 ka)? *Paleoceanography* **2008**, *23*. [[CrossRef](#)]
65. Chappell, J. Sea level changes forced ice breakouts in the Last Glacial cycle: New results from coral terraces. *Quat. Sci. Rev.* **2002**, *21*, 1229–1240. [[CrossRef](#)]
66. Martínez-Méndez, G.; Zahn, R.; Hall, I.R.; Peeters, F.J.C.; Pena, L.D.; Cacho, I.; Negre, C. Contrasting multiproxy reconstructions of surface ocean hydrography in the Agulhas Corridor and implications for the Agulhas Leakage during the last 345,000 years. *Paleoceanography* **2010**, *25*, PA4227. [[CrossRef](#)]
67. Reid, J.L. On the temperature, salinity, and density differences between the Atlantic and Pacific oceans in the upper kilometre. *Deep Sea Res.* **1961**, *7*, 265–275. [[CrossRef](#)]
68. Marchal, O.; François, R.; Stocker, T.F.; Joos, F. Ocean thermohaline circulation and sedimentary $^{231}\text{Pa}/^{230}\text{Th}$ ratio. *Paleoceanography* **2000**, *15*, 625–641. [[CrossRef](#)]

69. Mokeddem, Z.; McManus, J.F.; Oppo, D.W. Oceanographic dynamics and the end of the last interglacial in the subpolar North Atlantic. *Proc. Natl. Acad. Sci. USA* **2014**, *111*, 11263–11268. [CrossRef]
70. Irvah, N.; Ninnemann, U.S.; Kleiven, H.F.; Galaasen, E.V.; Morley, A.; Rosenthal, Y. Evidence for regional cooling, frontal advances, and East Greenland Ice Sheet changes during the demise of the last interglacial. *Quat. Sci. Rev.* **2016**, *150*, 184–199. [CrossRef]
71. Guihou, A.; Pichat, S.; Govin, A.; Nave, S.; Michel, E.; Duplessy, J.-C.; Telouk, P.; Labeyrie, L. Enhanced Atlantic Meridional Overturning Circulation supports the Last Glacial Inception. *Quat. Sci. Rev.* **2011**, *30*, 1576–1582. [CrossRef]
72. Labeyrie, L.D.; Duplessy, J.C.; Blanc, P.L. Variations in mode of formation and temperature of oceanic deep waters over the past 125,000 years. *Nature* **1987**, *327*, 477–482. [CrossRef]
73. Johnsen, S.J.; Dahl-Jensen, D.; Gundestrup, N.; Steffensen, J.P.; Clausen, H.B.; Miller, H.; Masson-Delmotte, V.; Sveinbjörnsdottir, A.E.; White, J. Oxygen isotope and palaeotemperature records from six Greenland ice-core stations: Camp Century, Dye-3, GRIP, GISP2, Renland and NorthGRIP. *J. Quat. Sci.* **2001**, *16*, 299–307. [CrossRef]
74. McManus, J.F.; Oppo, D.W.; Keigwin, L.D.; Cullen, J.L.; Bond, G.C. Thermohaline Circulation and Prolonged Interglacial Warmth in the North Atlantic. *Quat. Res.* **2017**, *58*, 17–21. [CrossRef]
75. Risebrobakken, B.; Dokken, T.; Jansen, E. Extent and Variability of the Meridional Atlantic Circulation in the Eastern Nordic Seas During Marine Isotope Stage 5 and its Influence on the Inception of the Last Glacial. In *The Nordic Seas: An Integrated Perspective*; American Geophysical Union: Washington, DC, USA, 2005; pp. 323–339. [CrossRef]
76. Khodri, M.; Leclainche, Y.; Ramstein, G.; Braconnot, P.; Marti, O.; Cortijo, E. Simulating the amplification of orbital forcing by ocean feedbacks in the last glaciation. *Nature* **2001**, *410*, 570–574. [CrossRef]
77. Tomczak, M.; Godfrey, J.S. Water mass formation, subduction, and the oceanic heat budget. In *Regional Oceanography*; Tomczak, M., Godfrey, J.S., Eds.; Pergamon: Amsterdam, The Netherlands, 1994; pp. 53–65. [CrossRef]
78. Roberts, J.; Gottschalk, J.; Skinner, L.C.; Peck, V.L.; Kender, S.; Elderfield, H.; Waelbroeck, C.; Vázquez Riveiros, N.; Hodell, D.A. Evolution of South Atlantic density and chemical stratification across the last deglaciation. *Proc. Natl. Acad. Sci. USA* **2016**, *113*, 514–519. [CrossRef]
79. Yu, E.-F.; Francois, R.; Bacon, M.P. Similar rates of modern and last-glacial ocean thermohaline circulation inferred from radiochemical data. *Nature* **1996**, *379*, 689–694. [CrossRef]
80. Bond, G.; Heinrich, H.; Broecker, W.; Labeyrie, L.; McManus, J.; Andrews, J.; Huon, S.; Jantschik, R.; Clasen, S.; Simet, C.; et al. Evidence for massive discharges of icebergs into the North Atlantic ocean during the last glacial period. *Nature* **1992**, *360*, 245–249. [CrossRef]
81. Bard, E.; Rostek, F.; Turon, J.-L.; Gendreau, S. Hydrological Impact of Heinrich Events in the Subtropical Northeast Atlantic. *Science* **2000**, *289*, 1321–1324. [CrossRef]
82. Duplessy, J.C.; Labeyrie, L.; Arnold, M.; Paterne, M.; Duprat, J.; van Weering, T.C.E. Changes in surface salinity of the North Atlantic Ocean during the last deglaciation. *Nature* **1992**, *358*, 485–488. [CrossRef]
83. Vidal, L.; Labeyrie, L.; Cortijo, E.; Arnold, M.; Duplessy, J.C.; Michel, E.; Becqué, S.; van Weering, T.C.E. Evidence for changes in the North Atlantic Deep Water linked to meltwater surges during the Heinrich events. *Earth Planet. Sci. Lett.* **1997**, *146*, 13–27. [CrossRef]
84. Elliot, M.; Labeyrie, L.; Duplessy, J.-C. Changes in North Atlantic deep-water formation associated with the Dansgaard–Oeschger temperature oscillations (60–10 ka). *Quat. Sci. Rev.* **2002**, *21*, 1153–1165. [CrossRef]
85. Lippold, J.; Gutjahr, M.; Blaser, P.; Christner, E.; de Carvalho Ferreira, M.L.; Mulitza, S.; Christl, M.; Wombacher, F.; Böhm, E.; Antz, B.; et al. Deep water provenance and dynamics of the (de)glacial Atlantic meridional overturning circulation. *Earth Planet. Sci. Lett.* **2016**, *445*, 68–78. [CrossRef]
86. Lynch-Stieglitz, J. The Atlantic Meridional Overturning Circulation and Abrupt Climate Change. *Ann. Rev. Mar. Sci.* **2017**, *9*, 83–104. [CrossRef]
87. Oppo, D.W.; Gebbie, G.; Huang, K.-F.; Curry, W.B.; Marchitto, T.M.; Pietro, K.R. Data Constraints on Glacial Atlantic Water Mass Geometry and Properties. *Paleoceanogr. Paleoclimatol.* **2018**, *33*, 1013–1034. [CrossRef]
88. Lippold, J.; Pöppelmeier, F.; Süfke, F.; Gutjahr, M.; Goepfert, T.J.; Blaser, P.; Friedrich, O.; Link, J.M.; Wacker, L.; Rheinberger, S.; et al. Constraining the Variability of the Atlantic Meridional Overturning Circulation During the Holocene. *Geophys. Res. Lett.* **2019**, *46*, 11338–11346. [CrossRef]
89. Keigwin, L.D.; Boyle, E.A. Detecting Holocene changes in thermohaline circulation. *Proc. Natl. Acad. Sci. USA* **2000**, *97*, 1343–1346. [CrossRef] [PubMed]
90. Oppo, D.W.; McManus, J.F.; Cullen, J.L. Deepwater variability in the Holocene epoch. *Nature* **2003**, *422*, 277. [CrossRef] [PubMed]
91. Caesar, L.; Rahmstorf, S.; Robinson, A.; Feulner, G.; Saba, V. Observed fingerprint of a weakening Atlantic Ocean overturning circulation. *Nature* **2018**, *556*, 191–196. [CrossRef]
92. Rahmstorf, S.; Box, J.E.; Feulner, G.; Mann, M.E.; Robinson, A.; Rutherford, S.; Schaffernicht, E.J. Exceptional twentieth-century slowdown in Atlantic Ocean overturning circulation. *Nat. Clim. Chang.* **2015**, *5*, 475–480. [CrossRef]
93. Thornalley, D.J.R.; Oppo, D.W.; Ortega, P.; Robson, J.I.; Brierley, C.M.; Davis, R.; Hall, I.R.; Moffa-Sanchez, P.; Rose, N.L.; Spooner, P.T.; et al. Anomalously weak Labrador Sea convection and Atlantic overturning during the past 150 years. *Nature* **2018**, *556*, 227–230. [CrossRef]
94. Argo. Argo Float Data and Metadata from Global Data Assembly Centre (Argo GDAC). SEANOE: 2000. Available online: <https://www.seanoe.org/data/00311/42182/> (accessed on 1 February 2021). [CrossRef]

95. Mortyn, P.G.; Charles, C.D. Planktonic foraminiferal depth habitat and $\delta^{18}\text{O}$ calibrations: Plankton tow results from the Atlantic sector of the Southern Ocean. *Paleoceanography* **2003**, *18*, 1037. [[CrossRef](#)]
96. Saraswat, R.; Khare, N. Deciphering The Modern Calcification Depth Of Globigerina Bulloides In The Southwestern Indian Ocean From Its Oxygen Isotopic Composition. *J. Foraminifer. Res.* **2010**, *40*, 220–230. [[CrossRef](#)]
97. Prasanna, K.; Ghosh, P.; Bhattacharya, S.K.; Mohan, K.; Anilkumar, N. Isotopic disequilibrium in Globigerina bulloides and carbon isotope response to productivity increase in Southern Ocean. *Sci. Rep.* **2016**, *6*, 21533. [[CrossRef](#)]
98. Kretschmer, K.; Jonkers, L.; Kucera, M.; Schulz, M. Modeling seasonal and vertical habitats of planktonic foraminifera on a global scale. *Biogeosciences* **2018**, *15*, 4405–4429. [[CrossRef](#)]
99. Schiebel, R.; Hemleben, C. Interannual variability of planktic foraminiferal populations and test flux in the eastern North Atlantic Ocean (JGOFS). *Deep Sea Res. Part II Top. Stud. Oceanogr.* **2000**, *47*, 1809–1852. [[CrossRef](#)]
100. Vázquez Riveiros, N.; Govin, A.; Waelbroeck, C.; Mackensen, A.; Michel, E.; Moreira, S.; Bouinot, T.; Caillon, N.; Orgun, A.; Brandon, M. Mg/Ca thermometry in planktic foraminifera: Improving paleotemperature estimations for G. bulloides and N. pachyderma left. *Geochem. Geophys. Geosyst.* **2016**, *17*, 1249–1264. [[CrossRef](#)]
101. Emiliani, C. Depth habitats of growth stages of pelagic foraminifera. *Science* **1971**, *173*, 1122–1124. [[CrossRef](#)]
102. Waterson, A.M.; Edgar, K.M.; Schmidt, D.N.; Valdes, P.J. Quantifying the stability of planktic foraminiferal physical niches between the Holocene and Last Glacial Maximum. *Paleoceanography* **2017**, *32*, 74–89. [[CrossRef](#)]

Article

The Environmental Impact of a Complex Hydrogeological System on Hydrocarbon-Pollutants' Natural Attenuation: The Case of the Coastal Aquifers in Eleusis, West Attica, Greece

Panayota Makri ^{1,*}, Eleni Stathopoulou ², Demetrios Hermides ³ , George Kontakiotis ¹ ,
Stergios D. Zarkogiannis ¹ , Hariklia D. Skilodimou ⁴, George D. Bathrellos ⁵ ,
Assimina Antonarakou ¹  and Michael Scoullou ²

¹ Department of Historical Geology-Paleontology, Faculty of Geology & Geoenvironment, School of Earth Sciences, National & Kapodistrian University of Athens, Zografou University Hill, 15784 Athens, Greece; gkontak@geol.uoa.gr (G.K.); stergiosz@geol.uoa.gr (S.D.Z.); aantonar@geol.uoa.gr (A.A.)

² Faculty of Chemistry, School of Earth Sciences, National & Kapodistrian University of Athens, Zografou University Hill, 15772 Athens, Greece; estath@chem.uoa.gr (E.S.); scoullou@chem.uoa.gr (M.S.)

³ Department of Natural Resources Management & Agricultural Engineering, Agricultural University of Athens, 11855 Athens, Greece; dermides@aua.gr

⁴ Department of Geomorphology and Climatology, Faculty of Geology & Geoenvironment, School of Earth Sciences, National & Kapodistrian University of Athens, Zografou University Hill, 15784 Athens, Greece; hskilodimou@geol.uoa.gr

⁵ Sector of General, Marine Geology & Geodynamics, Department of Geology, University of Patras, Rio, 26504 Patras, Greece; gbathrellos@upatras.gr

* Correspondence: pmakri@geol.uoa.gr

Received: 16 October 2020; Accepted: 10 December 2020; Published: 13 December 2020



Abstract: The study area is the Thriassion Plain, an important area, in antiquity, surrounding the famous ancient town of Eleusis, 20 km west of Athens. The modern town and port and the entire area were heavily industrialized (1965–1995) coupled with unregulated urban and agricultural development. The presence of two crude oil refineries and other oil-related industries have strongly impacted the entire environment, including soils, waters and sediments of the broader area. The purpose of this work is to better understand how a multi-layered groundwater system affects the potential underground spread of certain fuel volatile compounds, namely the BTEX (benzene, toluene, ethylbenzene and total xylenes) as well as their attenuation after their direct or indirect release into the aquifer system. The spatial distribution of BTEX in groundwaters show that they were concentrated mainly in four rather restricted locations. Three of them were spotted, as expected, in the close vicinity of known pollution sources (a military airfield and two crude oil refineries). The other one corresponds to an abandoned site with no outstanding pollution sources where wells exist, eventually used for illegal dumping of oily wastes. It is important that the concentrations decrease significantly from autumn to spring. This decline could be characterized as natural attenuation, related to natural dilution phenomena and a flushing out of pollutants discharging through underwater springs to the sea during the rainy period (October to April). This, in turn, could be associated to the specific geological conditions affecting the hydrology, such as the unconsolidated non-permeable deposits and the multi layered formations of the area's aquifers.

Keywords: BTEX natural attenuation; hydro-stratigraphy; multi-layered aquifer; Thriassion Plain; confined and unconfined aquifer; coastal aquifer; Gulf of Eleusis

1. Introduction

Our study area is the Thriassion Plain, in the Attica Prefecture, located 25 km west of Athens. It covers a surface of 480 km², characterized by a relatively smooth relief with altitudes up to 100 m and comprises the town of Aspropyrgos, Eleusis (pronounced Elefsis) and Magoula (Figure 1). The broader area is a historical and cultural landmark of Greece since prehistory. In the period 1965–1995, the area experienced a rapid unprogrammed, industrialization, which, in combination with the lack of environmental infrastructures, resulted in generation and accumulation of urban and industrial wastes, natural resources degradation and environmental hazards [1–3], turning the area into one of the most polluted Mediterranean regions. The drainage receptor of the study area is the Gulf of Eleusis, a semi enclosed embayment within the Saronikos Gulf, one of the most important areas in terms of the ecological status- and climate change-related coastal hazards [4,5] and biomonitoring [6] in the Eastern Mediterranean Sea. The Gulf of Eleusis and the Saronikos Gulf represent the seaward boundary of the metropolitan area of Athens and Piraeus whereas within the Thriassion Plain some of the biggest industrial installations of the country exist, such as oil refineries, steel mills and cement factories, and shipyards. The industrialization and land use changes have affected the sea bottom sediments [7–9], the soil [10,11], and the water column dynamics of the Gulf of Eleusis [12,13] which is the final receptor of human activities in the plain [14–17]. Among the industries involved with oil refining, processing and transport, the Refinery of Aspropyrgos (known as ELPE), the Refinery of Eleusis, and the relics of a petroleum recycling unit (CYCLON), along with the Military Airfield may potentially be responsible for hydrocarbon leakages to the groundwater, which is used in industries and for irrigation of agricultural lands. The first evidence of groundwater contamination from hydrocarbons was reported by Kounis et al. [18]. Ever since, the presence of aliphatic and PAHs pollution in coastal marine waters and tissues was documented [19] while some groundwater oil-remediation was merely reported for the area of the Refinery of Aspropyrgos [20].

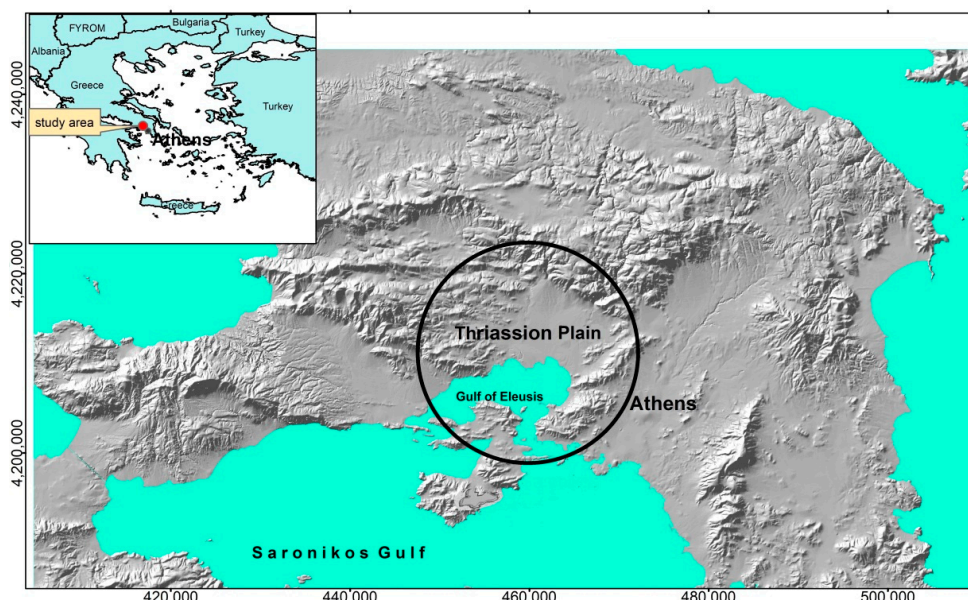


Figure 1. The study area.

The present study investigates the potential groundwater pollution from BTEX (benzene, toluene, ethylbenzene and xylenes) within the complex aquifer system of the Thriassion Plain. It was carried out by the National and Kapodistrian University of Athens and supported by the General Secretariat of Research and Technology. The research was considered of critical importance by the Local Authorities because it provided feedback to the environmental management of the area as well as a starting point for further investigations necessary to address the complex pollution issues of the region.

2. BTEX Characteristics and Fate into the Aquifers

The BTEX forms about the 16% of a typical gasoline blend and is associated with adverse impact on human-health. Although the individual BTEX compounds are widely used as solvents and in manufacturing, gasoline leaks from underground storage tanks and distribution pipelines are the primary contributor of BTEX contamination in ground water [21].

Among the four BTEX compounds, benzene is classified as a carcinogen by the European Union Council Directive 98/83/EC, the U.S. Environmental Protection Agency and the International Agency for Research on Cancer. As a result of this concern, threshold levels in freshwater have been established, namely the Maximum Contamination Limits (MCL) [22,23]. Nevertheless, respective thresholds or permissible levels in groundwaters have not been set, so far. Table 1 presents the BTEX MCLs, expressed in parts per million (ppm, or mg/L) in the EU and several other countries with high recorded oil pollution.

Table 1. The MCLs of BTEX.

	EU (mg/L)	US EPA (mg/L)	China (mg/L)	Canada (mg/L)	New Zealand (mg/L)	Japan (mg/L)
Benzene	0.001	0.005	0.01	0.005	0.01	0.01
Toluene	Not legislated	1	0.7	0.024	0.8	0.2
Xylenes	Not legislated	10	0.5	0.3	0.	0.4
Ethylbenzene	Not legislated	0.7	0.3	0.0024	0.3	Not legislated

It is well known that many organic contaminants exist in a liquid phase and are not soluble in water. These are the Non-Aqueous Phase Liquids (NAPLs) which include fuels (gasoline, aviation fuel), chlorinated solvents, and polychlorinated biphenyls. In a typical petroleum hydrocarbon contamination incident, such as an underground leaking of a storage tank or pipeline, the escaping organic substance (e.g., gasoline) usually moves downwards through the unsaturated or vadose zone until it reaches the aquifer. There, the mobility of the organic substance (e.g., hydrocarbon) decreases as water saturation increases respectively and accumulation takes place particularly at the interface, above the water-table.

Some important parameters determining the environmental fate of the organic substance are the compound's volatility (gaseous phase), solubility in water (aqueous phase), specific weight determining floating or sinking in the aqueous zone, and affinity to minerals and other organic compounds and surfaces, determining sorption (absorption/adsorption and dissolution) [24]. Furthermore, the degradation rate of the compound depends on the presence of bacteria and fungi species, the environmental conditions (temperature, aquifer minerals, organic matter content), and the availability and concentration of carbon sources available to the microbial consortia. The rate of biodegradation tends to slow down when DO concentrations are less than about 1–2 ppm. Anaerobic biodegradation of benzene appears to be more aquifer specific than that for the other monoaromatic hydrocarbons [25–27].

3. Geology and Hydrogeological Characteristics of the Study Area

The Palaeozoic formations, 300 to 400 m thick, are the geological basement of the broader area. The Palaeozoic is represented by (a) clastic materials, shales and sandstones, which alternate with greywackes and conglomerates; (b) basic igneous volcanic rocks; and (c) lenticular intercalations of thin bedded carbonate units. Weak metamorphism, successive folds and schistosity are also observed. This background is overlain by Mesozoic sediments such as: (a) phyllites and sandstone, (b) meta-pyroclastic and meta-volcanic rocks hornstones and tuffs; (c) Triassic limestones, dolomitic limestones and dolomites; and (d) Cretaceous limestones. The Cenozoic is represented by: (a) Paleocene flysch; (b) Neogene deposits of marls with lignite intercalations in places, sandstone, marly limestone; and (c) Pleistocene (clay, sands, gravels, torrential fans of loosely and cohesive conglomerates) and Late Quaternary alluvial deposits (clay, loams, sands and gravels) at the top [28–30]. The geological settings are illustrated in Figure 2.

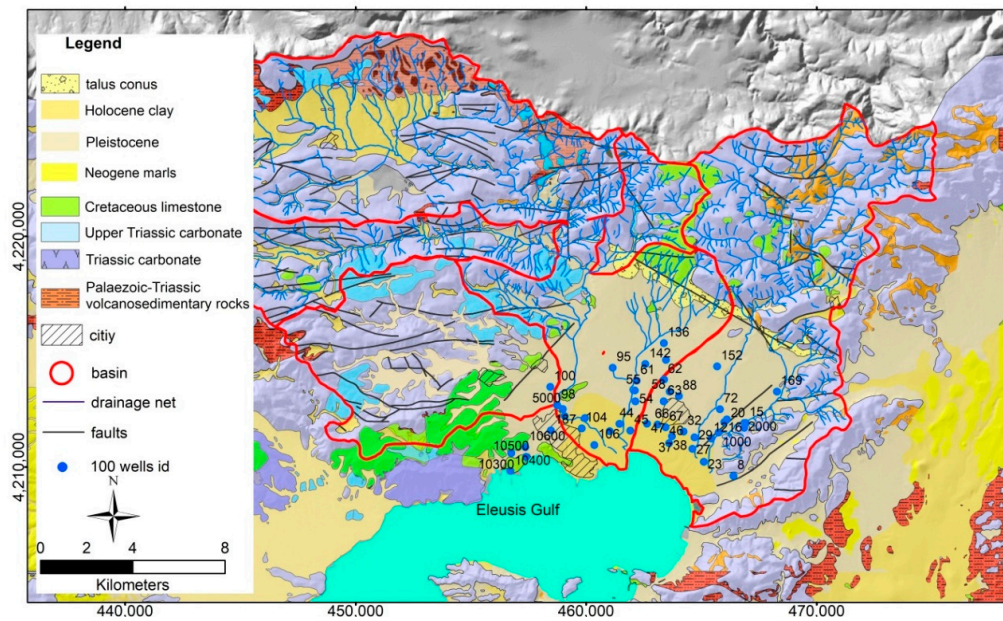


Figure 2. The geology of the study area.

The hydrogeology of the broader area has been extremely influenced by hydro-stratigraphic and tectonic factors as well as sea level changes [29–34]. The paleogeographic evolution, the aquifer geometry and thickness, the salinity controls, and the groundwater input are important features for the water source management. In past studies two main aquifer systems were described: (1) the Plio–Pleistocene sediments and (2) the Triassic limestone/dolomite and the Cretaceous limestone [18,28,35,36].

Recent detailed hydrogeological research studies [37,38] have recalculated the aquifer characteristics, providing a revised hydrogeological model of three distinct groundwater hydrostratigraphic units (including their subunits): (a) the Neogene–Quaternary sediments comprising (a.1) the Holocene–Upper Pleistocene aquifer system, generally unconfined and semi-confined consisted of clays, sands and gravels. It is recharged by rainfall and upward leakage from lower aquifers. The Holocene clays form local barriers to groundwater flow, causing the formation of marshes and swamps and/or upward leakage. The coastal clay strata prevent the lower standing aquifers from direct seawater intrusion where groundwater of good quality was found 90 m below sea level (m.b.s.l.) [37,38]; (a.2) the Pleistocene system, made up of marls with lignite layers in places, sands and marly limestones which is a multi-layered confined aquifer. There is Pleistocene sediments recharge and preferential lateral flow from the carbonate basement. The direction of the groundwater flow within the confined layers is SE, where a partly upward leakage onto the coastal zone occurs while, the main water volume is moving very slowly towards the Saronikos Gulf with hydraulic gradient 1–2‰. (b) The Cretaceous aquifer, west of the study area, is fractured and forms an unconfined aquifer of high productivity with not well-known thickness, but with hydraulic contact with the sea, and finally, (c) The Triassic aquifer, either confined or unconfined which has been affected by karstification and tectonism. The latter is comprised of limestones, dolomitic limestones and dolomites. The Cretaceous and Triassic aquifers flow to the southwest and discharge partly through coastal springs near the city of Eleusis and the entire North-Western coastline of the Eleusis Gulf and partly into Neogene–Quaternary deposits [39,40]. From this field work, the seasonal water level fluctuations in the unconfined aquifer were measured 0.4–0.5 m and within the confined aquifers 1.2–1.5 m. A conceptual model of the deposits in Figure 3 illustrates the multi-level aquifer conditions within the Pleistocene strata, where lenticular intercalation consists of a water-yielding formation [31].

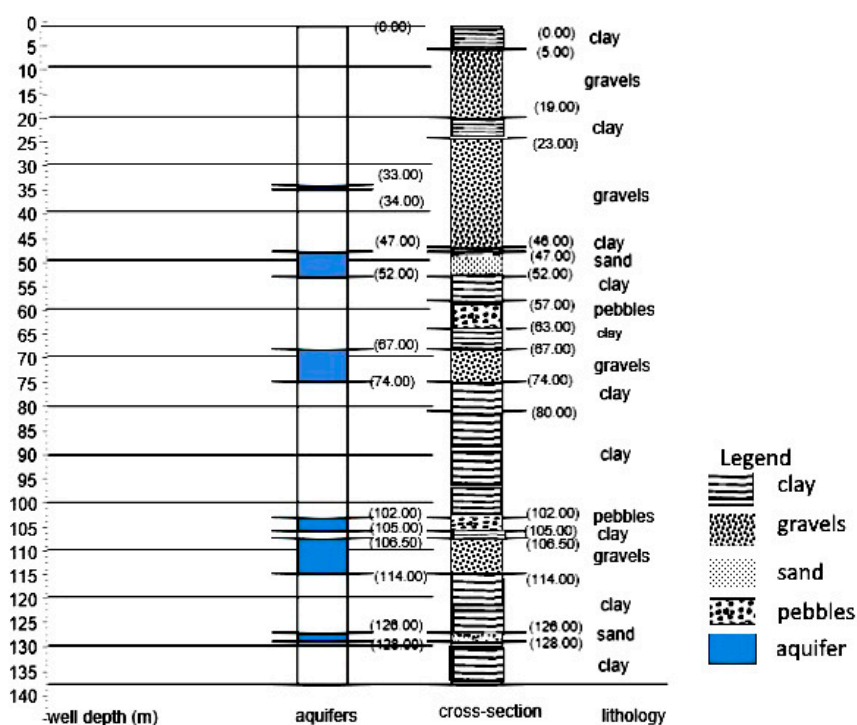


Figure 3. Conceptual hydro-stratigraphic column of the Plio-Pleistocene.

4. Materials and Methods

The sampled area included all major potential polluting sources, from crude oil refineries and other related industries and the Military Airfield, as well as the city of Eleusis itself. Thirty-four (34) to forty-five (45) groundwater samples were collected, twice a year, in November and May, when the water level was at the lowest and the highest level, respectively. The whole investigation lasted three years, from 2003 to 2005. The results of the in-situ survey, including water level measurements, and lithology identification of each sampling location, are reported in Table 2. Sampling, storage, shipping and laboratory characterization of the target analytes were carried out according to USEPA Analytical Method 524.2 [41] in the Laboratory of Environmental Chemistry, Department of Chemistry, National and Kapodistrian University of Athens (NKUA). The samples were collected from the first five centimeters of the water surface of the wells or by pumping from the boreholes. The Solid Phase Microextraction (SPME) was applied to pre-concentrate the BTEX [42–44]. Gas Chromatography (GC) was applied to separate the compounds from the water samples, and Mass Spectrometry (MS) to detect them. The chromatography results were validated through the protocol procedures (linearity, precision, recover, standards). The Limits of Detection (LOD) achieved with the method applied were 0.095 ppb for benzene, 0.077 ppb for toluene, 0.099 ppb for ethylbenzene and 0.089 ppb for total xylenes [44]. The quantified results were illustrated on a GIS database to assess the distribution of the pollutants within the aquifers. The estimation of the groundwater spatial dispersion (spatial analysis) was accomplished using an ArcGIS software. The data layers were digitized and stored in the database, including sampling-well locations with the analytical data, main industries and drainage network, road network and towns/settlements. The concentrations were presented on concentration-contour maps. Using the Geostatistical analyst extension of ArcGIS, the initial values of each parameter (i.e., concentration BTEX compound) for a sampling season were interpolated in grid layers with a cell size of 20 × 20 m. The inverse squared distance (ISD) method was used to interpolate the data obtained. The contour maps provided, refer to the concentrations of benzene for all sampling seasons. The classification of the concentration values in the contour maps is different among the four target analytes, therefore when a target analyte has a wide range of concentrations (e.g., xylenes) there are more classes in the GIS map.

Table 2. Hydrogeological characteristics of the wells; (U), (C) and (L) stands for unconfined, confined and semi-confined aquifer respectively; hydraulic head.

Well (W)/Borehole (B) Id	Age, Lithology, Aquifer Type	Hydraulic Head (M.A.S.L.)				
		03 November	04 May	04 November	05 May	05 November
1B	Triassic carbonate (U)	140.00 to 160.00				
3B	Triassic carbonate (U)	78.00 to 80.00				
8W	Pleistocene sediments (C)	4.35	4.68	4.37	4.77	4.63
12W	Pleistocene sediments (L)	5.00	5.53	5.47	5.55	5.65
15W	Pleistocene sediments (L)	no data				
16W	Pleistocene sediments (L)	4.90	5.51	4.22	6.57	5.24
20W	Pleistocene sediments (L)	4.85	5.35	4.99	5.47	4.88
22W	Pleistocene sediments (U)	5.53	5.88	no data		
23/24W	Holocene clay (U)	5.98	4.15	4.16	4.01	3.13
27W	Holocene clay (U)	2.91	3.56	2.82	3.43	2.91
29W	Pleistocene sediments (C)	3.10	4.52	4.93	4.73	4.68
32W	Pleistocene sediments (L)	no data			2.95	3.46
37W	Holocene clay (U)	2.20	2.95	3.38	3.35	3.40
38W	Holocene clay(U)	1.85	2.22	2.80	2.32	1.75
44W	Holocene clay (L)	1.96	2.23	1.93	2.17	1.78
45W	Holocene clay (U)	1.65	1.90	2.36	1.96	1.48
46W	Holocene clay (U)	2.38	2.70	2.40	2.10	1.69
47W	Holocene clay (U)	1.13	1.40	1.45	1.45	1.20
54W	Pleistocene sediments (L)	4.03	4.56	4.42	4.69	4.05
55W	Pleistocene sediments (L)	6.10	4.93	3.09	5.08	4.21
58W	Pleistocene sand with clay intercalations (C)	3.60	4.10	4.90	5.13	3.88
61W	Pleistocene pebbles (L)	4.96	5.01	4.74	4.82	4.52
62W	Pleistocene pebbles (L)	5.37	7.19	5.35	7.10	6.38
63W	Pleistocene pebbles with clay intercalations (L)	3.60	4.39	3.89	4.67	3.92
66W	Pleistocene sediments with clay intercalations (L)	1.00	1.40	1.20	1.50	0.77
67W	Pleistocene with clay intercalations (L)	2.40	2.73	2.45	2.10	1.69
72W	Pleistocene gravels (U)	4.90	5.70	5.38	6.04	5.43
86/88W	Clay (L)	3.30	3.90	4.86	4.96	5.25
95W	Pleistocene sediments (U)	1.12	1.82	0.62	1.92	1.22
98W	Pleistocene sediments (U)	4.98	5.26	5.03	5.10	4.61
100W	Pleistocene sediments (U)	4.20	4.40	4.15	4.25	3.90
102W	Pleistocene pebbles (U)	2.65	2.95	2.90	2.88	2.35
104B	Pleistocene pebbles (U)	26.00 to 27.00				
106W	Holocene sediments and pebbles (U)	0.70	1.20	0.55	1.28	1.60
134W	Pleistocene sediments (C)	4.80	6.00	5.30	7.40	6.99
136W	Pleistocene sediments (C)	5.20	6.05	4.95	5.90	7.01
142W	Pleistocene sediments (C)	6.10	6.14	5.92	6.24	7.11
152W	Pleistocene sediments (C)	95.00 to 102.00				
169B	Triassic carbonate (U)	85.00 to 88.00				
187W	Pleistocene (U)	3.26	3.76	3.40	3.74	3.19
1000W	Pleistocene sediments (U)	3.66	4.02	3.95	4.12	3.89
2000W	Triassic carbonates (U)					
3000W	Pleistocene aggregates (U)	1.50	1.65	1.84	1.50	1.76
5000W	Pleistocene conglomerates (U)	3.29	4.40	3.70	4.65	4.60
4000W	Pleistocene conglomerates (U)	6.29	6.63	6.42	6.48	6.15
(Petrola) ¹ 10300W	Holocene clay (U)	no data		6.92	7.00	no data
(Petrola) 10400W	Holocene clay (U)	no data		1.66	2.00	no data
(Pyrkal) 10500W	Holocene clay (U)	no data		0.25	0.25	no data
(Pyrkal) 10600W	Triassic carbonate (U)	no data		2.50	2.43	no data

¹ Refinery of Eleusis.

5. Results and Discussion

The nonspatial analysis which involves the results of the target pollutants laboratory determination, is provided with the concentration values presented in Supplementary Material (Table S1 for benzene, Table S2 for toluene, Table S3 for ethylbenzene and in Table S4 for the xylenes). All values are expressed in parts per billion (ppb). The sample id "22" was considered unsuitable for chromatographic determination, because its oily texture and odor appeared likely to provoke damage to the instrumentation. The produced results of the first year indicated the need to broaden/expand the sampling area.

The BTEX are not commonly found in nature, as for instance the metals, and since they are hazardous for human health, it could be considered that every concentration over a non-detectable level may be regarded as "pollution" or "contamination". Regarding benzene values, we remark that seventeen (17) out of forty-five (45) samples exceeded the EU MCL in all autumn monitoring seasons, and another five (5) once or twice again in autumn. Overall, benzene pollution might be alleged as not-at-a high-risk, though significant. More specifically, in November 2003, the concentrations of benzene range from the detection limit up to 29 ppb, in May 2004 the water level had an average rise of 0.45 m and the maximum concentration was 14 ppb, whereas the concentrations of all other samples were significantly lower than the ones in November 2003. In November 2004, new samples were collected from the Refinery of Eleusis (id Petrola "10300", Petrola "10400") and the industrial area of Pyrcal (id "10500", "10600", at the western boundary of the study area). Exactly at the same area, the maximum concentration (57 ppb) was found. Between May and November 2004, the average fall of the water level was 0.24 m. In May 2005 concentrations ranged from the detection limit up to 16 ppb, and the average rise of the water level was 0.39 m. Finally, in November 2005, the concentrations ranged from the detection limit up to 20 ppb and it seems that they were slightly lower than in the previous autumn sampling periods. Moreover, the sample id "22" was a mix of water and oil, which raised the question of its origin (a "backdoor" discharge?). This sample was not chromatographically characterized at all, to avert damage to the analytical instrumentation but has served as a "guide" for new sampling in the surrounding area.

As for the concentrations of toluene, ethylbenzene and xylenes, their values were much lower than their MCLs (Supplementary Material). More specifically, the pollution of toluene can be assumed as negligible to low, since its concentration values are much lower than the MCL. The maximum concentration of 45 ppb (still, lower than the MCL) was reported in the installations of the "Pyrcal" industry (id "10500" and "10600"). For ethylbenzene, almost all values are close to the detection limit. For the xylenes, the pollution should also be considered as negligible to low, compared to its MCL. Moreover, it is remarkable that, after the winter rainfall, the BTEX concentration values in May are significantly reduced, reaching very low to non-detectable levels. This may be attributed to the significant dilution of the target compounds by the recharge of the aquifer, which at the end, discharges to the sea through submarine water springs at the western boundary of the study area, mainly.

Concerning the spatial distribution depicted on the GIS contour maps, four separate locations of benzene pollution are developed: (a) northeast of the Hellenic Refinery of Aspropyrgos (ELPE), (b) at the western and the eastern boundaries of the Military Airfield of Eleusis, (c) south-east of the town of Aspropyrgos and (d) next to the Refinery of Aspropyrgos (ELPE). Figures 4–8 illustrate the estimated groundwater distribution. The spatial distribution of toluene, ethylbenzene and xylenes is the same as benzene; therefore, the results are not presented and commented for each compound individually.

The standard deviation is very high only for benzene for all monitoring seasons. As for the other compounds, the variability is potentially attributed to, either the existence of a non-permanent pollution input or, an eventually differentiated natural attenuation. The examination of the $(B + T)/(E + X)$ ratio could provide some useful information on the original time of gasoline release [44,45]. Due to the difference in their mobility, concentration ratios of the individual BTEX compounds (e.g., B/E, T/X, etc.) in fuel-contaminated groundwater tend to change uniformly with time. The relative content of BTEX compounds in manufactured gasoline has varied with time; initial ratio values are often unavailable, which limits wide application of these ratios as time indicators. Although, in the study area we cannot

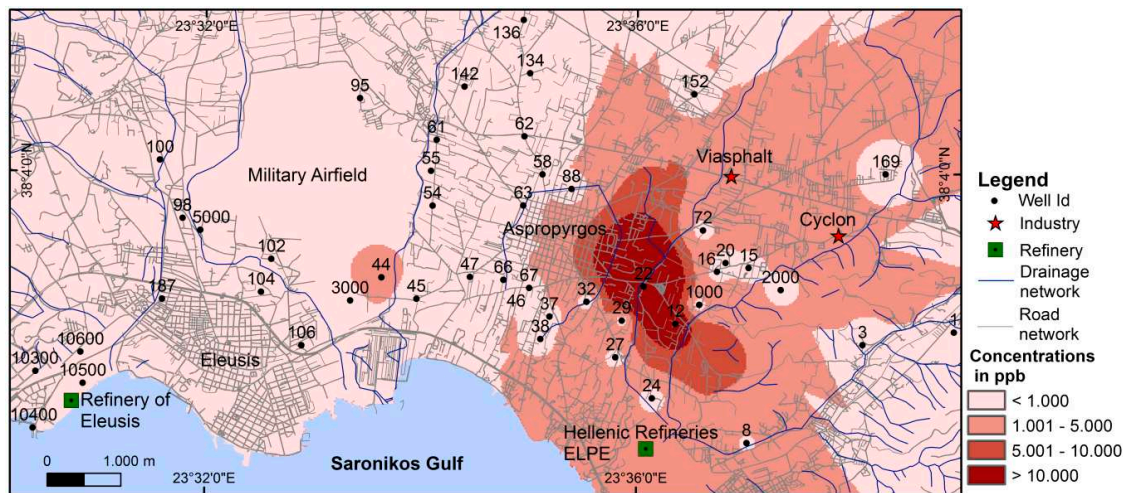


Figure 7. The estimated groundwater distribution of benzene in May 2005.

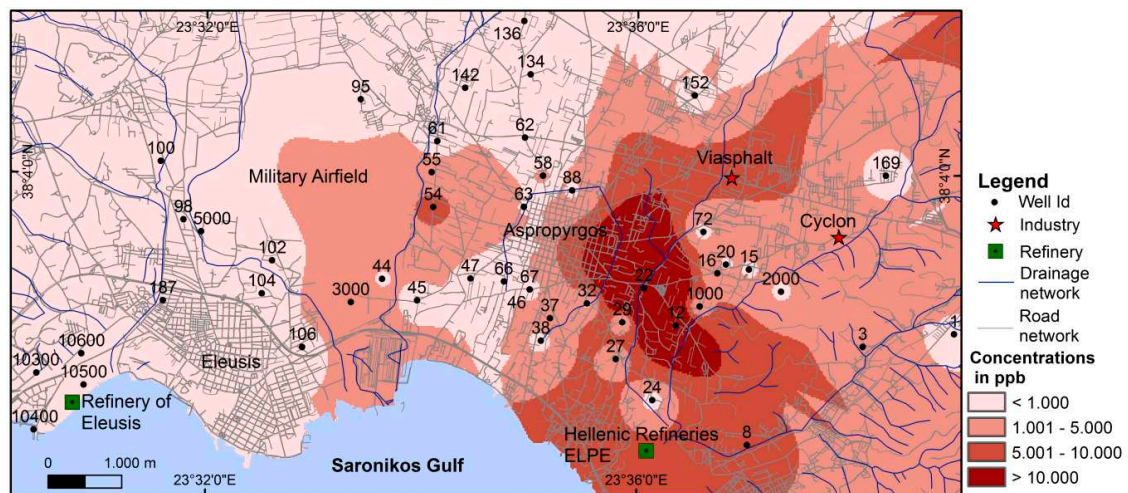


Figure 8. The estimated groundwater distribution of benzene in November 2005.

Kaplan’s multiple investigations [45,46], mostly empirical, have shown that near the source and immediately after a gasoline spill, R_b reaches values between 1.5 and 6, which indicates a recent release (typically <5 years). In the absence of NAPL, R_b in a dissolved gasoline plume is close to that of the original gasoline ($0.8 < R_b < 1.1$). The ratio then decreases as a function of time, and values less than 0.5 usually reflecting gasoline residence time longer than 10 years. $R_b = 6.6$ confirms the presence of a thick gasoline rich layer. In general, a two-fold decrease of R_b occurs in 2.3 years.

Applying the R_b values onto our reported concentrations, we may conclude that for the Refinery of Eleusis (id “10300”, “10400”, “10500” and “10600”), located at the western boundaries of the contour maps, where the highest concentration values were reported, the calculated $R_b < 0.5$ indicates a long permanent BTEX occurrence. For the second most polluted area surrounding the Military Airfield, (sample id “98”, “5000” at west, “3000”, “44” at south, “54”, “55” at east), the calculated $1.5 < R_b < 6$ reveals a recent release of BTEX, consistent to the nature of the pollution source, including heavy local atmospheric pollution from the fuel used in planes and the washing out of the atmosphere by rain. The fact that the groundwater from the southern boundaries of the Airfield (id “102”, “104”, “106”) seems not to be affected by BTEX release due to the confined nature of the groundwater system, might be partly attributed to geomorphological and hydrological specifications not yet fully understood. As for the concentrations near the Refinery of Aspropyrgos (id “8”), the $R_b < 0.5$ indicates a long permanent BTEX source. Apparently, the city of Eleusis itself seems not to be polluted from BTEX, though it is located at the furthest downgradient part of the aquifer flow lines. Theoretically, the

pollution should “track” the groundwater flow into the Gulf of Eleusis and, thus pollution should have visibly affected the southern areas, near the coastline. It is likely that the benzene has not reached the gulf because of biodegradation along the flow paths. Biodegradation is an important process attenuating benzene and other BTEX constituents in groundwater in many areas.

Finally, it is worthwhile to examine the occurrence of 0.6 ppb and 2.4 ppb at the boreholes with id “1”, “3”, located within the Triassic carbonates (limestone/dolomites). There, the groundwater is pumped within the Mesozoic limestones from a depth of 78 up to 160 m, with no evident pollution source nearby. If we exclude an ad hoc illegal pollution, benzene contamination may be explained by some hydraulic communication between the Pleistocene sediments and the carbonate ones.

Overall, the local character of the BTEX occurrence may be documented by the confined, multi-layered hydro-stratigraphic system as well as, the existence of impermeable aquifer barriers. Additionally, the very low concentrations of the spring sampling periods reveal both a good aeration and a dynamic seasonal enrichment/dilution of the groundwater system.

6. Conclusions and Suggestions

The laboratory determination and the spatial analysis and study of BTEX, in the Thriassion Plain lead to some useful general conclusions: Some high concentrations from BTEX were identified in autumn when the water table is at the furthest downgradient level. Benzene concentration values are much more elevated than those of the other BTEX compounds. The spring concentrations of all compounds are very low. The considerably reduced rainfall of the summer months coupled with enhanced abstraction through groundwater pumping could explain the difference between the autumn and spring benzene concentrations. The high values of benzene as well as the empirical Kaplan’s values, indicate that the pollution originates mainly from permanent sources namely oil refinery and handling sources, located relatively close to the sampling points. The spatial distribution of BTEX in groundwaters show that they were concentrated mainly in four, rather restricted locations. Three of them were in the close vicinity of evident pollution sources (a military airfield and two crude oil refineries), whereas, the other one corresponds to an abandoned site with no outstanding pollution sources where wells exist, eventually used occasionally for illegal dumping of oily wastes. The town of Eleusis seems not to be polluted from BTEX, despite the fact that it is located at the lowest part of the aquifer flow lines. This could be attributed to impermeable strata working as water and pollution barriers. The hydro-stratigraphic particularities, along with general hydrogeochemical conditions play an important role to the BTEX fate and attenuation rate.

Recent developments in the expansion of the works of the refineries, including changes in the operations of the Military airport, make it necessary, in our point of view, to proceed to a new and deeper BTEX pollution investigation, to revisit our approached attenuation after 15 years of operation. In case that further studies and monitoring demonstrate that the pollution persists, the National and Local Authorities should take urgently active and effective measures to prevent further deterioration and environmental damage. The designation of the city of Eleusis as cultural capital of Europe 2021, though somehow disturbed by COVID-19, may offer an opportunity for also refocusing on environmental pollution and the groundwater as a valuable natural resource that requires further attention including by keeping it free from hydrocarbon pollution.

Supplementary Materials: The following are available online at <http://www.mdpi.com/2077-1312/8/12/1018/s1>, Table S1. Concentrations of benzene, Table S2. Concentrations of toluene, Table S3. Concentrations of ethylbenzene; and Table S4. Concentrations of xylenes.

Author Contributions: Conceptualization, P.M.; methodology, P.M.; statistical analysis (GIS), H.D.S., G.D.B.; validation, P.M., E.S., D.H.; formal analysis, P.M.; investigation, P.M., E.S., D.H., G.K., M.S.; resources, P.M., D.H.; data curation, P.M., E.S.; writing—original draft preparation, P.M.; writing—review and editing, P.M., G.K., E.S., D.H., S.D.Z., A.A.; visualization, P.M.; supervision, M.S., A.A.; project administration M.S., A.A.; funding acquisition, M.S. All authors have read and agreed to the published version of the manuscript.

Funding: This research was co-funded by the General Secretariat of Research and Technology and the National and the Kapodistrian University of Athens (NKUA) in the context of the EU 3rd Framework Programme, Action 8.3.1. (01 ED 150).

Conflicts of Interest: The authors declare no conflict of interest.

References

1. Makri, P.; Kalivas, D.; Bathrellos, G.; Skilodimou, H. Spatio-temporal analysis of groundwater pollution from BTEX Thriassion Field, Attica, Greece. In Proceedings of the 10th IAEG International Congress, Nottingham, UK, 6–10 September 2006.
2. Karavitis, C.A.; Bosdogianni, A.; Vlachos, E.C. Environmental management approaches and water resources in the stressed region of Thriassion, Greece. *Glob. NEST J.* **2001**, *3*, 131–144.
3. Iliopoulos, V.; Stournaras, G.; Stamatis, G. Marine and Human Activity Effects on the Groundwater Quality of Thriassio Plain, Attica, Greece. In *Advances in the Research of Aquatic Environment*; Lambrakis, N., Stournaras, G., Katsanou, K., Eds.; Springer: Berlin/Heidelberg, Germany, 2011; Volume 2, pp. 409–416. [[CrossRef](#)]
4. Pavlidou, A.; Simboura, N.; Pagou, K.; Assimakopoulou, G.; Gerakaris, V.; Hatzianestis, I.; Panayotidis, P.; Pantazi, M.; Papadopoulou, N.; Reizopoulou, S.; et al. Using a holistic ecosystem-integrated approach to assess the environmental status of Saronikos Gulf, Eastern Mediterranean. *Ecol. Indic.* **2014**, *96*, 336–350. [[CrossRef](#)]
5. Karavoltsos, S.; Kalambokis, E.; Sakellari, A.; Plavšić, M.; Dotsika, E.; Karalis, P.; Leondiadis, L.; Dassenakis, M.; Scoullou, M. Organic matter characterization and copper complexing capacity in the sea surface microlayer of coastal areas of the Eastern Mediterranean. *Mar. Chem.* **2015**, *173*, 234–243. [[CrossRef](#)]
6. Antonarakou, A.; Kontakiotis, G.; Zarkogiannis, S.; Mortyn, P.G.; Drinia, H.; Koskeridou, E.; Anastasakis, G. Planktonic foraminiferal abnormalities in coastal and open marine eastern Mediterranean environments: A natural stress monitoring approach in recent and early Holocene. *J. Mar. Syst.* **2018**, *181*, 63–78. [[CrossRef](#)]
7. Karageorgis, A.P.; Botsou, F.; Kaberi, H.; Iliakis, S. Geochemistry of major and trace elements in surface sediments of the Saronikos Gulf (Greece): Assessment of contamination between 1999 and 2018. *Sci. Total Environ.* **2020**, *717*, 137046. [[CrossRef](#)] [[PubMed](#)]
8. Mavrakis, A.; Theoharatos, G.; Asimakopoulos, D.; Christides, A. Distribution of trace metals in the sediments of Elefsis Gulf. *Medit. Mar. Sci.* **2004**, *5*, 151–158. [[CrossRef](#)]
9. Sklivagou, E.; Varnavas, S.P.; Hatzianestis, I.; Kaniaris, G. Assessment of Aliphatic and Polycyclic Aromatic Hydrocarbons and Trace Elements in Coastal Sediments of the Saronikos Gulf, Greece (Eastern Mediterranean). *Mar. Geosources Geotechnol.* **2008**, *26*, 372–393. [[CrossRef](#)]
10. Katsinis, D. Light Hydrocarbon Tracing by Gas Chromatography Method. Contribution to Field Research and to Technical Works-Museum-Environment Protection. Ph.D. Thesis, Athens Polytechnic School, Athens, Greece, 1994; pp. 1–91.
11. Nakos, G. Pollution of soil and vegetation in the Thriasian Plain, Greece. *Plant Soil* **1982**, *66*, 271–277. [[CrossRef](#)]
12. Kontoyiannis, H. Observations on the circulation of the Saronikos Gulf: A Mediterranean embayment sea border of Athens, Greece. *J. Geophys. Res.* **2010**, *115*. [[CrossRef](#)]
13. Evangelidou, N.; Florou, H.; Scoullou, M. A preliminary study of particle dynamics in the water column of Saronikos Gulf, Greece, by using Th-234/U-238 disequilibrium approach. *Desalin. Water Treat.* **2010**, *13*, 290–302. [[CrossRef](#)]
14. Scoullou, M. Lead in coastal sediments—the case of Elefsis Gulf. *Sci. Total Environ.* **1986**, *49*, 199–219. [[CrossRef](#)]
15. Scoullou, M.; Pavlidou, A. Metal speciation studies in a brackish/marine interface system. *Glob. Nest* **2000**, *2*, 255–264.
16. Stathopoulou, E.; Dassenakis, M.; Scoullou, M. Total and methyl-mercury in water samples from Elefsis Gulf, Greece. In Proceedings of the 13th International Symposium on Environmental Pollution and Its Impact on life in the Mediterranean Region (MESAEP), Thessaloniki, Greece, 8–12 October 2005; pp. 119–127.
17. Galanopoulou, S.; Vgenopoulos, A.; Conispoliatis, N. Anthropogenic Heavy Metal Pollution in the Surficial Sediments of the Keratsini Harbor, Saronikos Gulf, Greece. *Water Air Soil Pollut.* **2009**, *202*, 121–130. [[CrossRef](#)]
18. Kounis, G.; Simos, N. *Spot Hydrogeological Survey of Thriassion Plain Aquifers for the Water Supply Needs of the Greek Aspropyrgos Refinery*; Institute of Geological and Mineral Explorations: Athens, Greece, 1991. (In Greek)
19. Valavanidis, A.; Vlachogianni, T.; Triantafyllaki, S.; Dassenakis, M.; Androutsos, M.; Scoullou, M. Polycyclic aromatic hydrocarbons in surface seawater and in indigenous mussels (*Mytilus galloprovincialis*) from coastal areas of the Saronikos Gulf (Greece). *Estuar. Coast. Shelf Sci.* **2008**, *79*, 733–739. [[CrossRef](#)]
20. Aivalioti, M.; Gidarakos, E. In-well air sparging efficiency in remediating the aquifer of a petroleum refinery site. *J. Environ. Eng. Sci.* **2008**, *7*, 71–82. [[CrossRef](#)]

21. U.S. Environmental Protection Agency. *Chemicals Evaluated for Carcinogenic Potential*; Office of Pesticide Programs, Health Effects Division: Washington, DC, USA, 2004; pp. 1–40.
22. U.S. Environmental Protection Agency. *National Drinking Water Standards*; 816-F-02-017; Office of Water: Washington, DC, USA, 2002. Available online: <https://www.epa.gov/ground-water-and-drinking-water/national-primary-drinking-water-regulations> (accessed on 2 September 2020).
23. ATSDR (Agency for Toxic Substances and Disease Registry). *Toxicological Profile for Benzene*; U.S. Public Health Service: Atlanta, GA, USA, 1989.
24. Zhao, B.; Huang, F.; Zhang, C.; Guoxin, H.; Qiang, X.; Fei, L. Pollution characteristics of aromatic hydrocarbons in the groundwater of China. *J. Contam. Hydrol.* **2020**, *233*, 103676. [[CrossRef](#)]
25. Chakraborty, R.; Coates, J.D. Anaerobic degradation of monoaromatic hydrocarbons. *Appl Microbiol. Biotechnol.* **2004**, *64*, 437–446. [[CrossRef](#)]
26. Salanitro, J.P. The role of bioattenuation in the management of aromatic hydrocarbon plumes in aquifers. *Groundw. Monit. Rev.* **1993**, *13*, 150–161. [[CrossRef](#)]
27. Chen, T.C. Understanding the fate of petroleum hydrocarbons in the subsurface environment. *J. Chem. Educ.* **1992**, *69*, 357. [[CrossRef](#)]
28. Katsikatsos, G.; Mettos, A.; Vidakis, M.; Dounas, A.; Pomoni, F.; Tsaila-Monopolis, S.; Skourtsi-Koroneou, V. *Geological Map of Greece, in Scale 1:50.000. "Athina-Elefsis" Sheet*; Institute of Geological and Mineral Explorations (IGME) Publication: Athens, Greece, 1986.
29. Mariolagos, H.; Theocharis, D. Shifting shores in the Saronic Gulf during the last 18,000 years and the Kychreia paleolimni. In Proceedings of the 9th International Conference, Bulletin of Hellenic Geological Society XXXVI 1, Athens, Greece, 26–28 September 2001; pp. 405–413.
30. Dounas, A. *The Geology Between Megara and Erithres Area*; PhD National and Kapodistrian University of Athens: Athens, Greece, 1971.
31. Hermides, D.; Kyriazis, D.; Makri, P.; Ermidou, A. Geochemical evolution of the Thriassion Plain groundwaters, Attica, Greece. *Environ. Monit. Assess.* **2020**, *192*, 561. [[CrossRef](#)]
32. Zacharias, A.; Sarandakos, J.; Andre, C. *Report on Sample Drilling and Morphotectonics Study in the Area Around Koumoundourou Lake*; 2nd Technical Report; Hellenic Center for Marine Research/IIW Anavyssos: Attica, Greece, 2003.
33. Lambeck, K. Sea Level change and shore-line evolution in Aegean Greece since Upper Palaeolithic time. *Antiquity* **1996**, *70*, 588–611. [[CrossRef](#)]
34. Deligiannakis, G.; Papanikolaou, I.D.; Roberts, G. Fault specific GIS based seismic hazard maps for the Attica Region, Greece. *Geomorphology* **2018**, *306*, 264–282. [[CrossRef](#)]
35. Dounas, A.; Panagiotides, G. *Precursor Report on the Hydrogeological Conditions of Thriassion*; Institute of Geology and Subsurface Research: Athens, Greece, 1964.
36. Parashoudis, V. *Hydrogeological Study of Western Attica*; Agricultural Ministry of Greece: Athens, Greece, 2002; p. 165.
37. Hermides, D.; Mimides, T.; Stamatis, G. Contribution to hydraulic characteristics of Plio-Pleistocene deposits of Thriassion Plain of Attica. *Bull. Geol. Soc. Gr.* **2016**, *50*, 967–976. [[CrossRef](#)]
38. Hermides, D. Hydrogeological Conditions of the Thriassion Plain Basin with Emphasis on the Geohydraulic Characteristics of the Aquifers and the Groundwater Quality. Ph.D. Thesis, Agricultural University of Athens, Athens, Greece, 2018; p. 283.
39. Hermides, D.; Stamatis, G. Origin of halogens and their use as environmental tracers in aquifers of Thriassion Plain, Attica, Greece. *Environ. Earth Sci.* **2017**, *76*, 306. [[CrossRef](#)]
40. Hermides, D.; Makri, P.; Kontakiotis, G.; Antonarakou, A. Advances in the coastal and submarine groundwater processes: Controls and environmental impact on the Thriassion Plain and Eleusis Gulf Attica. Greece. *J. Mar. Sci. Eng.* **2020**, *8*, 944. [[CrossRef](#)]
41. U.S. Environmental Protection Agency. *Methods for the Determination of Organic Compounds in Drinking Water—Method 524.2*; U.S. Environmental Protection Agency: Washington DC, USA, 1992.
42. Arthur, C.; Killam, L.; Motlagh, S.; Lim, M.; Potter, D.; Pawlitzyn, J. Analysis of substituted benzene compounds in groundwater using Solid Phase Microextraction. *Environ. Sci. Technol.* **1992**, *26*, 979–983. [[CrossRef](#)]
43. Zhang, Z.; Yang, M.J.; Pawlitzyn, J. Analysis of organic compounds in environmental samples by Headspace Solid Phase Microextraction. *J. High Resol. Chromatogr.* **1993**, *16*, 689–692. [[CrossRef](#)]

44. Makri, P. The Investigation of Petroleum Hydrocarbons in the Neogene-Quaternary Deposits of the Thriassian Plain. Ph.D. Thesis, National and Kapodistrian University of Athens, Athens, Greece, 2008; p. 265.
45. Kaplan, I.; Galperin, Y.; Lu, S.-T.; Lee, R.-P. Forensic Environmental Geochemistry: Differentiation of fuel-types, their sources and release time. *Org. Geochem.* **1997**, *27*, 289–317. [[CrossRef](#)]
46. Odermatt, J. Natural chromatographic separation of benzene, toluene, ethylbenzene and xylenes (BTEX compounds) in a gasoline contaminated ground water aquifer. *Org. Geochem.* **1994**, *21*, 1141–1150. [[CrossRef](#)]

Publisher’s Note: MDPI stays neutral with regard to jurisdictional claims in published maps and institutional affiliations.



© 2020 by the authors. Licensee MDPI, Basel, Switzerland. This article is an open access article distributed under the terms and conditions of the Creative Commons Attribution (CC BY) license (<http://creativecommons.org/licenses/by/4.0/>).

Article

Advances in the Coastal and Submarine Groundwater Processes: Controls and Environmental Impact on the Thriassion Plain and Eleusis Gulf (Attica, Greece)

Demetrios Hermides ^{1,*} , Panayota Makri ², George Kontakiotis ²  and Assimina Antonarakou ²

¹ Department of Natural Resources Management and Agricultural Engineering, Agricultural University of Athens, 11855 Athens, Greece

² Faculty of Geology & Geoenvironment, Department of Historical Geology-Paleontology, School of Earth Sciences, National & Kapodistrian University of Athens, Zografou University Hill, 15774 Athens, Greece; pmakri@geol.uoa.gr (P.M.); gkontak@geol.uoa.gr (G.K.); aantonar@geol.uoa.gr (A.A.)

* Correspondence: dermidis@aua.gr

Received: 30 September 2020; Accepted: 16 November 2020; Published: 20 November 2020



Abstract: This study focuses on the hydrogeological conditions in the coastal (Thriassion plain) and submarine (Eleusis Gulf) environment of West Attica, Greece. Up to now, the predominant aspect for the Thriassion plain groundwater—hosted within the Neogene-Quaternary sediments—was its direct hydraulic contact with the seawater. Due to that, the coastal plain groundwater is strongly believed to be of brackish quality irrespective of the local hydrodynamic conditions. Our major goal is to evaluate the actual mechanism controlling the groundwater flow, the origin and distribution of saline water, and the existence of fresh groundwater in the submarine environment. We summarize the following: (1) groundwater of the Thriassion plain is partly discharged as an upwards leakage from deeper aquifers, (2) modern direct seawater intrusion is not possible in the Neogene-Quaternary sediments, and (3) fresh groundwater possibly exists below the sea floor of the Eleusis Gulf. The results may serve as hint of further research in groundwater resources below the Mediterranean Sea floor, and, consequently, a new perspective on water resource management could emerge.

Keywords: offshore groundwater exploration; coastal aquifers; salt-/fresh-water relationship; Mediterranean Sea; Attica-Greece

1. Introduction

The sustainable management of coastal aquifer resources requires a good understanding of the relationship between salt and fresh water. Coastal aquifers have been extensively studied for more than a century by many researchers [1–18]. The common problem in coastal aquifers, which are hydraulically connected to the sea, is seawater intrusion mainly, but not exclusively, due to overpumping. Overpumping forces the salt-fresh water interface shift landward, resulting in the contamination of the fresh groundwater with seawater. This phenomenon is depended on (i) the geological-hydrogeological and hydraulic characteristics of the aquifer, (ii) human activities, and (iii) tidal effects and coastal and sea bottom conditions [5]. The hydrostatic equilibrium (Figure 1a) between salt and fresh water is described by the Ghyben-Herzberg principle, Equation (1):

$$z = \frac{\rho_f}{\rho_s - \rho_f} h_f \quad (1)$$

where z = is the depth to the salt-fresh water interface below sea level, h_f = is the height of the fresh water above sea level, ρ_s and ρ_f = salt-water and fresh-water densities, respectively, and g = acceleration due to gravity.

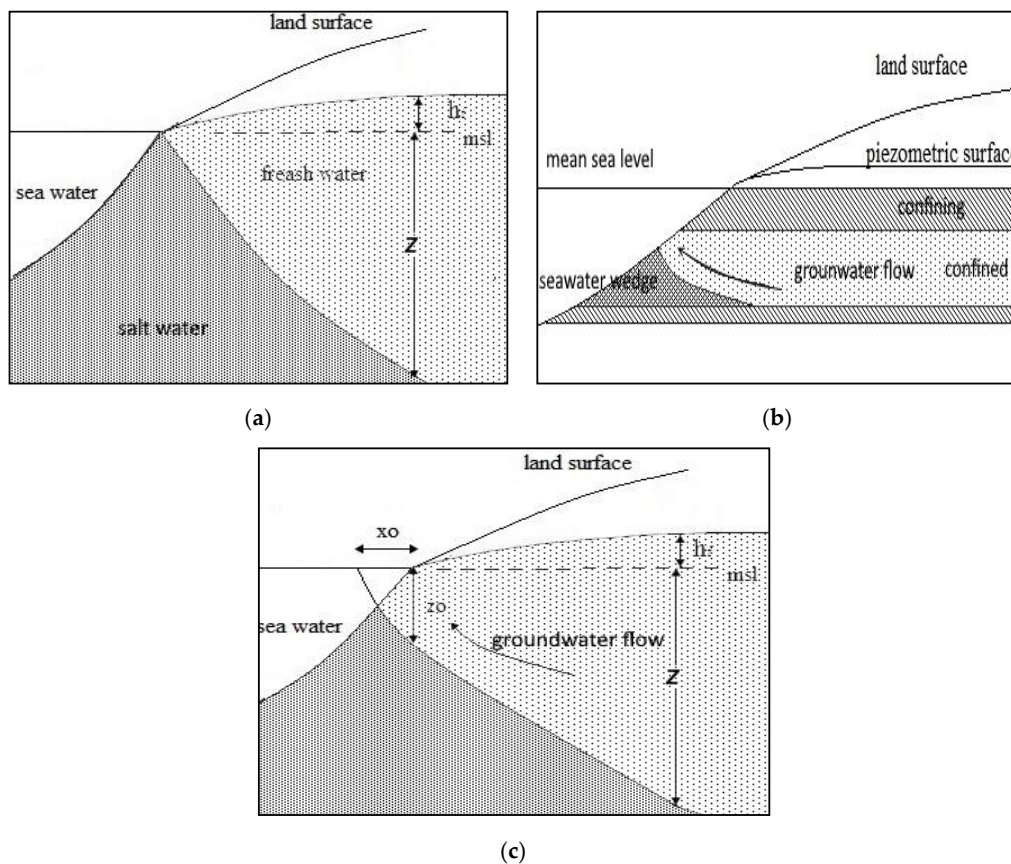


Figure 1. Dupuit-Ghyben-Herzberg model flow (a) in unconfined and (b) confined coastal aquifers, and the (c) actual groundwater discharge onto the sea floor; z is the depth to the salt-fresh water interface below sea level, h_f is the height of the fresh water above sea level, x_0 is the width of the submarine zone through fresh groundwater discharge into the sea, and z_0 the depth of the interface below the coastline.

In ideal conditions, the Ghyben-Herzberg principle states that the depth to the salt-fresh water interface z beneath sea level is approximately 40 times the height h of the fresh water above sea level. The application of the above principle is limited to conditions in which the two liquids are static, and it is valid under the occurrence of horizontal groundwater flow. It can be also applied in unconfined and confined aquifers (Figure 1b).

Based on the Dupuit–Forchheimer assumption that, in coastal aquifers, the equipotential lines are vertical (horizontal flow) in combination with the Ghyben-Herzberg principle, a one-dimensional flow can be used that yields the following expression for the x and z coordinates of the interface [2].

$$z^2 = \frac{2\rho_f q' x}{\Delta\rho K} \quad (2)$$

where q' = fresh groundwater outflow at the coastline per unit width, K = the hydraulic conductivity, and $\Delta\rho$ = the difference of the salt- and fresh-water densities.

Based on Glover’s analytical solution [12], Cheng and Quazar [16] determined the interface depth as:

$$z^2 = \frac{2\rho_f q' x}{\Delta\rho K} + \left(\frac{\rho_f q'}{\Delta\rho K}\right)^2 \quad (3)$$

where K = the hydraulic conductivity.

The width x_0 (Figure 1c) of the submarine zone through fresh groundwater discharge into the sea can be obtained from Equation (3) by setting z equal to 0, which provides Equation (4), and the depth of the interface below the coastline z_0 by setting x equal to zero, which provides Equation (5).

$$x_0 = \frac{\rho_f q'}{2\Delta\rho K} \quad (4)$$

$$z_0 = \frac{\rho_f q'}{\Delta\rho K} \quad (5)$$

In real field conditions, this interface does not occur; instead, a brackish transition zone exists where complex diffusion and mass transport theories are developed [19,20]. The overexploitation of coastal groundwater leads to both submarine groundwater discharge reduction, as well as an increase of seawater inflow and, consequently, an increase of the transition zone thickness [21].

Coastal aquifers, which are in hydraulic contact to the sea, are subject to fluctuations in the hydraulic head due to the tides [22]. The fluctuation parallels to the rise or fall of the tides after a time lag between the high tide and the peak of the groundwater level.

On the contrary, in confined aquifers extending below the sea floor without a sea front and which are separated from seawater by thick confining layers of very low permeability, fresh groundwater can be conserved against salinization. Identical geological-hydrogeological structures exist in many places all over the world, such as The Netherlands [1]; Eastern England [5]; Spain [20]; the Bay of Bengal; Bangladesh [23]; the USA [2,24]; and Estonia, Denmark, and France [25]. Thus, the boundary between the aquifer and seawater does not exist, or it migrates far from the coast. Therefore, the Ghyben-Herzberg seawater-fresh water interface does not occur near the coast. In these aquifers, fresh groundwater occurs beneath the sea floor fed from the onshore outcrops [1,2,4,24–27]. Offshore groundwater occurrence is a global phenomenon, but its direct observations are limited. The assessment of groundwater fluxes into the sea, or the submarine aquifers often need specific techniques and procedures, as well [28]. However, at many regions, onshore hydrogeological and hydrochemical data provide strong indirect evidence for the occurrence of fresh groundwater in submarine aquifers below the sea floor [25].

In this article, the functioning of the Thriassion Plain coastal aquifers was completely revised, and an attempt to evaluate the actual mechanism controlling the groundwater flow, the origin and distribution of saline water, and the existence of fresh groundwater in the submarine environment of the Eleusis Gulf in the East Mediterranean was made

2. Study Area

The Thriassion Plain is a coastal area of about 120 km² in extent (Figure 2) and lies from latitude 38.0 and 38.2° N and longitude 23.1 to 23.7° E. It is part of three hydrological basins of 475 km² in total extent. The plain is surrounded by the Mesozoic carbonate, which drains south into the Eleusis Gulf. A semiarid climate prevails in the area. The annual precipitation is around 380 mm/y, while the actual evapotranspiration is around 62% of the precipitation [29]. The mean groundwater temperature is 20.6°, which ranges between 17.5 and 22.8 °C [29]. The mean air temperature ranges between 9.2–29.9 °C in January and July, respectively. The mean sea surface temperature of the Eleusis Gulf ranges between 13 and 25 °C, while the mean sea temperature at the bottom of the Eleusis Gulf ranges between 12 and 13 °C. The Eleusis Gulf is a small and almost enclosed sea north of the Saronikos Gulf in the East Mediterranean Sea, which covers an area of 67 km², having a maximum depth of 33 m. It is surrounded by the study area to the north and the Salamis Island to the south. Its connection to the Saronikos Gulf is through two shallow channels of 8 m in depth at the western end and 12 m in depth at the eastern end, respectively. This area has been degraded environmentally due to uncontrolled agricultural and industrial development during recent decades [30–33].

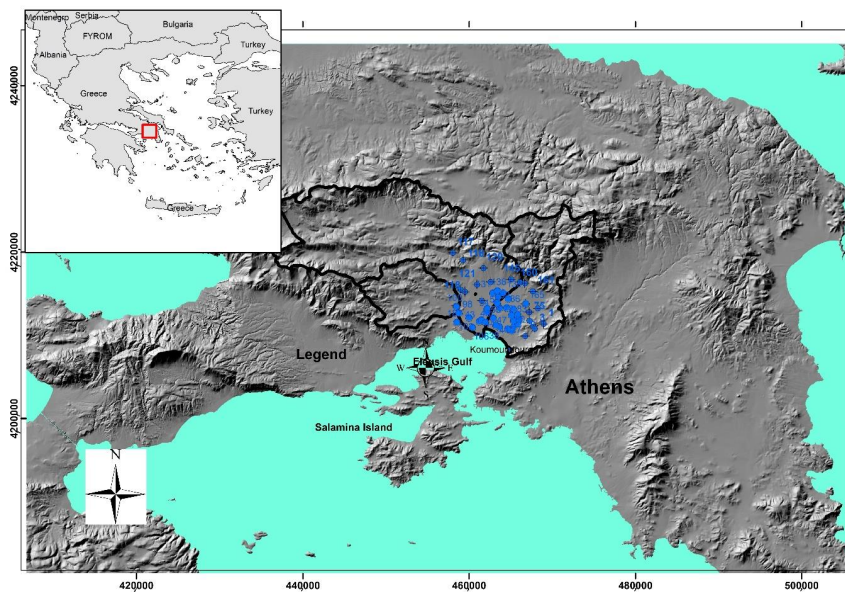


Figure 2. Study area.

3. Regional Setting

3.1. Geological Setting

The Thriassion Plain is located at the border between non-metamorphic and metamorphic rocks of Eastern Greece and Attica geotectonic units, respectively [34]. The geological structure (Figure 3) of the study area consists of: (1) a Palaeozoic volcano-sedimentary complex, 400–500-m thick, composed of: (a) clastic materials (arkoses, greywackes, shales in alternations with phyllites, conglomerate, and lenticular intercalations of limestone) and (b) basic-igneous volcanic rocks; (2) Mesozoic sediments consisting of: (a) Lower-Middle Triassic phyllites and sandstones with breccia-conglomerate intercalations; (b) volcanic rocks and tuffs; (c) Middle-Upper Triassic white carbonate, crystalline in places, comprising limestone, dolomitic limestone, and dolomite; (d) Upper Triassic black limestone, dolomitic limestone, and (e) Grey Cretaceous limestone; and (3) Cenozoic sediments of: (a) Neogene (Pliocene marls with lignite intercalations in places, clay, conglomerate, sandstone, and marly limestone); (b) Pleistocene deposits (clay, sand, gravel, and torrential fans of loosely and cohesive conglomerate); and (c) Holocene deposits (clay, loam, sand, and gravel) [35].

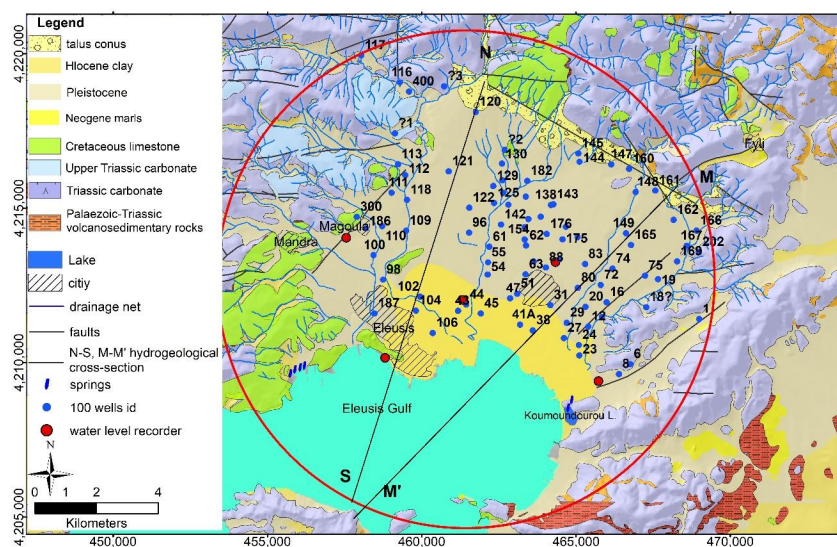


Figure 3. Geological map of the study area. The numbering is the wells id.

3.2. Structural and Lithostratigraphic Setting

The lithostratigraphic setting of the plain comprises sediments of the Plio-Pleistocene and Holocene ages. East of the study area, this sequence is underlain by marls. Marly limestone and marls have been found in some wells NE of Aspropyrgos City at depths between 63–71 and 96–170 m from the ground surface, respectively [36,37]. Cretaceous limestone and Triassic carbonate occur at the depths of 20–40 and 80–100 m from the ground surface, respectively, N of Eleusis City. Arkoses, greywackes, and shales of the Palaeozoic age have been found NE and SE of the study area in alternations with phyllites.

The Thriassion Plain was influenced by tectonic factors during the Neogene-Quaternary [34,35,38–40]. The Triassic carbonate is massive in a large extent, and, in some places, it is karstified, depending on the extent to which it has been affected by karstification and/or tectonism. During Pliocene and Pleistocene, intense tectonic actions created horsts and grabens (Figure 4). Geophysical research carried out in the area by [38] showed that the Mesozoic basement is not found to the depth of 320–450 m at the central part of the plain. The study area has been influenced by Pleistocene sea level changes, as well [41–44].

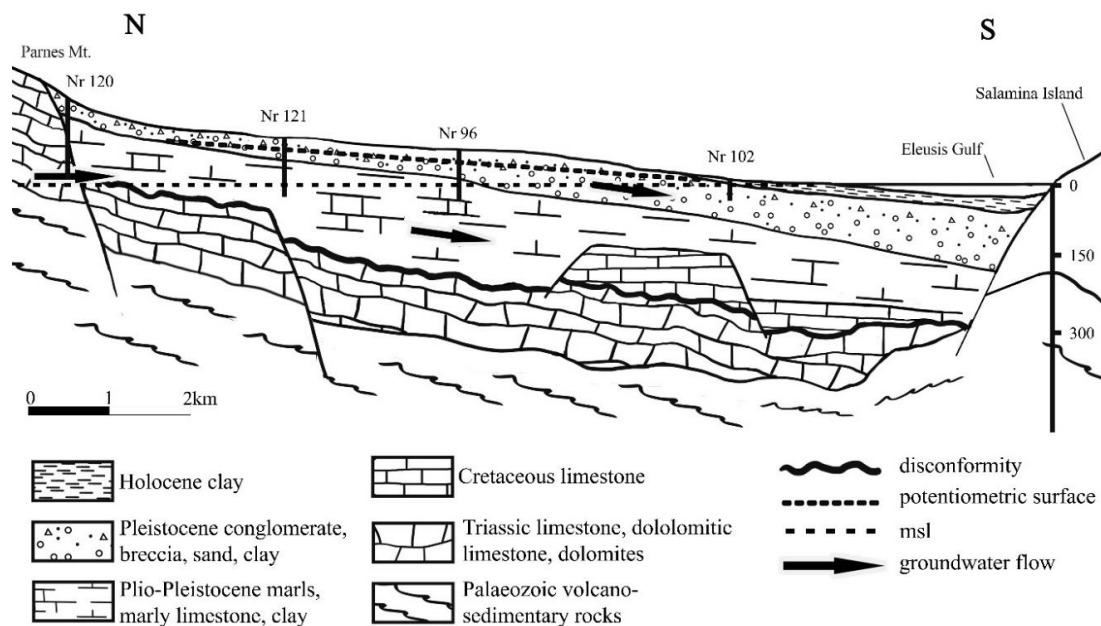


Figure 4. Geological-Hydrogeological cross-section of the N-S direction.

3.3. Hydrogeological-Hydrochemical Setting

The history of pumping started in 1900. Since then, brackish water has been found in the upper aquifers [45]. Some wells located west of the plain were connected by galleries, resulting in expanding the contamination of fresh water with brackish water. In order to study the origin of the saline water, the Institute for Geological and Underground Research monitored the tidal change impacts on the Thriassion aquifers [46]. Five automatic recording devices were placed more than a year at the study area. One device was placed in the Eleusis Gulf to monitor tidal changes. One device was placed at the Holocene sediments 1 km from the shoreline, while two of them were placed at the Pleistocene deposits 2 and 3 km far from the shore; the last one was placed in the Triassic carbonate 3.5 km from the shore north of Eleusis City. No influence of tidal changes was recorded on the Pleistocene-Holocene aquifers; instead, influence was observed in the borehole drilled in the Triassic aquifer. Groundwater response was 2 cm after a time lag (t_{lag}) between the high tide and the peak of the groundwater level, $t_{lag} = 36$ h. Tidal period was 24 h, and the tidal amplitude was 8 cm. The hydrogeological conceptual model that was proposed so far [30,46–48] suggested the existence of two unconfined aquifers in the plain: (i) the upper one, which occurs in the Pleistocene-Holocene deposits, and (ii) the lower one in the Mesozoic carbonate rocks, which both discharge at the shoreline of Aspropyrgos and Eleusis Cities.

A mathematical model, based on the previous conceptual model, failed to describe the hydrogeological regime of the plain.

Saline water in the plain aquifers is limited to a zone of 2 to 3 km in width from the shoreline. The Na/Cl molar ratio is between 0.73–0.87, and the chlorides are between 12–205 mmol/L. In the western, eastern, and the northern parts of the study area where carbonate outcrops, saline groundwater was found 8 to 9 km inland, with total dissolved solids (TDS) between 1500–6000 mg/L and the chlorides between 15–90 mmol/L [29–33,46–49]. Groundwater flows SW with hydraulic gradient 1‰. Transmissivity (T) in the Cretaceous aquifer is around 5000 m²/d (0.5787 m²/s) [48]. During the last five decades, due to the heavy pumping in the Plio-Pleistocene aquifers, at the central part of the basin, the dynamic level was lowered below sea level; however, the static level fluctuated between 5 m below sea level and 3 m above sea level, and groundwater of good quality (TDS values between 400–1200 mg/L and chlorides between 1–9 mmol/L) was preserved for a long time, despite the overpumping conditions [40,46–50].

Studies on the Eleusis Gulf seawater [51,52] presented data on its temperature, salinity, dissolved oxygen (DO), and inorganic nutrients. Both the studies were in accordance with each other. It was also reported [51,52] that the temperatures of the water at 1, 10, 20, and 30 m in depth remain stable at 12.5 °C in January and fluctuate between 12.5 and 17 °C in May. Salinity fluctuates between 38.3 and 38.5‰ in January and 38.2–38.5‰ in May [51].

4. Materials and Methods

Lithostratigraphic cross-sections from boreholes drilled in the Thriassion Plain during 1952–2007 by the Land Reclamation Service of Agricultural Ministry (LRSAM) were taken into consideration. Water samples from 45 wells were collected in June 2012. Electric Conductivity (EC) and pH were measured in situ on the head of the pumping column (HACH). The samples were analyzed in the laboratory of Mineralogy and Geology in the Agricultural University of Athens. The average analytical precision was better than 5%. Ion chromatography (Metrohm 732) was used for major component determination, and the method of titration was used in determination of HCO₃⁻. Water level was measured carefully 2–5 times/year for a 15-year period from 1999–2014 in 48 wells. Additionally, pumping tests in 7 agricultural large-diameter wells were carried out in the Plio-Pleistocene deposits during the 2009–2012 time period.

5. Results and Discussion

The study on the LRSAM data showed that the water level in most wells stood above the top of the aquifers as high as 1–5 m during the drillings phase. In addition, the monitoring of the water level, as well as the analysis and evaluation of the pumping test data, concluded that the larger part of the aquifers is confined and semi-confined. Hydrochemical data (Tables 1–3) of the onshore groundwater indicate that fresh groundwater is possibly hosted in the offshore submarine aquifers. The Pleistocene-Holocene clay layers occur very frequently in different depths from 0–170 m throughout the plain in alternations with gravel, sand, and conglomerates 2–10 m in thickness. This Pleistocene-Holocene sequence being partly of shallow marine, partly of terrestrial origin contains the coastal aquifers. Clay typically ranges from 0.5 m to 80 m in thickness.

Based on their hydrogeological and geological-lithostratigraphic characteristics, the aquifers are grouped into three hydrostratigraphic units (HSU): the Neogene-Quaternary unit, the Cretaceous, and the Triassic one. The first one is divided into the Plio-Pleistocene subunit, which is under confined conditions, and the Holocene-Pleistocene subunit, which is confined/semi-confined and locally unconfined.

Table 1. Hydrogeological and hydrochemical data from the wells of the Triassic HSU. TDS: total dissolved solids.

HSU	Well Nr	Distance from Shore (m)	Site Elevation (m)	Well Depth (m)	Head (masl)	TDS (mg/L)	Cl ⁻ (mmol/L)	Na ⁺ (mmol/L)	Ca ²⁺ (mmol/L)	Mg ²⁺ (mmol/L)	K ⁺ (mmol/L)	NO ₃ ⁻ (mmol/L)	SO ₄ ²⁻ (mmol/L)	HCO ₃ ⁻ (mmol/L)
Triassic carbonate	6	2559	50	60		2074	21.7	20.8	7.7	6.2	0.5	0.8	2.7	6.9
	18	4000	58	60		2476	29.9	23.8	7.4	6.6	0.5	0.4	2.5	7.8
	111	5041	63.5	85		1463	16.4	12.0	6.6	4.4	0.2	0.6	1.4	5.5
	121	5496	74			412	1.1	1.0	2.7	2.9	0.0	0.6	0.2	4.0
	169	5690	69.51	85		1731	11.7	10.8	7.5	5.0	0.3	0.5	1.2	9.2
	202	6080	76.5	80	6.17									
	147	6735	140	137		1259	12.3	10.7	4.5	3.6	0.5	0.2	2.3	5.0
	162	6800	140	140		354	1.0	1.0	2.7	2.1	0.0	1.1	0.3	3.3
	116	8625	115	154	13.63	900	7.2	5.8	5.9	3.0	0.2	0.6	0.9	5.0
	117	9410	175	220	12.63	950								

Table 2. Hydrogeological and hydrochemical data from the wells of the Cretaceous HSU.

HSU	Well Nr	Distance from Shore (m)	Site Elevation (m)	Well Depth (m)	Head (masl)	TDS (mg/L)	Cl ⁻ (mmol/L)	Na ⁺ (mmol/L)	Ca ²⁺ (mmol/L)	Mg ²⁺ (mmol/L)	K ⁺ (mmol/L)	NO ₃ ⁻ (mmol/L)	SO ₄ ²⁻ (mmol/L)	HCO ₃ ⁻ (mmol/L)
Cretaceous limestone	96	3460	38	76	4.8	1980	21.1	16.4	6.1	9.3	0.4	1.0	1.8	8.3
	118	4938	64	80		2695	36.5	28.1	7.2	7.3	0.5	0.4	3.1	5.6
	130	5697	81.35	95		1452	16.5	11.8	8.2	5.3	0.1	2.3	2.7	3.7
	120	7303	145	180		2044	27.1	20.9	5.3	5.4	0.4	0.2	2.1	5.0

Table 3. Hydrogeological and hydrochemical data from the wells of the Neogene-Quaternary HSU.

HSU	Well Nr	Distance from Shore (m)	Site Elevation (m)	Well Depth (m)	Head (masl)	TDS (mg/L)	Cl ⁻ (mmol/L)	Na ⁺ (mmol/L)	Ca ²⁺ (mmol/L)	Mg ²⁺ (mmol/L)	K ⁺ (mmol/L)	NO ₃ ⁻ (mmol/L)	SO ₄ ²⁻ (mmol/L)	HCO ₃ ⁻ (mmol/L)	
Confined Plio-Pleistocene subunit	24	1586	14.88	20	4.83	2869	34.0	29.6	7.7	8.9	0.7	2.2	3.6	8.5	
	31	1862	23.91	24	8.39										
	29	1884	22.53	30	5.24										
	20	1897	34.8	45	5.87	1843	18.8	11.7	8.7	10.0	0.1	1.9	4.9	5.9	
	54	2125	19.77	25	4.66	1177	5.7	12.2	3.2	3.2	0.3	1.8	2.2	7.7	
	12	2152	23	23	6.33	1653	15.0	12.1	8.4	7.9	0.3	3.2	3.1	6.6	
	55	2459	23.45	25	4.93	717	1.8	3.1	4.7	3.9	0.1	1.7	0.8	6.5	
	88	2794	42.61	45	6.21										
	58	2814	38.53	40	3.72	1127	8.9	2.9	9.6	10.7	0.1	6.4	2.3	5.0	
	100	2944	33.7	56		751	2.0	1.7	6.4	3.0	0.1	1.2	0.4	7.3	
	61	3005	28.49	40	4.98										
	80	3105	41.28	45	7.46	1985	24.5	12.7	12.3	9.8	0.1	2.5	3.5	4.6	
	16	3196	36.2	41	6.24										
	62	3260	45.24	70	6	706	5.4	1.5	6.6	6.1	0.1	3.6	0.6	3.9	
	86	3467	50.72	60	6.32	849	6.7	2.2	8.1	6.3	0.1	3.5	1.3	4.1	
	142	3738	38.44	50	7.73										
	186	3750	51.07	50	17.54										
	132	3793	50.76	60	7.23										
	109	3910	43	45	3.41										
	83	3912	58.26	65	7.08	862	7.4	7.0	4.0	2.9	0.1	1.1	0.9	4.5	
	175A	4000	63.18	80	7.6	398	1.4	0.9	3.3	2.8	0.0	1.7	0.5	3.3	
	134	4082	56.1	80	7.83	690	2.6	1.9	6.3	6.0	0.1	4.7	1.4	4.6	
	74	4156	64.2	70	8.14										
	140	4313	73.25	90	8.58	441	1.9	1.0	4.3	3.1	0.1	2.0	0.4	3.3	
	131	4391	47.84	65	9.05	751	4.5	1.8	6.8	6.3	0.1	3.8	0.9	4.7	
	75	4690	61.5	106		783	3.9	1.7	7.5	5.8	0.2	4.3	1.0	5.4	
	138	4729	73.85	170	8.78	670	6.9	1.8	5.4	4.4	0.1	0.6	0.2	3.3	
	128	4764	51.34	80	9.68	698	4.6	1.5	7.2	7.0	0.2	6.3	0.5	3.9	
	136	4769	59.13	80	7	891	8.9	3.0	6.8	6.5	0.1	2.2	0.7	4.1	
	129	4940	58.7	80	16.05										
165	5148	86.21	100	13.18											
181	5172	56	107	25.68											

Table 3. Cont.

HSU	Well Nr	Distance from Shore (m)	Site Elevation (m)	Well Depth (m)	Head (masl)	TDS (mg/L)	Cl ⁻ (mmol/L)	Na ⁺ (mmol/L)	Ca ²⁺ (mmol/L)	Mg ²⁺ (mmol/L)	K ⁺ (mmol/L)	NO ₃ ⁻ (mmol/L)	SO ₄ ²⁻ (mmol/L)	HCO ₃ ⁻ (mmol/L)
Unconfined Holocene-Pleistocene subunit	41	800	8.81	15	3.03	1683	10.4	16.8	5.8	5.1	0.1	2.9	2.8	9.9
	38	872	9.3	11	2.58	2337	26.4	18.1	11.1	8.6	0.3	1.2	3.9	7.3
	45	883	4.72	6.2	1.9	4318	59.5	48.4	10.9	12.4	0.7	6.7	6.6	6.3
	106	1010	5.91	8.5	0.96	3243	40.8	32.5	11.1	9.5	0.5	1.5	4.8	7.4
	187	1100	13.02	14	3.85	1406	15.6	12.4	4.7	4.5	0.4	0.4	1.4	5.4
	43	1156	5.1	5.93	1.8	2184	27.7	25.1	4.7	5.9	0.6	2.5	2.6	5.1
	47	1200	10.5	11.93	1.64	5026	80.7	34.6	24.8	26.8	0.6	3.5	4.6	4.5
	44	1222	7.51	9.8	2.52	1298	12.2	12.9	3.2	3.7	0.4	0.2	1.4	6.1
	27	1423	16.36	16	3.79	2608	29.2	27.7	9.3	7.5	0.4	0.8	4.0	7.2
	98	2200	25.98	32	5.26	1108	6.9	6.5	6.2	4.1	0.3	0.6	1.4	7.5
	102	2228	14.39	20	3.13	2395	26.0	22.9	7.6	8.5	0.4	2.5	3.0	8.5
	14	2601	28	30	4.68	3161	42.1	27.5	15.2	10.3	0.3	2.7	5.1	5.3
	100'	2945	33.9	35	9.36									
	154	3424	46.62	65	6.3	646	2.7	1.8	6.6	6.2	0.2	5.6	1.0	4.0
	72	3469	50.88	60	6.88	889	7.0	3.6	6.2	6.0	0.2	2.1	0.9	5.0

5.1. The Neogene-Quaternary Hydrostratigraphic Unit

The Holocene sediments, mainly made up of clay and sandy clay five m in thickness, confine the underlying Late-Pleistocene aquifer. Locally, in palaeovalleys and/or sandy parts of the deposits, the aquifer is unconfined (wells # 38, 41, 43, 45, and 47). The depth of the wells is 3–10 m. The annual head fluctuation ranges from 0.15–0.48 m. In general, they exhibit upwards leaky conditions, which form swamps and marshes in many sites on the ground. At the Kalimbaki site, artesian wells (or once artesian) onto the ground surface, as well as manifestations of surface water, such as springs, lakes (e.g., Koumoundourou Lake), or marshes on the coastal area of Eleusis and Aspropyrgos Cities, could betoken part of groundwater discharge of either the Quaternary aquifers or the Triassic carbonate. Salinization of the water may have taken place due to (i) the dissolution of evaporite relics, (ii) evaporation of the irrigation water, and (iii) farms and domestic sewage [50]. It is also very likely that salinization took place during the Holocene transgression or/and due to the presence of connate water from the contemporary deposition of clay during the transgressions. Taking into account that (i) groundwater is not subject to hydraulic head fluctuations caused by the tides of the sea, (ii) there is an upwards leakage at many sites on the ground of the coastal area, (iii) the occurrence of Holocene clay, which probably continues below the sea bottom and prevents seawater directly intruding through the clay, and (iv) the hydraulic head is above sea level; it is considered that groundwater is not in hydraulic contact to the sea, and, finally, modern direct seawater intrusion in Holocene sediments is not possible.

Pleistocene sands, gravels, clay, or conglomerates are under confined conditions, as well. In this strata sequence, up to six aquifers are developed 2–10 m in thickness (Figure 5) at depths 20–140 m from the ground surface. Plio-Pleistocene marls, marly limestone, sandstone, clay, and conglomerates form a confined aquifer that reaches up to 90 m below the sea level.

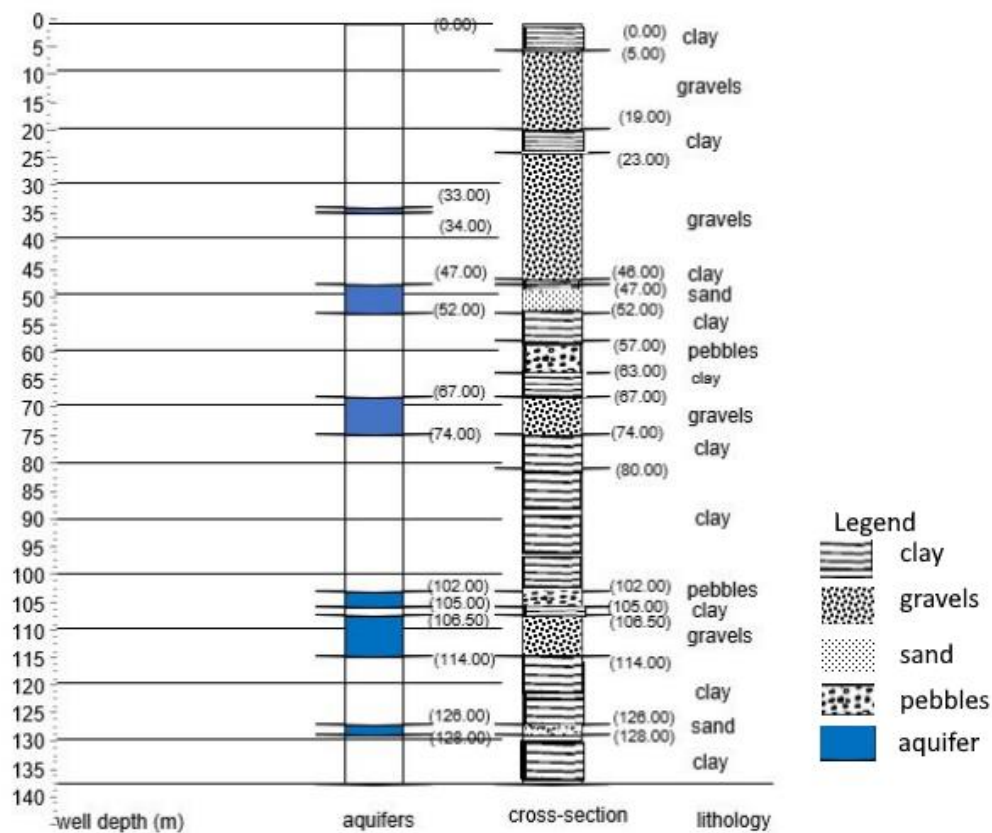


Figure 5. Geological-Hydrogeological characteristics of the wells in the Thriassion Plain.

Pumping tests carried out in the wells # 54, 86, 128, 129, 131, 154, and 154P2 in the Pleistocene sediments were analyzed and evaluated for both confined and unconfined aquifers, using mainly unsteady-state flow methods [53–56] and recovery methods. Drawdown after 6–12 h of pumping was 0.86, 1.11, 5.24, 9.74, 4.66, 1.31, and 1.26 m, respectively. The Schafer equation [57], which provides an estimation of time t_c at which the casing storage effect is negligible, was applied, as well. The analysis showed that the hydraulic characteristics of the wells were variable, depending on the sedimentation material that the aquifer was made up. Transmissivity T ranged from 3.5–275 m²/d (4×10^{-5} – 3×10^{-3} m²/s), storativity S ranged from 1.75×10^{-3} – 8.9×10^{-3} , and hydraulic conductivity K ranged from 0.4–25 m/d (4.6×10^{-6} – 3×10^{-4} m/s). The Pleistocene sediments are confined (dug wells 29, 31, 54, 58, 61, 74, 83, 128, 129, 131, 132, 134, 136, 140, 142, 175, and 176 and boreholes 75, 100, and 138) or semi-confined (12, 16, 20, 24, 44, 31, 54, 55, 62, 80, 86, 88, 109, 121, 165, 181, and 186), and, in some wells, unconfined aquifers are developed (dug wells 14, 27, 41, 43, 45, 47, 72, 98, 100', 102, 106, 154, and 187). The annual head fluctuation ranges between 1.43–2.40 m in the confined aquifer, 0.63–1.22 m in the semi-confined, and 0.36–0.58 m in the unconfined one. The head in the unconfined aquifer is between 1 and 34 masl and, in the confined/semi-confined system, is up to +9 masl. Figure 6 shows the hydraulic head in the Thriassion Plain aquifers in March 2014. An almost stagnant zone is developed under the coastal area, where the minor discharge occurs as an upwards leakage through the aquitards, forming wetlands or swamps on the ground surface. Groundwater discharge into the sea is negligible, as the seawater salinity and the temperature at the bottom of the Eleusis Gulf remained at 38.3‰ and 12.5 °C for many years [51,52]. It is very likely that the groundwater is prevented from progressing further beneath the seafloor due to the barrier of the Salamina Island and, therefore, moves very slowly eastwards.

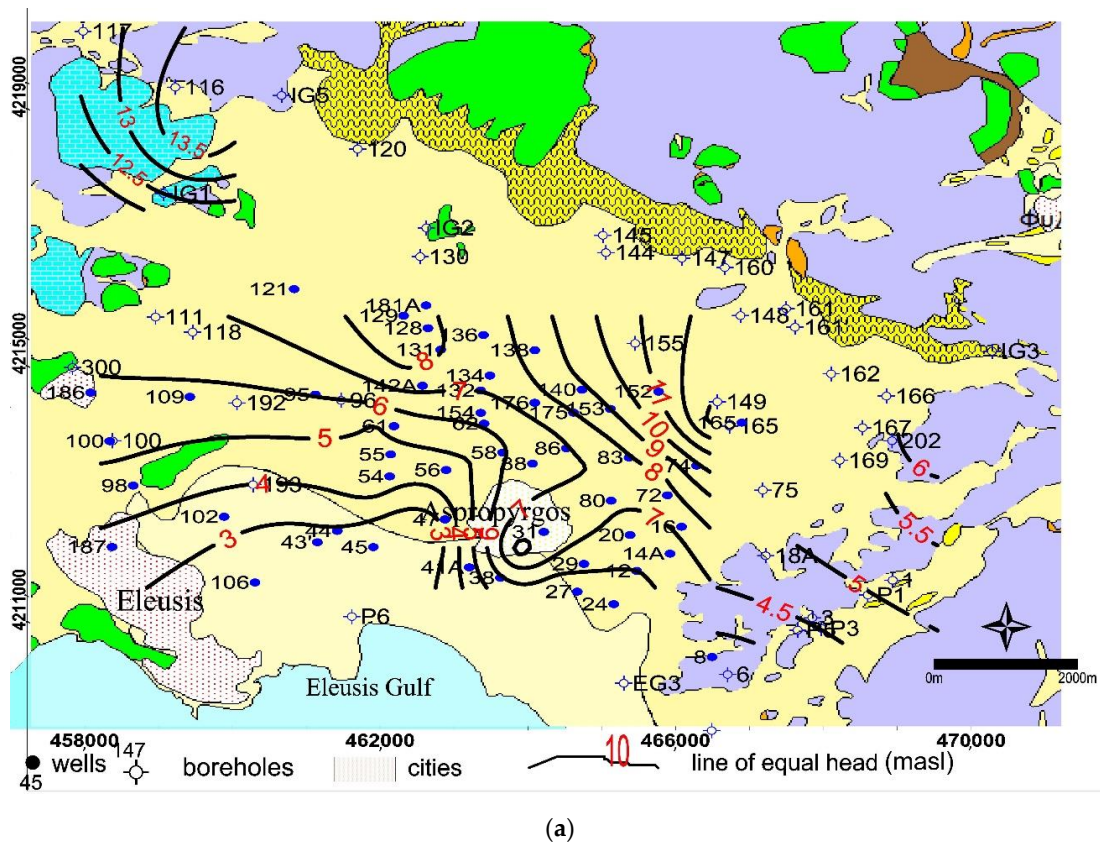


Figure 6. Cont.

(K , q' , and i) and geometric (thickness and slope) characteristics of the aquifer. Homogeneity of the aquifer is also the source of uncertainty.

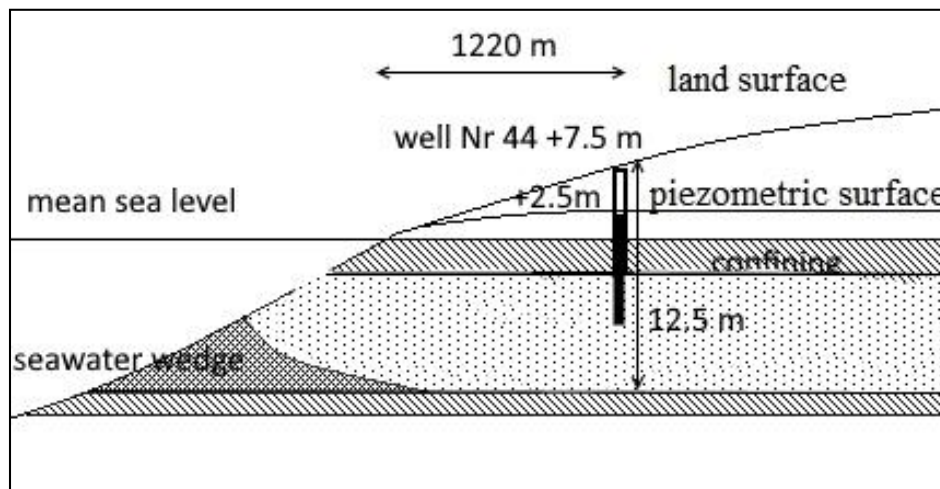


Figure 7. High salinity of groundwater in well Nr 44 could not be attributed to modern direct seawater intrusion, as the salt-freshwater interface is missing.

The hydrochemical data from such wells, as it is reported in the hydrochemical settings section, show that groundwater in the coastal area of about 2 to 3 km in width was found brackish during the drilling phase. This means that seawater intruded inland in a past geological time due to Pleistocene seawater fluctuations [17] or that it is entrapped (palaeo)seawater. Groundwater quality due to repeated irrigations with brackish water and the high evapotranspiration that is around 62% of the precipitation made the water quality worse, which led to high values of salinization.

5.2. The Cretaceous Unit

The Cretaceous limestone hosts an unconfined aquifer (# 111, 120, and 130) with a hydraulic head up to +8 masl. The water table annual fluctuation is around 0.60 m. Hydrochemical data indicate that Cretaceous limestone is contaminated with seawater. Chlorides range from 16.4–36.5 mmol/L and sodium from 11.8–28.1 mmol/L; the sodium/chloride molar ratio ranges from 0.72–0.77. In this aquifer, passive seawater encroachment could take place, which means that the head is above sea level, and groundwater still flows seawards. However, as the water was found brackish since the early 1950s, seawater intrusion seems to be happened in a previous geological time. Due to the Pleistocene sea level rise and, mainly, the last 12 ka and the fact that limestone is intensively fractured, the seawater intruded 9 km inland.

5.3. The Triassic Unit

The Triassic carbonate west and north of the study area is under confined conditions in massive limestone-dolomite (wells # 116, 117, 147, and 162), and it is unconfined in karstified and intensely fractured limestone-dolomitic limestone (wells # 6, 18, 169, and 202), with a hydraulic gradient 0.5–1‰ SW seawards. Transmissivity T ranges from 15–350 m^2/d (1.74×10^{-4} – 4.1×10^{-3} m^2/s). TDS ranges between 900–3000 mg/L. The confined units appear to maintain their fair quality with TDS between 400–1400 mg/L; instead, in the karstified units, the TDS is up to 2500 mg/L. The seawater front has intruded 8 to 9 km inland. Brackish water with $\text{EC} = 14,000$ $\mu\text{S}/\text{cm}$ has been found 10.5 km inland [36].

Trying to determine a salt water-fresh water interface, it is assumed the presence of two wells, A and B, located 8000 m and 10 m from the shoreline are tapping the Triassic aquifer, which has a saturated thickness of 50 m. It is also assumed that $T = 300$ m^2/d and $I = 0.001$; thus, $q' = T \times i = 300 \times 0.001 = 0.3$ m^2/d and $k = 300/50 = 6$ m/d. Then, the depth to the interface (i) at well A based on Equation (2), where no

vertical flow occurs, is $z = (2 \times 40 \times 0.3 \times 8000/6)^{0.5} = 179$ masl and, (ii) at well B based on Equation (3), where vertical flow occurs, the depth to the interface is $z = (2 \times 40 \times 0.3 \times 10/6 + (40 \times 0.3/6)^2)^{0.5} = 6.63$ m. In addition, based on Equations (4) and (5), the depth to the interface at the shoreline is $z_0 = 40 \times 0.3/6 = 2$ masl, and the width of the outflow face $x_0 = 40 \times 0.3/(2 \times 6) = 1$ m, respectively.

The hydrochemical data from such wells as it is reported in the hydrochemical settings section show that groundwater was found brackish during the drilling phase. This means that seawater intruded inland in a past geological time, probably due to Pleistocene seawater fluctuations, or that it is fossil or entrapped (palaeo)seawater.

In recent years, water samples from wells # 54, 41, 83, 86, 16, 98, and 27 in the Pleistocene deposits show that EC values and chloride concentrations have spectacularly been reduced. On the contrary, in the carbonate aquifers, EC values remain at high elevations, and an increase of chlorides has been observed in almost all the wells of this aquifer, e.g., # 120, 118, 18A, etc. [29–31]. In Figure 8, the TDS versus distance from sea graph is shown. The TDS decreases with the increasing distance from the sea. In the north part of the plain, however, it remains high.

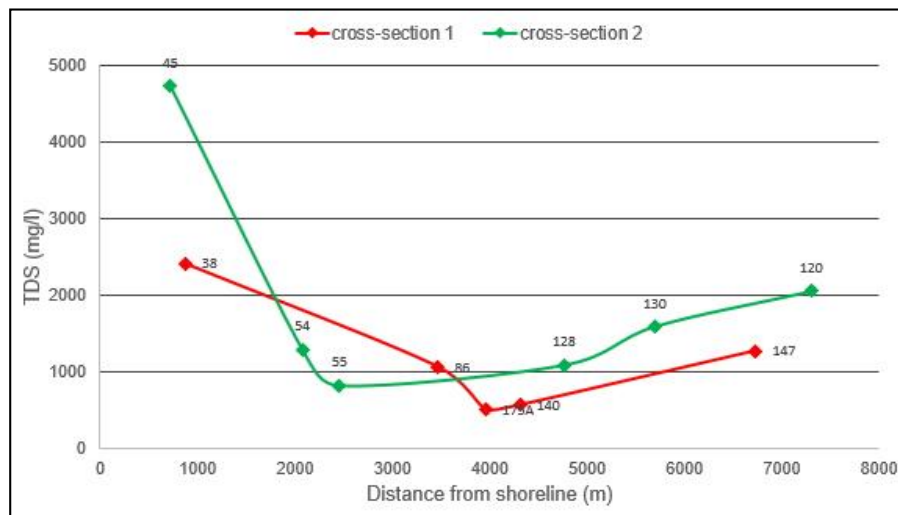


Figure 8. Total dissolved solids (TDS) decrease with increasing distance from the sea. In the carbonate located north (wells 120 and 147), it remains high.

All the data mentioned above provide the evidence that modern direct seawater intrusion could occur nowadays only in the carbonate aquifers [56] around the plain but not in the Neogene-Quaternary deposits. In addition, the occurrence of high fluoride concentration in the groundwater [50] indicates rock dissolution, which requires hundreds or thousands of years to be accomplished [58]. Besides, the F^-/Cl^- molar ratio up to 500 times more than that in modern seawater indicates that there is not an influence of modern seawater. It is very likely the occurrence of palaeo-seawater could explain those values.

5.4. Conceptual Model

Stratigraphic and tectonic factors and Pleistocene sea level fluctuations strongly influenced the hydrogeological regime of the study area. The existence of Pleistocene clays and Pliocene marls has protected, in many places, the Pleistocene and part of the Triassic carbonate aquifers against seawater intrusion. A complex groundwater salinity distribution is encountered, the origin of which is mainly related to the geological history of the area that includes transgressions and regressions of the sea during Pleistocene. The deposition of thick layers of reddish clay in alternation with coarse materials during Pleistocene was crucial [59]. As a sequence, a multi-layered aquifer system was established where the higher-standing aquifer was exposed to seawater intrusion and the lower ones were protected against this phenomenon. During Upper Pleistocene (18 Ka BP), the subjacent

marine strata was freshened up to depths of 100–120 m. The rapid increase of the sea level [41–43] resulted in seawater invading through the lowlands and the buried river valleys, as well as through fractured carbonate formations [60]. In this way, brackish water is encountered 8 to 9 km inland from the present shoreline through Mesozoic carbonates [29,37,49]. After Holocene clay deposition, seawater was entrapped due to the very low permeability of the clay, and the direct seawater intrusion stopped (Figure 9). Moreover, groundwater discharges on the ground surface as an upwards leakage through the preferential flow of clay deposition. Additionally, to the depth, marls protected the overlying aquifers from seawater, which intruded through the carbonate formations underlain marls. Fresh groundwater with fair quality, with EC values between 524 and 1481 $\mu\text{S}/\text{cm}$, is found at depths between 5 and 90 mbsl in the following wells: # 61, 74, 75, 100, 138, 140, 142, 154, 155, 161', 165, 175, and 176.

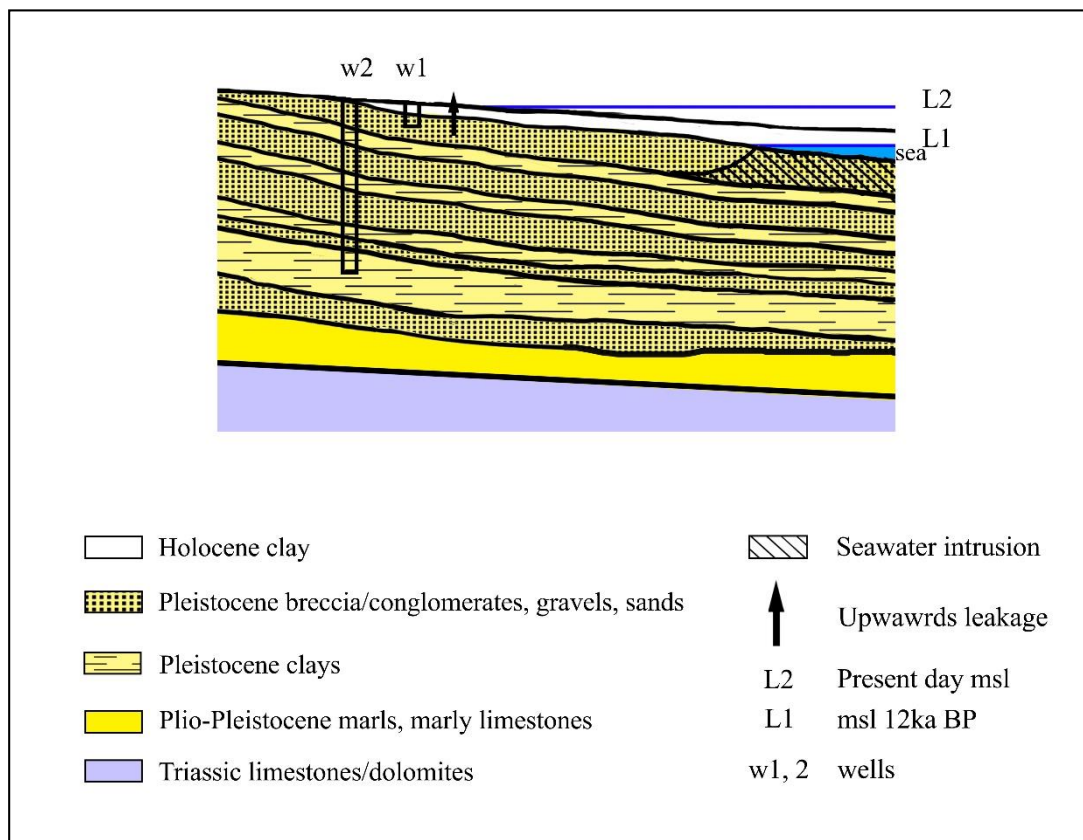


Figure 9. Schematic hydrogeological history 12 ka BP and present day. It is very likely that palaeo-seawater was entrapped in the Pleistocene sediments due to Holocene clay deposition.

Fresh groundwater is most likely to be found offshore under the seafloor of the Mediterranean Sea (Eleusis Gulf) (Figure 10). This is an important issue that could be investigated in detail. New ways of expanding the research in groundwater resources under the Eleusis Gulf seafloor could be sought. It is feasible due to the shallow waters of the Eleusis Gulf, which is 34 m in depth at the maximum (mean depth 18 m). In this way, a new perspective on water resource management could emerge. The wide Neogene basin around Attica, Euboea, and Peloponnese at least 15,000 km^2 in total extent presents the same hydrogeological conditions; the same conditions could prevail in many other coastal areas of Greece and even more around the world.

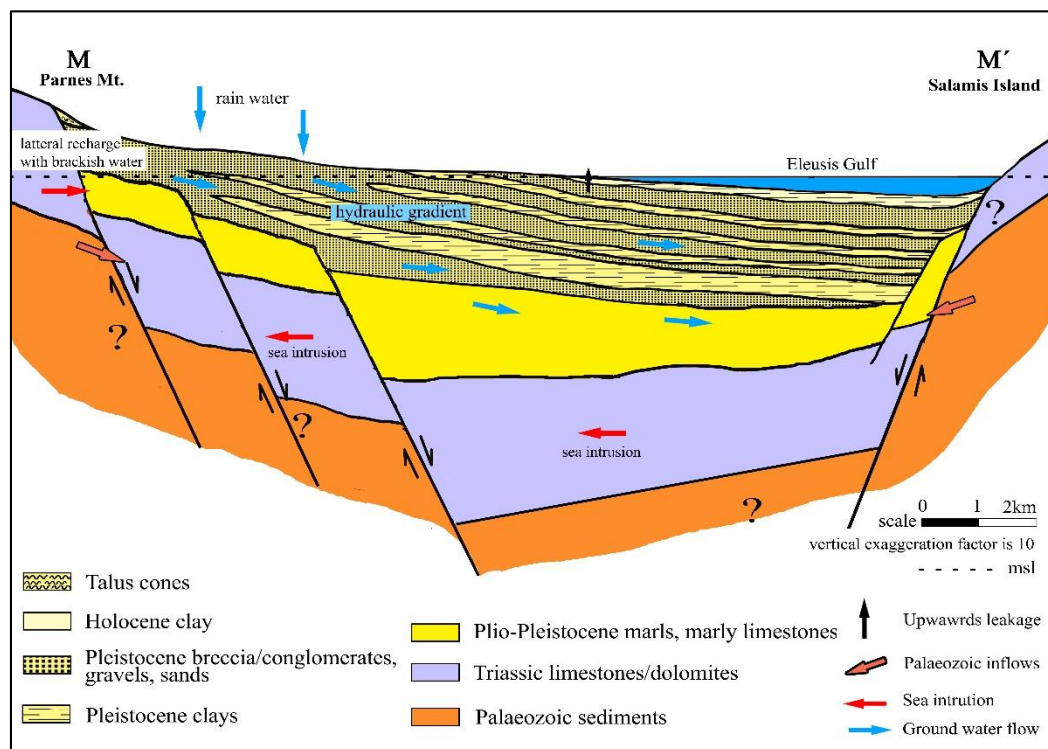


Figure 10. Hydrogeological conceptual model of the Thriassion Plain aquifers. Potential fresh groundwater under hydraulic gradient in submarine aquifers below the Eleusis Gulf is shown.

6. Conclusions

A completely revised hydrogeological conceptual model was proposed for the Thriassion Plain, West Attica, Greece. We suggest that the saline water hosted in the Neogene-Quaternary coastal aquifers is likely due to seawater entrapment prior Pleistocene-Holocene clay deposition. Due to that, any modern direct-seawater intrusion is precluded. Moreover, an almost stagnant zone is developed within the Pleistocene-Holocene sediments under the coastal area and the Eleusis Gulf seafloor. A minor quantity of groundwater is partly discharged as an upwards leakage through the clay strata, forming wetlands or swamps on the ground surface, whereas the major one moves very slowly southeast. Finally, coupling our data (chemical water analyses and aquifer types) with the existing stratigraphic ones (borehole data), we infer that the submarine fresh water possibly exists in the deeper aquifers beneath the seafloor of the Eleusis Gulf.

Author Contributions: Conceptualization, D.H.; methodology, D.H.; formal analysis, D.H.; investigation, D.H., P.M., G.K., and A.A.; resources, D.E.; data curation, P.M. and D.H.; writing—original draft preparation, D.H.; writing—review and editing, D.H., P.M., G.K., and A.A.; visualization, D.H.; supervision, D.H. and A.A.; and project administration, D.H. All authors have read and agreed to the published version of the manuscript.

Funding: This research received no funding.

Acknowledgments: This study was accomplished at the expense of the Agricultural University of Athens.

Conflicts of Interest: The authors declare no conflict of interest.

References

1. Post, V.E.A. Groundwater Salinization Processes in the Coastal Area of the Netherlands Due to Transgressions during the Holocene. Ph.D. Thesis, Vrije Universiteit, Amsterdam, The Netherlands, 2004; p. 138.
2. Fetter, C.W. *Applied Hydrogeology*, 3rd ed.; Prentice-Hall Inc.: Upper Saddle River, NJ, USA, 1994; p. 600.
3. Fetter, C.W. Intruded and relict groundwater of marine origin. *EOS* **1982**, *63*, 810. [[CrossRef](#)]

4. Custodio, E. Coastal aquifers as important natural hydrogeological structures. In *Groundwater and Human Development*; Bocanegra, M., Massone, M., Eds.; Taylor & Francis: Barcelona, Spain, 2002; pp. 1905–1918.
5. Custodio, E.; Bruggeman, G.A. (Eds.) *Groundwater Problems in Coastal Areas, Studies and Reports in Hydrology*; No. 45, UNESCO; International Hydrological Programme: Paris, France, 1987.
6. Lloyd, J.W.; Heathcote, J.A. *Natural Inorganic Hydrochemistry in Relation to Groundwater*; Clarendon Press: Oxford, UK, 1985; p. 296.
7. Todd, D.K. *Groundwater Hydrology*; John Wiley and Sons: Hoboken, NJ, USA, 1980; Volume 242, pp. 235–247.
8. Todd, D.K. Sea water intrusion in coastal aquifers. *Trans. Am. Geophys. Union* **1953**, *34*, 749–754. [[CrossRef](#)]
9. Bear, J. *Hydraulics of Groundwater*; McGraw-Hill: New York, NY, USA, 1979; p. 567.
10. Freeze, R.A.; Cherry, J.A. *Groundwater*; Prentice-Hall Inc.: Englewood Cliffs, NJ, USA, 1979; 604p.
11. Henry, H.R. Interface between salt water and fresh water in a coastal aquifer. In *Editors Sea Water in Coastal Aquifers*; Cooper, H.H., Jr., Kohout, F.A., Henry, H.R., Glover, R.E., Eds.; U.S. Geological Survey Water Supply: Washington, DC, USA, 1964; pp. C35–C70.
12. Glover, R.E. The pattern of fresh-water flow in a coastal aquifer. In *Sea Water in Coastal Aquifers*; U.S. Geological Survey Water-Supply: Washington, DC, USA, 1964; Volume 1613, pp. 32–35.
13. Hubbert, K.M. The theory of groundwater motion. *J. Geol.* **1940**, *48*, 785–944. [[CrossRef](#)]
14. Herzberg, A. Die Wasserversorgung einiger Nordseebder (The water supply of parts of the North Sea coast in Germany). *Z. Gasbeleucht Wasserversorg* **1901**, *44–45*, 815–819, 842–844.
15. Badon-Ghyben, W. Nota in verband met de voorgenomen putboring nabij Amsterdam (Notes on the probable results of well drilling near Amsterdam). *Tijdschrift van het Koninklijk Instituut van Ingenieurs* **1888**, *9*, 8–22.
16. Cheng, A.H.D.; Ouazar, D. Analytical solutions. In *Seawater Intrusion in Coastal Aquifers—Concepts, Methods and Practices*; Bear, J., Cheng, A.H.D., Sorek, S., Ouazar, D., Herrera, I., Eds.; Kluwer Academic Publishers: Dordrecht, The Netherlands, 1999; pp. 163–191.
17. Meyer, R.; Engesgaard, P.; Sonnenborg, T.O. Origin and Dynamics of Saltwater Intrusion in a Regional Aquifer: Combining 3-D Saltwater Modeling with Geophysical and Geochemical Data. *Water Resour. Res.* **2019**, *5*, 1792–1813. [[CrossRef](#)]
18. Warner, A. On the classification of seawater intrusion. *J. Hydrol.* **2017**, *551*, 619–631. [[CrossRef](#)]
19. Bredehoeft, J.D.; Pinder, G.F. Mass transport in flowing groundwater. *Water Resour. Res.* **1973**, *9*, 194–210. [[CrossRef](#)]
20. Segol, G.; Pinder, G.F.; Gray, W.G. A Galerkin-finite element technique for calculating the transient position of the saltwater front. *Water Resour. Res.* **1975**, *11*, 343–347. [[CrossRef](#)]
21. Custodio, E. Aquifer Overexploitation: What Does It Mean? *Hydrogeol. J.* **2002**, *10*, 254–277. [[CrossRef](#)]
22. Jacob, C.A. Flow of groundwater. In *Engineering Hydraulics*; Rouse, H., Ed.; John Wiley: New York, NY, SUA, 1950; pp. 321–386.
23. Alam, S.M.M. Hydrogeochemical evolution of groundwater of part of Ganges-Meghna Deltaic Plain. *AQUA Mundi* **2010**, *Am03029*, 071–082.
24. Cohen, D.; Person, M.; Wang, P.; Gable, C.W.; Hutchinson, D.; Marksamer, A.; Dugan, B.; Kooi, H.; Groen, K.; Lizarralde, D.; et al. Origin and Extent of Fresh Paleowaters on the Atlantic Continental Shelf, USA. *Ground Water* **2009**, *48*, 143–158. [[CrossRef](#)] [[PubMed](#)]
25. Edmunds, W.M.; Buckley, D.K.; Darling, W.G.; CJMilne, C.J.; Smedley, P.L.; Williams, A.T. Palaeowaters in the aquifers of the coastal regions of southern and eastern England. *Geol. Soc. Lond. Spec. Publ.* **2001**, *189*, 71–92. [[CrossRef](#)]
26. Post, V.; Groen, J.; Kooi, H.; Person, M.; Ge, S.; Edmunds, W.M. Offshore fresh groundwater as a global phenomenon. *Nature* **2013**, *504*, 71–78. [[CrossRef](#)]
27. Jiao, J.J.; Shi, L.; Kuang, X.; Lee, C.M.; Yim, W.W.; Yang, S. Reconstructed chloride concentration profiles below the seabed in Hong Kong (China) and their implications for offshore groundwater resources. *Hydrogeol. J.* **2015**, *23*, 277. [[CrossRef](#)]
28. Burnett, W.C.; Aggarwal, P.K.; Aureli, A.; Bokuniewicz, H.; Cable, J.E.; Charette, M.A.; Kontar, E.; Krupa, S.; Kulkarni, K.M.; Loveless, A.; et al. Quantifying submarine groundwater discharge in the coastal zone via multiple methods. *Sci. Total Environ.* **2006**, *367*, 498–543. [[CrossRef](#)]
29. Hermides, D. Hydrogeological Conditions of the Thriassion Plain Basin with Emphasis on the Geohydraulic Characteristics of the Aquifers and Groundwater Quality. Ph.D. Thesis, Agricultural University of Athens, Athens, Greece, 2018.

30. Kyriazis, D.; Zagana, E.; Stamatis, G.; Fillippidis, F.; Psomiadis, E. Assessment of groundwater pollution in relation to heavy metals of the alluvial aquifer of Thriassion Plain (NW Attica). *Bull. Geol. Soc. Greece* **2013**, *47*, 731–739. [[CrossRef](#)]
31. Christides, A.; Mavrakis, A.; Mitilineou, A. A case of intense seawater intrusion to aquifer of the Thriasio Plain. In Proceedings of the 12th International Conference on Environmental Science and Technology, Dodecanese, Greece, 8–11 September 2011; pp. 152–159.
32. Lioni, A.; Stournaras, G.; Stamatis, G. Degradation of Groundwater quality of Thriassion Plain through Natural Factors and human activity. In Proceedings of the 8th Hydrogeological Congress of Greece, Athens, Greece, 8–10 October 2008; Volume 2, pp. 577–586.
33. Makri, P. Investigating the Pollution from BTEX in the Groundwater of Thriassion Plain. Ph.D. Thesis, University of Athens, Athens, Greece, 2008; p. 260.
34. Papanikolaou, D.; Lekkas, E.; Sideris, C. Geology and tectonics of Western Attica in relation to the 7-9-99 earthquake. *Newsletter of E.C.P.F.E. Counc. Eur.* **1999**, *3*, 30–34.
35. Katsikatsos, G.; Mettos, A.; Vidakis, M.; Dounas, A.; Pomoni, F.; Tsaila-Monopolis, S.; Skourtsi-Koroneou, V. *Geological Map of Greece, in Scale 1:50.000, "Athina-Elefsis" Sheet*; IGME Publication: Athens, Greece, 1986.
36. Zacharias, A.; Sarandakos, K.; Andre, C. *Report on Sample Drilling and Morphotectonics Study in the Area around Koumoundourou Lake*; Technical Report; ELKETHE/IIW: Athens, Greece, 2003.
37. Lionis, M. *Hydrogeological Study of Poikilon Mt*; ASDA: Athens, Greece, 1992.
38. Goumas, G. Investigation of the Structure of Thriassion Plain based on Geophysics. Master's Thesis, University of Athens, Athens, Greece, 2006.
39. Mariolakos, H.; Fountoulis, I.; Sideris, C.; Chatoupis, T. Morphoneotectonic structure of Parnes' Mt of Attica Proceedings of the 9th International Congress, Athens. *Bull. Geol. Soc. Greece* **2001**, *XXIV/1*, 183–190.
40. Dounas, A. The Geology between Megara and Erithres Area. Ph.D. Thesis, University of Athens, Athens, Greece, 1971.
41. Poulos, S.; Ghionis, G.; Maroukian, H. Sea-level rise trends in the Attico–Cycladic region (Aegean Sea) during the last 5000 years. *Geomorphology* **2009**, *107*, 10–17. [[CrossRef](#)]
42. Mariolakos, H.; Theocharis, D. Shifting shores in the Saronic Gulf during the last 18,000 years and the Kychreia paleolimni. In Proceedings of the 9th International Conference, Bulletin of Hellenic Geological Society, Athens, Greece, September 2001; Volume XXXVI 1, pp. 405–413.
43. Lambeck, K. Sea level change and shore-line evolution in Aegean Greece since Upper Palaeolithic time. *Antiquity* **1996**, *70/269*, 588–611. [[CrossRef](#)]
44. Kambouroglou, E. Eretria Paleogeographic and Geomorphological Evolution during Holocene Relationship of the Natural Environment and Ancient Settlements. Ph.D. Thesis, UNKA, Athens, Greece, 1989; p. 493.
45. Kallieris, D. *Our Village*; Cultural Center M. of Aspropyrgos: Aspropyrgos, Greece, 2010; Volume 2, p. 586.
46. Dounas, A.; Panagiotides, G. *Precursor Report on the Hydrogeological Conditions of Thriassion*; Institute of Geology and Subsurface Research: Athens, Greece, 1964.
47. Paraschoudes, B. *Hydrogeological Study of Western Attica*; Agricultural Ministry: Athens, Greece, 2002.
48. Kounis, G.; Simos, N. *Hydrogeological Research of the Aquifers of Thriassion Plain, for the Water Supply of Hellenic Refinery*; IGME: Athens, Greece, 1990; p. 38.
49. Hermides, D. Geochemical evolution of the Thriassion Plain groundwaters, Attica, Greece. *Environ. Monit. Assess* **2020**, *192*, 561. [[CrossRef](#)]
50. Hermides, D.; Stamatis, G. Origin of halogens and their use as environmental tracers in aquifers of Thriassion Plain, Attica, Greece. *Environ. Earth Sci.* **2017**, *76*, 306. [[CrossRef](#)]
51. Hopkins, T.S.; Coachman, L.K.; Edwards, R.F. Seasonal change in Elefsis Bay, Greece. *Rapp. Comm. Int. Mer. Medit.* **1976**, *23*, 77–80.
52. Friligos, N.; Barbetseas, S. Water masses and eutrophication in a Greek anoxic marine bay. *Toxicol. Environ. Chem.* **1990**, *28*, 11–23. [[CrossRef](#)]
53. Theis, C.V. The relation between the lowering of the piezometric surface and the rate and duration of discharge of a well using ground water storage. *Trans. Am. Geophys. Union* **1935**, *16*, 519–524. [[CrossRef](#)]
54. Cooper, H.H.; Jacob, C.E. A generalized graphical method for evaluating formations constants and summarizing well-field history. *Trans. Am. Geophys. Union* **1946**, *27*, 526–534. [[CrossRef](#)]
55. Neumann, S.P. Analysis of pumping test data from anisotropic unconfined aquifers considering delayed gravity response of the water table. *Water Resour. Res.* **1975**, *11*, 329–342. [[CrossRef](#)]

56. Papadopoulos, I.S.; Cooper, H.J. Drawdown in a well of large diameter. *Water Resour. Res.* **1967**, *3*, 241–244. [[CrossRef](#)]
57. Schafer, D.C. *Casing Storage can Affect Pumping Test Data*; Johnson Drillers' Journal, Jan/Feb, Johnson Division, UOP Inc.: St. Paul, MI, USA, 1978.
58. Edmunds, W.M.; Smedley, P.L. Fluoride in natural waters. In *Essentials of Medical Geology*; Selinus, O., Ed.; Springer: Enschede, The Netherlands, 2013; pp. 311–336.
59. Tal, A.; Weinstein, Y.; Wollman, S.; Goldman, M.; Yechieli, Y. The Interrelations between a Multi-Layered Coastal Aquifer, a Surface Reservoir (Fish Ponds), and the Sea. *Water* **2018**, *10*, 1426. [[CrossRef](#)]
60. Bakalowicz, M. Coastal Karst Groundwater in the Mediterranean: A Resource to Be Preferably Exploited Onshore, Not from Karst Submarine springs. *Geosciences* **2018**, *8*, 258. [[CrossRef](#)]

Publisher's Note: MDPI stays neutral with regard to jurisdictional claims in published maps and institutional affiliations.



© 2020 by the authors. Licensee MDPI, Basel, Switzerland. This article is an open access article distributed under the terms and conditions of the Creative Commons Attribution (CC BY) license (<http://creativecommons.org/licenses/by/4.0/>).

Article

Physicochemical Property Indexes of Sediment Lixiviums in Sea–Land Interaction Zone of Subei Basin and Their Significance to Transgression

Qiang Shu ^{1,2,3,*}, Shunjie Zhang ¹ and Ye Chen ^{1,2,3,*}

¹ School of Marine Science and Engineering, Nanjing Normal University, Nanjing 210023, China; future_9898@tom.com

² Jiangsu Center for Collaborative Innovation in Geographical Information Resource Development and Application, Nanjing Normal University, Nanjing 210023, China

³ School of Geography, Nanjing Normal University, Nanjing 210023, China

* Correspondence: shuqiang@njnu.edu.cn (Q.S.); chenye@njnu.edu.cn (Y.C.)

Abstract: In current studies, the physicochemical properties of water, such as total dissolved solids, salinity, and electrical conductivity, are used mainly to investigate changes in the properties of surface water and groundwater. In our experimental study, we aimed to introduce the physicochemical properties of water bodies into the field of paleoenvironmental changes. We employed the physicochemical property indexes of sediment lixiviums in two research sections of the sea–land interaction zone in the eastern margin of the Subei Basin (China). Preliminary tests determined that the optimal solvent for preparing the sediment lixiviums is ultrapure water; the use of this water can prevent errors caused by soluble solids in the solvent. Using a container with a lid to prepare the sediment lixiviums could reduce errors caused by evaporation. Furthermore, we determined the appropriate process and duration for testing the physicochemical properties of sediment lixiviums. The optimal time for testing the physicochemical properties was 120 h (mixture fully stirred daily) or 168 h (no stirring). The weight of the sediment, volume of the solvent, and test time should be consistent in the same research section. Comparing the physicochemical property indexes of sediment lixiviums with geochemical elements and diatom indicators, we found that these indexes show obvious indications of transgression, and have an obvious advantage in indicating transgression.

Keywords: sea level fluctuations; soluble substances; coastal environment change; diatom; geochemical elements



Citation: Shu, Q.; Zhang, S.; Chen, Y. Physicochemical Property Indexes of Sediment Lixiviums in Sea–Land Interaction Zone of Subei Basin and Their Significance to Transgression. *J. Mar. Sci. Eng.* **2021**, *9*, 719. <https://doi.org/10.3390/jmse9070719>

Academic Editors: Markes E. Johnson and Timothy S. Collett

Received: 6 June 2021

Accepted: 26 June 2021

Published: 29 June 2021

Publisher's Note: MDPI stays neutral with regard to jurisdictional claims in published maps and institutional affiliations.



Copyright: © 2021 by the authors. Licensee MDPI, Basel, Switzerland. This article is an open access article distributed under the terms and conditions of the Creative Commons Attribution (CC BY) license (<https://creativecommons.org/licenses/by/4.0/>).

1. Introduction

Sea level fluctuations [1,2], hydrological dynamics and structural changes [3–5] are among the factors that trigger transgression and regression events [6–8] commonly recorded in coastal areas. In conjunction, these factors have an important impact on the evolution of a region's environment through time. In the past few decades, several researchers have conducted studies using micro-paleontology [9–14], geomorphological [15,16], and geochemical (stable isotopes and trace elements) [17–23] proxies with fruitful research results. However, most of these methods require complicated identification processes and professional skills, as well as expensive specialized instruments. Moreover, some indicators obtained through these proxies are not easily preserved to obtain continuous data because of the sedimentary environment [24]; some geomorphological markers and/or sedimentary structures will be affected and even destroyed [25]. Obviously, these factors will have a certain impact on the research results.

The question is, therefore, whether an index could be found that is relatively simple, fast, and does not require highly professional skills or complicated instruments to test for and reveal a transgression event. Considering the significant difference in the content of various soluble substances (such as various ions and compounds) between seawater and

fresh water, the amount of various soluble substances attached to the sediments in the process of sediment deposition should also be variable. Consequently, the physicochemical properties of the lixivium of these sediments should also differ significantly (Sediment lixivium refers to the mixed liquid of water and sediment formed by soaking the pretreated sediment in solution). Based on this concept, we propose a multiparameter water quality meter for use in paleoenvironment research to measure the physicochemical properties of sediment lixivium and to reveal these transgression and regression events.

The multiparameter water quality meter is an inexpensive and easy-to-operate portable instrument. It can measure the physicochemical properties of water, such as total dissolved solids (TDS), salinity (SAL), and electrical conductivity (EC), with high precision ($\pm 1\%$). These properties are currently used mainly to study their changes in various forms of water, such as surface water and groundwater [26–32]. Sylus [31] discussed the impact of regional seawater intrusion on water quality through EC and TDS measurements of the coastal aquifers of the Gurpur and Netravathi river basins in the Dakshan Kannada district in India. Salmani [32] studied TDS and the water flow of the Karoun River in southwest Iran, and proposed a model to predict the river flow and TDS changes. Yokoyama [33] studied the sedimentary environment of Lake Biwa (Japan) through EC and discussed its relationship with sulphate ions and sulphates. In fact, EC is not only related to sulphate ions and sulphates but also to the solubility of electrolytes in water. Fang [34,35] used the EC of clay turbid water to study the sediments in the old, drowned valley plain of the Liaodong Peninsula (Northeast China), and reconstruct changes in the regional environment. In these studies, in addition to applying the physicochemical properties of water bodies to the study of surface water and groundwater quality [31,32], some attempts were made to apply such properties to the study of paleoenvironmental changes [33–35]. However, the preparation and testing process of the sediment solution was not described in detail, sample spacing was large, and the resolution was not high. There is also a lack of research on the direct rebuilding of coastal environment change by TDS, which reflects the total amount of dissolved solids in water.

In view of the aforementioned discussion, we intended to introduce a multiparameter water quality meter to the field of paleocoastal environmental change research. Through preliminary experiments, we established an appropriate process for testing the physicochemical properties of sediment lixivium. According to the testing process, three physicochemical property indexes (TDS, SAL, and EC) of sediment lixivium of the Gangxi (GX) and Caoyankou (CYK) sections, located in the eastern margin of the Subei Basin, are determined. After comparing the test results of sediment lixivium with the indicators of diatoms and geochemical elements, we discuss the response of the physicochemical properties of sediment lixivium to changes in the sedimentary environment, as well as the feasibility of using these properties to reflect changes in coastal environment.

2. Regional Setting

The Subei Basin is located on the eastern coast of China in northeastern Jiangsu Province. It is the onshore part of the Subei–South Yellow Sea Basin, including the Lixiahe Plain and the coastal plain (Figure 1). The Subei Basin is a large-scale composite sedimentary basin formed during the Late Mesozoic on the basis of the Yangtze Block [36]. This basin is a key zone connecting the ocean and land, with significant interaction between sea and land. The sediments in the Subei Basin comprise deposits left by the cross action of rivers, lakes, and seas. After long-term deposition, the overall terrain of the Subei Basin is low and flat, slightly higher in the southwest region and lower in the northeast. The Lixiahe area has the lowest depression in the entire Subei Basin; the altitude of the center is less than 2 m. There are dense river networks, developed water systems, and numerous lakes in Subei Basin. The Huaihe and Yihe rivers and other water systems run through the Subei Basin and flow into the Yellow Sea in the east. Lakes of various sizes, such as Hongze, Gaoyou, and Dazong are distributed among these water systems, forming lake groups.

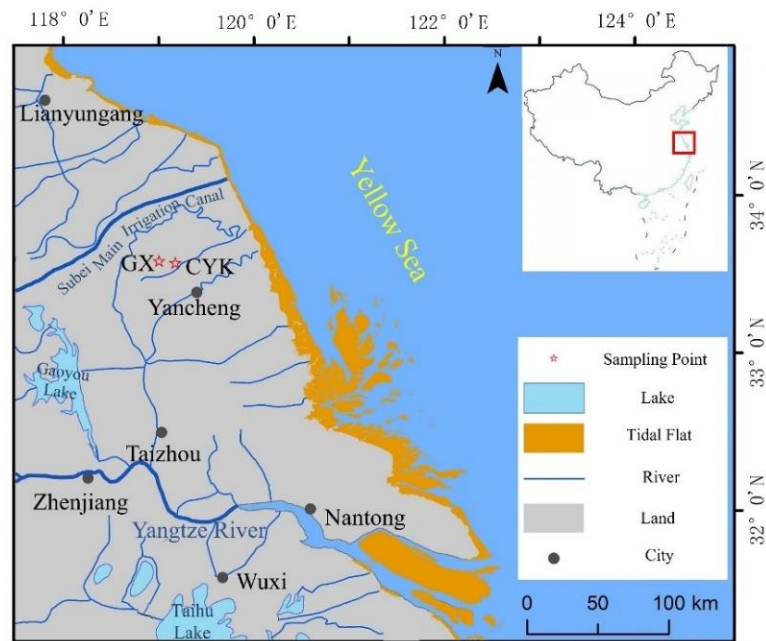


Figure 1. Location of the study area and sampling sites.

The Subei Basin is located at mid-latitudes between 32° and 34° north latitude. It has a subtropical humid monsoon climate, an average annual temperature of 13.4 °C, with the temperature gradually increasing from the northeast to the southwest. The average annual precipitation is 1000 mm, with more precipitation in the east than in the west and more in the south than in the north; the annual sunshine hours are 2130–2430 h, with the highest in summer and the lowest in winter. The factors that influence the atmospheric circulation in the study area are the same as those in the eastern coastal areas of China, i.e., monsoon circulation. In winter, the northerly wind from the interior of the high-latitude continent prevails and the climate is cold and dry, whereas in summer, the southerly wind from the low-latitude Pacific Ocean prevails and the climate is hot and humid.

3. Material and Methods

3.1. Sedimentary Profile and Sampling

The research materials were obtained from the GX (33°30′56.907″ N, 119°54′00.662″ E) and CYK (33°35′04.776″ N, 119°57′49.279″ E) sections in the northeast of Jianhu County (Figure 1). In this section, we will describe the lithology of the sediments in detail; we collected samples from the bottom to the top at a spacing of 2 cm. We collected 250 and 360 samples from the GX and CYK profiles, respectively.

The depth of the GX section is approximately 5 m, and the altitude is between 0.5 m and −4.5 m. The sediment composition characteristics of the entire section change significantly from bottom to top. The section between 500 and 446 cm depth comprises dark-grey compact clay silt, with tubular plant residues (reeds) preserved in the sediment. At depths of 446–426 cm, the sediment is mainly grey-black silty clay. At depths of 426–150 cm, clay silt of various colors with horizontal bedding and vein bedding, or interbedding of clay silt and silty fine sand, with the sediments containing calcified burrows and marine shell fragments. The bottom of this layer (426 cm depth) comprises a large number of shells and oysters. At 150–55 cm, the lithology of sediment is mainly dark-grey to greyish yellow compact clay silt with a large number of iron manganese nodules. From 55 cm to 0 cm, the sediment is disorderly and has no obvious natural sequence, which is the disturbance layer resulting from human activities (Figure 2).

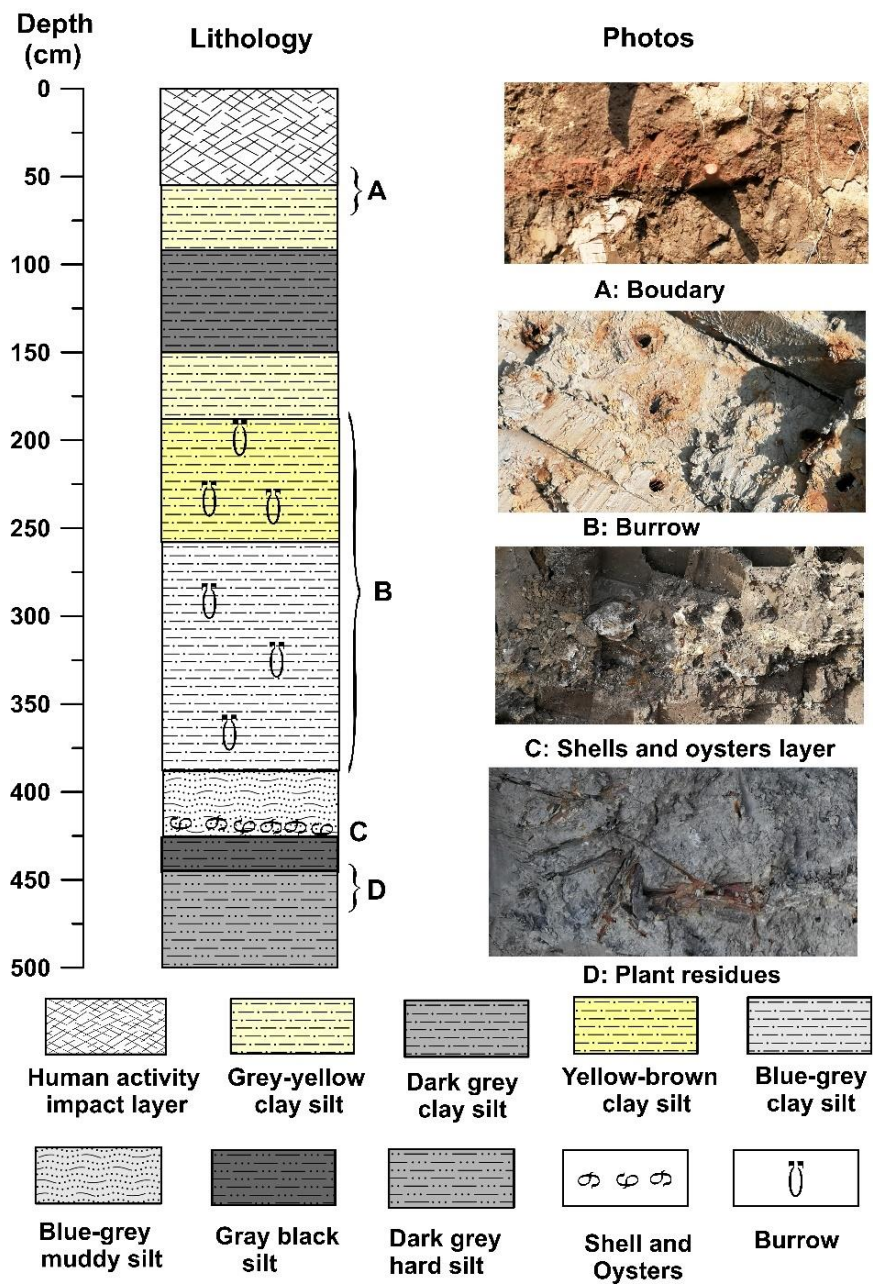


Figure 2. Lithological characteristics of GX profile in Subei Basin.

The depth of the CYK profile is approximately 7.2 m, and the altitude is between 1.92 and -5.28 m. The sediment composition of the profile changes significantly from bottom to top. At depths 720–658 cm, the sediment is grey compact clay silt with obvious sedimentary discontinuities at 658 cm. At depths of 658–345 cm, it is mainly grey to blue-grey mud silt with silt lamina. Grey mud silt with burrows is found at a depth of 345–240 cm. At depths of 240–210 cm, the sediment is mainly grey clay silt with burrows. At depths of 210–158 cm, there is grey clay silt with white silt lamina between the layers. At depths of 158–120 cm, the sediment is mainly yellow-brown compact clay silt with rust spots. Between the depths of 120 cm and 62 cm, the sediment is mainly dark-grey to grey-black clay silt, with the color gradually darkening upward. At depths of 62–0 cm, the sediment is mainly grey-yellow clay silt, the layer obviously affected by human activities (Figure 3).

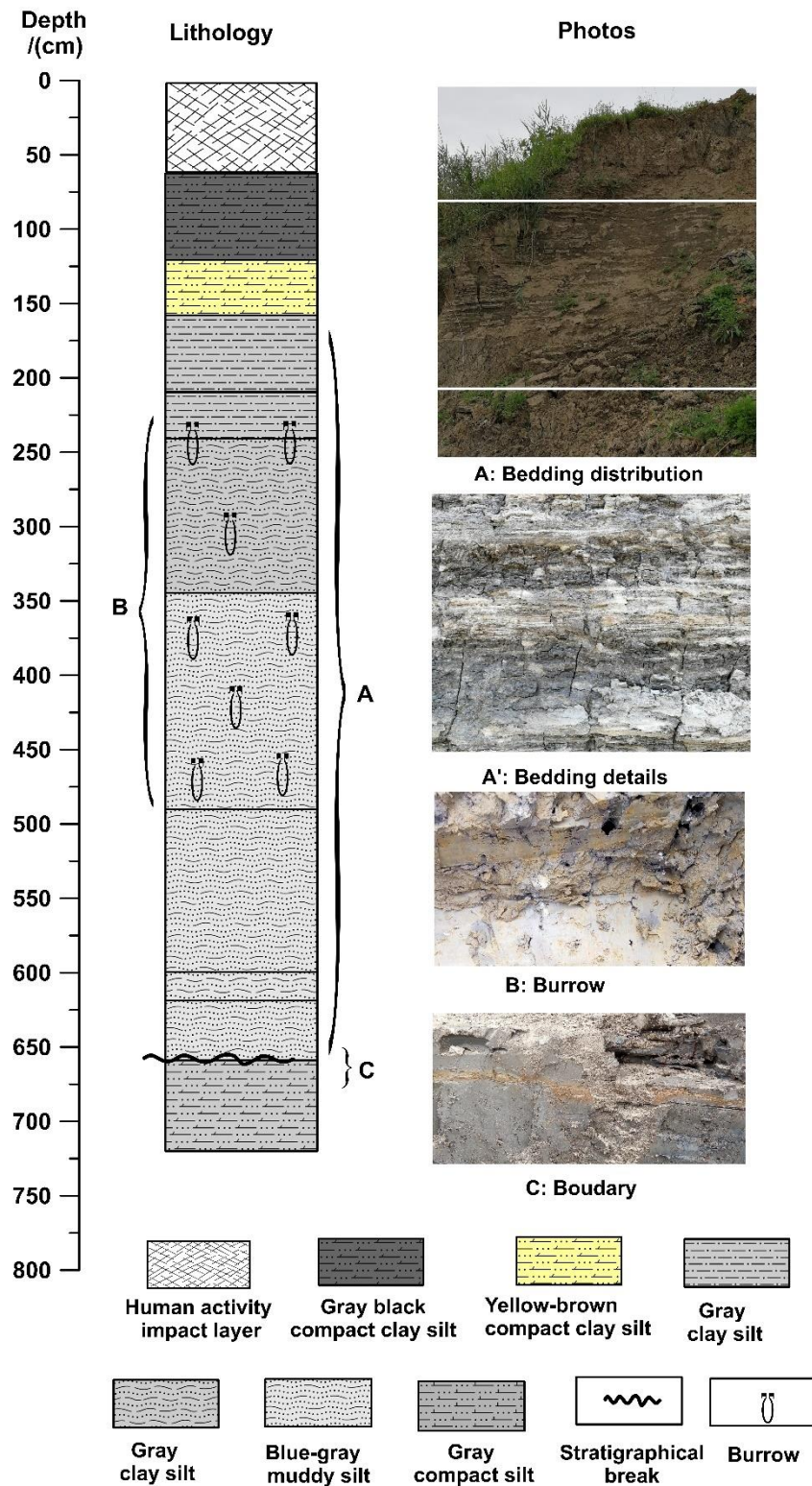


Figure 3. Lithological characteristics of CYK profile in Subei Basin.

3.2. Experimental Methods for Physicochemical Properties of Sediment Lixiviums

No systematic study has been conducted on the physicochemical properties (TDS, SAL, EC) of sediment lixiviums. Therefore, to obtain relevant stable data, we conducted several preliminary tests to determine the appropriate process and optimal test time for measurements (the detailed experimental process was shown in part 4). Subsequently, we obtained the physicochemical property indexes for the two profiles.

3.3. Geochemical Element (Sr, Sr/Ba) Analysis Method

The sediment sample was first dried at low temperature, after which approximately 10 g was weighed, ground into a powder using an agate mortar, and passed through a 200-mesh fine sieve. Finally, the samples were pressed into pellets using the boric acid pressing method [37] under high pressure. After completing sample preparation, the samples were instrument tested. The geochemical element content was assessed using an X-ray fluorescence spectrometer (PANalytical Co., Almelo, The Netherlands) at the Key Laboratory of Environmental Evolution and Ecological Construction of Jiangsu Province, School of Geography, Nanjing Normal University. The measurement error of the instrument was less than 5%.

3.4. Diatom Analysis Method

We selected 26 and 25 samples for diatom identification from the GX and CYK sections, respectively. Before identification, the sediments were pre-treated with hydrochloric acid and hydrogen peroxide. Subsequently, the samples were made into slices for observation under a microscope [38].

4. Test Process of Physicochemical Properties of Sediment Lixivium

Choice of solvent: Water is the most commonly used solvent; moreover, distilled, deionized, purified, or ultrapure water is used often as a solvent in experiments. The physicochemical properties of the different types of water obviously differ. As regards distilled water, because of process differences, the lower the number of distillations, the greater the TDS of the water; the TDS will be close to zero after multiple distillations. Deionized water uses an anion/cation exchange resin to remove the anions/cations in the water; the TDS of the water can be reduced to less than $20 \text{ mg}\cdot\text{L}^{-1}$. Pure water contains a certain amount of dissolved solids, and the TDS is usually between 0 and $50 \text{ mg}\cdot\text{L}^{-1}$. Ultrapure water removes the conductive medium in the water almost completely and removes or reduces the non-dissociated colloidal substances and organic substances in the water to an extremely low level; the TDS test result is zero. Accordingly, aiming to minimize the influence of the solvent on the test results, we selected ultrapure water as solvent to prepare the sediment lixivium.

Preparation of sediment samples: Sediment shows differences in water content, particle size, cementation degree, and the like, because of the influence of the sedimentary environment, sediment source, compaction, and other factors. We intended to eliminate the influence of the precipitation rate of the attached substances on the sediment in the solvent, which is caused by the difference in the water content and the degree of cementation of the sediment. To achieve this, we uniformly dried the samples at a low and constant temperature. Subsequently, we ground them into powder and passed them through 200 mesh sieves. The experimental samples prepared in this manner could precipitate the attached soluble substances more quickly after being dissolved in the solvent.

Choice of container: Open containers are not suitable for storage during the experiment, as the sediment powder has to remain in the container for an extended time after dissolving. The solvent will evaporate and reduce, leading to a large error in the measured results. To minimize the error, a container with a lid should be chosen for the production of the sediment lixivium and the container should be covered to prevent or reduce evaporation.

Preparation of sediment lixivium and determination of the test time: For comparison, the weight of the sample taken from the same section and the volume of added ultrapure water should be the same. We weighed 5 g of dried and ground sample with an electronic balance, placed it in a 150 mL container with a cover, added ultrapure water (100 mL), and stirred the mixture using a glass rod. Subsequently, we measured the physicochemical properties. After covering the container tightly and letting it stand for 24 h, we measured the physicochemical properties again, and then used a glass rod to fully stir the mixture again. This process was repeated six times. We discovered that the physicochemical

properties tended to be stable (Figure 4). To determine whether stirring the sediment lixivium every day is conducive to accelerating the dissolution of substances, we set up a reference group for comparative experiments. The samples in the reference group were stirred fully during the preparation but were not stirred again afterward. These samples were also measured every 24 h. After seven tests, the results tended to be stable (Figure 2). Based on the test results, we concluded that if the sediment lixivium were stirred fully every day, the best test time should be 120 h. However, if the sediment lixivium were fully stirred only when it was prepared and then left unstirred, the best test time should be 168 h. The test instrument was a multiparameter water quality meter (model SX751; Shanghai Sanxin Instrument Factory, Shanghai, China). During the test, the probe of the instrument was immersed completely in the upper clarified solution of sediment lixiviums, and each index was measured three times, after which the average value was calculated.

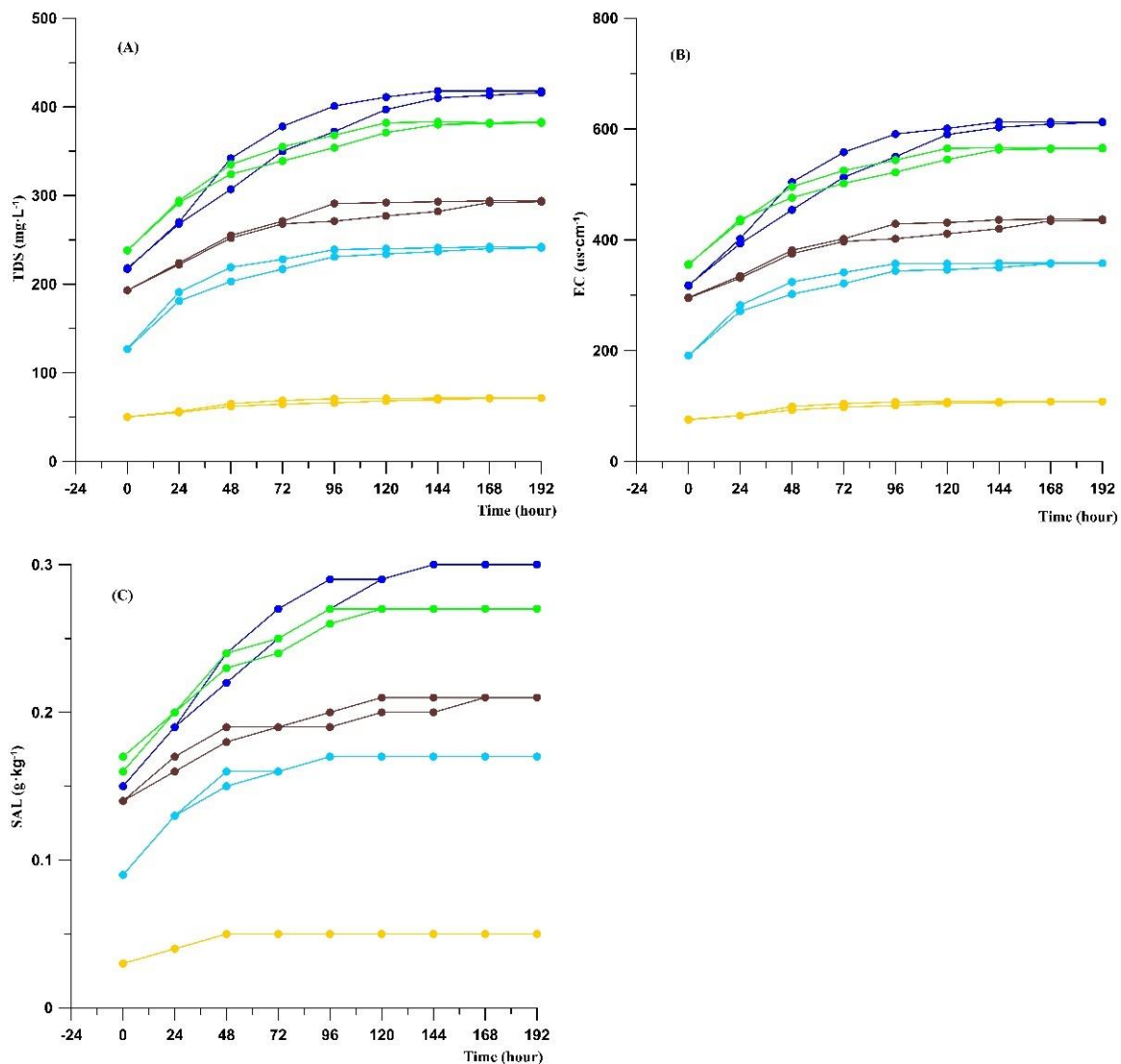


Figure 4. Change curve of the physicochemical property indexes of sediment lixivium with and without stirring with time (different color symbol lines represent the test result of different sediment lixivium, with the top same color symbol line being the test results under stirring, and the bottom the test results without stirring. (A): Change curve of TDS of sediment lixivium with time; (B): Change curve of EC of sediment lixivium with time; (C): Change curve of SAL of sediment lixivium with time).

5. Results

5.1. Variation Characteristics in Physicochemical Properties of Sediment Lixivium

The three physicochemical property indexes TDS, EC, and SAL were measured in sediment lixiviums of the GX and CYK sections, with all showing obvious changes (Figure 5, Table 1). The changes in the three indices indicated that both the GX and CYK profiles could be divided into three stages. In stage I, the three indices TDS, EC, and SAL were all in the low-value stage and showed a gradual increasing trend. In stage II, the three indices all showed high values, and there were certain fluctuations in the CYK section. In stage III, the three indexes all showed low values. In addition, Figure 5 shows extremely good consistency among the TDS, EC, and SAL, with the calculated correlations between TDS and EC, and TDS and SAL all being close to 1 (Figure 6).

5.2. Variation Characteristics of Geochemical Elements Sr and Sr/Ba Ratio

The Sr/Ba ratios are also often used to indicate the changes in salinity and distinguish continental and marine sedimentary environments [39–43]. Sr and Sr/Ba ratios were selected for geochemical analysis (Figure 7, Table 2). The changes in Sr and Sr/Ba indicated that both the GX and CYK profiles could be divided into three stages. In stage I, the Sr and Sr/Ba ratios were low with small fluctuations. In stage II, the Sr and Sr/Ba ratios were high, with obvious fluctuations, and in stage III, the Sr and Sr/Ba ratios became low again with small fluctuations.

In addition, in stage II of the GX profile, it could be divided into two sub stages according to the changes of Sr and Sr/Ba. In stage II-1, Sr and Sr/Ba increased rapidly and then decreased, and the overall values were low (average values: 119.98 mg·kg⁻¹ and 0.26, respectively); in stage II -2, Sr and Sr/Ba were overall high values (average values: 141.17 mg·kg⁻¹ and 0.32, respectively) with small fluctuations.

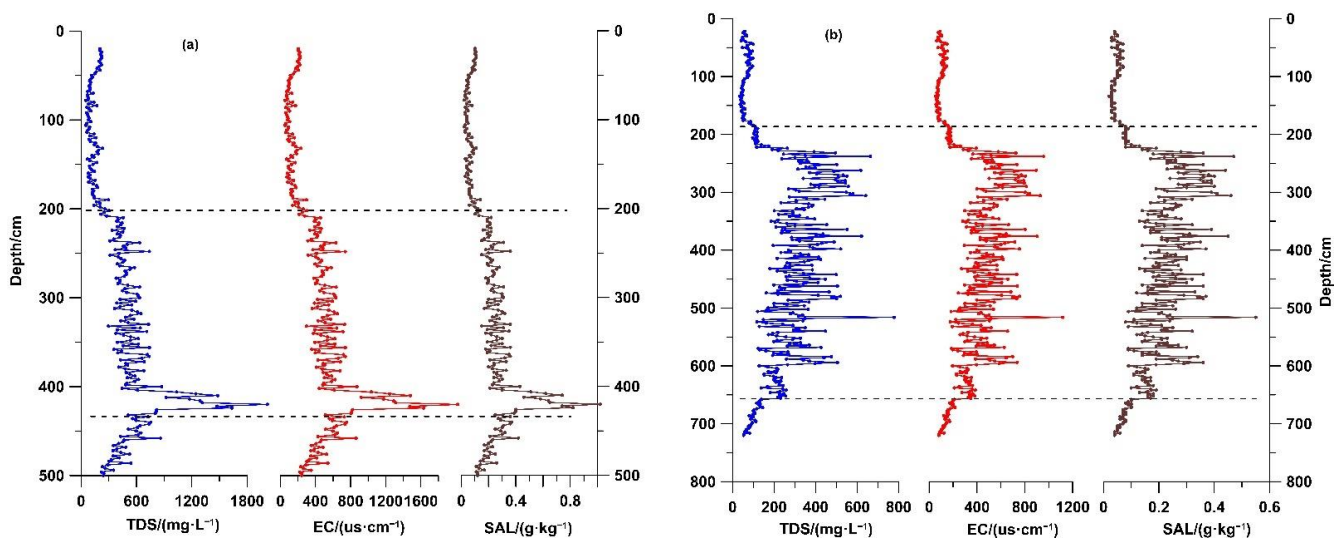


Figure 5. Variation characteristics of physicochemical property indexes of sediment lixivium in GX (a) and CYK (b) profiles.

Table 1. Changes of physicochemical properties of sediment lixiviums of GX and CYK profiles.

	GX Profile			CYK Profile		
	TDS (mg·L ⁻¹)	EC (µs·cm ⁻¹)	SAL (g·kg ⁻¹)	TDS (mg·L ⁻¹)	EC (µs·cm ⁻¹)	SAL (g·kg ⁻¹)
Mean	266.39	392.72	0.19	227.01	336.46	0.16
Max	1470	2020	1.02	778	1117	0.55
Min	33.6	51.9	0.02	35.4	54.8	0.02
C.V (%)	77.8	75.0	77.0	66.5	65.2	66.5

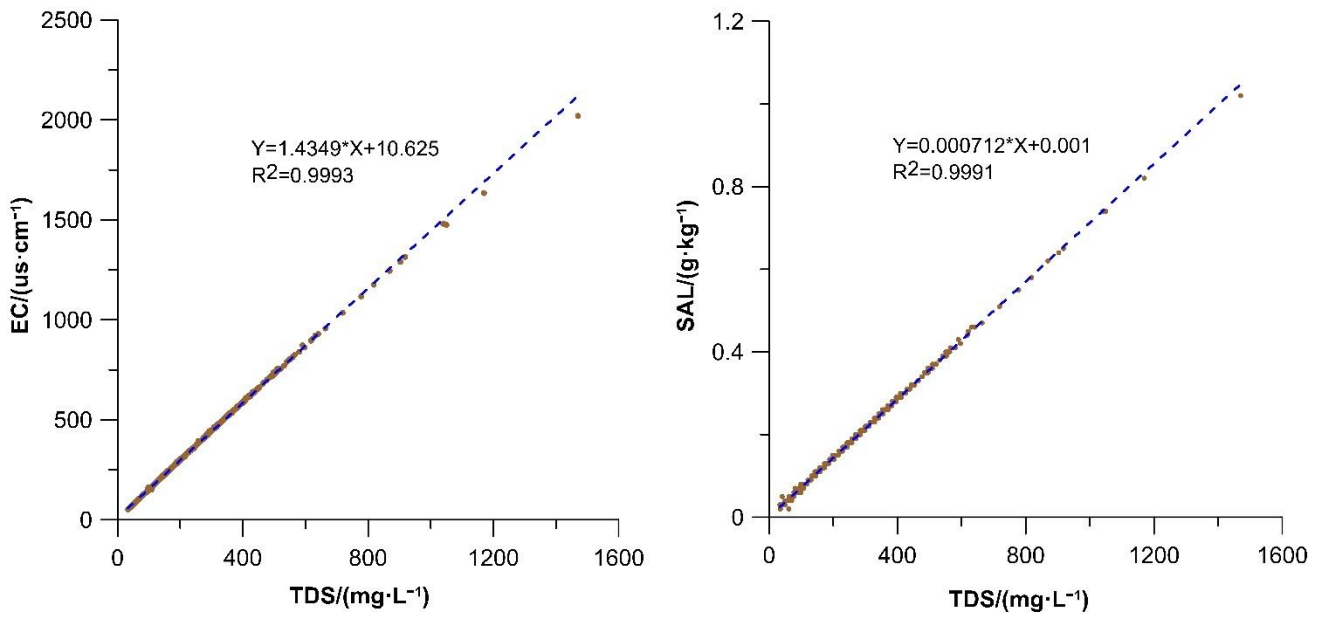


Figure 6. Correlation between TDS and EC, and TDS and SAL in sediment lixivium study section (blue dotted line is the trend line).

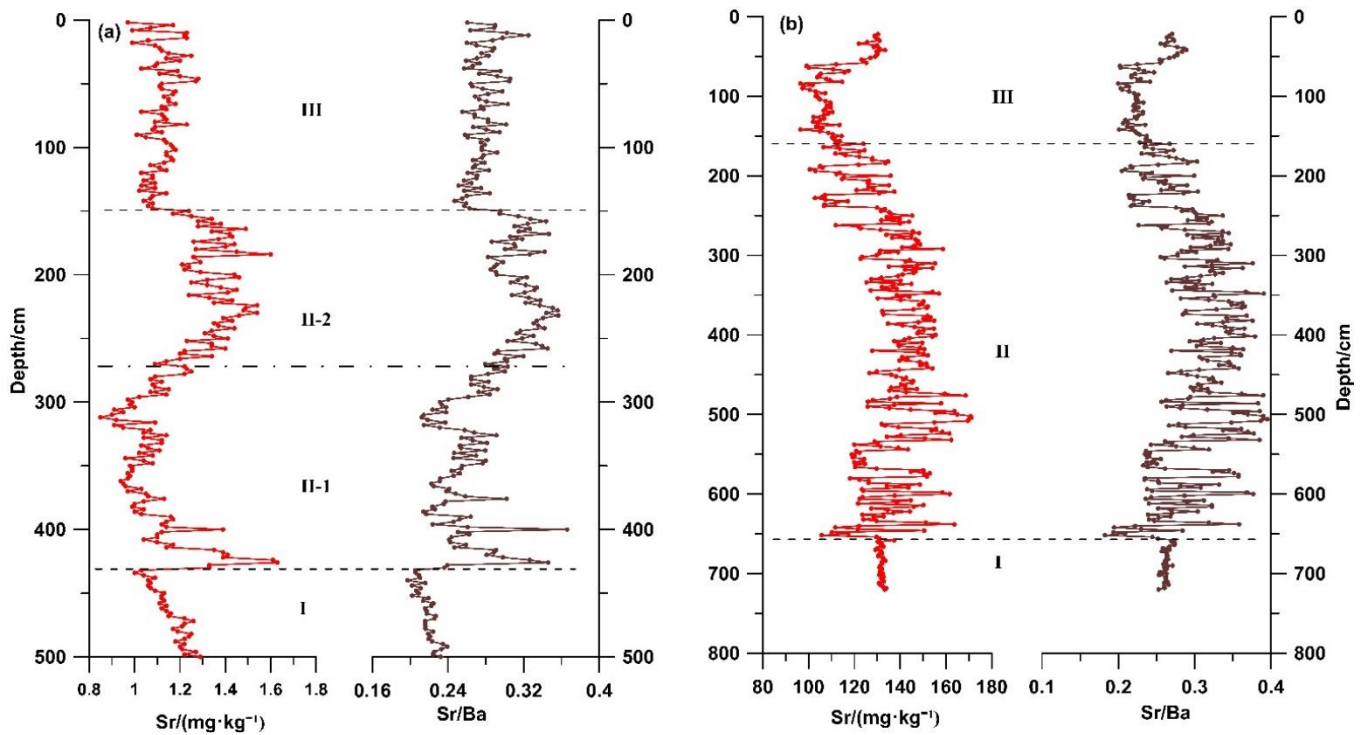


Figure 7. Variation characteristics of Sr and Sr/Ba ratio of sediments in GX (a) and CYK (b) profiles.

Table 2. Changes of Sr and Sr/Ba of sediment of GX and CYK profiles.

	GX Profile		CYK Profile	
	Sr (mg·kg ⁻¹)	Sr/Ba	Sr (mg·kg ⁻¹)	Sr/Ba
Mean	126.69	0.27	131.27	0.28
Max	154.90	0.37	171.10	0.40
Min	101.70	0.20	96.40	0.18
C.V (%)	9.6	14.1	12.4	17.3

5.3. Variation Characteristics of Freshwater–Saltwater Diatom Proportion

The diatom fossils of 26 and 25 samples were identified from GX and CYK profiles, respectively, and a total of 34 species of diatoms were identified. Among these were eight freshwater and 26 brackish water diatom species. The changes in the combination of diatom species indicated that the GX and CYK profiles could be divided into multiple diatom distribution zones from bottom to top (Figures 8 and 9). The distribution zones reflected a freshwater sedimentary environment, tidal flat–shallow sea sedimentary environment, and freshwater sedimentary environment, respectively.

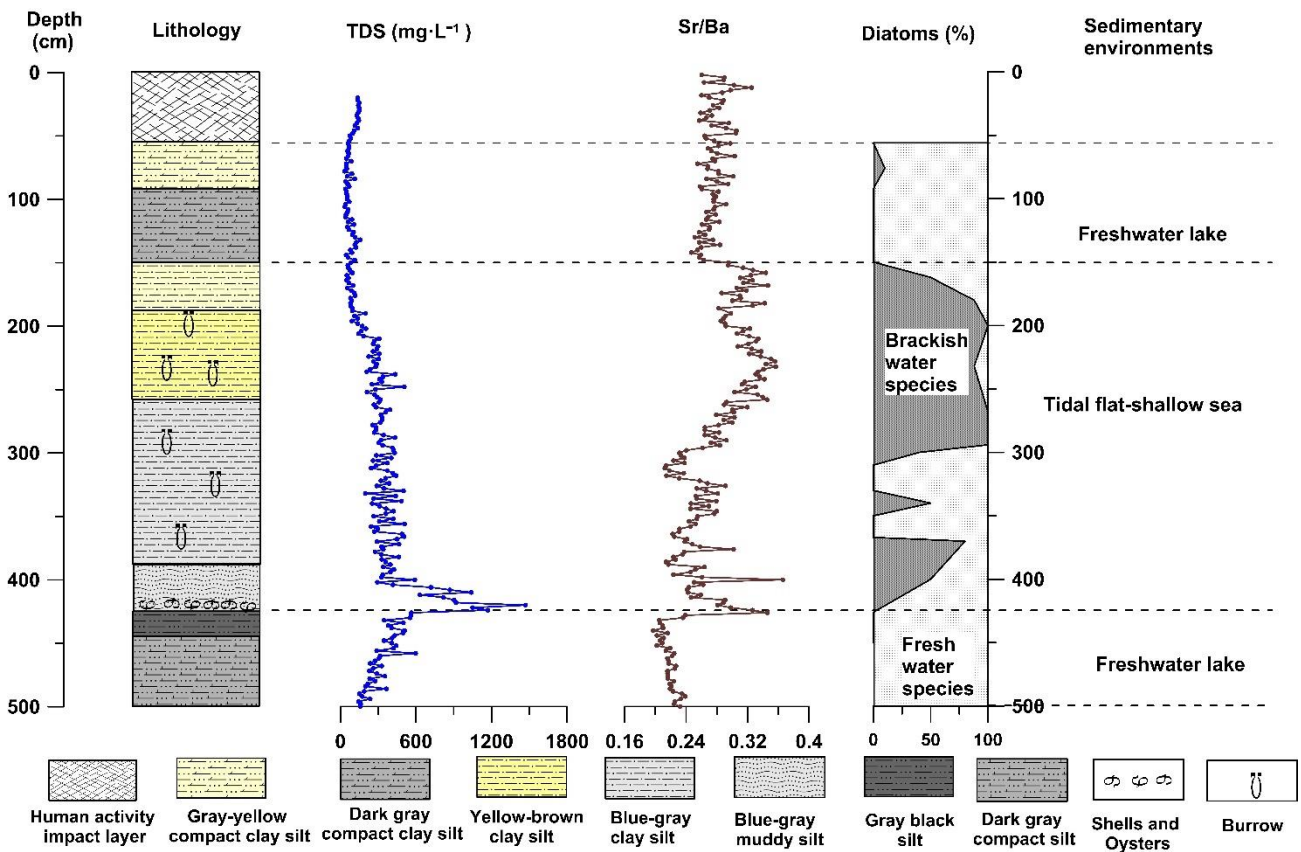


Figure 8. Comparison of lithology, TDS, Sr/Ba, and diatoms of GX section and sedimentary.

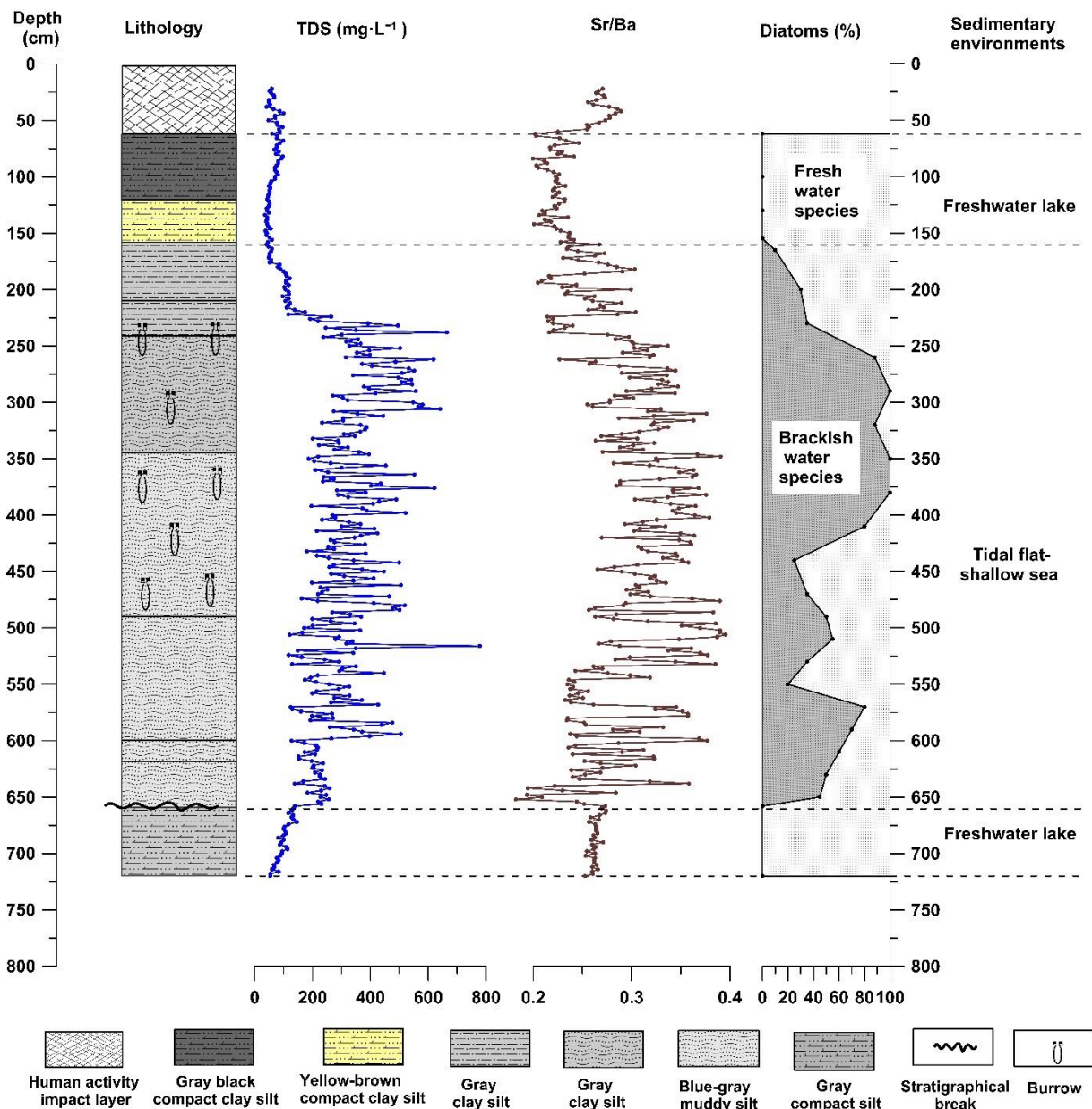


Figure 9. Comparison of lithology, TDS, Sr/Ba, and diatoms of CYK section and sedimentary environment.

6. Discussion

6.1. Reasons for Changes in Physicochemical Properties of Sediment Lixivium in Coastal Areas

The physicochemical properties of water reflect the amount of TDS, size of EC, and level of SAL in the water. TDS in the water was significantly correlated positively with EC and SAL (Figure 6). The physicochemical properties were related mainly to the amounts of soluble substances attached (or adsorbed) by the sediment itself. When sediments are deposited, the concentration of TDS in the water will differ when the sedimentation environment differs (i.e., fresh water and salt water). These soluble substances can change the total amount of TDS attached to the sediments through adsorption (precipitation), precipitation (dissolution), ion exchange, and other methods. When the amount of TDS in the water is high, the amount of TDS attached to the sediments is also large, and vice versa. When the dried and ground sediment powder was dissolved in a sufficient amount of ultrapure water, the soluble solids attached to the sediment were released because of the extremely low TDS concentration in the ultrapure water, thereby increasing the amount of

TDS in the solution. The larger the amount of TDS in the water of the original sedimentary environment, the larger would be the amount of TDS released into the ultrapure water, and vice versa. Therefore, the water environment of sediment deposition can be reconstructed according to the dissolved TDS (EC, SAL) in the ultrapure water.

6.2. Physicochemical Properties Index of Sediment Lixivium: A New Index Reflecting the Changes of Coastal Environment

Different sedimentary characteristics can be formed because of the differences in the dynamic conditions and the biological species living in the environment, as well as climate changes and sources of sediment. Therefore, sedimentary characteristics can also be used to invert the sedimentary environment. The distribution of diatom species in the sediments is controlled by environmental variables in the area, such as water temperature, salinity, depth, size of the water body, water depth, pH, and nutrients [44]. Diatoms are extremely important indicators for reconstructing the environment of ancient coastal areas [45–52]. The geochemical elements Sr and Ba are both soluble in water and migrate with water. The concentration of sulfate ion in water increases because of evaporation or seawater intrusion into the water environment. Then the Ba ions in the water body form barium sulphate and precipitate first. The solubility of strontium salts (sulphate and carbonate) would be slightly higher than that of barium salts, and the strontium salts would be precipitated after barium sulphate precipitation [53]. The change in the Sr and Sr/Ba ratio could indicate changes in salinity [39–43].

Sediment lithology, diatom species, geochemical elements and ratios, and physicochemical properties of sediment lixivium in the GX and CYK sections of the Subei Basin corresponded well. Their changing trends indicated that both profiles could be divided into three stages of sedimentary environments (Figures 8 and 9), implying that these physicochemical property indexes could indicate the evolution of the coastal sedimentary environment. Furthermore, Figures 8 and 9 show that the physicochemical property indexes agree well with the geochemical elements and ratios, as well as the diatom species generally. In particular, the stratigraphic boundary indicator at the beginning of transgression is highly consistent (the position of the dotted line in the lower part of Figures 8 and 9). However, some slight differences are detected in the details of the record. The first difference is that in the process of transgression, some minor fluctuations recorded in the diatom species, and geochemical elements and ratios are not reflected in the physicochemical property indexes of sediment lixivium. For example, at a depth of 370–300 cm in the GX profile, the diatom species, geochemical elements, and ratios fluctuated significantly; however, the physicochemical property indexes of sediment lixivium were not recorded. This could be ascribed to the rapid deposition rate, loose sediments, and easy infiltration of the upper salty water when transgression occurred, which obscured the small fluctuation records. The second difference is that at the end of transgression, the boundary line indicated by the physicochemical property indexes of sediment lixivium was slightly lower than was the boundary line indicated by the diatom species, geochemical elements, and the ratios. This could be ascribed to the fact that after transgression, the research section was located in a freshwater lake sedimentary environment and, because of the long-term immersion in fresh water, the soluble solids in the adjacent strata were dissolved and diluted.

7. Conclusions

Based on a study of the experimental process and change mechanism of TDS, EC, and SAL of sediment lixivium in the sea–land interaction zone of the Subei Basin, as well as comparison with geochemical elements and ratios and diatom species, the following conclusions can be drawn:

- (1) Through preliminary tests, a reasonable method of preparing sediment lixivium and the appropriate time for determining the physicochemical properties of sediment lixivium were determined. Ultrapure water had to be used in the process to ensure that the solvent did not contain soluble solids and to reduce the introduction of

external errors. The reasonable time for testing the physicochemical property indexes of the sediment lixivium was determined as 120 h (fully stirred daily) or 168 h (no stirring) after the production of sediment lixivium. The physicochemical properties measured at this time were stable, which could reflect the difference in the water environment in the sediment deposition to the greatest extent. It should be noted that the test time for the physicochemical properties of sediment lixivium on the same profile should be tested simultaneously.

- (2) The physicochemical property indexes (TDS, EC, and SAL) of the lixivium of sediments are extremely sensitive to changes in the water properties of the sedimentary environment, and could correspond well with geochemical elements and ratios and diatom species generally, indicating changes in the coastal sedimentary environment.
- (3) Compared with other indexes, the physicochemical property indexes of sediment lixivium have obvious advantages. Large (expensive) instruments or advanced professional knowledge is not required. The test is simple, highly sensitive, accurate, and inexpensive. Accordingly, this method could be considered a relatively ideal new indicator for studying paleoenvironmental changes in coastal areas. Therefore, the method has broad application prospects.
- (4) The physicochemical property indexes of sediment lixivium have many advantages, but also certain shortcomings. These include the fact that the records of the details during the transgression process are not obvious and, after the end of the transgression, the TDS adsorbed on the sediments could be reduced owing to the dilution effect of fresh water, resulting in a slight decrease in the boundary line that indicates the end of the transgression.

Author Contributions: Conceptualization, Q.S. and Y.C.; methodology, Y.C. and S.Z.; software, Q.S. and Y.C.; investigation, Q.S. and Y.C.; data curation, S.Z. and Y.C.; writing—original draft preparation, Q.S.; writing—review and editing, Q.S.; project administration, Q.S. All authors have read and agreed to the published version of the manuscript.

Funding: This work was supported by the National Natural Science Foundation of China (Grant No. 41671195 and 41801005); Marine science and technology innovation project of Jiangsu province (No. JSZRHYKJ202002).

Institutional Review Board Statement: Not applicable.

Informed Consent Statement: Not applicable.

Data Availability Statement: The data that support the findings of this study are available from the corresponding author upon request.

Acknowledgments: The authors would like to thank editors and reviewers for their valuable comments for the improvement of the manuscript.

Conflicts of Interest: The authors declare no conflict of interest.

References

1. Louvari, M.A.; Drinia, H.; Kontakiotis, G.; Di Bella, L.; Antonarakou, A.; Anastasakis, G. Impact of latest-glacial to Holocene sea-level oscillations on central Aegean shelf ecosystems: A benthic foraminiferal palaeoenvironmental assessment of South Evoikos Gulf, Greece. *J. Mar. Syst.* **2019**, *199*, 103181. [[CrossRef](#)]
2. Drinia, H.; Antonarakou, A.; Tsourou, T.; Kontakiotis, G.; Psychogiou, M.; Anastasakis, G. Foraminifera eco-biostratigraphy of the southern Evoikos outer shelf, central Aegean Sea, during MIS 5 to present. *Cont. Shelf Res.* **2016**, *126*, 36–49. [[CrossRef](#)]
3. Kontakiotis, G.; Karakitsios, V.; Mortyn, P.G.; Antonarakou, A.; Drinia, H.; Anastasakis, G.; Agiadi, K.; Kafousia, N.; De Rafelis, M. New insights into the early Pliocene hydrographic dynamics and their relationship to the climatic evolution of the Mediterranean Sea. *Palaeogeogr. Palaeoclimatol. Palaeoecol.* **2016**, *459*, 348–364. [[CrossRef](#)]
4. Kontakiotis, G.; Besiou, E.; Antonarakou, A.; Zarkogiannis, S.D.; Kostis, A.; Mortyn, P.G.; Moissette, P.; Cornée, J.-J.; Schulbert, C.; Drinia, H.; et al. Decoding sea surface and paleoclimate conditions in the eastern Mediterranean over the Tortonian-Messinian Transition. *Palaeogeogr. Palaeoclimatol. Palaeoecol.* **2019**, *534*, 109312. [[CrossRef](#)]

5. Vasiliev, I.; Karakitsios, V.; Bouloubassi, I.; Agiadi, K.; Kontakiotis, G.; Antonarakou, A.; Triantaphyllou, M.; Gogou, A.; Kafousia, N.; De Rafélis, M.; et al. Large Sea Surface Temperature, Salinity, and Productivity-Preservation Changes Preceding the Onset of the Messinian Salinity Crisis in the Eastern Mediterranean Sea. *Paleoceanogr. Paleoclimatol.* **2019**, *34*, 182–202. [[CrossRef](#)]
6. Lambeck, K.; Chappell, J. Sea level change through the last glacial cycle. *Science* **2001**, *292*, 679–686. [[CrossRef](#)] [[PubMed](#)]
7. Lambeck, K.; Antonioli, F.; Purcell, A.; Silenzi, S. Sea-level change along the Italian coast for the past 10,000 yr. *Quat. Sci. Rev.* **2004**, *23*, 1567–1598. [[CrossRef](#)]
8. Miller, K.G.; Kominz, M.A.; Browning, J.V.; Wright, J.D.; Mountain, G.S.; Katz, M.E.; Sugarman, P.J.; Cramer, B.S.; Christie-Blick, N.; Pekar, S.F. The Phanerozoic Record of Global Sea-Level Change. *Science* **2005**, *310*, 1293–1298. [[CrossRef](#)]
9. Kontakiotis, G.; Antonarakou, A.; Mortyn, P.; Drinia, H.; Anastasakis, G.; Zarkogiannis, S.D.; Möbius, J. Morphological recognition of *Globigerinoides ruber* morphotypes and their susceptibility to diagenetic alteration in the eastern Mediterranean Sea. *J. Mar. Syst.* **2017**, *174*, 12–24. [[CrossRef](#)]
10. Kontakiotis, G.; Efstathiou, E.; Zarkogiannis, S.; Besiou, E.; Antonarakou, A. Latitudinal Differentiation among Modern Planktonic Foraminiferal Populations of Central Mediterranean: Species-Specific Distribution Patterns and Size Variability. *J. Mar. Sci. Eng.* **2021**, *9*, 551. [[CrossRef](#)]
11. Antonarakou, A.; Kontakiotis, G.; Zarkogiannis, S.D.; Mortyn, P.; Drinia, H.; Koskeridou, E.; Anastasakis, G. Planktonic foraminiferal abnormalities in coastal and open marine eastern Mediterranean environments: A natural stress monitoring approach in recent and early Holocene marine systems. *J. Mar. Syst.* **2018**, *181*, 63–78. [[CrossRef](#)]
12. Giamali, C.; Koskeridou, E.; Antonarakou, A.; Ioakim, C.; Kontakiotis, G.; Karageorgis, A.P.; Roussakis, G.; Karakitsios, V. Multiproxy ecosystem response of abrupt Holocene climatic changes in the northeastern Mediterranean sedimentary archive and hydrologic regime. *Quat. Res.* **2019**, *92*, 665–685. [[CrossRef](#)]
13. Giamali, C.; Kontakiotis, G.; Koskeridou, E.; Ioakim, C.; Antonarakou, A. Key Environmental Factors Controlling Planktonic Foraminiferal and Pteropod Community's Response to Late Quaternary Hydroclimate Changes in the South Aegean Sea (Eastern Mediterranean). *J. Mar. Sci. Eng.* **2020**, *8*, 709. [[CrossRef](#)]
14. Zarkogiannis, S.; Kontakiotis, G.; Antonarakou, A. Recent planktonic foraminifera population and size response to Eastern Mediterranean hydrography. *Revue Micropaléontologie* **2020**, *69*, 100450. [[CrossRef](#)]
15. Lighty, R.G.; MacIntyre, I.G.; Stuckenrath, R. Submerged early Holocene barrier reef south-east Florida shelf. *Nature* **1978**, *276*, 59–60. [[CrossRef](#)]
16. Goff, J.A.; Austin, J.A.; Goodman-Tchernov, B.N. Estuarine development and early Holocene transgression across an aeolianite substrate, Caesarea, central Israel. *Cont. Shelf Res.* **2018**, *158*, 33–44. [[CrossRef](#)]
17. Liu, R.; Qin, J.; Mei, X. Sedimentary environment changes of the Ningshao Plain since the later stage of the Late Pleistocene: Evidence from palynology and stable organic carbon isotopes. *Quat. Int.* **2014**, *333*, 188–197. [[CrossRef](#)]
18. Jarvis, I.; Mabrouk, A.; Moody, R.T.; de Cabrera, S. Late Cretaceous (Campanian) carbon isotope events, sea-level change and correlation of the Tethyan and Boreal realms. *Palaeogeogr. Palaeoclimatol. Palaeoecol.* **2002**, *188*, 215–248. [[CrossRef](#)]
19. Kontakiotis, G. Late Quaternary paleoenvironmental reconstruction and paleoclimatic implications of the Aegean Sea (eastern Mediterranean) based on paleoceanographic indexes and stable isotopes. *Quat. Int.* **2016**, *401*, 28–42. [[CrossRef](#)]
20. Kontakiotis, G.; Mortyn, P.G.; Antonarakou, A.; Martínez-Botí, M.A.; Triantaphyllou, M.V. Field-based validation of a diagenetic effect on *G. ruber* Mg/Ca paleothermometry: Core top results from the Aegean Sea (eastern Mediterranean). *Geochem. Geophys. Geosyst.* **2011**, *12*. [[CrossRef](#)]
21. Kontakiotis, G.; Moforis, L.; Karakitsios, V.; Antonarakou, A. Sedimentary Facies Analysis, Reservoir Characteristics and Paleogeography Significance of the Early Jurassic to Eocene Carbonates in Epirus (Ionian Zone, Western Greece). *J. Mar. Sci. Eng.* **2020**, *8*, 706. [[CrossRef](#)]
22. Kontakiotis, G.; Mortyn, P.G.; Antonarakou, A.; Drinia, H. Assessing the reliability of foraminiferal Mg/Ca thermometry by comparing field-samples and culture experiments: A review. *Geol. Q.* **2016**, *60*, 547–560. [[CrossRef](#)]
23. Antonarakou, A.; Kontakiotis, G.; Mortyn, P.G.; Drinia, H.; Sprovieri, M.; Besiou, E.; Tripsanas, E. Biotic and geochemical ($\delta^{18}\text{O}$, $\delta^{13}\text{C}$, Mg/Ca, Ba/Ca) responses of *Globigerinoides ruber* morphotypes to upper water column variations during the last deglaciation, Gulf of Mexico. *Geochim. Cosmochim. Acta* **2015**, *170*, 69–93. [[CrossRef](#)]
24. Wang, P. The use and misuse of microfossils in marine transgression studies. *Quat. Sci.* **1992**, *12*, 321–331.
25. Zhang, M.; Liu, S.; Chen, M. *Late Quaternary Event Geology of Coastal Zone in China*; Geological Publishing House: Beijing, China, 2000.
26. Makri, P.; Stathopoulou, E.; Hermides, D.; Kontakiotis, G.; Zarkogiannis, S.D.; Skilodimou, H.D.; Bathrellos, G.D.; Antonarakou, A.; Scoullou, M. The Environmental Impact of a Complex Hydrogeological System on Hydrocarbon-Pollutants' Natural Attenuation: The Case of the Coastal Aquifers in Eleusis, West Attica, Greece. *J. Mar. Sci. Eng.* **2020**, *8*, 1018. [[CrossRef](#)]
27. Hermides, D.; Makri, P.; Kontakiotis, G.; Antonarakou, A. Advances in the Coastal and Submarine Groundwater Processes: Controls and Environmental Impact on the Thriassion Plain and Eleusis Gulf (Attica, Greece). *J. Mar. Sci. Eng.* **2020**, *8*, 944. [[CrossRef](#)]
28. Pesce, S.F.; Wunderlin, D.A. Use of water quality indices to verify the impact of Córdoba City (Argentina) on Suquía River. *Water Res.* **2000**, *34*, 2915–2926. [[CrossRef](#)]
29. Cude, C.G. Oregon water quality index a tool for evaluating water quality management effectiveness. *JAWRA J. Am. Water Resour. Assoc.* **2001**, *37*, 125–137. [[CrossRef](#)]

30. Subramani, T.; Elango, L.; Damodarasamy, S.R. Groundwater quality and its suitability for drinking and agricultural use in Chithar River Basin, Tamil Nadu, India. *Environ. Earth Sci.* **2005**, *47*, 1099–1110. [[CrossRef](#)]
31. Sylus, K.; Ramesh, H. The Study of Sea Water Intrusion in Coastal Aquifer by Electrical Conductivity and Total Dissolved Solid Method in Gurpur and Netravathi River Basin. *Aquat. Procedia* **2015**, *4*, 57–64. [[CrossRef](#)]
32. Salmani, M.H.; Jajaei, E.S. Forecasting models for flow and total dissolved solids in Karoun river-Iran. *J. Hydrol.* **2016**, *535*, 148–159. [[CrossRef](#)]
33. Yokoyama, T. Measurement of Electric Conductivity. In *A Handbook of Quaternary Research (2)*; Japan Association for Quaternary Research, Ed.; University of Tokyo Press: Tokyo, Japan, 1993; pp. 109–118.
34. Fang, J.; Wu, Y.; Li, R.; Zhou, J.; Kang, L.; Chai, R.; Ma, N. Discussion on the marine regression event during the Early-Middle Holocene in the Liaoning Coast. *Earth Sci. Front.* **2009**, *16*, 396–403.
35. Fang, J.; Yang, Y.; Ma, H.; Liu, B.; Wang, H.; Yu, L.; Liu, J.; Hu, K. Edimentary environmental analysis based on the electric conductivity and Ph of stirred clayed drilling cores in water and diatom recovered from the old drowned valley plain in the Dagu Mountain, Liaodong Peninsula in china. *Acta Oceanol. Sin.* **2012**, *34*, 133–141.
36. Chen, Y.; Yan, Q.; Xu, S. Evolution of the sedimentary environments in north Jiangsu basin and its tectonic setting. *Sci. Geol. Sin.* **1993**, *28*, 151–160.
37. Ji, A.; Tao, G.; Zhuo, S.; Luo, L. *X-ray Fluorescence Spectrometric Analysis*; Science Press: Beijing, China, 2003; pp. 201–203.
38. Shu, Q.; Zhao, Y.; Frechen, M.; Zhang, J.; Chen, Y.; Liu, Y.; Yang, P. Chronology of a sedimentary sequence from the land–ocean interaction zone in the North Jiangsu Basin. *Quat. Int.* **2021**, *580*, 78–86. [[CrossRef](#)]
39. Zhao, Y.; Yan, M. *Geochemistry of Sediments of the China Shelf Sea*; Science Press: Beijing, China, 1994; pp. 43–48.
40. Liu, Y.; Song, T. Discussion on characteristics of geochemical and sedimentary environments of the Shisanlitai Formation of Fuzhou Bay, Liaoning province. *Acta Sedimentol. Sin.* **2009**, *27*, 1018–1026.
41. Yu, Y.; Zhang, C.; Zhang, S.; Shi, H.; Du, J. Research on source direction of Neogene Zhujiang Formation in Huizhou Depression. *Fault Block Oil Gas Field* **2012**, *19*, 17–21.
42. Wei, W.; Algeo, T.J. Elemental proxies for paleosalinity analysis of ancient shales and mudrocks. *Geochim. Cosmochim. Acta* **2020**, *287*, 341–366. [[CrossRef](#)]
43. Wei, W.; Algeo, T.J.; Lu, Y.; Lu, Y.; Liu, H.; Zhang, S.; Peng, L.; Zhang, J.; Chen, L. Identifying marine incursions into the Paleogene Bohai Bay Basin lake system in northeastern China. *Int. J. Coal Geol.* **2018**, *200*, 1–17. [[CrossRef](#)]
44. Bradshaw, E.G.; Anderson, N.J.; Jensen, J.P.; Jeppesen, E. Phosphorus dynamics in Danish lakes and the implications for diatom ecology and palaeoecology. *Freshw. Biol.* **2002**, *47*, 1963–1975. [[CrossRef](#)]
45. Zong, Y.; Huang, G.; Switzer, A.D.; Yu, F.; Yim, W.W.-S. An evolutionary model for the Holocene formation of the Pearl River delta, China. *Holocene* **2009**, *19*, 129–142. [[CrossRef](#)]
46. Long, A.J.; Barlow, N.; Dawson, S.; Hill, J.; Innes, J.B.; Kelham, C.; Milne, F.D.; Dawson, A. Lateglacial and Holocene relative sea-level changes and first evidence for the *Storegga tsunami* in Sutherland, Scotland. *J. Quat. Sci.* **2016**, *31*, 239–255. [[CrossRef](#)]
47. Lund, J.W.G.; Hendey, N.I. An Introductory Account of the Smaller Algae of British Coastal Waters. Part V. Bacillariophyceae (Diatoms). *J. Ecol.* **1965**, *53*, 549. [[CrossRef](#)]
48. Sancetta, C. Oceanographic and ecologic significance of diatoms in surface sediments of the Bering and Okhotsk seas. *Deep Sea Res. Oceanogr. Res. Pap.* **1981**, *28*, 789–817. [[CrossRef](#)]
49. Round, F.E.; Crawford, R.M.; Mann, D.G. *The Diatoms*; Cambridge University Press: Cambridge, UK, 1990; pp. 1–747.
50. Tomas, C.R. *Identifying Marine Phytoplankton*; Academic Press: San Diego, CA, USA, 1997.
51. Pushkar, V.; Roof, S.R.; Cherepanova, M.V.; Hopkins, D.M.; Brigham-Grette, J. Paleogeographic and paleoclimatic significance of diatoms from middle Pleistocene marine and glaciomarine deposits on Baldwin Peninsula, northwestern Alaska. *Palaeogeogr. Palaeoclimatol. Palaeoecol.* **1999**, *152*, 67–85. [[CrossRef](#)]
52. Lan, B.; Lan, D.; Zheng, Z.; Shi, X. Diatoms and their palaeoenvironments from the cores of Xijiang Delta in China. *Acta Oceanol. Sin.* **2008**, *30*, 93–99.
53. Liu, Y.; Cao, L. *Introduction to Element Geochemistry*; Geological Publishing House: Beijing, China, 1993; pp. 42–56.

MDPI
St. Alban-Anlage 66
4052 Basel
Switzerland
Tel. +41 61 683 77 34
Fax +41 61 302 89 18
www.mdpi.com

Journal of Marine Science and Engineering Editorial Office

E-mail: jmse@mdpi.com
www.mdpi.com/journal/jmse



MDPI
St. Alban-Anlage 66
4052 Basel
Switzerland

Tel: +41 61 683 77 34
Fax: +41 61 302 89 18

www.mdpi.com



ISBN 978-3-0365-1697-4